Continuous and Stochastic Descriptions of Active Matter

Ilyas Djafer-Cherif

NNT : 2017 SACLS 216

Thèse de doctorat de l'Université Paris-Saclay préparée à l' Université Paris-Sud

Ecole doctorale n°564
Physique en Ile-de-France
Spécialité de doctorat : Physique

par

M. Ilyas Djafer-Cherif

Descriptions continues et stochastiques de la matière active

Thèse présentée et soutenue à Institut des Systèmes Complexes,113 rue Nationale 75013, Paris France, le 24 juillet 2017.

Composition du Jury :

M.	Marcel Filoche	D.R PMC Polytechnqiue UMR7643	(Président)
M.	Hugues Berry	D.R INRIA Rhone-Alpes UMR5205	(Rapporteur)
Mme.	Nelly Henry	D.R Laboratoire Jean Perrin UMR 8237	(Rapportrice)
M.	Guillaume Grégoire	C.R MSC UMR 7057	(Examinateur)
M.	Hugues Chaté	D.R SPEC CNRS/UMR 3680	(Directeur de thèse)

Résumé

1 Introduction

La “matière active” définit au sens large des systèmes macroscopiques qui sont composés d’entitées au niveau microscopiques qui sont capables de produire du mouvement sans forçage externe. C’est à dire qu’elles produisent du mouvement en consommant de l’énergie. Cette définition étant très générique, elle concerne une très large gamme de systèmes ce qui caractérise bien la diversité des recherches sur ce sujet. En effet la matière active concerne aussi bien la sédimentation de particules de “Janus” - une classe particulière de coloïdes exhibtant une activité quand un champ électrique est appliqué dans le fluide environnant, au comportement des piétons dans les environnements clos en passant par les vols d’étourneaux ce qui en fait un sujet particulièrement *à la mode*.

Bien que le sujet même de la nature “hors d’équilibre” de la propulsion puisse être un sujet d’étude intéressant en-soi, la caractéristique fascinante de tels systèmes est de pouvoir faire émerger des comportemements collectifs. C’est à dire des phénomènes d’auto-organisation sans présence d’un leader, par exemple on peut observer l’apparition de phénomènes “d’attroupement” (flocking en anglais) pour les oiseaux [3], les bancs de poisson [2] ou encore dans les bactéries confinées telles que le maintenant fameux système de microtubules mis en mouvement par des moteurs moléculaires de kinésine [4].

Parmi les modèles les plus célèbres permettant de modéliser de tels systèmes il y a le fameux “modèle de Vicsek” qui modélise les oiseaux, poissons et autres par des particules ponctuelles qui se déplacent *à vitesse constante* et s’alignent polairement dans un certain rayon d’intéraction, en plus d’un bruit modélisant l’incertitude sur l’alignement ou d’autres phénomènes. Ce modèle très simple à montré qu’une compétition entre alignement et bruit est à l’origine des phénomènes des mouvement collectifs.

Dans ce cadre nous allons présenter deux modèles aux objectifs différents. Le premier sur les nématiques actifs est une extension du modèle de Vicsek et le second

sur la bactérie *Neisseria meningitiids*

2 Nématiques actifs

2.1 Symétrie nématique

Comme le nom l'indique notre modèle s'intéresse principalement aux nématiques. La nématicité est une type de symétrie de particules qu'on considère. La symétrie la plus connue est polaire c'est à dire que les particules s'alignent toutes *dans le même sens* et vont donc au final se déplacer en groupe, c'est notamment le cas des précédents systèmes que nous avons énuméré: oiseaux, poissons ... La symétrie nématique est moins contraignante, puisqu'elle signifie que les particules sont seulement alignées *dans la même direction* , typiquement l'on considère des particules longilignes possédant un axe principal de symétrie qui fait émerger ce genre de symétrie, cette symétrie se manifeste dans notre modélisation des collisions des particules comme illustré dans la figure 1 où on considère des batonnets collisionnant tête-bêche ou tête-à-tête, (les vecteurs rouges sont les vecteurs vitesses) : quelque soit le cas considéré l'issue est la même la même du point de vue de la direction des batonnets, ils sont alignés. La symétrie nématique est omniprésente à l'échelle bacterienne car de nombreuses bactéries sont longilignes et interagissent donc de la sorte (même si les détails de la collision peuvent-être plus complexes que la vision idéalisée que nous présentons).

2.2 Modèle

Nous allons donc modéliser des particules nématique en ajoutant le plus de caractéristiques nous permettant de modéliser des systèmes de bactérie:

- Un alignement qui doit être nématique
- Un terme de répulsion permettant de rendre compte de l'extension spatiale des partiucles
- Un contrôle sur la propulsion qui peut être soit diffusive

Notre modèle est donc résumé par l'équation suivante (2) décrivant le déplacement de chaque particule i dont la position est x_i et la direction $\mathbf{u}_i$:

$$x_i(t+1) = x_i(t) + v_0 \mathbf{u}_i(t+1) \tag{1}$$

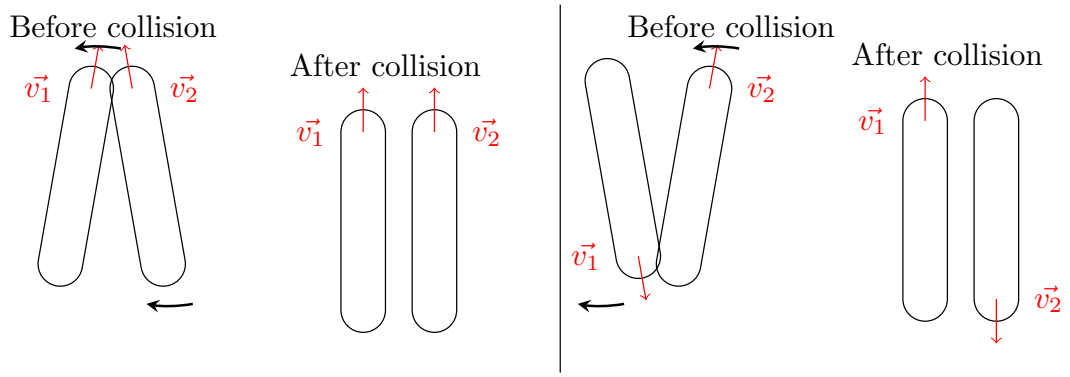

Figure 1: Lors d'une collision nématique les particules se réiorientent selon leur "direction" moyenne en gardant leur orientation relative (elles ne tournent pas de plus de $\frac{\pi}{2}$)

Et θ_i , angle de $\mathbf{u}_i$ est donné par le terme (2):

$$\theta_i(t+1) = \arg\left\{\epsilon_i \mathbf{A}_i(t) + \beta \mathbf{R}_i(t)\right\} + \eta\xi_i(t) \tag{2}$$

η est l'amplitude angulaire du bruit (ξ est un bruit blanc sur $[-1, +1]$)

ϵ_i est un terme qui vaut stochastiquement ± 1 avec une probabilité $1 - kf$ et k_f respectivement et contient la persistence de l'auto-propulsion .

L'alignement nématique est contenu dans le terme $\mathbf{A}_i$

$$\mathbf{A}_i(t) = \frac{1}{N_i} \sum_{j \in \partial i} \operatorname{sgn}\left\{\cos(\theta_i(t) - \theta_j(t))\right\} \mathbf{u}_j \tag{3}$$

Quant à la répulsion elle est contenue dans le terme $\mathbf{R}_i$ et son intensité est β:

$$\mathbf{R}_i(t) = \frac{1}{N_i - 1} \sum_{\partial i, i \neq j} \mathbf{u}_{ji} \tag{4}$$

2.3 Principaux résultats

Nous avons principalement décrit les différentes phases nouvelles générées par ce modèle puis opéré à des simulations systématiques nous permettant d'obtenir divers diagrammes des phases en fonction des paramètres précédemment énumérés. Dans toutes les figures suivantes la couleur indique l'orientation nématique (comprise entre $[-\pi, \pi]$

2.3.1 Tiges

Dans cette phase caractéristant les tiges les particules interagissent nématiquement mais leur propulsion est essentiellement polaire (c'est à dire que $k_f = 0$) , on retrouve ainsi une phase de bandes polaires 2(b) mais bien différente des bandes repertoriées dans le modèle de Vicsek. Par ailleurs la phase nématique homogène est relativement instable et il existe une instabilité longitudinale (le long de l'ordre) qui est d'abord linéaire 2(a) puis aboutit à un régime chaotique. Finalement la transition transition ordre désordre classique est toujours présente ce qui est résumé dans le diagramme de phase 2(c).

2.3.2 Nématiques purs

Nous considérons maintenant le cas où la propulsion est elle aussi "nématique" : c'est à dire que les particules diffusent selon leur grand axe indifféremment à droite ou à gauche. Dans ce cas là le diagramme de phase conserve toujours une transition ordre/désorde ainsi qu'une phase nématique homogène mais on voit l'apparition de structures nouvelles qu'on appelle "arches" 3(a), ces structures sont symétriques, inhomogènes et occupent une grande partie du diagramme de phases. Nous avons montré que ces structures sont polaires ce qui permet d'expliquer l'apparition d'un régime de "défauts ordonnés" 3(b) (à bas ρ et bas v_0) déjà répertorié dans la littérature. Nous avons par ailleurs placé ces structures dans le diagramme des phases 3(c).

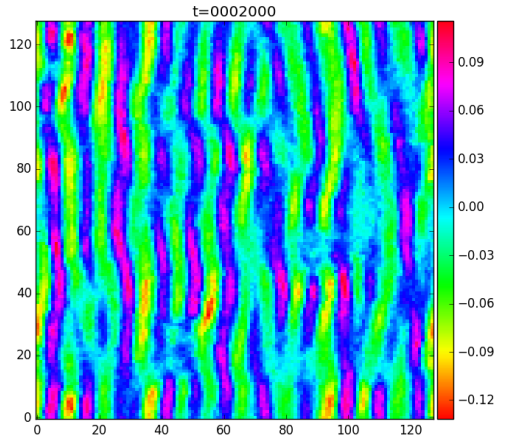

(a) Les ondulations linéaires qui vireront vers le chaos plus tard ($t = 2000$)

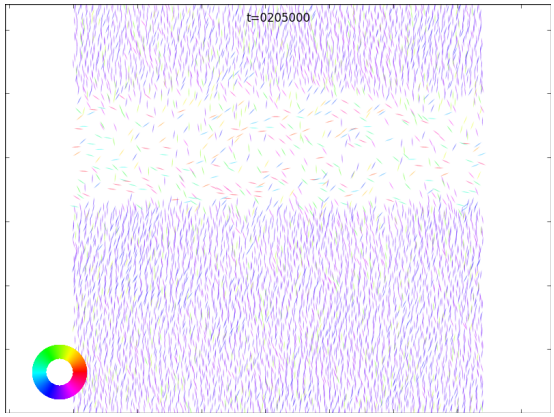

(b) Les bandes polaires dans notre modèle sont très homogènes

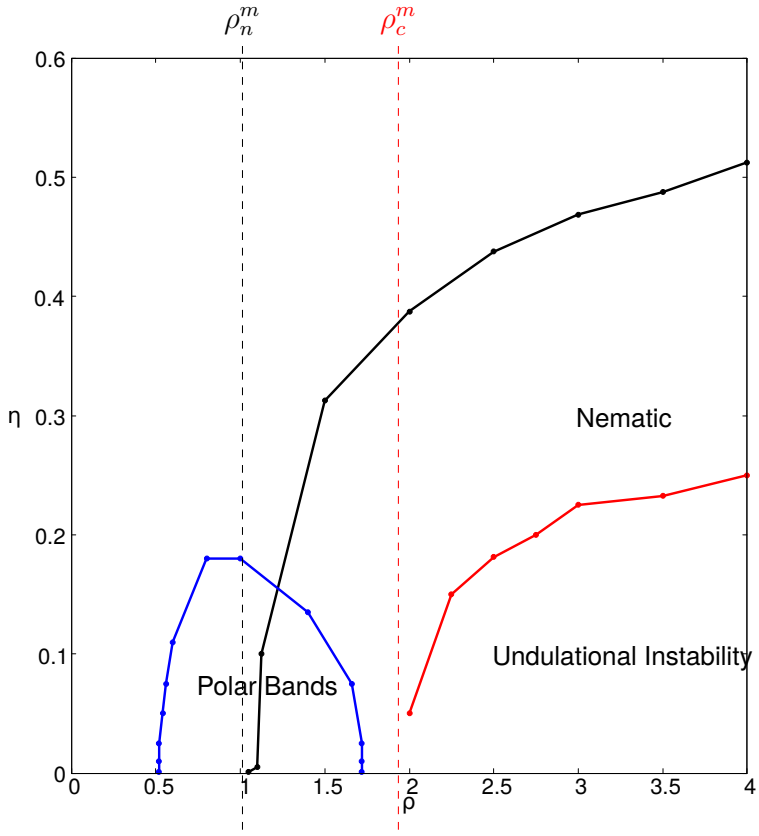

(c) Diagramme de phase des tiges

Figure 2: Le diagramme des phases pour les “batonnets” ainsi que les structures obtenues.

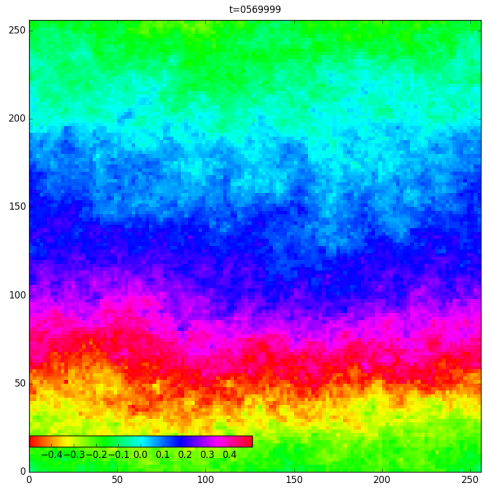

(a) Une arche, l'angle nématique varie continuement le long de l'axe O_y

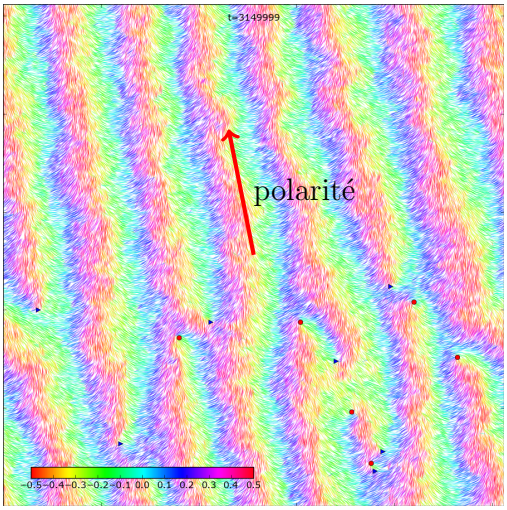

(b) A plus basse densité les arches advectent les défauts ("défauts ordonnés").

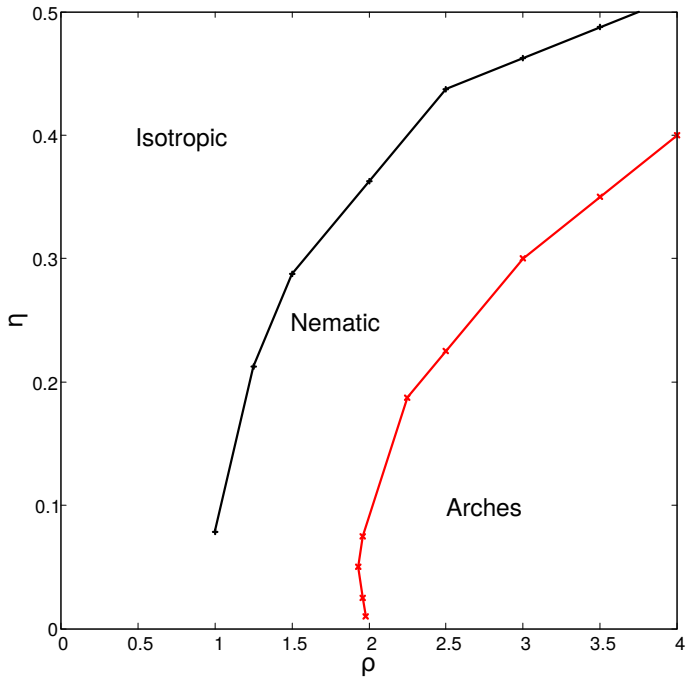

(c) Le diagramme de phase pour les nématiques purs à haute vitesse (pas de "défauts ordonnés")

Figure 3: Les arches sont la nouvelle structure qui apparaît dans le cas de particules purements nématiques ($k_f = 0$)

3 *Neisseria Meningitidis*

Ce modèle plus précis s'intéresse à la modélisation d'une bactérie dont la caractéristique principale est de pouvoir

Dans un second temps, nous étudions la bactérie Neisseria Meningitidis qui présente la particularité de générer des "pili", filaments de plusieurs micromètres de long. En dépolymérisant ces structures, à vitesse constantes (≈1 μm/s), elle est capable de en générer des forces gigantesques pour le vivant [1] (≈100 pN). Cette bactérie a tendance à former des aggrégats sphériques, présentant toutes les propriétés d'un liquide, pour coloniser l'organisme de l'hôte. Des mesures de viscosité et de tension de surface de ces aggrégats ont montré le rôle crucial du nombre de pili. Fort de ces constats nous avons bati un modèle microscopique dont la particularité est l'introduction de potentiels stochastiquement attractifs, c'est à dire que les particles transitent entre un état attractif et un état diffusif. Cette partie retranscrit l'évolution du modèle au cours du temps.

3.1 Modèle

La dynamique des bactéries suit une équation de Langevin classique qui s'écrit dans le cas où le système est à 2 dimensions (5):

$$\frac{d\vec{r_i}}{dt} = \frac{1}{\gamma}\sum_{j\in\partial i}\vec{F}_{ij} + \sqrt{4D}\vec{\eta} \tag{5}$$

- "∂i" représente les voisins de Voronoï de la bactérie indicée i (voir 4(a)
- η est un bruit Gaussien vectoriel normé (de moyenne 0 et de variance unité : $< \eta(t)\eta(t') >= \delta(t-t')$)
- D est le coefficient de diffusion dû aux effets thermiques.
- $\vec{F}_{ij}$ est la force exercée entre voisins, elle reste à déterminer.
- γ est le coefficient de friction avec le liquide, dans la suite nous nous en passons en l'ajustant à 1 via un changement d'unité.

La forme de la force répulsive n'est pas fondamentalemnt importante puisqu'elle doit être juste suffisamment forte pour éviter l'interpénétration des particules (6).

$$F(r \leq r_0) = \alpha\frac{1}{r^2}\vec{\mathbf{e}}_{ij} \tag{6}$$

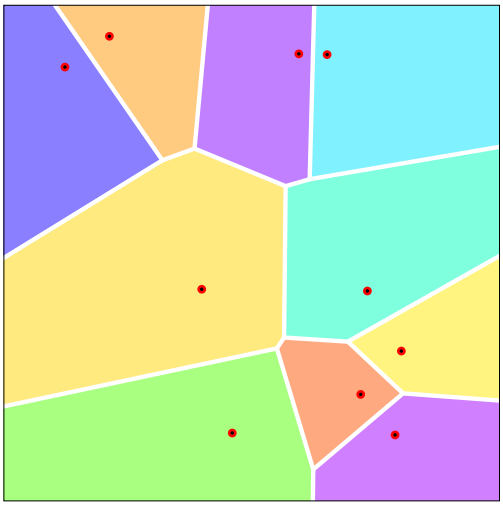

(a) Le voisins de voronï sont les cellules adjacentes de la cellule considérée

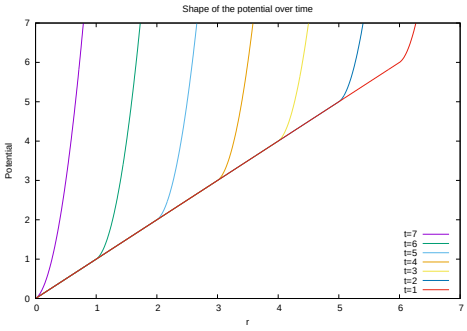

(b) L'allure du potentiel attractif qui bouge au cours du temps

Figure 4: La modélisation

La forme de la force d'attraction F_{ij}^{att} est beaucoup plus importante puisqu'elle doit imposer la contrainte de vitesse de rétraction des pili de $\approx 1\mu\text{m/s}$, nous avons utilisé l'équation (7) qui est une force qui tent à corriger l'erreur produite à chaque pas de temps δt entre la position "espérée" et la position effective. On peut voir ça en terme de potentiel "mouvant" qui devient de plus en plus fort au fur et à mesure du temps 4(b)

$$F_{ij}^{\text{att}} = \frac{\gamma}{2}\frac{(r_{ij} - (r_{ij}^0 - v_r(t_{ij} + \delta t)))}{\delta t}\mathbf{e}_{ij} \tag{7}$$

La chose la plus importante pour le modèle est l'intégration de deux phases: la force d'attraction est stochastiquement activée (état ON) ou éteinte (état OFF) caractérisés par deux temps de persistance t_{on} et t_{off} c'est à dire (8)

$$\begin{aligned} P(\text{off} \to \text{on}) &= dt/t_{\text{off}} \\ P(\text{on} \to \text{off}) &= dt/t_{\text{on}} \end{aligned} \tag{8}$$

3.2 Résultats

Nous avons essentiellement caractérisé le système grâce à deux quantités: le rayon de gyration R_g (9) qui permet de caractériser une phase cohésive quand il fluctue autour d'une moyenne (liquide) par rapport à une phase non-cohésive lorsqu'il croit (gaz) ainsi que la MSD (lisée) globale de l'aggrégat (10) qui nous permet de différencier un solide d'un liquide car elle est très faible dans un solide. Nous avons ainsi pu obtenir un "diagramme de phase" montrant de manière unifiée ces 3 phases en détectant un saut de l'un ou l'autre des paramètres d'une manière unifiée. Essentiellement on peut décire l'état du système en fonction du rapport $\frac{t_{\text{off}}}{t_{\text{on}}}$, et nous avons choisi $t_{on} = 15$ car c'est la valeur expérimentale, comme on peut le voir dans 5(a) on obtient bien ces 3 phases : solide, liquide puis gaz au fur et à mesure que ce rapport augmente.

$$R_g(t) = \sqrt{\frac{1}{N}\sum_{i=1}^{n}(r_i(t) - < r_i(t) >)^2} \tag{9}$$

$$\text{MSD}(t) = \frac{1}{N}\sum_{i=1}^{N}\frac{1}{T-t}\int_0^{T-t} d\tau |\mathbf{x}_i(t+\tau) - \mathbf{x}_i(\tau)|^2 \tag{10}$$

L'aspect non monotone de la courbe de la diffusion globale des aggrégats associée au fait qu'elle dépasse la imple diffusion thermique nous a amené à nous interroger sur la signature hors signature de l'aspect "hors d'équilibre" du système. Il se trouve qu'elle se trouve principalement au bord où l'on mesure une diffusion plus élevée au bord que la simple diffusion thermique ($\approx 1\mu$m/s). Ces inhomogénéités de l'aggrégat sont reproduites de manière synthétique dans 5(b) et reproduisent très bien les résultats expérimentaux (courbe rouge)

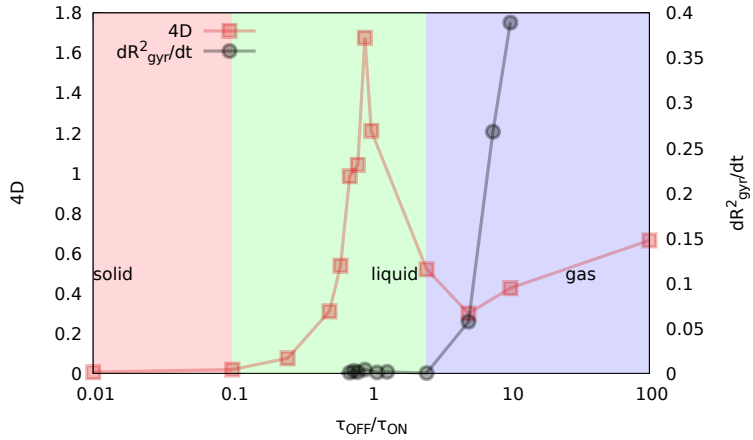

(a) Le diagramme de phase du modèle, on passe du solide au liquide puis au gaz en augmentant le rapport $\frac{t_{\text{off}}}{t_{\text{on}}}$

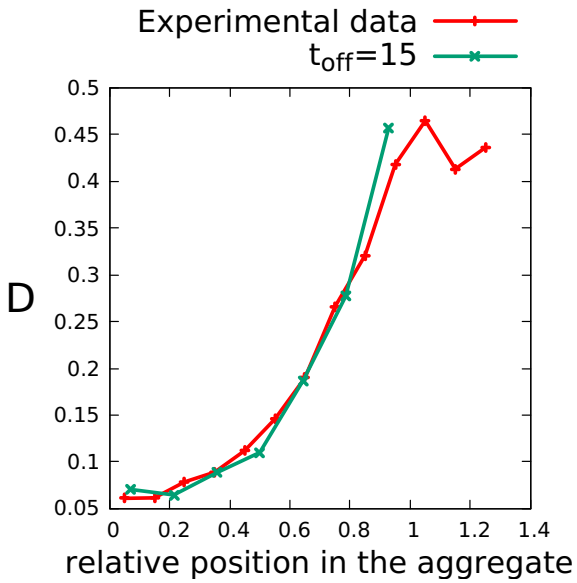

(b) Evolution de la diffusion en fonction de la distance au centre de masse de l'aggrégat

Figure 5: Principaux résultats du modèle

References

[1] Nicolas Biais et al. “Cooperative Retraction of Bundled Type IV Pili Enables Nanonewton Force Generation”. en. In: *PLoS Biology* 6.4 (2008). Ed. by Manfred Schliwa, e87. ISSN: 1544-9173, 1545-7885. DOI: 10.1371/journal.pbio.0060087. URL: http://dx.plos.org/10.1371/journal.pbio.0060087.

[2] Dirk Helbing et al. “Simulation of pedestrian crowds in normal and evacuation situations”. In: *Pedestrian and evacuation dynamics* 21 (2002), pp. 21–58.

[3] Nagy Máté et al. “Hierarchical group dynamics in pigeon flocks.” In: *Nature, 464(7290) :890893* (2010).

[4] Tim Sanchez et al. “Spontaneous motion in hierarchically assembled active matter”. In: *Nature* 491.7424 (Nov. 2012), pp. 431–434. ISSN: 0028-0836, 1476-4687. DOI: 10.1038/nature11591. URL: http://www.nature.com/doifinder/10.1038/nature11591.

Contents

Chapter 1

Generalities

1.1 Active Matter

We start by defining what *Active Matter* is : in its broader definition a system can be qualified as such at the macroscopic level if it is composed of entities, at the microscopic level, which are able to produce movement without any external forcing - in other words on their own: locally consumming energy in order to produce movement. The other term encountered in the literature is *Self-Propelled Particles* (often abbreviated SPP for convenience).

This definition is so generic that it might include all the "non inert" matter, as soon as it shows some kind of self-propulsion, which gives this term a quite wide applicability which is typical of the diversity of research on this particular subject. Indeed, the field of research on Active Matter is ranging from sedimentation of Janus particles [61] - a particular class of colloids showing activity when an electrical field is applied - to pedestrian behaviour in constrained environments [21] through bird flocks [33] making it a very "*fashionable*" subject.

SPP particles also encompass the category of “active granulars” which are mostly experimental systems[1] in which grains which can be of various shapes are vibrated. Hence the grains don’t produce movement by an internal mechanism but are rather agitated from an external source. However it still falls in the active systems definition because if we restrict the observations to the system of particles and exclude the external forcing it is clear that the behaviour is not equilibrium-like [24]. These experimental systems are very useful to understand the influence of departure from equilibrium because we can control the source of movement contrary to more complex systems where the movement production is in itself an ongoing research subject.

Even if only the out-of-equilibrium nature of the propulsion is in itself an interesting topic, what is even more striking is how assemblies of such self-propelled entities behave. For instance we can observe flocking behaviours for birds [33] (figure 1.1(a)), fish schools [3] (figure 1.1(b)), spontaneous flows of bacteria under confinment [64] (figure 1.1(c)) or even prototypical microscopic systems composed of elongated cargo (microtubules or MT) and molecular motors (kinesin) which give them motion through “fuel” (ATP) consumption [47]. Consequently, these *self-organization* phenomena

[1] even though numerical simulations of such system exist, hard core repulsion and high packing fraction require significant computationnal resources

are quite common in living systems as shown by these examples. Self-organization means that these systems possess organized phases originating solely by the interaction *between* the individual entities composing the system and not because some global coupling/force acts.

(a) A flock of european starlings, this compact assembly shows brutal changes of shape, evidence of collective motion. author : http://www.flickr.com/photos/tofsrud/4171421134/

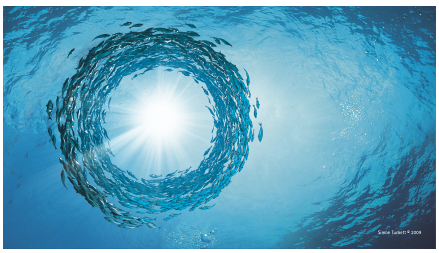

(b) A fish school which shows a ring shape, author : http://www.simontuckett.com

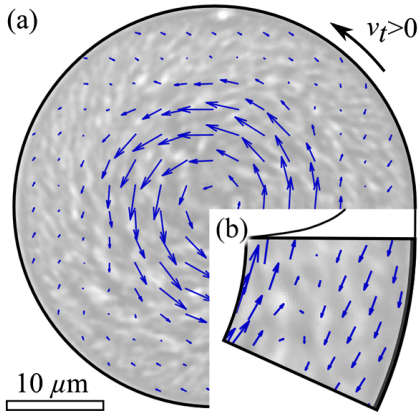

(c) Spontaneous bacterial flow in a confined environment (an "elongated" droplet). The arrow indicate the bacteria flow motion direction, source [64]

FIGURE 1.1: A few examples of spectacular manifestations of active matter in several contexts, at different scales.

1.1.1 Objectives of this thesis

One of the objectives we can seek for, is to unify all of these systems into the largest possible "ensemble" which share common properties and that is what we've done by studiying a microscopic "Vicsek-like" model in chapter 2 known as "Active nematics with velocity reversal". On the other hand more precise modelization are also desirable if we want to finely investigate particular properties. In chapter 3 such case is investigated, with the aim of a finely tuned modelisation of the bacteria *Neisseria Meningitidis*. We will see that most of its propreties can be explained by the ability to create long filamentous structures known as pili (singular: pilus). This thesis is therefore at the same time focusing on general considerations without neglecting

more practical aspects by using observational data on a particular system to build a “custom made” model.

1.2 A model system : Active-Nematics

1.2.1 The Vicsek model

The type of models we will focus here aims to mimic the movement of animals at the collective level based on the simplest set of rules possible. This is the direction that led to the, now famous, Vicsek model [58] which is an example of these idealized systems made of simple key elements , shown in figure 1.2. The agents are pointlike particles indexed by i which position $\mathbf{x}_i$ and orientation vector $\mathbf{u}_i$ dynamics evolves at discrete time, off-lattice, according to the following set of rules:

- each particle i change its initial orientation $\mathbf{u}_i(t)$ (red vector) to the average of the orientation of its neighbours located within a radius r_c (blue vectors): it yields the green vector $(\frac{1}{N}\sum_{k\in\partial i}\mathbf{u}_k)$
- to account uncertainty or variability of behaviour we add a white noise of amplitude η (uniformly sampled between $-[\eta,+\eta]$) on the orientation angle which rotates $\mathbf{u}_i(t)$ (orange rotation)
- finally position x_i is updated. The particle displacement is performed at constant speed v_i of constant norm v_0 along $\mathbf{u}_i$'s direction: $\mathbf{x}_i(t+\Delta t) = \mathbf{x}_i(t) + \mathbf{v}_i(t+\Delta t) = \mathbf{x}_i(t) + v_0\mathbf{u}_i(t+\Delta t)$

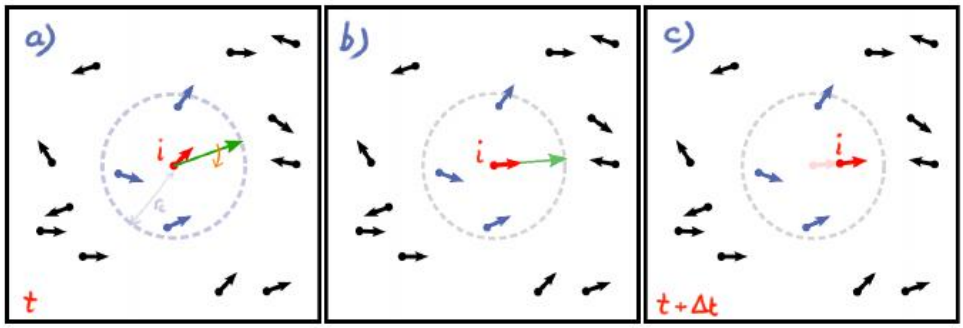

FIGURE 1.2: One step of the Vicsek model (source: [37])

The system state is basically described by a polar order, *i.e* the fact that neighbours are aligned and (thus) moving in the same direction. Given that this order is essentially caused by a competition between a short-ranged interaction which create oder and a noise which destroys it, we can understand that the two main control parameters for such system are the density ρ and the noise intensity η.

This system shows a high polar order (figure 1.4(a)) region - at low enough noise or high enough density - to disorder (figure 1.4(b)) transition, when noise is high enough or density low enough. The low order region is called the gas while the high order is called "liquid".

In the plane (ρ,η), the transition line $\eta_t(\rho)$ delimiting the boundary between the disordered and ordered region is shown in figure 1.3. This curves roughly follows a power law $\eta_t \propto \sqrt{\rho}$, as predicted by the theory. In order to obtain this curve, that is the location of the order-to-disorder transition we need an order parameter P which caracterizes the orientational order

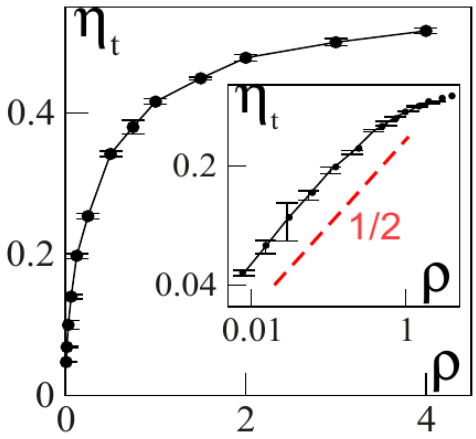

FIGURE 1.3: Basic phase diagram of the vicsek model. Above the transition line (high noise) is the disordered phase, below the homogeneous ordered phase. The inset shows that the transition line η_t scales as $\propto \sqrt{(\rho)}$.

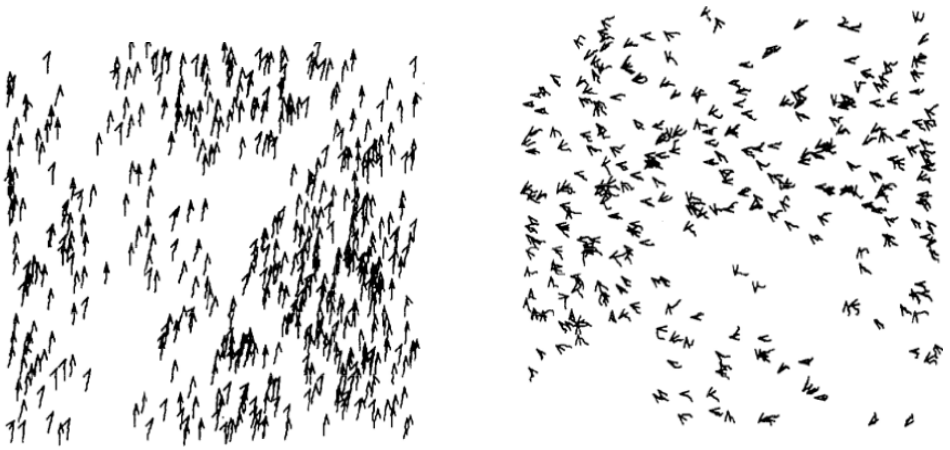

(a) "High" polar order in the Vicsek model, particles are aligned and move in the same direction

(b) Disorder in the Vicsek model, particle orientations are not correlated

FIGURE 1.4: Vicsek model shows ordered (resp disoreded) phase at low noise (resp high noise), source [58]

and which drops (or raises) when we cross this boundary by tuning the systems control parameters ρ or η. Consider N particles oriented along $\mathbf{u}_i$, this orientational order parameter P is defined as the norm of the mean polar vector, see equation (1.1). It is by construction valued in the $[0, 1]$ range : with 0 corresponding to the perfectly disordered (isotropic) case whereas 1 corresponds to perfect alignement.

$$P = ||\frac{1}{N}\sum_{i=1}^{N}\mathbf{u}_i|| \tag{1.1}$$

Order-to-disorder transitions are not specific to SPP systems but can also

arise at equilibrium, for instance in the Ising model [2] which also exhibit an order-disorder transition. However if the latter model has been extensively studied and is well understood by means of classical statistical dynamics, the former on the other hand lacks a unified theory caused by its intrinsically out of equilibrium nature and is therefore the subject of intense research. For instance the appearance of a phase separated region of dense inhomogeneous structures called *bands* (see figure 1.5) in near the transition line cannot be explained within the framework of usual order/disorder phase transition.

New methods had to be developped to study these systems and make the link between the microscopic rules we just described and the larger scale dynamics. The most fruitful attempt is probably the derivation of hydrodynamics equations based purely on symmetry considerations by Toner & Tu in [57]. In this seminal paper they consider the simplest equations respecting the symmetries of the problem, which allow important predictions to be done, the most important being that long range order [3] exists for $d \geq 2$ (d being the dimensionnality of space) , which proves that the Mermin-Wagner theorem cannot be generalized for non-equilibrium systems.

The Tonner-Tu equations are the "simplest" equation describing Vicsek-models in terms of velocity field $\mathbf{v}$, density field ρ and a noise term $\mathbf{f}$. The terms ρ and $\mathbf{v}$ are coupled in the transport equation (1.2) and $\mathbf{v}$ evolutions in (1.3). We can understand equation (1.3) as a complexified Navier-Stokes. The $D_.$ coefficients are diffusive terms (second-order spatial derivative), λ is the coefficient for the convective term, α, β are terms maintaining $\mathbf{v}$ (thus order) to non-zero values (Ginzburg-Landau). Despite its success, the main criticism we can put on this method is that any link to a real system is lacking because most coefficients have arbitrary values, as nonlinear equations even slight changes on the value of these coefficients can drastically modify the behaviour the system. What's more the time scales and the length scales associated to these coefficients, which estimates are essential in a biological context are lacking.

$$\partial_t \rho = -\nabla(\mathbf{v}\rho) \tag{1.2}$$

$$\partial_t \mathbf{v} + \lambda(\mathbf{v}.\nabla)\mathbf{v} = (\alpha - \beta|\mathbf{v}|^2)\mathbf{v} - \nabla P + D_L \nabla(\nabla.\mathbf{v}) + D_1 \nabla^2 \mathbf{v} + D_2(\mathbf{v}.\nabla)^2 \mathbf{v} + \mathbf{f} \tag{1.3}$$

Nowadays it is still a popular method to infer equations describing active matter based on the interaction and self-propulsion symmetry. These complexified methods consist in adding higher and higher order spatial derivatives of the basic fields (see section 1.2.6.2).

An important step toward a better understanding has been performed in [5].The authors derived partial differential equations based on microscopic

[2] because when the symmetry is continous there is no possible breakeage of the symmetry according to the Mermin-Wagner theorem.

[3] In a classical XY spin system, the spin-spin correlation function decays to 0 at large distances. Meaning that at very large scales the order cannot be maintained ($\lim_{L\to\infty} P = 0$ for a system of size L). On the contrary in Vicsek model in the liquid phase the correlation functions don't decay. This is what long-range order means.

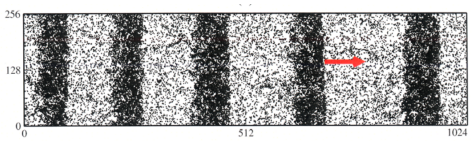

FIGURE 1.5: Five bands as can be seen in the vicsek model for a rectangular system $\eta = 0.42$, system size: 1024×256). The red arrow indicates the bands motion direction.

collision rules using a Boltzmann framework and obtaining explicit master equations for the particle density distribution f [4]. The fundamental interest of this method compared to the one of Toner & Tu is that we obtain equations which coefficients are *explicitely* depending on the microscopic rules we've chosen. Also it is worth to mention methods based on microscopic collision rules called "Smoluchowski" in [1] which lead to very similar equations but with different coefficients dependance on the microscopic parameters, the origin of these discrepencies is studied in [6].

One a side note, important questions which might seem simple took some time to be answered. For instance the nature of the transition in the original Vicsek model has been a long standing debate as it was first argued to be of second order in the original Vicsek paper [58] in 1995, however later in [11] because of strong finite sizes effect it was demonstrated it was a first order transition using as a tool a statistical quantity known as the *Binder cumulant*[5]. Lastly the connection was made between the nature of the noise in the microscopic dynamics and the shape of the stable states with band namely "phase" or "micro-phase" separation obtained in [52].

1.2.2 MIPS

Another popular topic in active matter is the "Motility Induced Phase Separation" (abvr. MIPS) phenomenon, which is a quite generic mechanism occuring in self-propelled particles systems.

Given the name we understand the root of these events is phase separation, between a liquid "dense" phase and a gaz "sparse" one (see figure 1.6). Though phase separation can exist at equilibrium, what's more striking here is this phenomenology doesn't come from the enegetic cost of the creation of an interface: everything comes from the slow-down of particles in the dense phase with respect to the gas phase. Indeed the generic model for MIPS consists of self-propelled active particles possess only "repulsive" interactions between themselves, and are all equivalent (there's not two populations with different interactions).

What's been demonstrated in [10] is that the only requirement to obtain these phase-separating regimes is that the self-propulsion speed v must depend on the local density (the density of the neighbourhood of the self-propelled particle) ρ. The usual density dependance relation is $v(\rho) = v_0(1 - \frac{\rho}{\rho_0})$

[4] more detail in 1.2.6.1

[5] which is a fourth order moment of the polar order parameter P

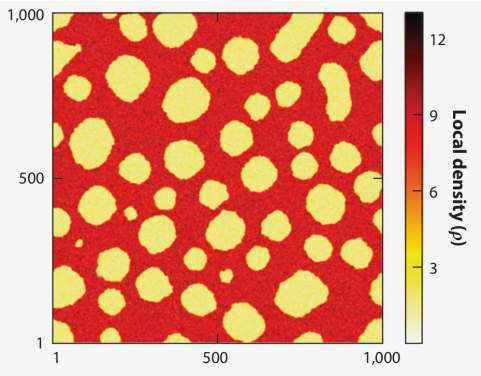

FIGURE 1.6: A MIPS phenomenon occuring in a "run and tumble" system, the color bar indicates density. We see low density domains of fast particles separated by high density regions of slow particles. Sourced from [10]

We thus understand that this velocity dependance which acts effective repulsion embedded in the slowing down for dense region (high ρ) causes moving particles to accumulate and to slow down even further as a feedback mechanism. This mechanism causing in the end a coarsening, like if there were *effective* attractive forces !

1.2.3 Dry/Wet systems

Nowadays, there is a clear consensus to define two main families of active matter systems according to the type of interaction between the agents : dry and wet ones.

In dry systems the essential source driving the order in the system are the collisions between the agents which leads to alignement *with no consideration for the medium in which the particles lie*, these collisions are not momentum-conservative as a result of the complex interaction forces during collision.

On the contrary in wet systems the substrate/medium is of essential importance because it is the vector of the alignment interactions which can also be long ranged. What's more contrary to dry systems the global momentum is conserved upon collisions. A prototypical wet system is the microtubules & kinesin assay of [47].

In each of these categories the behaviour differs because of the presence or not of these long range *hydrodynamic* interactions and therefore each requires particular mathematical treatment.

In this thesis we will focus on a dry microscopic model essentially because we want to be able derive continous equations based on the microscopic model using the the Boltzmann-Ginzburg-Landau (abrv. BGL) framework of *Bertin, Chaté & al*.

Our Vicsek-style models are by construction dry because all the terms are short ranged, it avoids to compute complex interaction which depend on

the shape, velocities and other parameters of the agents [6] and allow large scale systems to be simulated. Keeping in mind that large scale propreties might require *really* large systems on long durations to emerge.

But short ranged interactons are also essential in order to be able to apply the BGL method. Otherwise the calculations would be untractable. As we will see even the introduction of a repulsive term is already a tedious task and requires careful treatment. The big advantage of our way to procede is therefore to be able to have microscopic models, to compute the equations and to compare if the equations are agreeing with the microscopic system. Unfortunately this method is still restricted to dry systems for now because of the complexity to take into account long-ranged interactions.

1.2.4 Dense sytems

Most Vicsek-style models do not provide a spatial extension to the self-propelled agents, these are point-like particles. While this assumption is legitimate when considering "sparse" assemblies such as starling flocks, it starts to be important when considering large populations of dense particles. Bacteria can show close packing or vibrated grains which could experience phenomenon of "jamming" playing an importance in the collective motion, even for human crowd gathering in front of stores during the "Black Friday" [9] (see fig. 1.7) ! The most obvious solution is to implement hard-core repulsion (see [49] for details about simulations of hard core repulsion) but it stays computationally intensive even nowadays and restrict the population and timescales observation drastically (because it requires continuous time algorithm).

We aim to study dense systems sticking to a Vicsek-style model in order to keep low computational cost. Our solution to this problem is to embed the repulsion under a term similar to the alignment.

1.2.5 Symmetry of the alignment

In the class of dry systems we can also subdivide in categories a finer granularity assuming there are two essential symetries which drive the system's behaviour : the symmetry of the alignment and the one of the self-propulsion. Each of these terms can either be polar or nematic.

When the alignment is polar the collision is summed-up by a *vectorial* average of the velocity vector carried by the particles, the outcom being parallel vector moving with the same orientation. On the contrary for nematic alignment we compute the average *direction* keeping the relative orientation: particle stay head to tail or head to head.

The propulsion is polar when a free particle conserve its self-propulsion vectorial orientation over time. When it is nematic the direction is kept

[6] Yet, one could at the microscopic level, decide to add a field for the fluid and use the Stokes equation to establish a link between self-propelled particles and the surrounding fluid.

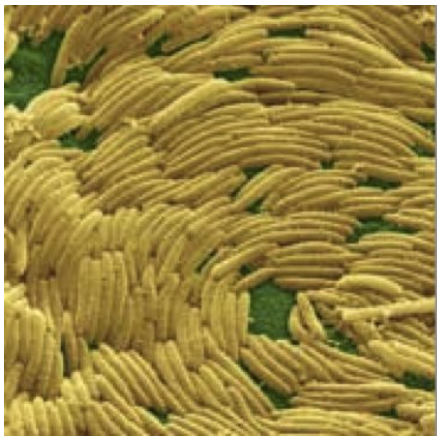

(a) Myxobacteria show close packing , source: [31]

(b) The crowd during the "Black friday" is closely packed near a store's entrance, source [9]

FIGURE 1.7: Examples of system where spatial extension role is critical

constant but the particle can reverse the vectorial orientation will diffuse over time : it will switch with probability $\frac{1}{2}$.

We can therefore consider, in all generality, 2×2 categories of system which posses one or the other symmetry for both propulsion and alignment. The most studied case is of course the fully polar case because that is the Vicsek model. The other cases have been studied both from microscopic simulation but also at the continous level using the BGL method: polar propulsion with nematic alignment (known as rods) has been studied in [46] while *active nematics* - nematic propulsion with nematic alignment (known as pure active nematics)-have been studied in [38]. These models confirmed the relevance of the BGL method, showing good agreement between the microscopic level and the continuous one. It is important to note that these models lack a repulsion term and thus are not suited to study dense assemblies of particles.

From the point of view of symmetries, our model is closing the gap between the two models with nematic alignment symmetry: we introduce a flipping rate $k_f \in [0, \frac{1}{2}]$ which is the probability to reverse the speed of the particles, because for some reason the particles can reverse their direction of motion on a certain timescale. For $k_f = 0$ we are back to the polar propulsion case, while for $k_f = \frac{1}{2}$ the pure-active nematics. Inbetween we will we will try to see a coherent picture where k_f is tuned in section 2.7.

1.2.6 Equation derivation

1.2.6.1 Boltzmann approach

We now briefly introduce the the BGL approch in a generic way. The detailed equations will be derived in 2.3.

The starting point is to describe the system in terms of density of state $f(r,\theta,t)$, where $f(r,\theta,t)d^3rd\theta$ is the number of particles around position r oriented along θ at time t. The Boltzmann master equation is a way to write the evolution of f in terms of entering fluxes and exiting fluxes. In our case it can be written as follows:

$$\frac{\partial f}{\partial t} + \mathbf{v_0}.\frac{\partial f}{\partial \vec{r}} = I_{\text{coll}} + I_{\text{diff}} + I_{\text{other}}$$

On the left hand side the two first terms are simply the Lagrangian derivative of f, that is we have its temporal variation term $\frac{\partial}{\partial t}$ and the advection term $\mathbf{v_0}\frac{\partial}{\partial \vec{r}}$ where $\frac{\partial}{\partial \vec{r}}$ is the gradient. On the right hand side we describe this varations is explained in terms of fluxes which come from collison I_{coll} and self-diffusion I_{diff} *of the angle* respectively and *eventually* I_{other} accounts for other phenomenom (ex: velocity reversal).

However these equations are still untractable. As in our model the module $||\mathbf{v_0}||$ is constant, we are allowed to expand f in terms of its angular fourier components, that is :

$$f(r,\theta,t) = \sum_{k=0}^{\infty} f_k(r,t)e^{-ik\theta}$$

where

$$f_k(r,t) = \int_{\theta=0}^{2\pi} f(r,\theta,t)e^{+ik\theta}$$

The first three harmonics of the series have a clear physical interpretation and will be of particular interest in our model:

- $f_0 = \int_{\theta=0}^{2\pi} f(r,\theta,t)d\theta$ is simply the density $\rho(r,t)$ (we integrate over angular degrees of freedom).
- $f_1 = \int_{\theta=0}^{2\pi} f(r,\theta,t)e^{i\theta}d\theta$ is the polar field, its argument is the polar angle (if $\vec{v} = v_0e^{i\theta}$ then the previous integration is the averaged velocity).
- $f_2 = \int_{\theta=0}^{2\pi} f(r,\theta,t)e^{i2\theta}d\theta$ is the nematic field which argument is **twice** the nematic angle ϕ , indeed we see that the function $\theta \to e^{i2\theta}$ is invariant under a transformation $\theta \to \theta + \pi$ which means it only depends of the direction and not the side the arrow points to, thus f_2 caracterize direction of particles around point r. Thereafter we will study in more detail this essential termin section 2.1.1.

At the end of the day we have derived three coupled equations for these three fields $f_0, f_1,$ and f_2 which are similar to the ones obtained in [53] [14] or [43] but we have the interesting addition that the coefficients in front of all derivative terms of the equation have an explicit dependence on the the Boltzmann collision scheme we chose, which matches as closely as possible the microscopic dynamics we use, thus establishing an almost 1:1 correspondance between the macroscopic parameters and the microscopic ones. This is a very nice feature which permits to go back and forth from microscopic scales to mesoscopic scales and *vice versa*.

These hydrodynamics equations enable us to explore very large systems limit quickly and eventually confirm features of such systems using microscopic simulations with appropriate set of parameters. On the contrary we can go from the microscopic to the mesoscopic in order to answer specific questions, this was done for instance to explore the nature of the "nematic bands" in the active-nematics model [38] bands structures first thought to be stable in the microscopics where shown to be instable by linear stability analysis of the continuous equations.

For the interested reader and given the length of the calculations, the dervivation of these equations will be performed at the end of chapter 2 concerning active nematics in section 2.3.1.

1.2.6.2 Symmetry based equations

Following the pionnering work of Toner & Tu, continous equations based purely on symmetry principles have been written for various symmetries of the particle in an attempt to describe in a unified view the systems of the same "symmetry group" [2, 14, 43]. Considering both the symmetries of the self-propulsion of the particles and the symmetries of the interaction, we can indeed infere "semi-heuristically" partial differential equations describing the dynamics by containing the terms allowed by these symmetries. For instance if the particles are purely nematically interacting, that is both propulsion and alignment have the nematic symmetry, the only "relevant" fields will be the nematic field f_2 and the density ρ and all the power of their derivatives. We can then write equation for the dynamics of these fields using terms known from equilibrium. This will not be performed here

Again we want to point the fact that this method lacks some physical interpretation in the sense that all the coefficient in front of the terms will have to be set to "reasonable" values to be able to describe any real system. The appropriate setting of the coefficients being let to the physicist intuition. Also given the number of parameter any thorough exploration of parameter space is untractable and relavant significant terms have to be guessed. However one could argue that most of these terms are known from equilibrium theories of liquid cristals (ex: Landau-De Gennes) and have physical interpretations in terms of elementary deformation of the nematic field [7] but this doesn't solve the problem of spatial scales and timescales caused by the setting of coefficients.

[7] see chapter where we describe the nematic field 2

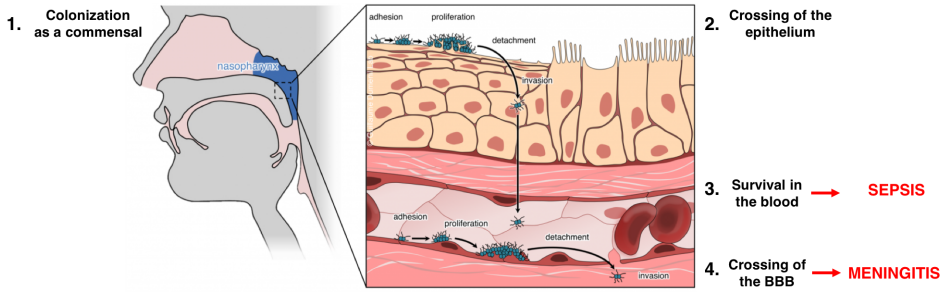

FIGURE 1.8: Spreading mechanism of *Neisseria Meningitidis*

1.3 Neisseria Meningitidis modelization

We now address the second model we designed to describe aggregates of the bacteria *Neisseria Meningitidis* where self-propulsion still exists but doesn't fit any previously existing model. We start by describing the biological situation and wonder why this bacteria must be studied. We continue by describing the experiment which were the basis of this work. Finally we briefly tackle other works which adress the bacteria molecular motor via the prism of motility or aggregation.

1.3.1 Biological interest

The transport of a bacteria inside the body is a complex phenomenon but this process is essential for the proliferation of illnesses inside the host body . Consequently, it is of critical importance to understand what are the essential parameters enhancing this proliferation. In other words we try to determine what are the relevant mechanisms to inhibit this proliferation in order to elaborate an efficient treatment. This understanding of the underlying mechanisms is called *pathogenesis* by biologists.

Our focus will be made on one of these bacteria, *Neisseria Meningitidis*, which triggered our interest because of its rather unique proliferation mechanism. Indeed, for most people it is mostly harmless and live in the nasopharyx (see l.h.s of figure 1.8, it is the region of the pharynx located in the lower part of the nasal cavities). Unfortunately for unknown reasons this bacteria might cross the epithelial barrier in some cases and reach the bloodstream where it becomes pathogenic, it can then invade the host, leading to the meningitis illness and to severe consequences (figure 1.8 shows the mechanism leading to infection). While proliferating, meningococci forms tight aggregates in order to resist the blood flow generated shear stress, this is why bacterial aggregation is a keyfactor in the process of vascular colonization and pathology progression.

In this particular case, bacterial aggregation is mediated by type-IV pili (abreviated T4P) :these are several μm long molecular structures (see figure 1.9). *Neisseria Meningitidis* possess an advanced molecular machinery

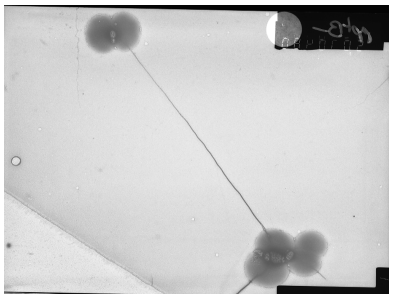

FIGURE 1.9: A close-up picture showing couple of bacteria and a pilus liking them

able to produce these long dynamic filaments which extend out of the bacterial body and can also retract exerting *very strong* forces up to $100\,\mathrm{pN}$ (see [39]) in order to get retractions speeds $\approx 1\,\mu\mathrm{m\,s}^{-1}$. These pili being the only mean of motion, they are a key factor, it is therefore essential to understand their role in the aggregation process.

1.3.1.1 Experiments

In this context the team of Guillaume Duménil developed a series of both *in vitro* and *in vivo* experiments (see [25]) on *Neisseria Meningitidis*, aimed at giving an extensive exploration of the determining parameters for aggregates properties. Their peculiar interest is on the *in vitro* experiments as they allow to get rid of all the unknown interactions which might occur between the host and the bacteria, allowing to focus on the intrinsic properties of the bacteria and thus to discriminate between pure bacterial properties and bacterial-host ones.

Of course from a pure biologcal point of view the cell-host interaction is even more important in order to understand illness spreading in the host. However these *in vitro* experiments are both more reproducible and quantifiable, thus easier to modelize.

They initial focused on the aggregation dynamics of *Neisseria Meningitidis* in "free space" in the sense that the bacteria were cultivated - diluted at a certain concentration in a water based solution (with nutrients) and then centrifuged to ensure they would obtain a homogeneous solution of dispersed bacteria with no preformed aggregates in the begining. The particles then start to aggregate in their environment.

This procedure was followed by imaging via confocal microscopy of the aggregation dynamics.

The tracking of the aggregation is done with confocal microscopy, thus in 2D, setting focal plane near the bottom of the culture recipient. Indeed the aggregates are quickly big enough to sedimentate and fall at the bottom. The obtained movies are rather spectacular (see 1.10) where extremely fast fusion events can bee seen. From these movies various data processing were done to obtain dynamical properties of the system.

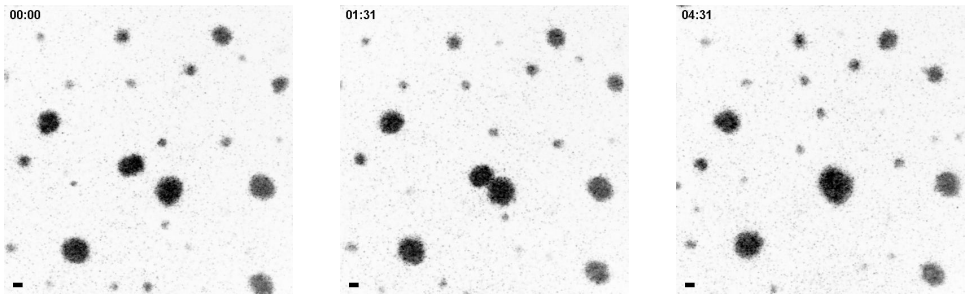

(a) initially homogeneous solution shows many aggregates after a few minutes

(b) near the center two massive aggregates are undergoing fusion

(c) after $\approx$ 3 minutes they totally fused : no sign of the preceeding aggregates persist

FIGURE 1.10: Confocal microscopy observations of aggregation in an initially aggregate-free solution, source Duménil & al.

In a second step, the mechanical properties of these aggregates were probed via a micropipette aspiration technique allowing to obtain precise viscoelastic measurements. The theoertical description of this experiments is done in section 3.1.4 and the results from experiments are shown in section 3.5.2.

The next step would be to study the dynamic of pili inside live aggregates but we are confronted to the impossibility of such thing because obtaining spatiotemporal data with sub μm space and ms time resolutions at the same time is not possible. The only solution to circumvent this issue is to "freeze" the system at some time but this way is far from perfect because by doing so we loose track of all the dynamical aspects of the processes which, from our knowledge, are essential to explain the aggregates properties.

This is why using the existing numerous experiments which make up a solid basis of data, and the idea that pili are the essential ingredient of the aggregation, this thesis focus on the implementation of a microscopic minimal model. This model is aimed at reproducing some if not all the features of the live aggregates in a controlable manner which allows us to enlarge the understanding of bacterial proliferation.

Consequently, our numerical simulations are a powerful complimentary resource to biological assay. Indeed simulations allow a much more precise control over the dynamics parameters. Simulating is also useful in order to get rid of technical constraints which are unavoidable in experiments: long time regimes are hard to probe, particles tracking can fail to detect precisely the bacteria position, etc.

1.3.2 Other works

From the biophysicist point of view there exists a strong interest to modelize these bacteria because of the very intringuing properties of the pilus. Other topics have been studied so far and not only the aggregative properties, the broached topics are :

- The ability for *Neisseria Menitigitidis* to "twitch" - that is having these intriguing, chopped, motions - on substrates, for instance in [69] and [30]
- The derivation of hydrodynamic equations describing essentially the density of bacteria based on a Boltzmann type approach [8], which lead to identify phase-separating regimes in [62]
- Precise modelization of the mechanical properties of the pili at "molecular levels" in terms of assembly of n rigid body, using simulations. These enable to explain the force-velocity relation of this particular molecular motor in [70]

We also have to note that aggregates akin to ours have been reported on a totally different system: colonies of fire ants [55]. While this can be astonishing because fire ants don't posess pili, they however have legs which can produce traction by pulling on their neighbours. In this experimental paper the authors have analysed the mechanical properties of aggregates of ants, which appear quite similar to *Neisseria Meningitidis ones*. Indeed while subject to mechanical forces these ants colonies recover their shape in a few seconds as figure 1.11 shows, these aggregates are also "living" because the ants are constantly moving inside the aggregate.

This probably means that our model extends to a wider class of self-propelled agents than pili-enabled bacteria ones. Indeed this system doesn't share some properties : firstly there's no fluid so no possible hydrodynamic interaction that might exist for bacteria in water , also the ants are interacting with their legs so the attractive force is shorter range (pili can be as long as 7 bacteria sizes whereas legs are 0.5–1 ant long) and probably less intense, third thing is about the nature of the free ant displacements which is not purely Brownian but is somehow more correlated than the thermal movement of bacteria. Knowing that no modelisation of the ants aggregates has been provided it could be interesting to see to what extent our model could fit in this context.

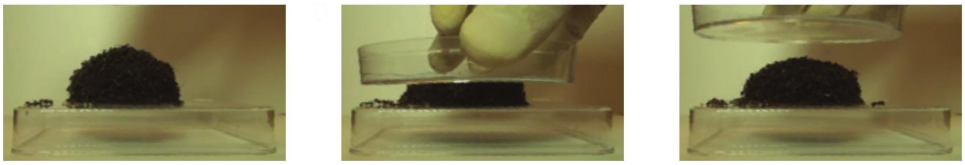

FIGURE 1.11: A fire ant colony shows elastic properties: it recovers its initial shape even after significal crushing. Source: [55]

1.4 Structure of this thesis

We finally conclude this introductory chapter by recalling the structure of the two next chapters of this thesis.

[8] Which is allowed by assuming two attaching bacteria as a collision event.

The second chapter will adress the Vicsek-like model : *Active Nematics with velocity reversal and repulsion*. We will describe the various phases encountered and their properties 2.6.1 2.6.2, and link them in a coherent manner as phase(s) diagram(s) 2.7, 2.5.5, 2.6.2.3. Finally we will derive the equations fully in 2.3 and exhibit how this theory matches the microscopic system 2.8.0.1.

The third chapter is naturally concerning *Neisseria meningitidis*. The first sections 3.1 and 3.2 will be dedicated to generalities about state of matter and why such biological system is interesting for physics in general. Also we will describe morepreciselythe biological aspects of the system. The following chapters 3.4 and 3.6 are more straightforward and follow chronologically the evolutions of the model. These evolutions adress different questionings and requirement which emerged during over time and are thus complimentary. Finally we will have a technical discussion in 3.7 concerning the lastest experiment performed in order to obtain input parameters for the model[9] which is mostly post-treatment and image analysis and provide as well evidence for the telegraphic process of pili attachment.

[9] precisely the experiment allows to obtain the ON/OFF transition times

Chapter 2

Active Nematics

2.1 Nematic state

Nematicity is ubiquitous in the living world, from the bacterial world to granular grains through liquid crystals. *Per se*, it has triggered a lot of interest from physicists because the symmetry of theses phases required a common theory. For equilibrium systems, the work from Pierre Gilles de Gennes (see [16]) has been fundamental in the comprehension of liquid crystals. In chapter 1 we defined polar order, the nematic symmetry possess an equivalent nematic order as we will see in 2.1.1. In figure 2.1 we can see different phases of nematically ordered phases. The first one, on the left hand side, is the simple nematic phase. For a single particle the nematic angle characterizes the average direction (and not orientation) of particles, it is a fairly intuitive notion: it consists in taking the particles orientation only considering the upper half in the trigonometric circle (thus an angle $\phi \in [0, \pi]$), in this figure it is therefore pointing upward $\phi = \frac{\pi}{2}$. In this example it is fairly easy to see however, compared to the polar order, nematic order has a more complex algebra (we recall that for polar order it is simply the norm of the averaged orientation vectors u_i). The second phase exists if if in addition to angular order there exist also a positional order (particles form regular pattern) we refer this as *smectic*, the middle sketch shows such smectic order.

The last phase, called *cholesteric*, exists only for the 3-dimensional case, indeed this phase corresponds a rotating nematic direction along a third axis: inside each 2D layer particles are nematically ordered, but each layer is rotated with respect to each other in the other direction.

The nematic order emergence from collisions can be understood when considering*nematic* collisions as shown in figure 2.2. Assume two particles with velocity vectors v_1 and v_2 initially: between the left hand side and the right hand side picture v_1 and v_2 are both pointing upward or upside-down before collision.

After the collision the fact that v_1 and v_2 are pointing upward or upside-down is kept but overall they are parallel corresponds to a *nematic* alignment. On the contrary for a polar alignment the orientation would be lost and both would be pointing in the same direction.

We can now clarify the vocabulary and mathematical tools we will be using thereafter.

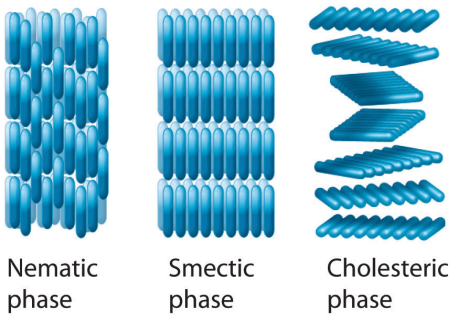

FIGURE 2.1: Different phases for liquid crystals. Simple nematic shows alignment, if their is spatial order it is smectic, and if we're in 3D it can also be cholesteric source https://saylordotorg.github.io/text_general-chemistry-principles-patterns-and-applications-v1.0/s15-08-liquid-crystals.html

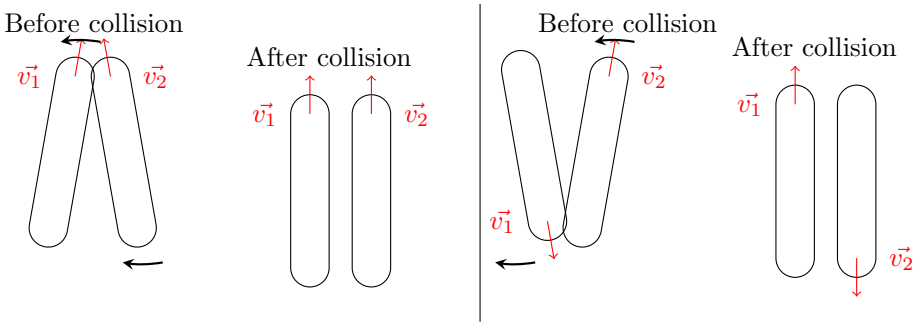

FIGURE 2.2: After a nematic collision the particle reorient along the average "direction" while keeping their orientation (they cannot rotate more than $\frac{\pi}{2}$)

2.1.1 Nematic Tensor

As we previously summarized, the equilibrium theory is nowadays well developed. We will now review the tools from this theory that we need to build an out of equilibrium theory for particles exhibiting nematic symmetry.

First we need to have a quantity that describe the level of "nematicity" in the system that is the order in terms of nematic angle. The natural thing to do is to take the 2×2 tensor $\mathbf{S}$ -called the nematic tensor- is defined as (where the components α and β refer to axis x or y):

$$\mathbf{S}_{\alpha\beta} = \frac{1}{N}(\sum_{i=1}^{N} u_\alpha^i u_\beta^i - \frac{1}{2}\delta_{\alpha\beta}) \tag{2.1}$$

We recall that $\mathbf{u}_i$ is the normed speed vector (or the orientation vector), of particle i characterized by an angle θ such as $\mathbf{u}_i = \mathbf{v}_i/v_0 = (\cos(\theta_i), \sin(\theta_i))$, u_α^i is its component on axis α and $\delta_{\alpha\beta}$ is the Kronecker symbol ($\delta_{\alpha\beta} = 1$ if $\alpha = \beta$ else $\delta_{\alpha\beta} = 0$). It is the simplest choice of an invariant quantity by nematic symmetry. Indeed if ones flips $\mathbf{u}_i$ for any particle i this quantity is invariant. Notice that the $\frac{1}{2}$ factor comes from the fact that we are working with 2D systems (otherwise in D dimension the term becomes $\frac{1}{D}$).

This parameter can be either global, in which case N represents all the particles in the system, or local in which case we can define a local nematic tensor $\mathbf{S}_{\alpha\beta}(r)$ as the average over N particles located around the position r, which is $\rho(r)\mathcal{V}$ on a volume $\mathcal{V}$ that requires to be defined.

This tensor being symmetric traceless we can find the main axis, namely n_α and the associated eigenvalues and we can also rewrite the tensor component $\mathbf{S}_{\alpha\beta}$ as:

$$\mathbf{S}_{\alpha\beta} = S(n_\alpha n_\beta - \frac{1}{2}\delta_{\alpha\beta}) \tag{2.2}$$

Such that the scalar quantity S contains the degree of order in the system and the tensor contains information about the direction of the order. S is thus the scalar nematic order parameter we were looking for, indeed it can be proven that S is bounded and $S = 1$ when the system is perfectly nematically ordered whereas $S \leq 1$ when it is not and $S = 0$ when the system is isotropic (no orientational order). What's more the argument of the eigenvector ϕ is characterizing the average orientation is also $\in [0, \pi]$.

Considering N particles $\{x_i, v_i\}$. Comparing equations (2.1) and (2.2) we can show that ($\mathbf{S}$ is symmetric traceless) S is defined by equation (2.3) and ϕ by equation (2.4) where $\langle\rangle$ defines averages over all particles ($\frac{1}{N}\sum_{i=1}^{N}$) :

$$S = \sqrt{< \cos(2\theta) >^2 + < sin(2\theta) >^2} \tag{2.3}$$

and

$$\phi = \frac{1}{2}\arg\begin{pmatrix} < \cos 2\theta > \\ < \sin 2\theta > \end{pmatrix} \tag{2.4}$$

If we recall what we've seen in chapter 1 these quantities are related to the Fourier transform of the density field which is the complex valued field f_2 . The relations are the following, the nematic angle is half the argument of f_2 : $\phi = \frac{1}{2}\arg(f_2)$ while the norm of f_2 is directly the nematic order : $S = ||f_2||$.

2.2 Description of the model

As stated in the introductory chapter 1, the goal of our Vicsek-style model is to keep the minimum set of elements allowing us to reproduce a rich phenomenology while preserving the following necessary ingredients :

- The alignment interaction needs to be nematic.
- We should also have a a term equivalent to a repulsion, acting on the self-propulsion direction, which tends to repel too close particles.
- Particles diffusivity should be controlled, that means we have a control parameters which will be related to the persistence time.

The justification is as follows, nematicity is defined solely as the symmetry of the phase, this symmetry depends mostly on the shape of particle. Still, we don't want to be limited and into describing system which constituents self-propulsion is absolutely symmetrical and thus might not be propel via diffusion [1]. However we want to enlarge the scope of the model and consider asymmetrical motors, which would eventually lead to long time ballistic motions (ex: myxobacteria [45]). Lastly we want to introduce a term similar to a repulsion because its influence is essential

As usual, in Vicsek-style models the time is discretized and the update rules are then as follow for particle which position, speed, orientation vector and angle are respectively referred to as x_i , v_i , u_i , θ_i (2.5):

$$x_i(t+1) = x_i(t) + v_0 \mathbf{u}_i(t+1) \tag{2.5}$$

The dynamics equation is unchanged and corresponds to the Vicsek dynamics rule : constant displacements steps over distances v_0 in the direction $\mathbf{u}_i$

The direction of motion θ_i which is the argument of u_i is given by (2.6):

$$\theta_i(t+1) = \arg\{\epsilon_i \mathbf{A}_i(t) + \beta \mathbf{R}_i(t)\} + \eta \xi_i(t) \tag{2.6}$$

Note that, as most Vicsek-style models do, we don't consider any torque nor acceleration : particles might instantaneously (over 1 timestep) modify their propulsion direction $\mathbf{u}_i$. This regime is often qualified as "overdamped". This limit is understandable when we aim to modelize systems which viscosity is low or irrelevant (if there is a substrate for instance). However there exist models such as [34] in which continuous rotation of the speed direction is included, in which case we would have an equation for $\frac{\mathrm{d}\theta}{\mathrm{d}t}$ instead of θ as we have in (2.6)

The first term $\mathbf{A}_i$ contains the nematic alignment, while the repulsion -one of the novelty of this model- is $\mathbf{R}_i$. Finally the last term is also typical of Vicsek-style models, it is an angular noise which comes on top. In this case the noise is called "scalar" (meaning it acts on θ_i and not u_i) of amplitude

[1] which is the "natural" displacement mode for symmetrical propulsion modes which have no reason to favor one way more than the other (ex: vibrated grains)

η (ξ_i is a random variable sampled from the uniform distribution over the range $[-1:1]$).

The term ϵ_i contains the persistence of the self-propulsion orientation, in other words the persistence length. ϵ_i is a random variable which values $+1$ is -1 with probabilities $1-k_f$ and k_f respectively. When $\epsilon_i = -1$ this corresponds to a "event" event.

We call k_f the flipping rate, we can consider it like an inverse persistence length $l_p \approx \frac{v_0}{k_f}$ during which the particle won't reverse its direction of motion. In the model $0 \leq k_f \leq 0.5$. This persistence can come from the environment, for instance in the case of shaken granulars the asperities of the surface will favor one or the other direction of motion, but still along the axis. But the persistence can also be at the particle level : self-propelled agents such as myxobacteria show "periodic" reversal of motion [66] thus there are reasons to believe that the internal machinery is able to reverse its direction of propulsion from times to times and must be included in the model. The limit $k_f = 0$ corresponds to particle never spontaneously reversing (flipping) their self-propulsion orientation ($l_p \to \infty$) it will be called *rods*, whereas the limit $k_f = 0.5$ (diffusive limit with equal probability to "hop" in each direction) will be called *pure active nematics*.

The first term of the left-hand side of equation (2.6) is the nematic alignment vector $\boldsymbol{A}_i$ is :

$$\mathbf{A}_i(t) = \frac{1}{N_i} \sum_{j \in \partial i} \operatorname{sgn}\left\{\cos(\theta_i(t) - \theta_j(t))\right\} \mathbf{u}_j \tag{2.7}$$

Where the sum is performed over neighbors particles $j \in \partial i$ is performed on all particles within a radius r_a (radius of alignment), including the particle itself (we recover $\mathbf{A_i} = \mathbf{u}_i$ when i is alone: i "aligns" with itself). As required by the nematic symmetry this vector is invariant under the reversal of any particle, that is the transformation $\boldsymbol{u}_k \to -\boldsymbol{u}_k$. Indeed the transform $-$ sign in front of the vector which is compensated by the cosine change of sign: $\cos(\theta_i(t) - \theta_j(t))\boldsymbol{u}_j \to \cos(\theta_i(t) - \theta_j(t) + \pi)(-\boldsymbol{u}_j) = \not{-}\cos(\theta_i(t) - \theta_j(t))(\not{-}\boldsymbol{u}_j)$

The second term appearing in (2.6) is the repulsion $\boldsymbol{R}_i$:

$$\mathbf{R}_i(t) = \frac{1}{N_i - 1} \sum_{\partial i, i \neq j} \mathbf{u}_{ji} \tag{2.8}$$

Where u_{ji} is the normed vector pointing from particle j to i, thus repelling the pair when $\beta \geq 0$, that is $u_{ji} = \frac{x_i - x_j}{||x_i - x_j||}$. The neighborhood ∂i is defined as particles located within a radius r_β (though we kept $r_a = r_\beta$ in all simulations) from x_i. This so called "repulsion" is in fact acting as a torque given that this term is only acting on the angular part(in equation (2.6)) and not on the positions (equation (2.5)) where it should also act if it were a force. Introducing a non torque-like repulsion would lead to non-conservation of the norm of the speed v_0. It would get us out of Vicsek-like models and could lead to MIPS phenomenon among other things. Notice that this time

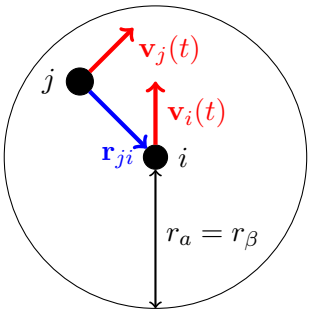

FIGURE 2.3: A schematics showing the different parameters shown in equation (2.6)

the sum does not include particle i, obviously because it is a repulsive interaction (u_{ii} is not defined). Finally the coefficient β, defines the repulsion intensity.

The geometry of the space the agents are lying on is essential and must be precised. We recall that in disk-like confined spaces some bacteria spontaneously flow in phases keeping the circular invariant geometry. All this work has been performed with a 2D toroidal geometry, also named "periodic boundary conditions". More precisely we have a box of length L_x , height L_y and a particle that crosses for instance the boundary $x = L_{x/y}$ will appear on the opposed side of the box $x/y = 0$, equivalently the particle is subject to a translation $x_i \to x_i - L_{x/y}$ without affecting the velocity $\boldsymbol{v}$.

Finally we summarize the importance of the various parameters we will explore :

- ρ and η as in usual Vicsek-style models with an order-disorder transition high enough noise / low enough density
- the repulsion intensity β and its associated range r_β which will define what a dense region is ($\rho_c \geq 1/r_\beta^2$)
- the alignment range r_a
- the flipping rate k_f which totally changes the phenomenology as we go from the diffusive $k_f = \frac{1}{2}$ to the propagative regime $k_f = 0$ as we will see.
- the speed v_0, in Vicsek models without density this term is not relevant at the mesoscopic scale as it can be ruled out by adimensionalization (we have a length scale r_a , a time scale set to 1 here) . However introducing the repulsion brings another length scale. Consequently, this parameter relevance will be highlighted in the next sections (defects velocity in 2.4 , arches/defect ordered state in 2.6.2 / 2.6.1 *etc.*).

This work has mainly consisted on phase exploration of this model which shows new phases and thus a rich phase diagram. Additionally we will make a comparison with the hydrodynamic theory we developed [2], these will be the focus made in the next sections.

[2] see 2.3 for calculation of the hydrodynamic theory

2.3 Derivation of the hydrodynamics equations

As we have mentioned in chapter 1 we have developed in parallel a hydrodynamic theory using the Boltzmann-Ginzburg-Landau scheme of Bertin *et al.*. This section is dedicated for those who are interested in more details in this derivation as much as providing a clearer understanding of what we will explain in the following chapters.

2.3.1 Boltzmann equation

First of all we start with the Boltzmann integral (2.9):

$$\partial_t f + v_0 \mathbf{e}(\theta).\vec{\nabla} f = a\left[f(\boldsymbol{r},\theta+\pi,t) - f(\boldsymbol{r},\theta,t)\right] + I_{diff}\left[f\right] + I_{col}\left[f\right] \quad (2.9)$$

On the right hand side the terms account for fluxes of particles which are subject to different interactions changing their direction/position.

- The first term on the right hand side accounts for the particles reversing their direction ($v_0 \to -v_0$) with a rate a
- The collision term accounts for the particles which interacts and change their angles due to the interaction. Of course this term will depend strongly of the model we choose and must respect the simple symmetries of the collision type we chose.
- The diffusion term account for the fact that we put noise over the angle, consequently the angle of each particle diffuses. It might also include positional diffusion

In more details, the self-diffusion term I_{diff} is the simplest and reads:

$$I_{diff}\left[f\right] = \lambda \int_{-\pi}^{\pi} d\theta' f(\theta') \left[\langle \delta_{2\pi}(\theta'+\eta-\theta)\rangle_\eta - \delta(\theta'-\theta)\right] \quad (2.10)$$

Where we introduced $\delta_{2\pi}$ which is 2π periodic Dirac function ($\delta_{2\pi}(2n\pi) = \infty\, \forall n \in \mathbb{N}$ else 0). The collisional integral I_{col} reads :

$$I_{col}[f] = \int_{-\pi}^{\pi} d\theta_1 \int_{-\pi}^{\pi} d\theta_2 f(\mathbf{r},\theta_1) \int_0^{\infty} ds\, s$$
$$\int_{-\pi}^{\pi} d\phi \mathrm{K}(s,\phi,\theta_1,\theta_2) f(\mathbf{r}+s\mathbf{e}(\phi),\theta_2)\Big[\langle \delta_{2\pi}\big(\Psi(\theta_1,\theta_2)+\eta-\theta\big)\rangle_\eta - \delta_{2\pi}(\theta_1-\theta)\Big] \quad (2.11)$$

Where the average notation $<>_\eta$ means averages over the noise distribution $P(\eta)$, usually this noise distribution is chosen to be a wrapped over 2π Gaussian distribution (meaning that we transform the standard Gaussian distribution as a 2π periodic function). And $\mathbf{r}' - \mathbf{r} \equiv s\mathbf{e}(\phi)$ is the relative position of the two particles implied in the collision. $K(s,\phi,\theta_1,\theta_2)$ is the

collision kernel which translates the outcome of the collision as a function of its input parameters (θ_1 , θ_2 , ϕ). Considering initially collision of hard spheres we are developing the expression of K.

We define an angle ϕ_0 parameterizing the collision with relation (2.12) :

$$\mathbf{e}(\theta_2) - \mathbf{e}(\theta_1) = -||\mathbf{e}(\theta_2) - \mathbf{e}(\theta_1)||\ \mathbf{e}(\phi_0) \tag{2.12}$$

After some trigonometry we can finally write the collision kernel in (2.13):

$$\mathrm{K}(s,\phi,\theta_1,\theta_2) = g(s)\,||\mathbf{e}(\theta_1)-\mathbf{e}(\theta_2)||\cos\left(\phi-\phi_0(\theta_1,\theta_2)\right)\Theta\Big(\cos\left(\phi-\phi_0(\theta_1,\theta_2)\right)\Big) \tag{2.13}$$

Which is written assuming that collision occurs between, hard spheres that is only when the distance between particles is exactly d_0 translated by function $g(s) = \delta(s - d_0)$. Note that $\Theta(x)$ is the Heaviside function. Finally the term $||\mathbf{e}(\theta_1) - \mathbf{e}(\theta_2)||$ can be expressed as $||\mathbf{e}(\theta_1) - \mathbf{e}(\theta_2)|| = 2|\sin\frac{\theta_1-\theta_2}{2}|$ for ballistic particles (it's a simple trigonometry problem).

Expression (2.13) allows us to go beyond hard-spheres collisions as we can choose another $g(s)$, function which simply translates the collision rate dependence as a function of the distance. We consider for simplicity a power law dependence on s.

During a collision the particles repel each other by a force that depends on the their relative distance s, which in the Boltzmann framework is microscopic. The distribution function on such distance does not vary appreciably and we can develop it in gradients around the position $\mathbf{r}$ of particle 1

$$f(\mathbf{r} + s\mathbf{e}(\phi), \theta_2) \sim \left(1 + s\mathbf{e}(\phi)\cdot\vec{\nabla} + \frac{s^2}{2}(\mathbf{e}(\phi)\cdot\vec{\nabla})^2 + \mathrm{O}(\vec{\nabla}^3)\right) f(\mathbf{r},\theta_2)$$

2.3.2 In Fourier space

Going into Fourier space seems natural because the microscopic velocity norm v_0 is constant and we derive the equations from this microscopic model. We thus we ruled out the speed $\mathbf{v}$ in favor of the more convenient parameterization by θ keeping in mind that $\mathbf{v} = v_0 e^{i\theta}$.

However we are dealing with averaged quantities and a hypothesis should be taken with particular care. There is a strong hypothesis behind this assumption: we assume is that the order is strong enough locally and field vary slowly with respect to θ so that $\vec{v} =< \mathbf{v_i} > \approx v_0 e^{i\arg(<v_i>)} = v_0 e^{i\theta}$ We then see that we can obtain a system of coupled equations relating the f_k to the other f_i by equating the terms of equal harmonics. We could in principle continue this expansion of f in series of f_k *ad nauseam*, but the system of coupled equations is unsolvable analytically.

Some precisions: using the complex notation and defining the complex differential operator $\nabla = \partial_x + \imath\partial_y$, we have the identities

$$\mathbf{e}(\phi)\cdot\vec{\nabla} = \frac{1}{2}\left(e^{\imath\phi}\nabla^* + e^{-\imath\phi}\nabla\right), \qquad (\mathbf{e}(\phi)\cdot\vec{\nabla})^2 = \frac{1}{4}\left(2\triangle + e^{2\imath\phi}\nabla^{2*} + e^{-2\imath\phi}\nabla^2\right), \quad \triangle = \nabla\nabla^* = \nabla^*\nabla$$

The Fourier transform of Eq. (2.9) is

$$\partial_t f_k + \frac{v_0}{2}\left(\nabla f_{k-1} + \nabla^* f_{k+1}\right) = \left(\lambda(P_k - 1) - a[1-(-1)^k]\right) f_k + \int_{-\pi}^{\pi} e^{\imath k\theta} I_{\mathrm{col}}[f] d\theta \tag{2.14}$$

where the first term on the r.h.s. comes from the Fourier transform of the self-diffusion term (thus the λ factor) and from the transform of the velocity-reversal, hence the a factor.

The collision term can be written as follows :

$$\sum_q f_{k-q+n}\mathcal{L}_n^m f_q e^{-\imath n\pi/2}\int_{-\pi}^{\pi} d\Delta e^{\imath\Delta(n/2-q)}\mathrm{K}(\Delta)\left[P_k e^{\imath kH(\Delta)} - 1\right]\frac{\cos(n\pi/2)}{n^2-1}\frac{2}{\pi}\int_0^{\infty} s^{m+1}g(s)ds$$

Where $\Delta = \theta_2 - \theta_1$ and the alignment is encoded in $\psi(\theta_1, \theta_2) = \theta_1 + H(\Delta)$ and $H(\Delta)$ takes into account the symmetry of the alignment interaction:

$$H(\Delta) = \frac{\Delta}{2} + \begin{cases} 0, & 0 < \Delta < \frac{\pi}{2} \\ \frac{\pi}{2}, & \frac{\pi}{2} < \Delta < \frac{3\pi}{2} \\ \pi, & \frac{3\pi}{2} < \Delta < 2\pi \end{cases}$$

The $\mathcal{L}_n^m$ are differential operators acting on the spatial variables of order m, and that behaves under global rotation as f_n: for example $\mathcal{L}_{-1}^1 = \nabla$, $\mathcal{L}_1^1 = \nabla^*$ and $\mathcal{L}_0^2 = \triangle$ and $\mathcal{L}_0^0 = 1$.

The last operation consist in integrating on the spatial dependency s , which translates into the b_m terms:

$$b_m = \int_0^{\infty} s^{m+1} g(s) ds \tag{2.15}$$

Finally having developed at the second order in s expansion we have:

$$\begin{aligned}\partial_t f_k = &-\frac{v_0}{2}\left(\nabla f_{k-1} + \nabla^* f_{k+1}\right) + \left(P_k - 1 - a[1-(-1)^k]\right) f_k \\ &+ b_0 \sum_q J_{k,q,0} f_{k-q} f_q + 2b_1 \sum_q \left(J_{k,q,1} f_{k-q+1} \nabla^* f_q + J_{k,q,-1} f_{k-q-1} \nabla f_q\right) \\ &+ b_2 \sum_q \left(J_{k,q,0} f_{k-q} \triangle f_q + \frac{1}{6} J_{k,q,-2} f_{k-q-2} \nabla^2 f_q + \frac{1}{6} J_{k,q,2} f_{k-q+2} \nabla^{*2} f_q\right)\end{aligned} \tag{2.16}$$

2.3.3 Closure and final equations

The next step is truncate the system of coupled equations up to order n in f_k with two constraints: first we need to consider all f_k which are relevant for our problem (ex: f_0 and f_1 for polar particles, f_0 and f_2 for nematic ones.). Secondly, the higher order f_n truncation is done at the first stable mode after the ones of interest, allowing to have non explosive equations.

More importantly this coupled system need to be closed by the choice of a *scaling ansatz*. We assume that, "close to the transition" from order to disorder all the fields are small, all the fields are slowly varying in space, thus the gradient ∇ is small as a quantity, the same goes for temporal variations thus temporal derivatives are "small". In the end all these fields and derivative go as $\partial\epsilon^j$. Equating the terms lead to the correct scaling of all fields and derivatives. It is then possible to start from the highest order f_n term and to enslave it to lower order terms f'_k (by construction, this term is stable and decaying quickly *close to the transition*). This way to proceed allows to decouple the terms of interest from these high order enslaved variables. Also we are ensured that close to the transition the equations are stable (compared to Marchetti & a.l approach in which they put stabilizing terms by hand).

Now into details: slow variation of fields allows to write $\nabla \sim \epsilon$. Balancing the other equations leads to the following scaling:

$$\delta\rho \sim \epsilon, \qquad f_{2k-1} \sim f_{2k} \sim \epsilon^{|k|}, \quad \forall k > 0$$

We can obtain the equation for the temporal variations of the density field, that is the continuity equation:

$$\partial_t \rho = -\frac{v_0}{2}\left(\nabla^* f_1 + \nabla f_1^*\right) \tag{2.17}$$

We can then enslave f_3 and f_4 (not developed here) because these fields are stable and thus will quickly decay to values depending on f_1 and f_2 as and close the hierarchy of equations, finally we have the equations for the polar field f_1 and the nematic field f_2:

$$\begin{aligned}\partial_t f_1 &= (\alpha[\rho] - \beta|f_2|^2)f_1 + \zeta f_1^* f_2 \\ &\quad -\mathrm{v}_\rho[\rho]\nabla\rho - \mathrm{v}_n[\rho]\nabla^* f_2 \\ &\quad +\gamma_2 f_2 \nabla f_2^* + \gamma_1 f_2^* \nabla f_2 \\ &\quad -\lambda_n f_2 \nabla^* \rho \\ &\quad +\lambda_1 f_1 \nabla^* f_1 + \lambda_2 f_1 \nabla f_1^* + \lambda_3 f_1^* \nabla f_1 \\ &\quad +\upsilon_3 \triangle f_1 + \upsilon_4 \nabla^2 f_1^* \end{aligned} \tag{2.18}$$

and

$$\begin{aligned}\partial_t f_2 &= (\mu[\rho] + \tau|f_1|^2 - \xi|f_2|^2)f_2 + \omega f_1^2 + \nu\triangle f_2 \\ &\quad -\mathrm{v}_p[\rho]\nabla f_1 \\ &\quad +\chi_1 \nabla^*(f_1 f_2) + \chi_2 f_2 \nabla^* f_1 + \chi_3 f_2 \nabla f_1^* \\ &\quad +\kappa_1 f_1^* \nabla f_2 + \kappa_2 f_1 \nabla\rho \\ &\quad +\upsilon_2 \nabla^2 \rho \end{aligned} \tag{2.19}$$

with all coefficients which depend on density are noted $[\rho]$, their dependence on all microscopic parameters is not detailed for simplicity.

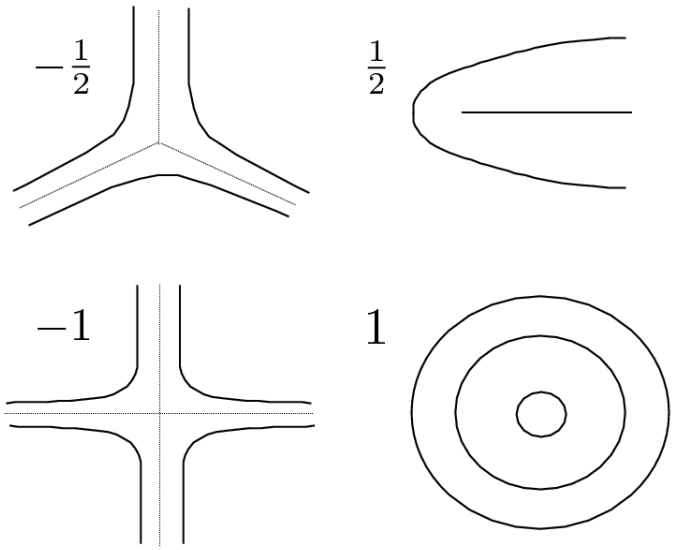

FIGURE 2.4: Defects classified by their charges. What is represented as straight lines are few field lines, that is the curves defined by the condition that particles are parallel to these lines. source: http://inspirehep.net/record/821794/plots

2.4 Defects

An essential difference between active nematics and nematics at equilibrium is the dynamics of topological defects. Topological defects in a nematic are defined as discontinuities of the nematic angle, the point where it is discontinuous is called the defect core. We restrict ourselves to the 2D case because defects structure depends also on the space dimensionality.

In figure 2.5, we can see the parameterization of the defects topology by an angle theta $\in [0, 2\pi]$ and an angle $\phi(\theta)$ which indicates the local orientation of the nematic field around the defect. Over one full rotation around the defect core (θ goes from 0 to 2π), ϕ angle might perform a certain number of rotations (in the "nematic sense" a rotation corresponds to a loop over π) or none. This $\phi(\theta)$ relation is essential to characterize defects, indeed to the number of loops of ϕ corresponds shape of the defect, and if ϕ doesn't loop there is no defect.

Defects have been classified by providing them a charge q which value is a half integer ($\{\frac{1}{2}, 1, \frac{3}{2}, ...\}$ and their negative counterparts) and corresponds to the number of rotations of ϕ. As we can see in 2.4 , the case $q = \frac{1}{2}$ correspond to the defect with a comet-like shape, whereas the case $q = -\frac{1}{2}$ has a three branches shape . Higher q defects exist, for $q = 1$ we have asters and vortices for $q = -1$ as we can see in 2.4

Topology implies deep constraints on these defects. For instance the fact that the quantum of topological charge is a half-integer, is caused by the nature of symmetry of the system: given a system with nematic symmetry ϕ might perform π rotations because of its symmetry group. However if one would consider a system with *polar* rotational symmetry- i.e. ϕ indicated the polar order and thus where $\phi \in [0, 2\pi[$, the value of q is an integer

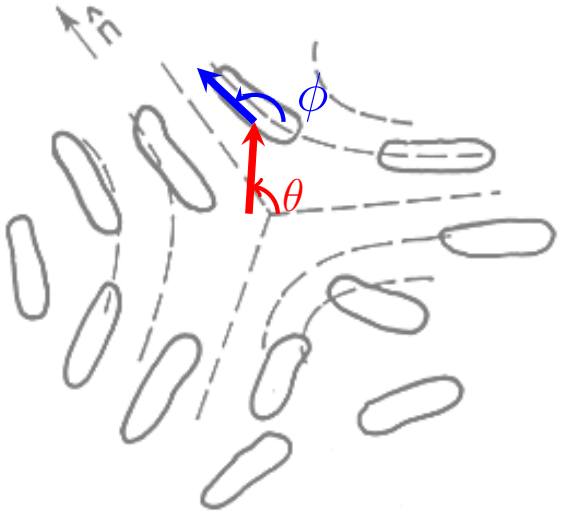

FIGURE 2.5: Parameterization of the defect $\phi(\theta)$, here a -1/2, θ characterizes the position around the defect while ϕ gives the nematic angle, source: http://www.lassp.cornell.edu/sethna/OrderParameters/

simply because it it imposed by topology. Imagine that ϕ doesn't perform a full 2π then the polar field would not be continuous. That means that in Vicsek-style models where the relevant field is the polar field, there is no $\pm\frac{1}{2}$ defects.

Another essential property is the fact that the global topological charge is a conserved quantity : if the most stable phase of the system is defect free , the global charge of the system would be $q = 0$ and thus if for some reason a $q = \frac{1}{2}$ defect is generated, its negative counterpart $q = -\frac{1}{2}$ will also be present. It comes in fact from the very process of defects nucleation where defects are always generated in pairs.

At equilibrium we can show that [3]the energy of half integer defects is lower than those of integer defects and so on, the most stable phase of lowest energy consequently being the defect-free one. Therefore, defects are not stable at equilibrium, except in liquid crystals where relaxation timescales might allow for long lived defects configuration, if defects are present in the systems *and the global initial topological charge is 0* (we recall it is a conserved quantity over time), these defects should annihilate for energetic reasons and lead to the nematic phase *always*. And if there are none they won't spontaneously appear. Thus defects are not stable at equilibrium

Out of equilibrium, the situation is less clear. As energy is constantly injected locally local rearrangement of particles happen, allowing spontaneous nucleation, recombining and annihilation of pair of defects. All these phenomena have been spotted in both experiment and in our simulations.

From the experimental point of view the most interesting experiments are those of Dogic [47]: microtubules are driven out of equilibrium by kinesin

[3]In [18] the free energy of a defect pair is computed : $F = \pi K k^2 log(R/a) + \epsilon_c$ where R is the size of the system, a the radius of the core, k the winding number of the defects and ϵ_c "the contribution to the total energy due to the isotropic defect core"

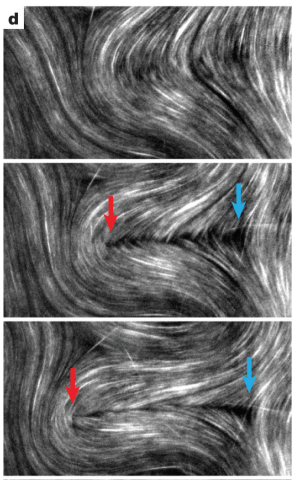

FIGURE 2.6: Nucleation of a pair of 1/2 charge defects as seen in microtubule experiments [47]

- a molecular motor - these microtubules are nematically interacting (and thus good candidates to be compared with our microscopic model and hydrodynamic theory) and are attracting a lot of interest. Indeed microtubules are a key component of eukaryotic cell and have an essential role in its shape and internal organization.

In figure 2.6 we can clearly see pair of half charged defects being smoothly created. The $+$ defect moves as expected from its symmetry, whereas the $-$ defect is almost static. The dynamics of such defects on larger scales is less clear and depends clearly on many parameters. Indeed the system exhibit $\frac{+1}{2}$ defects which interact "nematically" [4] and propel as shown in 2.7 and $-\frac{1}{2}$ whose movement is almost static. It can be simply understood as the $\frac{+1}{2}$ defect has an asymmetric (one could say polar) shape (we can define a head and a tail) whereas the $-\frac{1}{2}$ is symmetric in that sense (the defect shape is invariant under $\frac{2\pi}{3}$ rotations.

Giomi et al. introduced a theory on topological defects in 2D nematic in [18]. In this paper they use similar hydrodynamic equation than those of Marchetti *et a.l.* They consider pair of opposed $\frac{1}{2}$ charge defects in a periodic system of size $L \times L$ separated by a distance $\frac{L}{2}$ and they measure the velocities of $\frac{+1}{2}$ (resp $-\frac{1}{2}$) v_+ (resp $v-$)

The main result is that the positive defect has a ballistic motion when it is far enough from its negative counterpart. Compared to the system at equilibrium it seems that out of equilibrium, the "activity" is speeding up the $\frac{+1}{2}$ defect.

We have to pinpoint that, contrary to [17], our microscopic model doesn't include any "explicit" activity parameter. However it is probably a good guess to view activity as a mix between the speed v_0 and the persistence time $\propto \frac{1}{k_f}$. As a consequence we will study the behavior of the defects varying these parameters. The following section is dedicated to show the

[4] That is, if one puts arrow on the $+$ defects to indicate their polarity, these arrows configuration shows is itself a high nematic order.

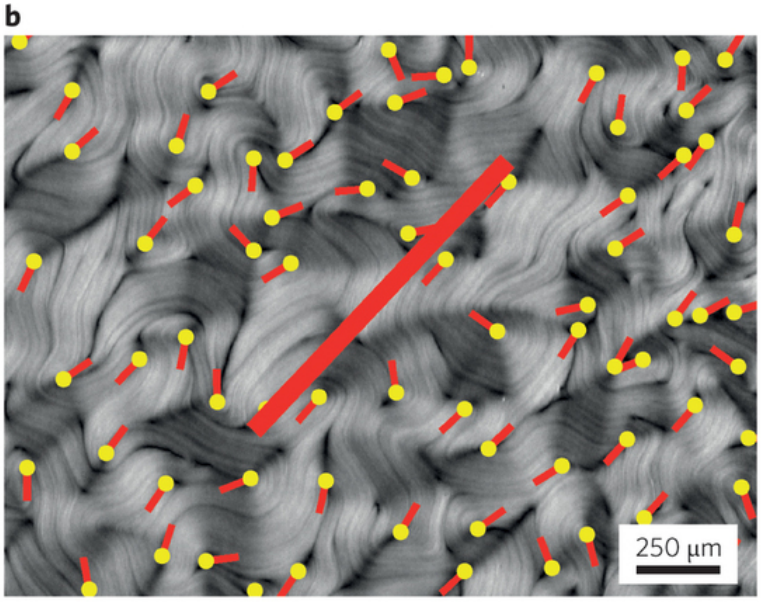

FIGURE 2.7: $\frac{1}{2}$ defects are shown, orientation is shown as arrows while their position corresponds to the yellow tip. The large red bar at the center shows the average nematic direction of these defects. One can see that some defects pairs seem to interact head to tail though it is not frequent. Also from [47]

techniques, for the interested reader, we used to have obtain simple and systematic defects localization.

2.4.0.1 Defects localization

As we already briefly presented in section 2.4 , the main characterization of a defect is its topological charge q, which we compute from the winding number, *i.e.* the following integral (2.20) on a contour $\mathcal{C}$ looping over the defect "core" parameterized by the angle θ and where the nematic angle is ϕ:

$$\begin{aligned} q &= \frac{1}{2\pi} \oint_{\mathcal{C}} \vec{\nabla}\phi \cdot d\vec{l} \\ &= \frac{1}{2\pi} \oint_{\mathcal{C}} d\phi \\ &= \frac{1}{2\pi} \oint_{\mathcal{C}} \frac{d\phi}{d\theta} d\theta \end{aligned} \tag{2.20}$$

The last expression is used to numerically compute this integral. We have to compute a continuous integral $\int \nabla\phi \cdot d\vec{l}$ at discrete positions around the defect, that is $\sum_{k=1}^{n} \delta(\phi_{k+1}, \phi_k)$, where $\delta(\phi_{k+1}, \phi_k)$ is a function that computes nematic angle differences, taking into account that such difference

can't be greater than π we have the following definition of the δ function [5] :

$$\delta(\phi_{k+1}, \phi_k) = \begin{cases} \phi_{k+1} - \phi_k + \pi, & \text{if } \phi_{k+1} - \phi_k \leq 0 \\ \phi_{k+1} - \phi_k - \pi, & \text{if } \phi_{k+1} - \phi_k \geq \pi \end{cases} \tag{2.21}$$

These are actually all these additional $\pm\pi$ terms which correspond to a "whole rotation" of the nematic angle which makes q nonzero. Geometrically that corresponds to the crossing of the defects *disclination* line (the periodic boundary) where ϕ goes from π to 0 , that is when the vector ϕ performed one

2.4.0.2 Defects orientation

Defects are not only characterized by the position of their core. They also possess an orientation. There are two methods to compute this orientation, the first method is geometrical whereas the second one relies that the defect self-propulsion is dictated by a *backflow* and its orientation is along this term backflow. Both of these characterization are studied in [60]. In the following we will consider only working with $\frac{+1}{2}$ defects, the properties of the $-\frac{1}{2}$ defects are similar if we restrict ourselves to $1\!3$ of the angular space around the defect because of their 3-fold symmetry (these defects are invariant under a $\frac{2\pi}{3}$ rotation .)

Now consider that we have parameterized this positive defect by the nematic angle $\phi(\theta)$ as in figure 2.5. The symmetry axis of the defect is the line characterized by the angle ϕ such that :

$$\phi(\theta) = \theta \quad \text{or} \quad \phi(\theta) = \theta + \pi \tag{2.22}$$

Numerically we proceed as follows : we assume that we have computed the discrete (coarse grained) nematic field, see 2.4 and we detected the defect core's position at (x_c, y_c). Using the same n positions x_k we extract $\phi(x_k, y_k) = \phi_k$ over a closed loop around the defect (we index by k using the natural counterclockwise orientation around the defect) . We have both ϕ_k and $\theta_k = \text{atan2}(x_k - x_c, y_k - y_c)$, therefore we can find the intersection of the two curves characterized by equation (2.22). In practice it is a little bit more complicated because the function ϕ_k might not be very smooth (theoretically we recall that the $\pm\frac{1}{2}$ defects are characterized by a parameterization $\phi(\theta) = \pm\frac{\theta}{2}$) and we have to find some interpolation of ϕ_k between the n points.

The other method is more straightforward. It consists in assuming that the defect self-propulsion term is given by the value of the vectorial field $\nabla \boldsymbol{S}$ (which is itself a symmetric traceless tensor) at the defect core position *and also that its orientation is along this term.* We therefore just compute this term at position x_c, y_c using finite difference method, given that we already computed the map of $\boldsymbol{S}_{xy}$.

[5] Note that for the summation $\phi_n + 1 = \phi_1$

Note that these two methods give similar but approximate results, at least in microscopics simulations. Several reasons exist for these discrepancies: first of all all these quantities ($\boldsymbol{S}, \vec{\nabla}\boldsymbol{S}$ etc.) can be ill-defined close from the defect because the density of particle at this position is too low. Secondly it is an assumption that the $\nabla \boldsymbol{S}$ term is leading the defect propulsion direction and defect orientation of $+$ defects. It is only true when the defect is far apart from any other defect but when short range interaction start to lead the behavior of defects, the self-propulsion nature of these defects is also affected (we recall that they speed up).

2.4.1 Velocity measurements

2.4.1.1 Generating defects

As we've clarified how we can characterize defects we can now detail the various experiments we proceeded with defects. In order to obtain systematic results we don't let the system nucleate defects itself. The reason is simple: in the stability region of the nematic phase, especially at high density, defects are very unlikely to appear and we would have to wait very long times to observe spontaneous nucleation of a pair. On the contrary if we choose an isotropic initial conditions (random initial positions and orientations of particles) we are generating a large number of defect at random position, an hardly reproducible and controllable case! Therefore in order to obtain defects in a controlled manner we were able to use an initial configuration which create pair of defects with following parameterization of the field (2.23) :

$$\begin{aligned} f_2(x,y) &= \{\tanh(r - R_0), -\tanh(A\sin(\frac{2\pi}{L_x}(x+y)))\} \\ r &= \sqrt{(x-x_c)^2 + (y-y_c)^2} \end{aligned} \tag{2.23}$$

This equation allows us to create a pair of defects centered around position $(x_c, y_c) = (\frac{L_x}{2}, \frac{L_y}{2})$ separated by a distance $2 \times R_0$ as figure 2.8 illustrates.

We can now check the velocity of defects for various parameters. We will focus on the flipping rate and the self-propulsion velocity v_0 mainly. To simplify the analysis we will only consider the y position of the defects and assume that the movements with respect to the x axis are not significant in the initial phase of interaction. If this assumption can always be assumed true at short times, we should note that at low flipping rates[6] we see on relatively short timescales this hypothesis fail. In that case the y position is clearly not diffusive and we can see a drift of the y position. This maybe indicates stronger interaction when the flipping rate becomes low.

[6] Also when v_0 becomes high we notice strange behavior for the positive defect which becomes immobile whereas the negative one starts to move

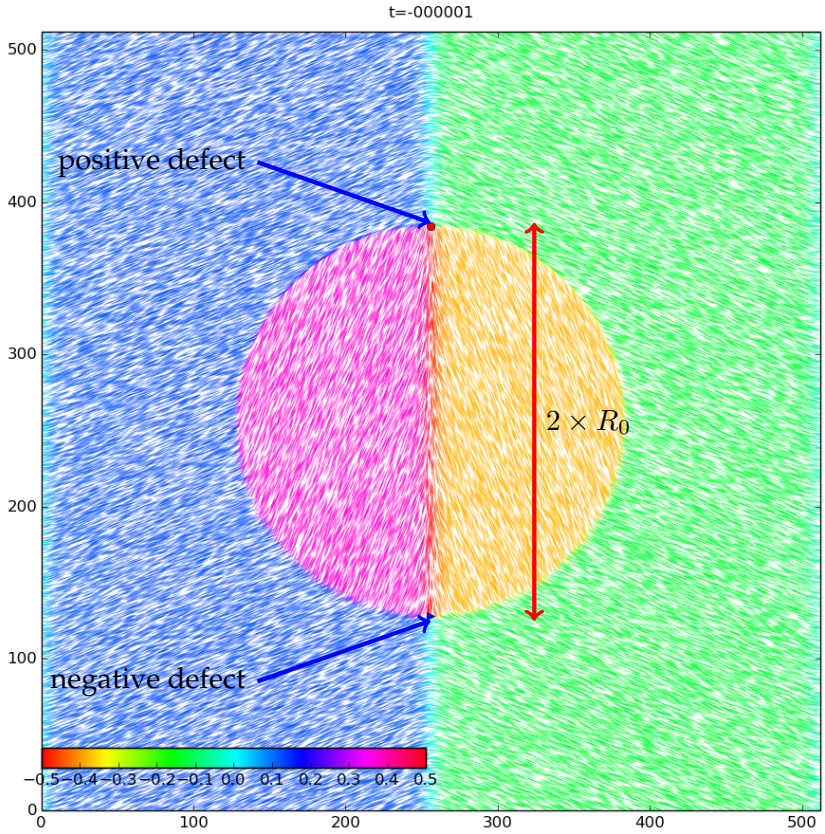

FIGURE 2.8: initial configuration of the pair of defects. The coloring is as usual giving the nematic angle ϕ

2.4.1.2 Minimal system size

We have checked that we needed large enough system to obtain *asymptotic* defects velocities. Meaning that if the initial defects separation $2 \times R_0$ is too small, even in the very first steps the interaction will be the one of strongly interacting defects and not the *asymptotic* interaction we expect to measure.

For the positive defect, figure 2.9(a) already suggests a system size of 128 is too small because the initial velocity is high compared to bigger systems, what's more another sign of interaction is that for $t \geq 3000$ the y-position stays steady (in fact the defects already start to rotate). On the contrary for $L \geq 128$ during the whole tracking the defects moves downward with the same speed (fits for $L = 256$ and $L = 512$ corresponds respectively to black and grey lines).

Secondly, considering the negative defect, it appears clearly in figure 2.9(b) that it self-propels upwards for the smaller system ($L = 128$). On the contrary, on bigger system, it doesn't seem to move in one or the other direction, while it shows fluctuations of its position it is at most a diffusive behavior. In the hydrodynamics theory, for sufficient separation distances, this defect doesn't move. This suggest again that $L = 128$ is not suited and defects are already interacting. Though we could argue that for all sizes the position is not constant we stress the fact that the fluctuations are natural because of the noisy nature of the system.

In conclusion, for system size ≥ 256, the interaction between the two defect is not significant for short timescales and our results agree with the hydrodynamic theory, we reached the "∞" distance regime.

Taking these minimal size requirement into account, we considered a large system with $L_x = L_y = 1024$. Figure 2.10 illustrates what happens when we change the spacing R_0 between the two defects. Tracking the y position ($y - y(t = 0)$ actually) of the $+$ defects we note that for duration ≤ 4000 the initial defect spacing has no influence on the steady velocity. Indeed the curves are linear and thus it confirms the existence of an asymptotic velocity, at least when considering short enough duration. The timescale for which the we exit the linear regime depends on the separation distance and are coherent with the fact that close defects start to interact "non-linearly" quicker (at time ≥ 4000 for short separation $R_0 = 0.05L_x$ whereas ≥ 15000 for for higher separation $R_0 = 0.4L_x$).

2.4.2 Velocity measurements

As we have seen, a system size of $L_x = L_y = 1024$ with a separation distance $2 \times R_0 = 512$ leads to correct asymptotic speeds, we set these quantities and observe the influence of several parameters on the the early speed of defects.

2.4.2.1 Pure active nematics ($k_f = 0.5$) : importance of v_0

Study of the hydrodynamics equations suggest that the positive defect velocity v_+ is a function of the microscopic speed v_0 [7]. We performed a systematic study of the positive defect speed for maximal flipping rate $k_f = 0.5$ *varying* v_0. The defects y position was tracked during 50000 timesteps and we measured the mean velocity of the defects in the y direction as the slope of the trajectory $v_y = \frac{\Delta y}{\Delta t}$.

The results in figure 2.11 are agreeing with the predictions of the hydrodynamics theory. Indeed both predict a similar shape for the defects velocity, that is a peak region then a decrease and a change of sign. What's more, for the hydrodynamics as well as the microscopics, there is a possible change of self-propulsion orientation by tuning v_0. In the microscopic case it happens around a critical velocity $v_r \approx 0.09$.

We stress that this change of sign is essential because of its implications: if a pair of defect is nucleated it means that at "high velocities" this pair of defects has a tendency to come close from each other and thus to "self-heal", whereas in the "low velocities" case the defects escape apart from each other and persist for long time. In the latter case it will lead to spectacular regime known as "ordered-defects" as we will see in section 2.6.2.

Note that in the hydrodynamics simulations we can see a very slight positive speed for the negative defect but in the microscopics simulation it is not the case, it is probably washed out by the noise fluctuations.

[7] Actually the analogous to v_0 in hydrodynamics v_s is a function of both the flipping rate and v_0

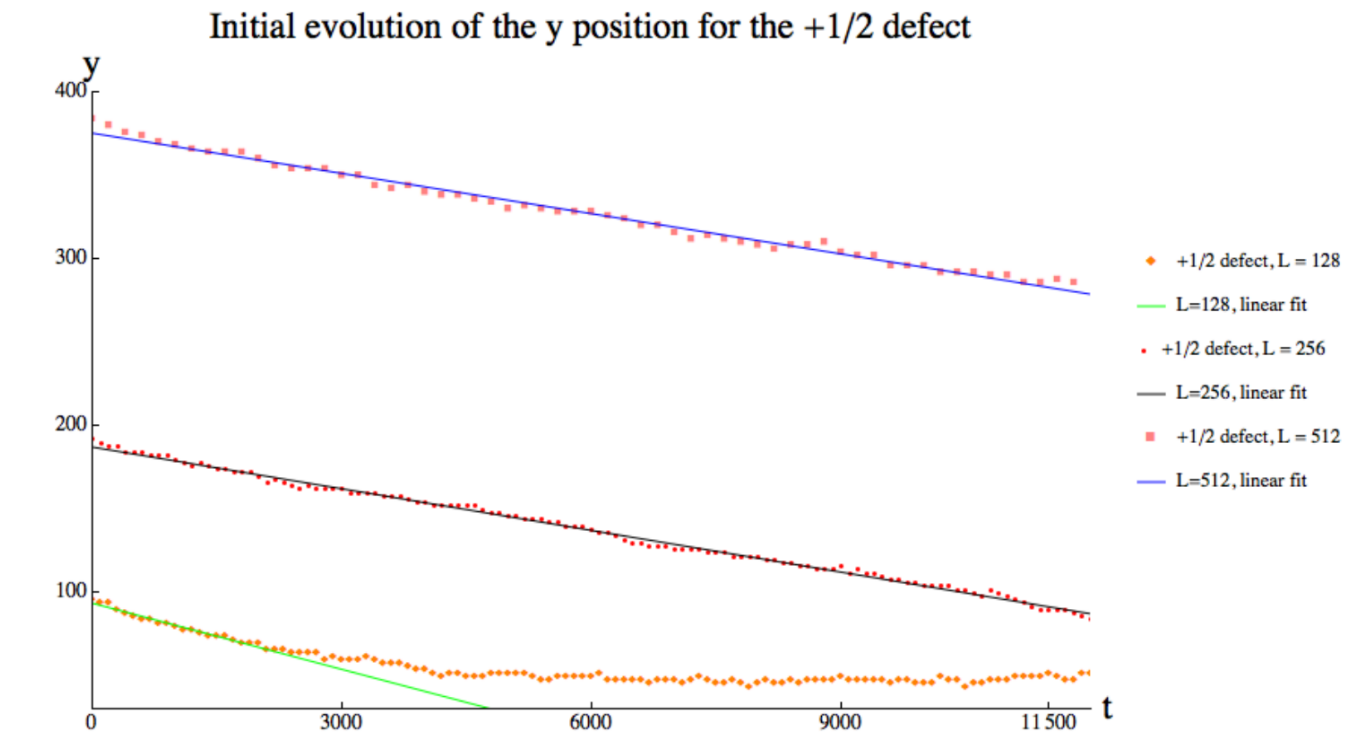

(a) evolution of the position of the positive defect for different system sizes $L \in \{512, 256, 128\}$ from the top down and proportional separation distances ($R_0 = \frac{L}{4}$)

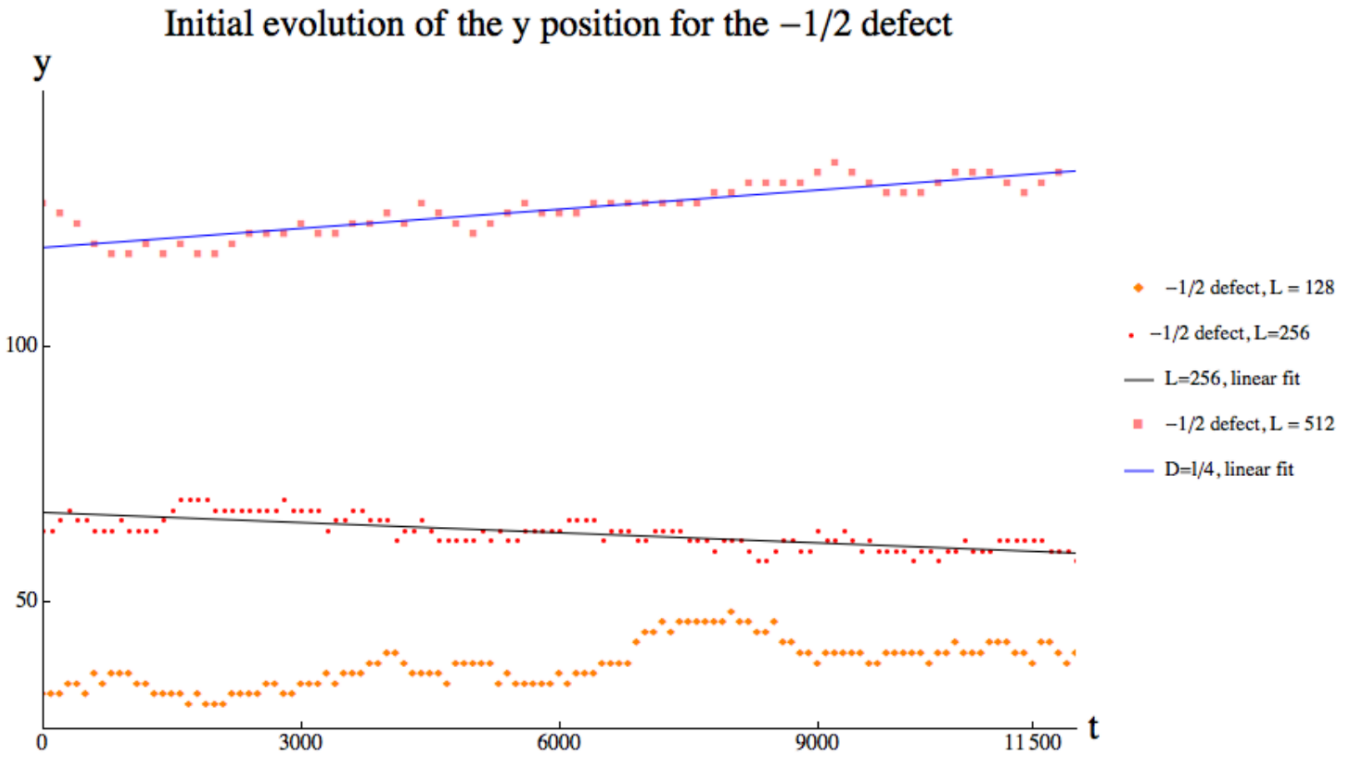

(b) evolution of the negative defect for different system sizes $L \in \{512, 256, 128\}$ from the top down and proportional separation distances ($R_0 = \frac{L}{4}$)

FIGURE 2.9: The $\pm$ defects velocity is constant for big enough systems.

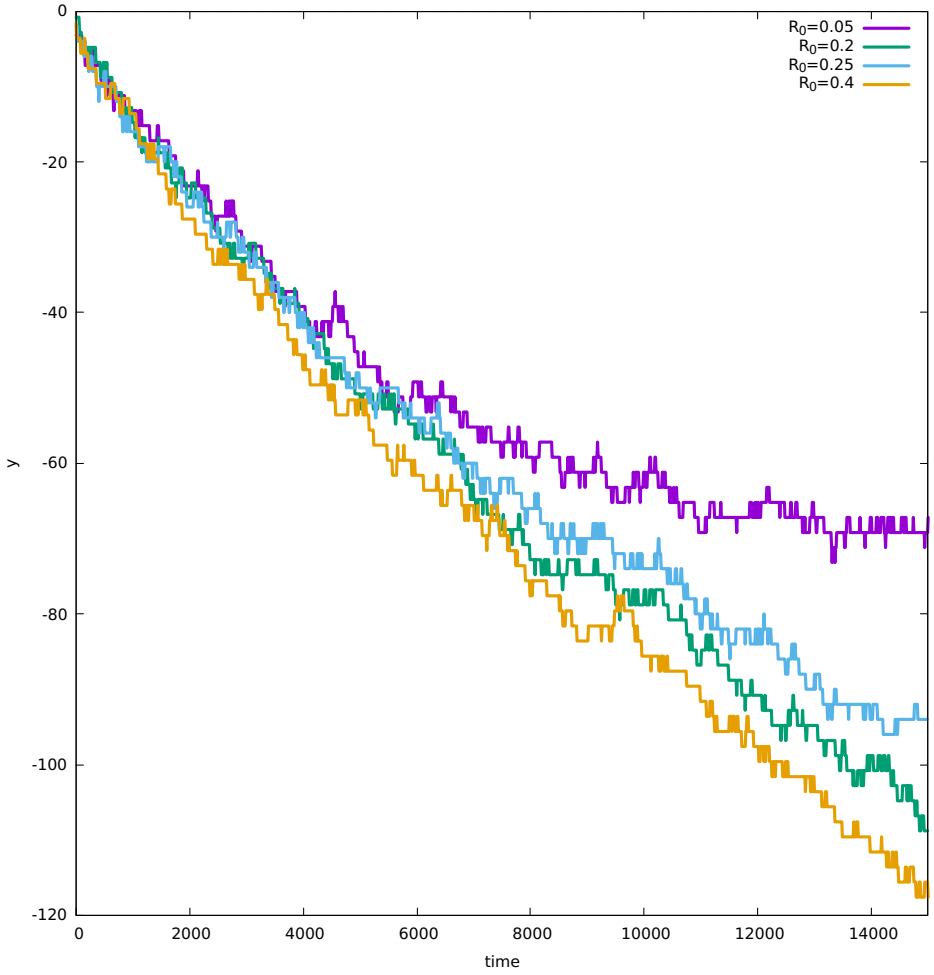

FIGURE 2.10: $L = 1024, \quad k_f = 0.5$. Evolution of the +1/2 defects position (y_+) for various separation distances

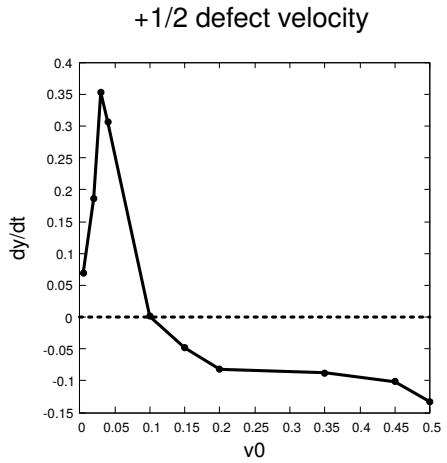

(a) Average velocity of the $\frac{+1}{2}$ defect in the y direction over 50000 timesteps for the microscopics case

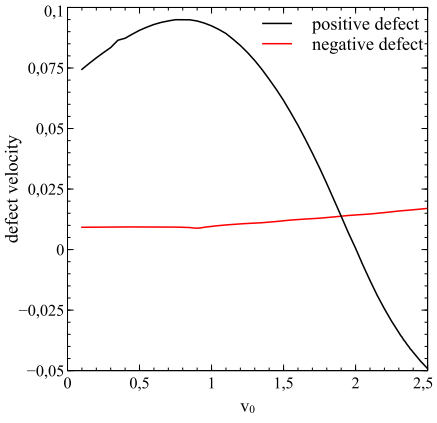

(b) Measured velocity (also y direction) of the $\frac{+1}{2}$ (black) and $\frac{-1}{2}$ (red) defects in the hydrodynamics case.

FIGURE 2.11: Comparison of defects velocity in the microscopics and hydrodynamics simulations

2.5 Case $k_f = 0$: rods

If we consider bacteria, rod shaped ones are so common that they are a category in itself named bacilli (singular : bacillus) however this categorization isn't taking into account the nature of their self-propulsion, which might differ from bacteria to bacteria. In this section the case $k_f = 0$ is aimed to focus on the class of bacteria which, for some reason, has an asymmetry in the propulsion and thus conserve the direction of motion over large timescales. For instance *Bacillus subtilis* in [71] is an elongated symmetric bacteria which self-propel with its flagella, it evolves in a µm-thick thin Agar substrate (a kind of sugar,very easy to shape). Considering the typical size of these bacteria ($\approx 1\,\mu\mathrm{m}$ in length with an aspect ratio ≈ 4) it is a reasonable to assume this experiment is quasi two-dimensional. However in this paper the focus is largely on giant density fluctuations and collective-motion emergence, a topic largely covered by [45]. Here we will focus more deeply on the chaotic regime and its link to defects behavior.

But the kind of system we could render is not limited to bacteria, the now well developed experiment of Dogic we already mentioned [47] is the prototypical quasi two dimensional system which we aim to reproduce and understand the key features [8] using our microscopic model.

2.5.1 Chaotic regime

The alignment is what dictates the symmetry of the phases we expect to see in the system: even if rods self-propulsion is polar we expect to see a nematic stable phase and an isotropic phase at high enough noise. However the introduction of the repulsion generates an instability of the nematic state.

We've also studied the hydrodynamics equation with a standard linear instability analysis of its deformation modes. This study predicts a fastest growing mode which makes the nematic unstable with respect to fluctuations along the axis of symmetry. That is to say that if we consider the nematic tensor defined in section 2.1.1 $\boldsymbol{S} = (S_{xx}, S_{xy})$ (we recall that the nematic tensor is symmetric traceless) and if we consider arbitrarily, but without loss of generality, that the nematic order is along x, then S_{xy} which is initially ≈ 0 grows *exponentially*.

This linearly evolving regime is then replaced by a nonlinear evolution: the system evolve to some *chaotic* regime as can be seen in figure 2.12 , this chaotic regime is also visible in the experiments of [47]. This chaos in the microscopic model is shown in figure 2.12 where the color indicates nematic orientation (in units of π in the color bar) as usual. We can see that the "chaos" is made of ordered dense regions with high nematic order which stand alongside holes: disordered low density regions (in fact in this figure, these sparse regions are indicated by lots of close defects, which are in fact spurious, the low density implies that the defect the detection algorithm fails), for clarity we indicated a few of these holes with black circles. In

[8] at least some of their features, particularly the defects dynamics

between a lots of defects (real this time!) which travel in the system also [9] in a chaotic manner in the sense that their motion is indescribable: it is neither ballistic nor diffusive. These defects frequently change their direction of motion and travel large distances. When the chaos is reached, defects are constantly nucleating and annihilating in the whole system.

Finally, as complex as the dynamical aspects can be, we can still name some typical features of this chaotic regime:

- A steady distribution over time of the number of defects.
- A highly fluctuating *nematic* order parameter S over time, as shown by figure 2.16

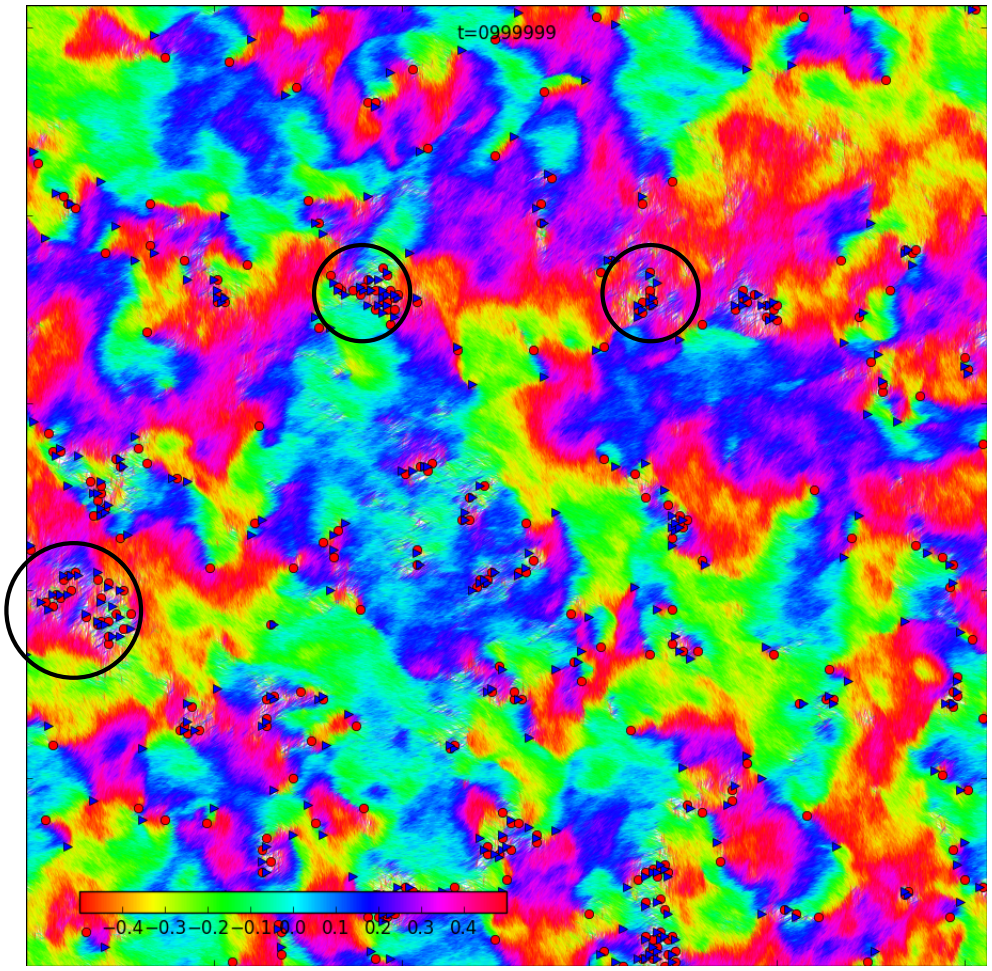

FIGURE 2.12: A picture of the "fully developed" chaos, the color indicates the local nematic orientation. No order can be seen in these pictures as no colored pattern appear. Red circles indicate $\frac{1}{2}$ defects and blue triangles $\frac{-1}{2}$ ones, however lots of detected defects are non-existent because located in low density regions, these regions are indicated by black circles.

[9] Of course from a static figure it is difficult to understand such description but

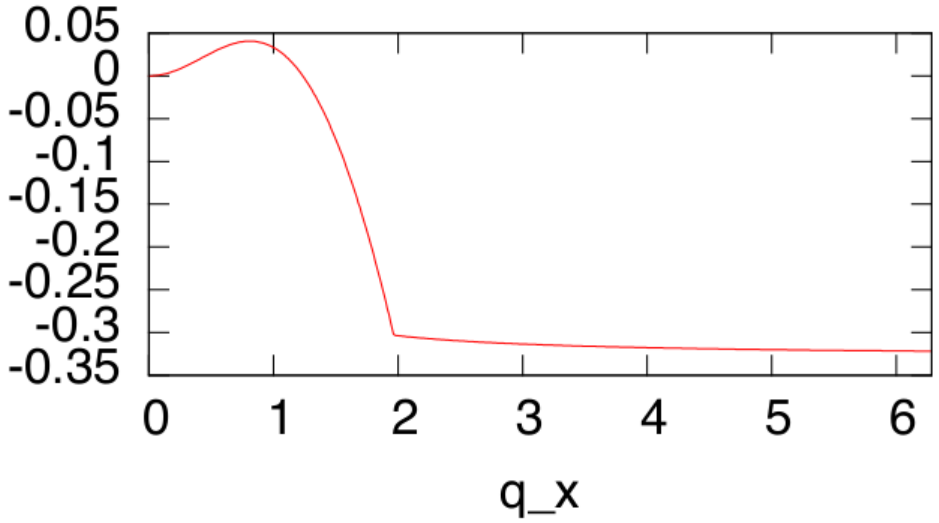

FIGURE 2.13: The hydrodynamics dispersion relations shows the growth rate of each mode as a function of its longitudinal wave vector q_x. A maximum can be seen around $q_x \approx 0.8$

2.5.2 Undulational instability

On some region of parameter space the nematic is unstable and before reaching the chaotic regime we can see growing stripes 2.14 along the direction of the nematic order. These data are in accordance with the linear stability analysis of the nematic state performed on the hydrodynamics equation. The analysis shows that the flat nematic state ($f_2(x, y) = 1$ $f_1 = 0$ $f_0 = \rho_0$) is unstable to perturbations. Indeed a dispersion relation, that is the growth rate of each mode (expressed as a function of the wave vector $q_x = \frac{2\pi}{\lambda}$ where λ wavelength of each mode) is the is shown in figure 2.13, shows that a range of modes long wavelength mode $q_x[0, 1.3]$ is unstable because their growth rate is ≥ 0. What's more this relation shows that their is a "most unstable" mode because the function possess a global maximum around $q_x \approx 0.8$, this confirms that at some point this mode will be more visible among the others. The sole presence of an undulating pattern with a clear wavelength confirms the most unstable mode prediction of the hydrodynamics equation. This part will focus on the study of these structures. We stress that these undulations are only seen at *low noise* (generally $\eta \leq 0.05$). At higher noise the global nematic order is so quickly broken - in a matter of a few thousand timesteps - that no pattern is observable in this time window and all we observe chaos and strong density fluctuations without having seen undulations.

2.5.2.1 Observations

The undulational instability is supposedly purely an instability of the nematic field in the sense that no other fields should be involved. We thus verify how it appears in the microscopic system and check some results of the predictions of the hydrodynamics equations where this assumption

was made. As 2.14 shows in simulations we see stripes are appearing on an initially homogeneous nematic field oriented along (O_x) (as all particles are aligned in the same direction, the initial order parameter $S = 1$). The other fields are initially homogeneous, we checked that their evolution was not typical patterns as well. These stripes evolve more or less slowly - depending on the flipping rate k_f - their typical width is also dependent on k_f. Note that the undulations are typically broken by massive polar clusters (quite noticeable in the top right corner by their the "magenta" color), that is cluster of particles moving in the same direction coherently (similarly to Vicsek bands), as we can see in 2.14(c), once these cluster are present they inevitably lead to what the "developed chaos" in the sense that any sign of order are no longer visible.

2.5.2.2 Can we obtain a dispersion relation ?

We now address the problem of the dispersion relation from the linear stability analysis shown in 2.13. In the same spirit we tried to verify these results. The method is to consider an initial configuration of the system with small sinusoidal perturbation of the nematic field along the initial nematic direction (see equation 2.24).

The initial perturbed condition is given by the following procedure :

- We generate random initial positions for the n particles at positions $\{x_1, x_2, ..., x_i, x_n\}$, this ensures an homogeneous density of the system.
- We choose the orientation these particles according to a sinusoidal perturbation of the angle of the particles with amplitude ξ and wavelength λ along axis (O_x)

$$\begin{aligned} v_x^i &= \xi A \cos(2\pi x_i/\lambda) \\ v_y^i &= \xi A \sin(2\pi x_i/\lambda) \end{aligned} \tag{2.24}$$

The undulation on the unperturbed system (homogeneous nematic initially) is clearly showing a pattern with "a given wavelength" as can be seen in figure 2.14: we see the appearance the undulations appear just before breaking. For instance for this system we measure a wavelength ≈ 25.

Thus the method was to choose the wavelength λ to be close to the value we've observed from unperturbed systems. This choice is based on the assumption that the dispersion relation in the microscopics has a similar form than the theoretical one and that the visible wavelength is "close enough" from the most unstable mode.

The problem is that even when forcing an initial λ close to the unperturbed wavelength there is still a mode-mixing occurring. Consequently even the "simple" computation of the growth rate of the most unstable mode is unable. This mode mixing occurring at all wavelength, no such thing as a full dispersion relation neither a dispersion relation is obtainable for now. We can imagine some reasons why: the theoretical calculation don't assume noise thus mode won't mix, while in the microscopics we can easy imagine

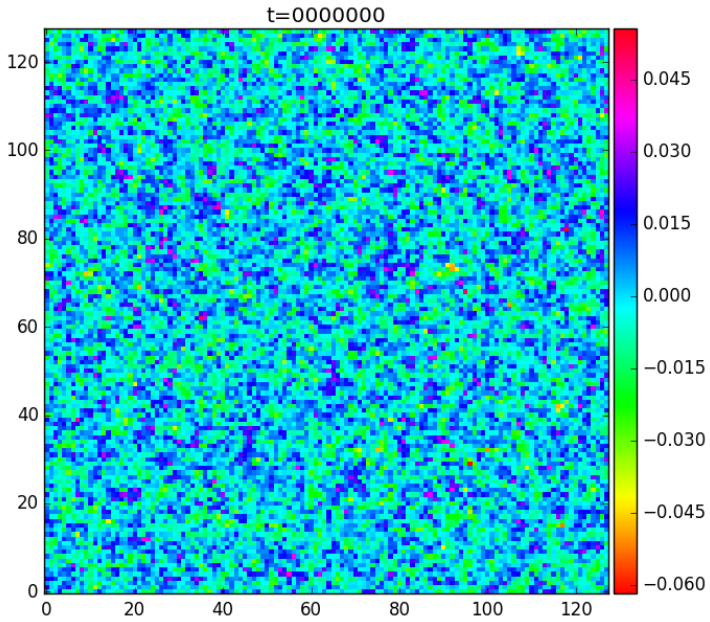

(a) Initial configuration : homogeneous nematic ($t = 0$)

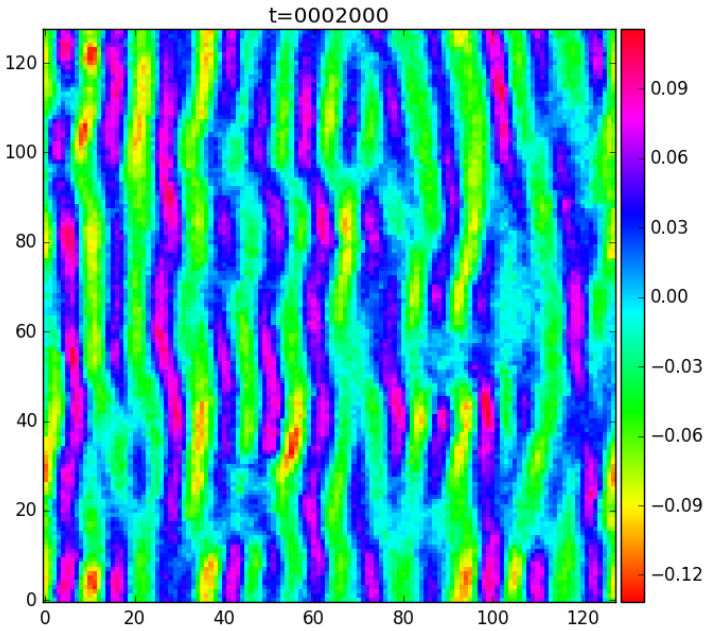

(b) A clear pattern is now visible ($t = 2000$)

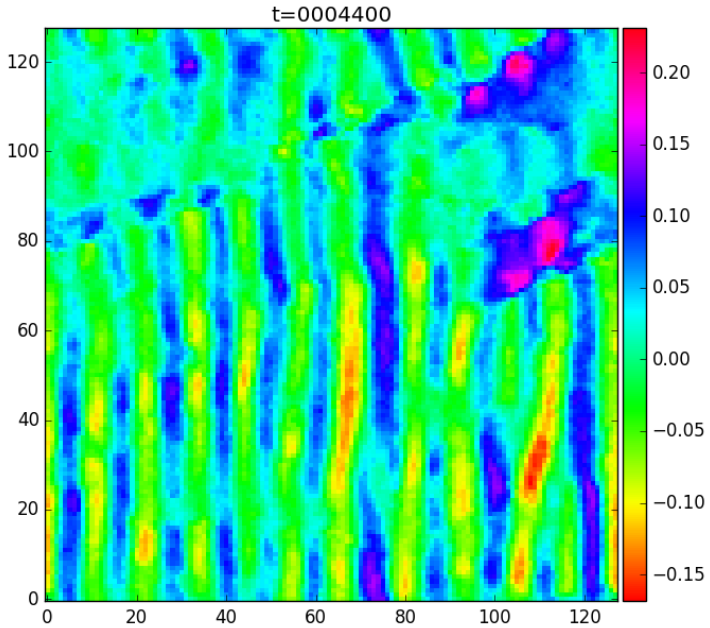

(c) The undulations are now at their maximal "amplitude" , one can see rupture sign as irregularities on the pattern appear ($t = 4400$

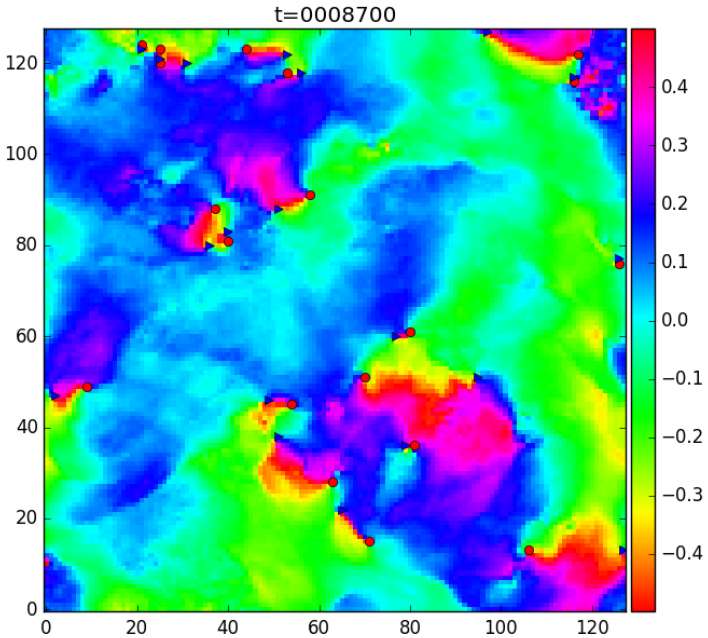

(d) The fully developed chaos $t \geq 4400$ (here $t = 8700$)

FIGURE 2.14: These snapshot show the nematic field over time, the flipping rate is $k_f = 10^{-3}$ here. Typical stripes characterizing the linear undulational instability over time, then their breaking and the evolution towards *fully developed* chaos at ≈ 4000 timesteps

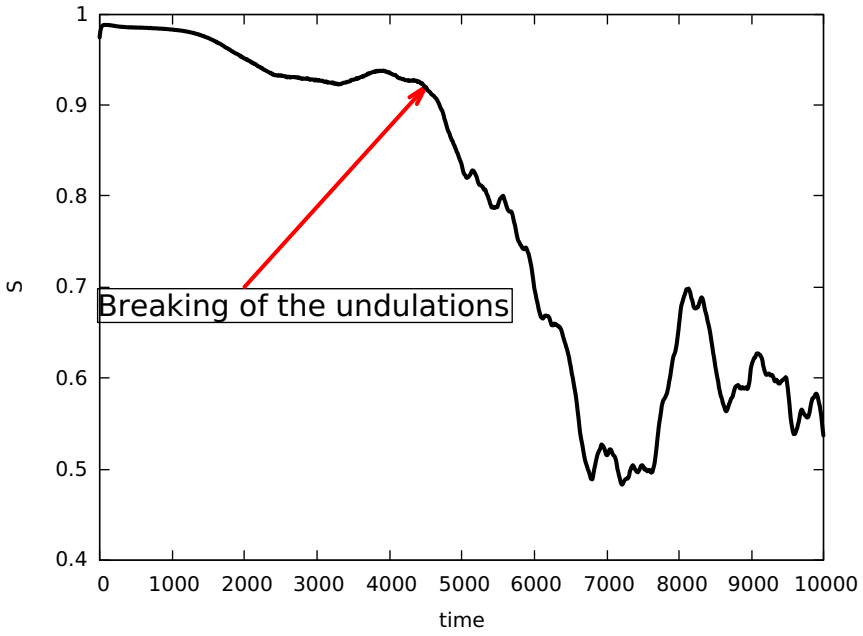

FIGURE 2.15: Timeseries of the global nematic order parameter, after slowly evolving in the first ≈ 4400 timesteps, the breaking of the undulations in favor of a chaotic regime is characterized by a sudden drop of the nematic order parameter

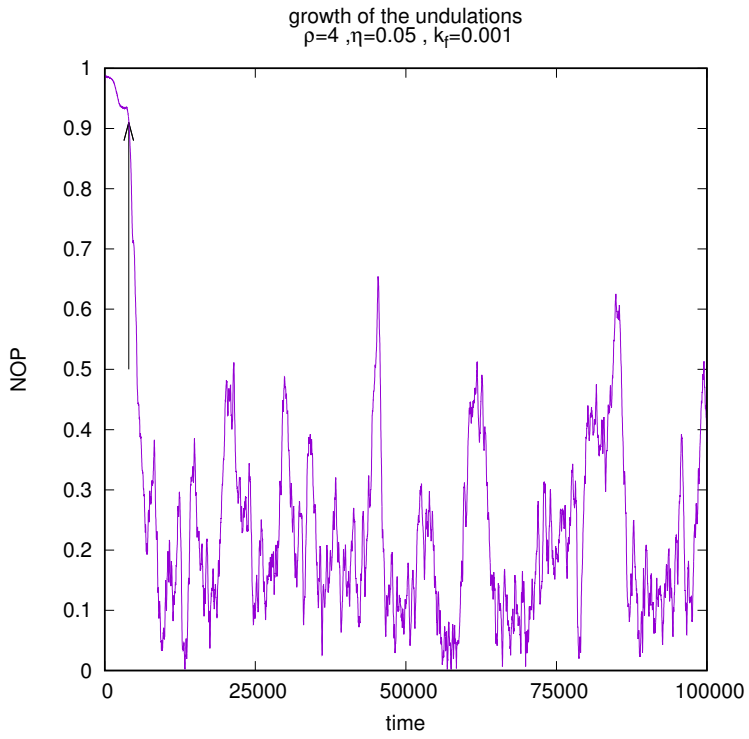

FIGURE 2.16: Timeseries of the nematic order parameter S (indicated NOP here). The black arrow indicates the breaking of the undulations as in figure 2.15. On longer timescales (10^5 timesteps) we clearly see that the fully developed chaos is different from the nematic stable state as high fluctuations of the timeseries appear.

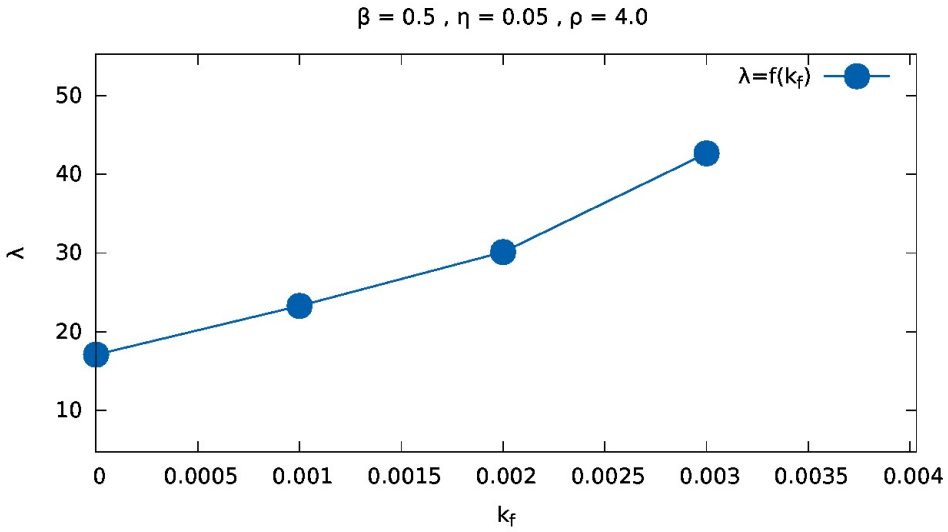

FIGURE 2.17: Natural wavelength λ with varying flipping rate k_f

that noise will lead to modes mixing. The second reason is that we probably quickly get out of the linear instability regime and thus the theoretical calculations are no longer valid.

2.5.2.3 "Natural" wavelength

Facing the impossibility to obtain a dispersion relation using the current method to perturb the system, we've decided to obtain the much simpler systematic measures of the wavelength of the typical width of the stripes pattern of the instability in figure 2.17. Simulations were performed on a an elongated system ($L_x = 512\,, L_y = 128$) , such elongated system is necessary because simulation duration become quickly prohibitive for large square systems. What's more we know that the wavelength grows quite quickly while varying k_f requiring to increase the system dimensions. Given that we are measuring a instability purely longitudinal along (O_x) increasing L_y would be necessary only if the spatial amplitude of the modulation becomes significant in that direction, this is clearly not the case from our observations (the modulation amplitude is quite small)

As we can see in figure 2.17 the undulational instability region in k_f space is a very narrow area close to 0: $k_f \in \left[0, 3 \times 10^{-3}\right]$. We tried see if we could push forward this limit (assuming the higher k_f boundary is mainly limited by the quick growth of the undulation wavelength) by taking even further elongated systems ($L_x = 2048\,, L_y = 64$). However, we are not able to currently produce conclusive results because both the timescales grow exponentially and also the required system size needs to grow at least as quickly as the wavelength does too. We also think that at some points we need to increase L_y direction because some modulations in the y direction too could happen too but we are not yet ready to confirm this possibility.

Still these initial observations confirm that we are facing a long wavelength instability which most visible pattern, though it might be mix of several modes, grows very fast with respect to k_f and thus the undulational instability might totally overlap the chaotic region *at low noise*[10]

[10] Again we pinpoint the fact that the undulational instability is seen at low noise, ≤ 0.05 at higher noise the chaos exists without initial undulations.

2.5.3 Polar Bands

We now address a totally different phase exhibited by the system but nonetheless showing the rich phenomenology shown by this simple model. Indeed, for small systems sizes and *exactly* 0 flipping rate we noticed the existence of polar bands (see fig. 2.21(a)) that is cluster of particles spanning the transversal direction of the system and traveling at constant speed in the perpendicular direction, the longitudinal one,[11]. These structures form spontaneously starting from nematic initial conditions (random particles position and particle have initial speed $v_x = \pm 1$ with equal probabilities $\frac{1}{2}$). These polar band triggered our interest because they differ from the ones obtained in the original Vicsek model. In this section we will review the formation of these polar bands, their structures as well as an extensive exploration of their existence region.

2.5.3.1 Formation

The favoring of polar clusters seems counter-intuitive at first look given the conditions of appearance: because we are starting from a nematic initial condition with an alignment interaction which is also nematic it is quite astonishing that some polar order emerges despite these two "constraints". However it's not hard to guess why such bands should appear: particles moving in the same direction will have a high tendency to stay neighbors because their motion associated to the alignment interaction keeps them close from one another. On the other hand particles propelling in opposite direction will only be aligned for a few timesteps (even less as v_0 increases) then their motion will be uncorrelated as they exit their interaction range.

This mechanisms enhance particles going in the same direction to stay together, therefore it can lead to formation of polar clusters even though the initial interaction is nematic[12]. Collision of these polar cluster would lead to even bigger clusters and eventually to *a unique* giant cluster. The size of which then reaches the size of the periodic-boundary box, thus a phenomenon of "percolation" occurs: the two sides of the cluster connect and disappear and then lead to the formation of a band which can persist indefinitely given its geometry. Thus we understand their existence is mainly a consequence of the toroidal topology of space (the periodic boundary conditions). Simulations show evidence that the only allowed direction of existence for these bands is along the main axis of the box (it should be possible to see them in the diagonal directions but it never occurred in our experience). Bands structures are well known in the original Vicsek model and were first spotted in [11] near the order-to-disorder transition.

Likewise, the presence of bands is strongly related to the debate concerning the order of the phase transition, these bands coexist with the other phases (far from the order to disorder transition the only two phases existing are called correspondingly the "liquid" ordered phase and the "isotropic" disordered one) around the transition and therefore they make a case for a

[11] Note that it is possible the bands also exist at very small but non-zero k_f

[12] actually a nematic interaction is "effectively" a polar one when the collision is head-to-head

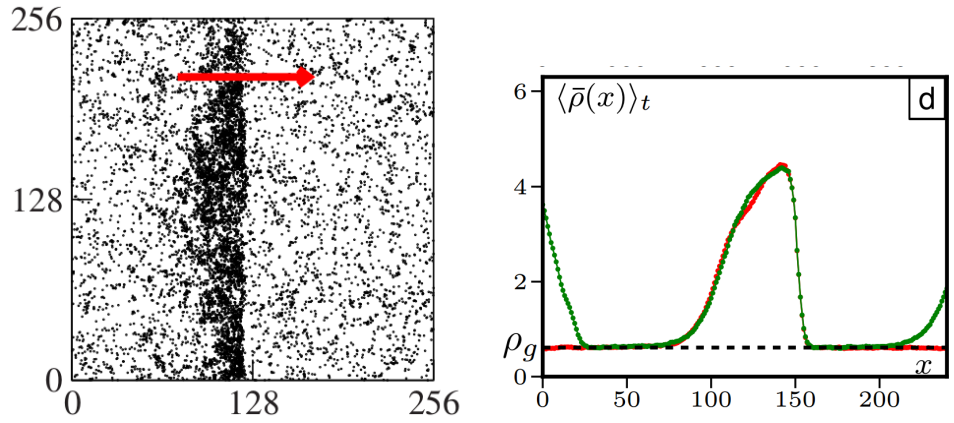

(a) Snapshot showing the trail let by bands as they move in the less dense gaseous phase (source : [11])

(b) The averaged (in the y direction) density profile $\rho(x)$ of these bands shows a clearly noticeable front (source:[52])

FIGURE 2.18: The polar bands in the Vicsek model have a sharp front which leaves a trail of decreasing density

transition of the 1^{st} order. Vicsek *et al.* argued that this difference of order for the transition between their model and Chaté *et al.* is caused by the choice of v_0: in [35] they claim that the difference came by the fact they were working in the low velocity regime ($v_0 \leq 0.1$) whereas in the high velocity regime ($v_0 \geq 0.3$) regime these bands start to appear.

In that sense it is interesting to spot the existence of these bands in these two velocities regimes.

In our case, polar bands we first spotted in small systems (square 64×64 system), at low density ($\rho = 1.5$) in the high velocity regime ($v_0 = 0.3$), the other parameters were set to usual values ($\eta = 0.1$ and $\beta = 0.5$). We stress that in all the simulations performed here the flipping rate k_f is **strictly** 0 , these bands seem to be a singularity in parameter space as they don't persist at low but non-zero flipping rate (again we think they might actually exist for flipping rates as low as 10^{-5} but we cannot conclude for the time being). Observing the timeseries of the nematic order parameter 2.19 it is already obvious that a violent event happened at time $t \approx 2 \times 10^5$ from the values of the order parameter which abruptly "jump". This is confirmed by the even striking jump of the polar order parameter (in pastel purple) from ≈ 0 to ≈ 0.7. For both order parameter(s), not only do we see a jump of their value, but also it appears that *their fluctuations are decreasing* a lot.

Further inspection of the system snapshots shows the emergence of these bands 2.20 , which even from the qualitative point of view, are very different from the ones obtained in models without repulsion : they appear as very homogeneous structures (see fig 2.21) - in the polar Vicsek model the front is very dense and straight but the tail is sparse and badly defined (compare with the profiles seen in 2.18(b)) - and moreover we see **strong smectic order** inside the band. It is interesting to note that just before the formation of this one band several "proto-bands" of badly defined shape are visible, but already present the same orientation and smectic structure of final one.

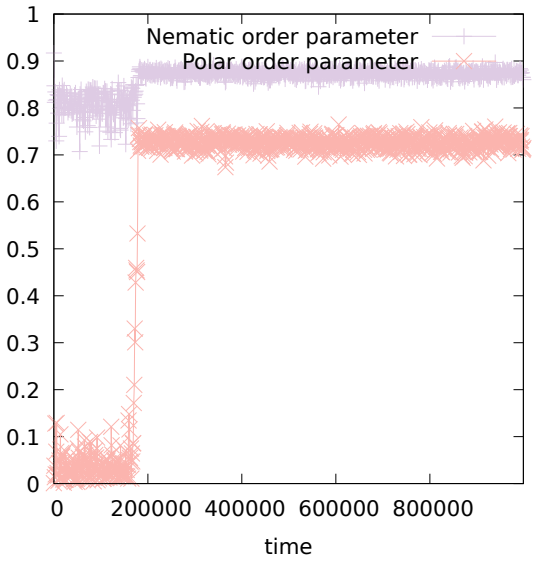

FIGURE 2.19: timeseries of the nematic (purple) and polar (pink) order parameter

The bands structures we observe are very different than those seen in the original Vicsek model: in the latter case the band is characterized by a very stiff front of particles which leaves a trail of particles which longitudinal (in a reference frame co-moving with the band, considering the band as invariant 1D structure) density profile roughly scaling exponentially as we go away from the front :$\rho(x) \propto \rho_0 + \exp(x/l_0)$ [13]. In our case, on the contrary, in our case the the density profile profile of the band is very flat $\rho(x) = \rho_{band}$, this discrepancy is probably caused b the introduction of repulsion and as we will see later

2.5.3.2 Stability with size

Even though little is known about the conditions which favor the bands formation, we can still suggest that the optimal conditions are the following:

- Low noise: that favors smecticity
- Low density: Indeed if the band becomes too wide it'll break. Given that the density is pretty constant inside the band $\rho_{band} \approx 1.8$ the width of the band is given by the global density, thus there's an upper value for the density.

As we said first bands were observed for small systems and might be thought as a curiosity, limited to small systems sizes. However we were also able to obtain spontaneous formation of this polar bands for a bigger system $L_x = L_y = 128$ but for a way smaller noise $\eta = 0.001$. The question that that these bands exist for the same parameters for all system sizes but with longer formation timescales stays unanswered at the moment. Keeping the initial system size $L_x = L_y = 64$, we can say that bands are not robust with

[13] for detailed information see [11] fig. 13

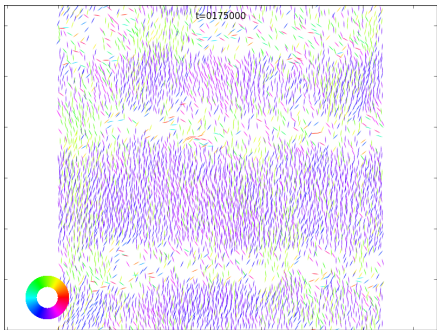

(a) three "proto-bands" $t = 176000$

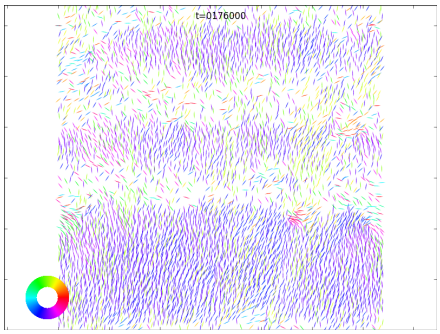

(b) one gets almost absorbed $t = 177000$

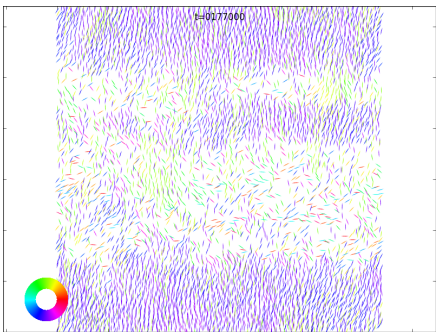

(c) the bigger one will become the homogeneous band $t = 178000$

FIGURE 2.20: Polar bands birth in a small system $L_x = L_y = 64$. It starts with the appearance of smallish bands which fuse after a while. The disk in the bottom left-hand corner gives color-orientation match. Given the purple color, the bands move up down.

respect to parameters change . We briefly review what parameters we can change in the next section(s).

2.5.3.3 Phase or microphase separation?

In [52] the authors exhibit differences between the Vicsek-model and the "active Ising model" (abbreviated AIM) where particles carry a spin $\vec{s}$ (aligned with O_x for simplicity, thus we write it it s from now on) and self propel on lattice. The particle spin reverse its orientation ($\pm \mathbf{e_x}$) with a probability $\propto \exp(-\frac{sm}{k_B T \rho})$ where $m = \sum_{j \in \partial i} s_j$ is the local magnetization and $\rho = \sum_{j \in \partial i} 1$ the local particle density. The model is "on-lattice" in the sense that the interaction are within the same lattice cell, multiple particles can lie on the same lattice. The self-propulsion is embedded as a biased diffusion process: the diffusion coefficient to go to the right depends on the sign of the spin s_i and is $p_{+s} = D(1 + s\epsilon)$, the diffusion coefficient to the left has a different value: $p_{-s} = D(1 - s\epsilon)$. Consequently $+$ particles are favored to go to the left while $-$ are favored to go to the right leading to a self-propulsion speed (a drift actually) for spins ± 1 equal to $\pm 2D\epsilon$. The particles also diffuse upward and downward with equal diffusion coefficients D.

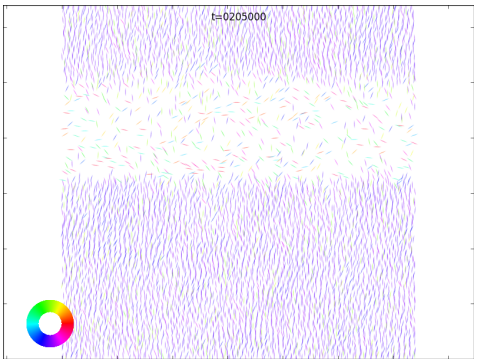

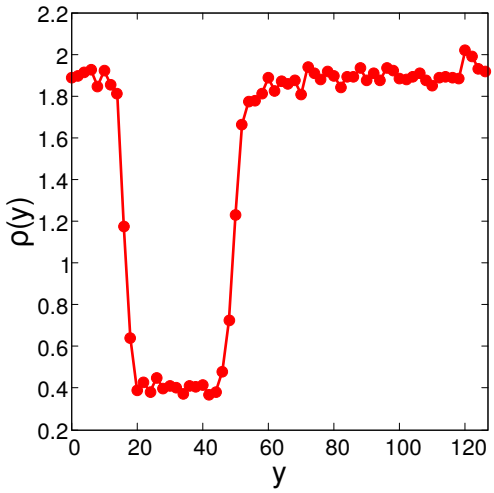

(a) The final state of a polar band our model after the process depicted in figure 2.20 occurred.

(b) The corresponding density profile averaged in the (Ox) direction

FIGURE 2.21: The polar bands in our model differ much from those in the Vicsek model as seen in 2.18

Even though the difference on the algorithm might seem important, the phase diagram keeps the same structure (with the noise η replaced by the temperature T), even the bands structures are present in both case. However the main difference lies in the number of bands in the system : in the polar Vicsek model bands exhibit what's called "microphase separation" , that is when we increase the global density ρ_0 the number of bands will increase accordingly (their number scales $\propto L_x L_y(\rho_0 - \rho_g)$ with ρ_g the density of the gas). On the contrary in AIM there is always one band which size grows with increasing ρ_0. In the same article, it is explained that the physics of the two models is the same from the hydrodynamic equations point of view the essential difference lies in that different solutions are authorized according to the scalar or vectorial nature of the fields: in Vicsek-style models the particles carry a vector and consequently their vectorial nature has to be kept in the hydrodynamic equations, *i.e.* the fields are vectorial. On the contrary in AIM the magnetization is a scalar quantity and thus the equations are those of a scalar field.

In our case the polar bands appear at very low noise as shown by the high smecticity exhibited by the bands. It is therefore possible to imagine that we are *close to the limit* of a scalar field and therefore that phase separation is authorized here. Several simulations were performed in that direction.

The first experiment we imagined to this end is to perform multiples copies of one band in order to obtain a system of several bands. However to spot phase or microphase separation we would have to wait for extremely long times as the traveling bands don't exchange particles most of the time. To speed up things we've put two identical bands together and varied the separation distance. The fact that the separation between the two bands increase tends to back for micro-phase separation however the fact that this configuration is not stable in the end might also tend to prove that the only

stable configuration is one band (meaning that we think that, ultimately, after extremely long times we might recover 1 band in the system, however computing limitations couldn't confirm this assumption).

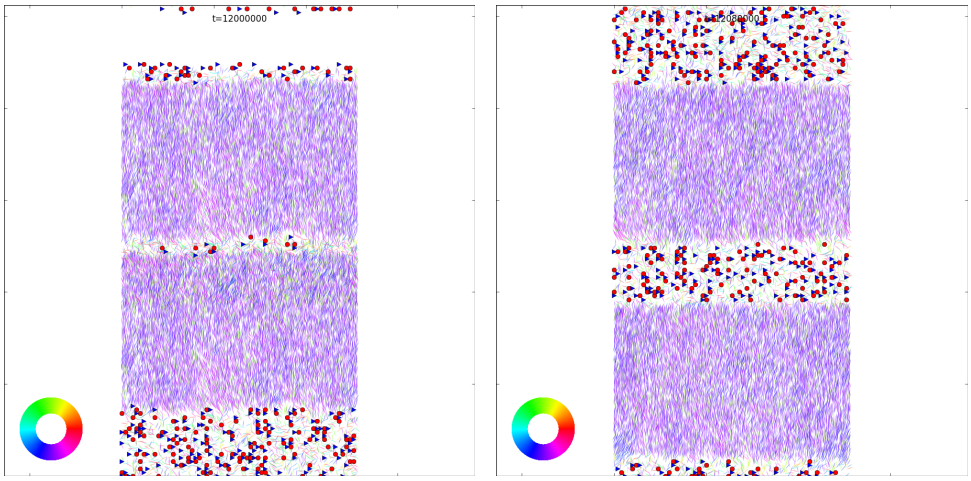

(a) Two bands are put very close to each other

(b) Quickly after the gap increases

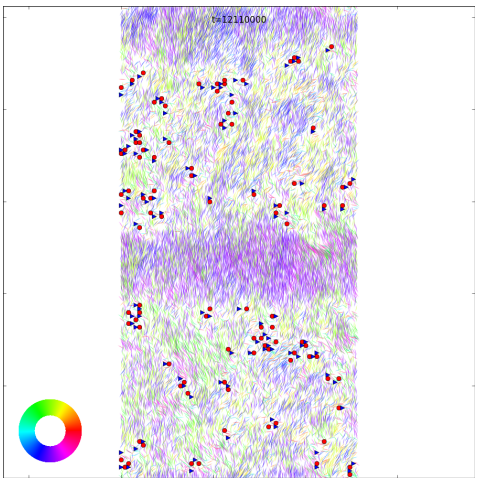

(c) However the two bands system break shortly after

FIGURE 2.22: Separation of two bands $L_x = 128\, L_y = 256, \rho = 1.5\eta = 0.1 v_0 = 0.3$

2.5.3.4 Varying ρ

As we've pointed out earlier, the bands observed in this model are very homogeneous. A property of phase vs micro phase separation is the non-conservation of the density of the band which we explored by changing the global density ρ_0. The procedure to increase (respectively decrease) the density adding particles randomly (respectively remove), though it might destroy the band if we remove too many particles inside the band (creating a hole or a defect), if $\Delta\rho_0$ is small enough that should not happen (or we are very unlucky!). The parameters of this procedure were $\Delta\rho_0 = 0.02$ with a time of relaxation of $t_r = 10^6$ timesteps.

If we choose to decrease density we observe the band thickness decreases and ultimately it breaks around $\rho = 0.52 \pm 0.02$ 2.23. There's no splitting or such thing.

It is important to note that at this density we are *below* the critical isotropic-nematic transition density meaning that the bands coexist with the gas. It is probably a metastable state given that the smecticity in these bands is a stabilizing factor preventing density fluctuations which would break the band.

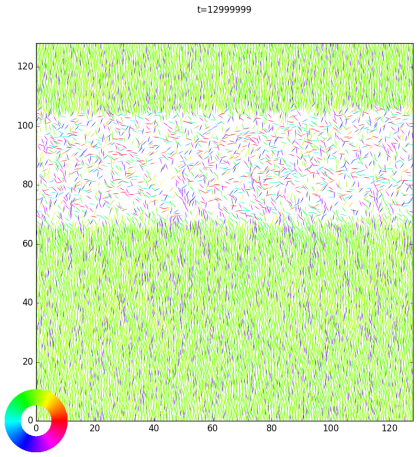

(a) One band at density $\rho = 1.4$

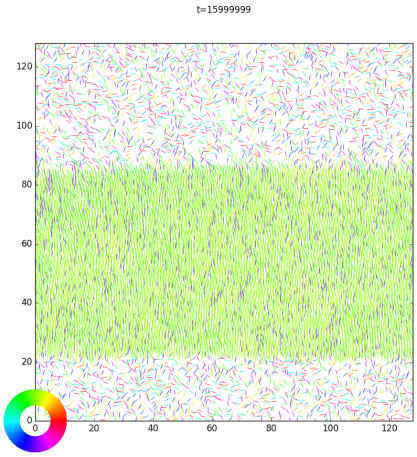

(b) The band is already smaller but still well defined at density $\rho = 1.1$

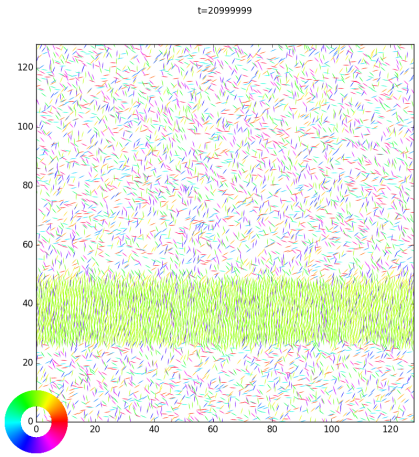

(c) At density $\rho = 0.6$ it is still up!

FIGURE 2.23: The band is getting thinner with decreasing density (system size 128×128)

Based on these two experiments we are not able at the moment to cannot confirm if the polar bands are still micro-phase separating or if they phase separation: both seem possible solutions. Indeed, if phase separation seems possible because the bands look similar to those of AIM (constant density ρ_b and width depends on global density with respect to the gas phase $\rho_0 - \rho_g$). On the other hand it also appears that at high density bands appear to split

from time to time: it might be systematic and thus it is micro-phase separation but in that case the timescales of micro-phase separation are gigantic ($\geq 10^8$ timesteps) because of the low noise, smectic state of the system. In conclusion this is definitely a question that should be answered to close the gap, another method should be found to discriminate between phase and microphase in reasonable timescales.

2.5.4 Formation of lanes

Last noticeable discovery in the rods limit is the formation of lanes structures (see figure 2.24). These are clusters of particles moving in the same direction polarly.Again this is quite surprising to obtain such phenomenon in a model where the alignment interaction is nematic and therefore where no preference toward neighbors going in the same direction should occur. However in section 2.5.3 we explained why our model is probably favoring the formation of polar bands. A similar mechanism is probably at stake here. Strong smectic order is present in both structures and might play a role in their existence, though other models without smectic order report laning (the phenomenon of lanes formation). In the case of lanes smecticity probably prevent lateral diffusion allowing them to have "sharp" borders (compared to nematic bands where the borders are not well defined). Even if doesn't explain the stability of these structures the smecticity seems to create a "line tension" by analogy with fluid-fluid interfaces, the counter-moving lanes seem to create an interface which prevent them from moving into one another.

This phenomenon is ubiquitous in models of pedestrian walkers. Indeed, it is very easy to understand why a pedestrian wanting to reach a target point as fast as possible will walk faster on lanes of people walking in the same direction than bumping or zig-zaging against people walking on the other direction. The simplest pedestrian walker model known as the "social force model" by Helbing et a.l. [21] is able to reproduce this feature.

In our model these lanes seem to be stable for extremely long times ($\geq 10^7$ timesteps) in small systems($L_x = L_y = 128$) and *only for small systems yet* For larger system they still exist but are not as well defined 2.24(b). Again the question to know if these structures are long-range ordered or not has not been studied conscientiously but is a pending question that is worth to study.

Except pedestrian models, such structures also appear in a different system where particle with different type of motilities are mixed (a fraction is of these particles are self-propelled and the rest are simple Brownian particles) but also in the case of purely "active" particles, the model in question is [32]. It is worth to note that in this model they are dealing with spherocylinder interacting via hard-core interactions, contrary to our torque-like repulsion. A remark of importance, the lanes they observe are **not stable** ultimately. Another model in which we see lanes is the Vicsek-style model with continuous rotation [34] (the angle rotation speed $\frac{\mathrm{d}\theta}{\mathrm{d}t}$ diffuses and not the angle θ itself), but this time they seem to be stable. These models have in common to share continuous time dynamics, thus maybe the noise cannot so "easily" break the order because it slowly diffuses contrary to Vicsek-like models where the noise is discrete, this might favor the formation of interfaces because the timescales to get out of the interface are large. In our model the noise is discrete so no such assumption can be made, but the smecticity is what "stabilizes" the interfaces by decreasing the noise influence.

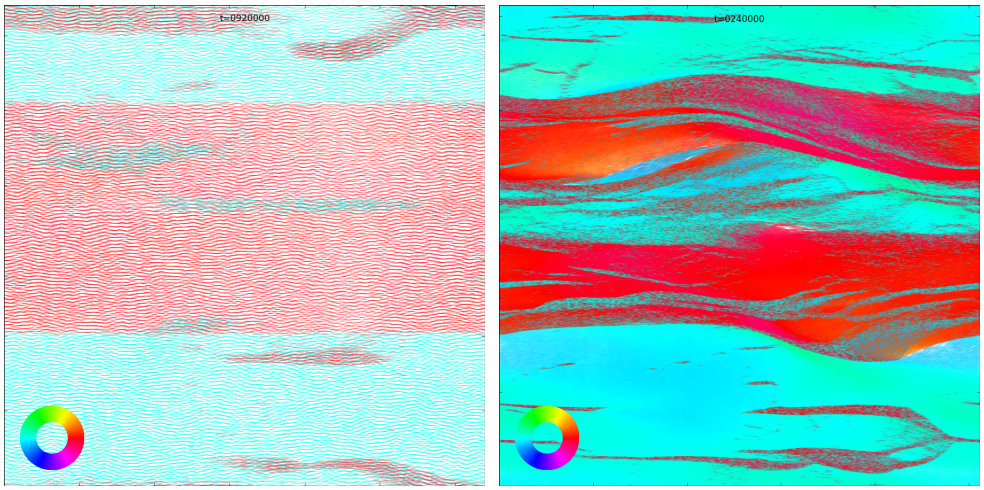

(a) two main lanes on a system of size 128×128

(b) In a bigger system 512×512 lanes are more deformed.

FIGURE 2.24: Lanes in different sizes systems. The polar angle is colored according to the color wheel in the bottom left-hand corner.

2.5.5 Phase Diagram

Now that we have established what structures we will obtain in the rods $k_f = 0$ limit, we can now build its phase diagram with the usual Vicsek parameters ρ, η. The result shown in figure 2.25 exhibit the different structures we have encountered which are all spanning well defined regions of parameter space.

The first eye-catching difference with Vicsek-models without repulsion is that the nematic-isotropic transition line doesn't meet the $(0, 0)$ point. Indeed, adding repulsion has important consequences over the "trivial" isotropic-nematic transition. In the current case, there exists a minimal density $\rho_m^n \approx 1$ below which the only state is isotropic. That is essentially caused by the way we implemented the repulsion. Indeed when the global density is low, binary collisions will be a statistically dominating, thus the repulsive term will "scale as" $\approx \beta < r > \approx \frac{\beta}{\sqrt{\rho}}$ and will be significant at low density. On the contrary, in high density regions the collisions will likely imply several particles and the effective repulsive contribution, sum of the individual contributions, $\beta || \sum_j \vec{r_{ji}} \leq \frac{\beta}{\rho}$, will drastically be less important in high density regimes

Then second new region is where lies the chaotic regime. As we can see its existence region is also lower bounded in terms of density, but this boundary is different from the $\rho_m^c \approx 2$ of the isotropic-nematic transition. This fact is in qualitative agreement with the phase diagram of the continuous theory which can be seen in the section dedicated to the comparison between the hydrodynamics equations and microscopics system 2.8.0.1 in figure 2.41(a). The hydrodynamics phase diagram show also that the chaos region requires a minimal density. From the microscopic point of view it is understandable as we've seen in section 2.5.2 that the undulational instability was always accompanied by smectic order and there's no reason for

the minimal density for triggering smecticity to be the same as the one for nematic order. That said, there is a difference with the continuous theory, at high densities the nematic should be unstable everywhere and lead to a chaotic state. However in our case we see that there is a wide gap separating the unstable region and the isotropic transition, these two line seem to behave the same and the gap not closing, we can't exclude that at high enough densities the gap might close. Nonetheless we performed simulations at higher densities up to $\rho = 10$ but other problems might arise given the nature of the repulsion term we use. The smecticity becomes so important that it has a stabilizing effect and the timescales to see the undulation are growing extremely quickly, therefore the computational cost is too high for us to conclude about this seeming contradiction.

The last region is the polar bands one. It is very interesting to see that these bands can exist below the nematic-isotropic transition line. This is probably a finite size effect, indeed on large scales it "might" be easier to destroy a band because the probability to create a hole/defects increase with system size, but it might also be an effect of the smecticity preventing giant number fluctuations from breaking the bands [14]. Note that again, with the density dependance of the "effective" repulsion we see that such bands are bounded by a maximal and a minimal density, which is not the case in the original Vicsek model where such band exist arbitrarily low (or high) densities.

2.5.5.1 Technical discussion: determine the transitions

We need to briefly mention how we chose to determine the lines of the phase diagram, which are subject to a bit of arbitrary power given that we are working on finite sizes systems on finite time scales. We also precise the initial conditions.

The initial conditions to obtain the phase diagrams we proceeded as follows:

Nematic The isotropic-nematic transition and chaotic regions were obtained by starting from homogeneous nematic initial condition, relaxed for $t = 10^6$ timesteps.

Bands We took the band obtained from $\rho = 1.5 \quad , \eta = 0.01 \quad , \beta = 0.5$ and perturbed this solution by continously moving in parameter space by steps of $\Delta\rho = 0.01$ in density and $\Delta\eta = 0.025$ in noise, while relaxing these solutions 10^6 timesteps each.

Concerning the methods to obtain the transitions.

Isotropic-Nematic transition determination Several methods to obtain the order-disorder transition have been used in the past :

[14] in [51] one can find detailed description on how to obtain the gas-bands transition lines with accuracy. They also obtain bands below the transition line but assume that when the system reaches infinite sizes the hysteresis cycles vanish, leaving the band impossible to exist below the line.

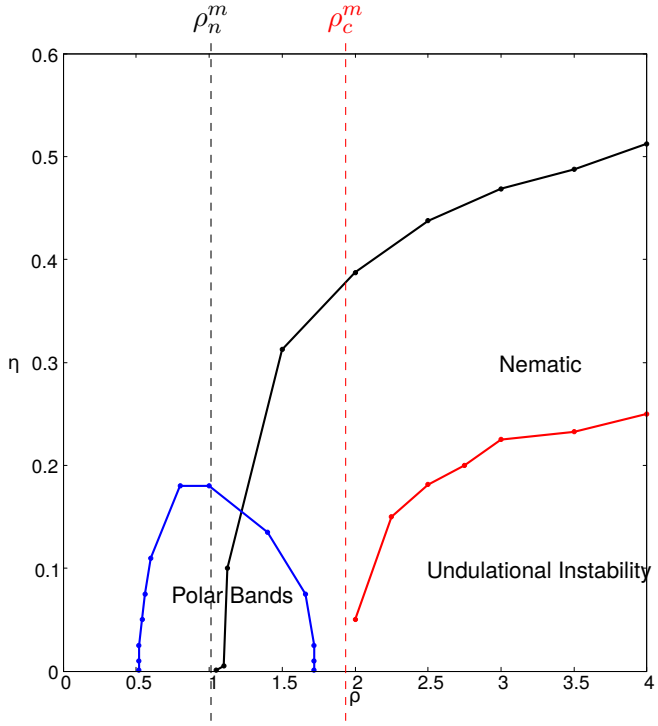

FIGURE 2.25: The phase diagrams for the "rods". The isotropic-nematic transition as well as the chaos region were obtained for $L = 256$ system sizes. The bands stability region was performed for a system of $L = 128$

- One can choose to look at the fluctuations (standard deviation) σ_s of the nematic order parameter s and decree that the transition occurs when the fluctuation become maximum.
- A more subtle approach is to consider the binder cumulant, that is a quantity similar to the 4th order moment of the timeseries : $G = 1 - \frac{<s^4>}{3<s^2>^2}$. A peak toward negative values is sign of a 1st order transition occuring at the location of the drop.
- The two previous methods have been used to obtain very precise measures of the transition points and the (dis)continuous nature of the transition. This thesis object was not to obtain transitions with such details because there is nothing new, instead we chose the less costly method to set the transition at the point where $\frac{ds}{d\eta}$ is maximum (resp $\frac{d<s>}{d\eta}$ if we scan while varying ρ, see 2.26 for an illustration). Even for the relatively small sizes considered we have obtained well enough behaving curves to locate with enough precision the transition.

Chaos determination The chaotic region is characterized by high fluctuations of the order parameter giving rise to a drop of the nematic order parameter $< s >$ (see fig. 2.27) giving rise to a non monotonous behaviour to the curve $< s > (\eta)$. This drop is even clearer as we increase the system size, we chose size $L = 256$ as it seems sufficient. Our criterion is to consider that the limit the chaos-nematic is where

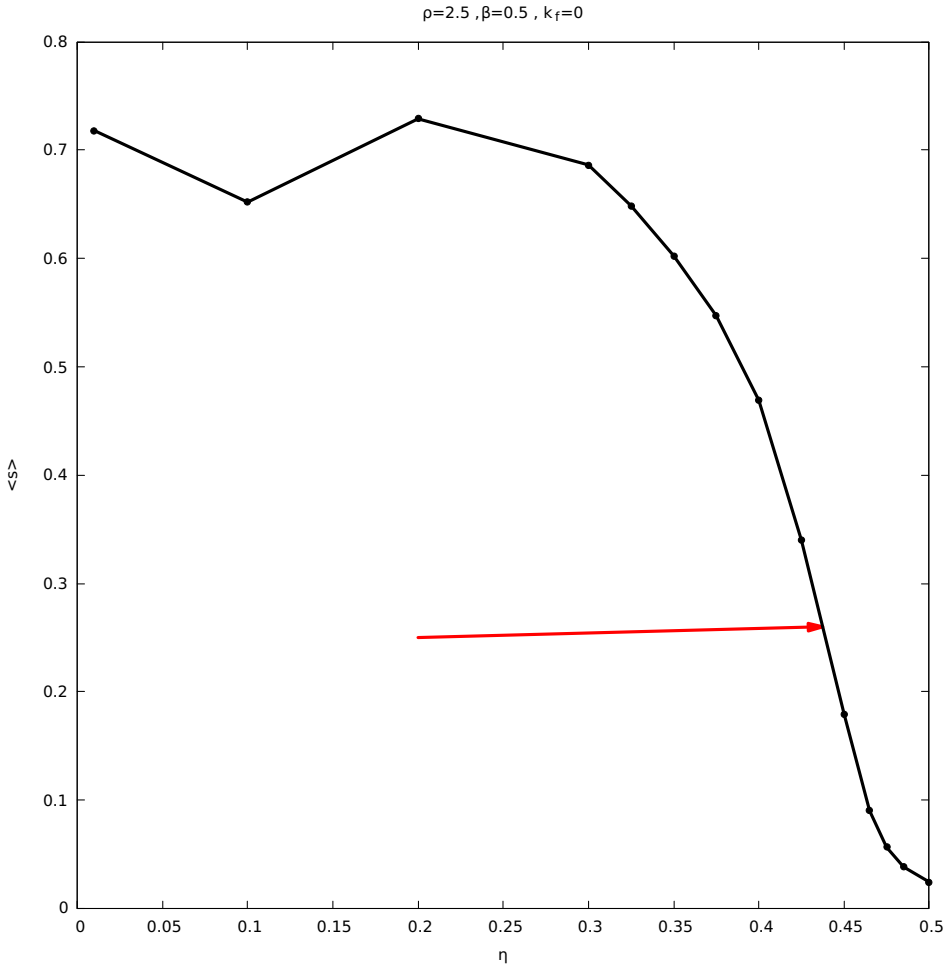

FIGURE 2.26: The transition point is roughly located where $\frac{d<s>}{d\eta}$ is minimum, indicated by the red arrow, the corresponding value is $\eta \approx 0.4375$ (L=128)

lies the maximum $\frac{d<s>}{d\eta}$, a careful look at pictures of the system confirms that this criterion seems quite accurate.

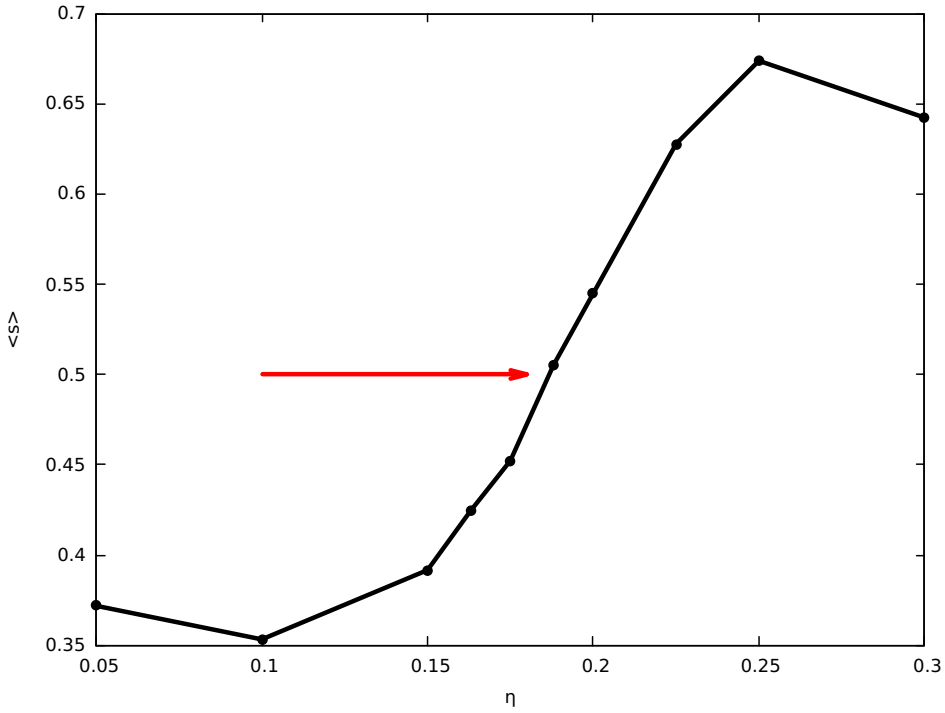

FIGURE 2.27: Increasing the system size ($L = 256$) , the chaotic region the nematic order parameter <s> is anomalously low, the end of this region is located where $\frac{d<s>}{d\eta}$ is maximum, indicated by the red arrow, the corresponding value is $\eta \approx 0.1875$

2.6 Case $k_f = 0.5$: pure active nematics

We now focus on the situation where we turned off the self-propulsion of particles in favor a diffusive behaviour along their direction main axis, that is left and right movements have equal probabilities $k_f = 0.5$. This limit case is known as *pure active nematics*. Representative experiments [36] are mainly those which use vibrated elongated grains on a substrate where the energy comes from a vibrating plate and which movement will consequently be diffusive and mainly along the long axis (because of the elongated shape and the head-tail symmetry). In this section we will extensively introduce the new structures that appear as an effect of the repulsion: arches. Then we will study the phase diagram which shows the arches on top of the usual homogeneous nematic state and isotropic state.

2.6.1 Arches

The behaviour of defects is totally different from the rods ($k_f = 0$) case here and in a quite large region of the parameters space. In dense region defects can *eventually* anihilate in a certain way, leading to the formation of structures we called "arches". *Similar* structures [15] have been reported in [53] where they name it "kinks", they only consider hydrodynamic equations taking into account the nematic field $\mathbf{Q}$ but also its gradient $\mathbf{u} = \nabla\mathbf{Q}$. In this section their will be a particular focus on establishing the different propreties of these structures and comparison with the claim of this article.

2.6.1.1 Formation of arches: high velocity limit

In section 2.4 we were interested in the limit of ∞ separation distance for the defects, neglecting the behaviour at longer times. However when defects are at close distance from each other their behaviour is worth to study. Note that we restrict to the "high velocity" ($v_0 > 0.1$) limit for now as the "low velocity" arches formation mechanism is different and will be detailed in section 2.6.2.

Figure 2.28 illustrates the different steps leading to an arch creation. After the positive defect moved enough, we exit from the previous regime of steady speed, as it is close from its negative counterpart. The pair of defects starts to rotate 2.28(a), this is due to the initial configuration as we've seen in figure 2.8 the nematic field far from the defects is *almost* perpendicular to the initial pairs disclination line, therefore the pair of defect will naturally perform a $\frac{\pi}{2}$ rotation in order to align with the nematic field (for continuity constraints). Once this rotation is performed, the two defects move "coherently" for a certain time (2.28(b),2.28(c),2.28(d)), the $+$ defect being the fastest one, and loop several times around the periodic boundaries. An important point has to be made, depending on the way the rotation occurs two outcomes are possible: whether the two defects anihilate and we are

[15] The structures are similar because they show a rotating nematic angle but they also differ because their wavelength is fixed.

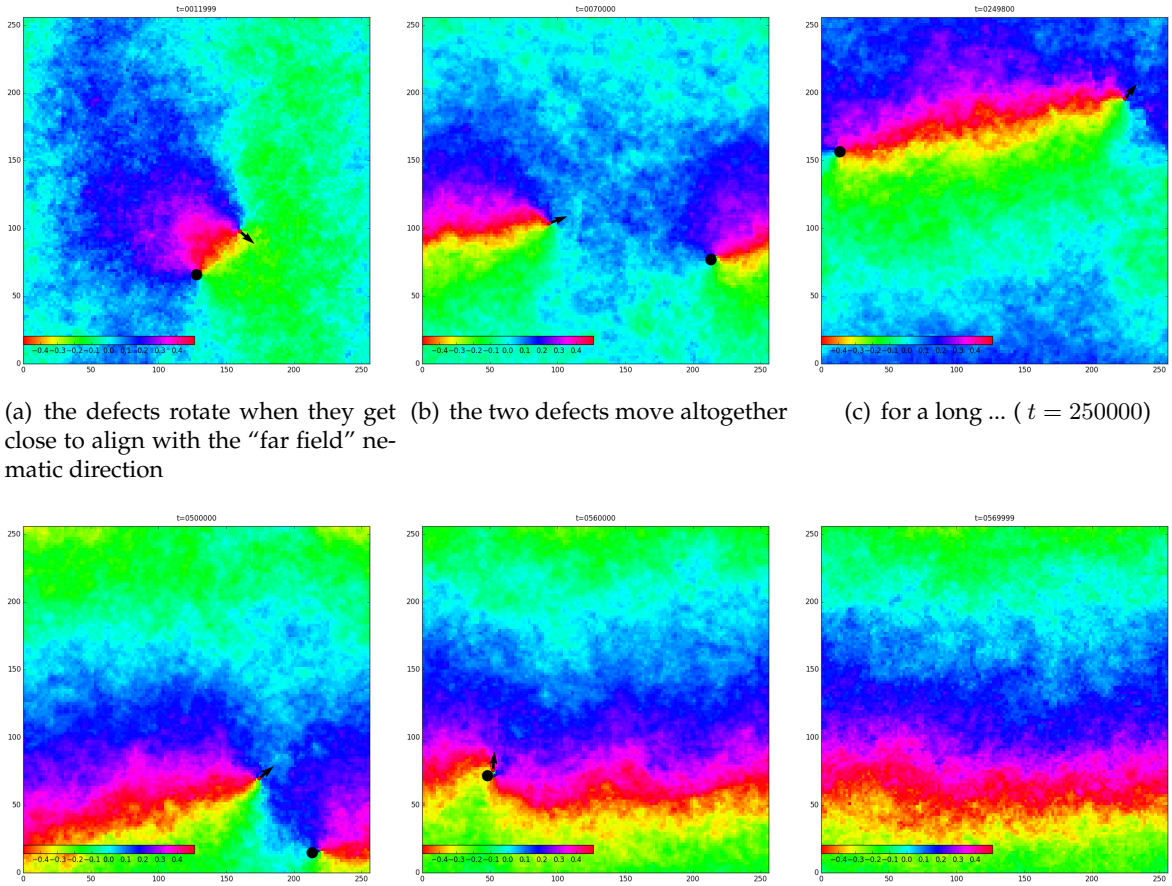

(a) the defects rotate when they get close to align with the "far field" nematic direction

(b) the two defects move altogether

(c) for a long ... ($t = 250000$)

(d) long time ($t = 500000$), essentially because they need to be aligned to annihilate

(e) finally they catch each other

(f) And annihilate to form the x invariant, symmetric structure we call arches

FIGURE 2.28: Creation process of an arch: a pair of defects ($\frac{+1}{2}$ orientation given by a small arrow) and $\frac{-1}{2}$ indicated by a black bullet

left with the homogeneous nematic state 2.29, whether the anihilation occurs in the reverse direction and a pattern between the two defects start to form, when the anihilation is complete we are let with what we call arches 2.28(f): a structure that spans all the system and which axis of symmetry is in the direction that used to join the two defect.

2.6.1.2 Polarity

Arches are surprisingly, "polar" structures in the nematic stable nematic region. Not only in the sense that we are able to measure an instantaneous non-zero global polar order, but we have clearly seen that particles inside an arch are slowly "sheared". As shown in figure 2.30 we colored a stripe perpendicular to the axis of symmetry of the arch, with a color is given by its initial y coordinate Allowing us to track particles. We can see that while they keep more or less the same y coordinate over time, particles are advected, advection which is more pronounced at the sides of the arches the high density region (see figure 2.32) where the nematic angle varies

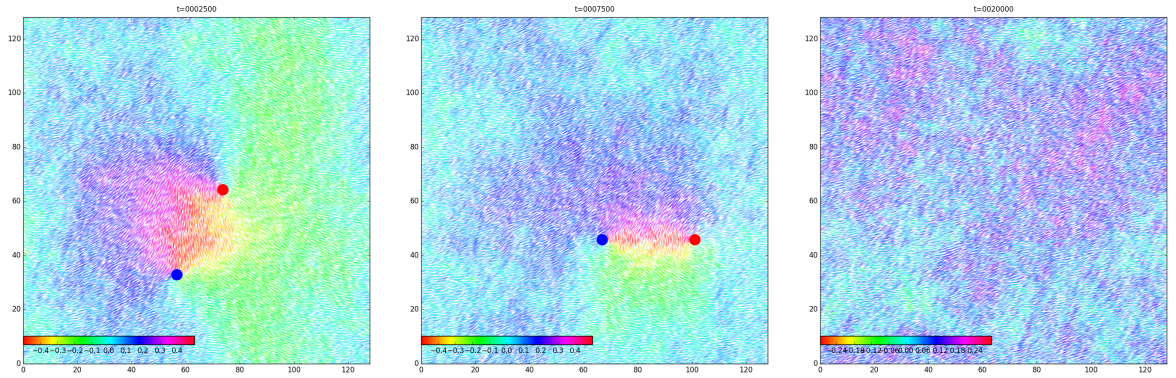

(a) the defects also rotate($t = 2500$) (b) they are aligned with the field too ($t = 7500$) (c) but they disappear($t = 20000$)

FIGURE 2.29: Defects don't always lead to arches! ($\frac{+1}{2}$ defect in red $\frac{-1}{2}$ one in blue, small 128×128 system.)

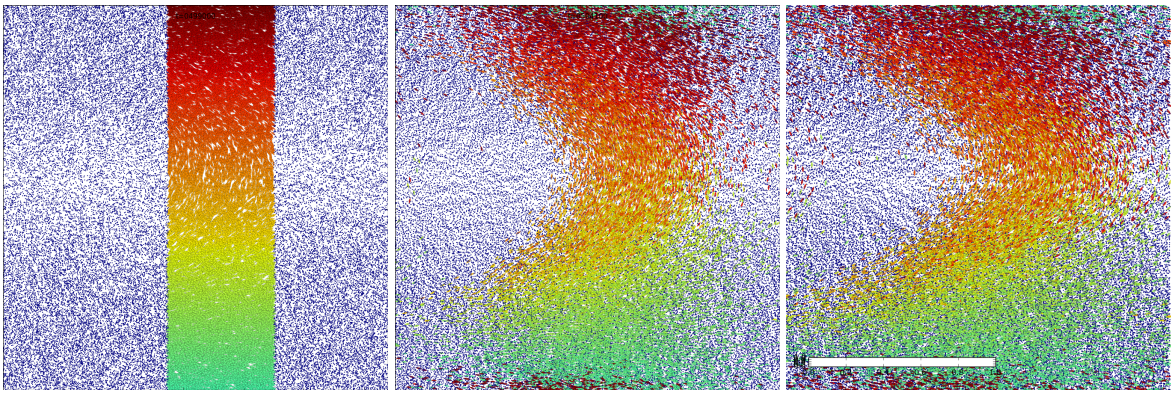

(a) colored stripe initially

(b) after 5000 timesteps, shearing is shown as particles displace coherently : particles on the side of the arch slide to the left whereas those at the center move to the right

(c) after 9000 timesteps, we can see clearly that particles preferentially move when located on the sides (the dense region)

FIGURE 2.30: An initially colored stripe is slowly sheared by the arch.

slowly, than in the center (the low density, more curved, region) in a way reminiscent of the shearing of a material under a "Couette flow".

This technique is very useful to *observe* this polarity but we are also interested in a more quantitative qualification: such polarity should be present in the polar field f_1. If we assume the polar field just to be a spatial average of the vectorial speed v_0 coarse grained over some size l_{cgs} it is clearly not sufficient. The quantities we have to measure here are so small and subject to so much fluctuations that the fields extracted from the coarse graining procedure look too noisy to be the material for any statement.

However we know from experience that arches are more or less static structures.It is a matter of millions of timesteps to see significant evolution of their positions, they don't rotate either, which is essential for the following procedure. Assuming that with respect to time the dynamic of particles at

fixed position is invariant, we thus consider the field obtained from coarse grain size procedure and perform temporal self-average of these fields on top of the coarse graining :

$$f_{avg} = \frac{1}{t_a} \sum_{t=t_0}^{t=t0+t_a} f_{cgs}(x,y)(t)$$

Figure 2.31 shows how the fields are affected by this self-averaging over time. For the fields which values are already high such as density and nematic order the effect is just to damp the fluctuations a lot. The borders correspond the region of high density. This is natural to expect high nematic order in this region because density $\implies$ order. We also start to observe some signs of a higher polarity region in the bottom right-hand corner for averaging times ≥ 1000 in figures 2.31(b) and 2.31(c). However, in order to obtain smooth profiles we need to average over way longer time: $\approx 10^6$ timesteps (fig. 2.32)!

In figure 2.32 we see the profiles indeed self-regularize well with this procedure. The profiles have been shifted such that we will refer $x = \{0, 128\}$ as the "sides" of the arch and $x = 64$ as the center. Analyzing these profile it appears clearly that the polarity is higher in the central region. It is quite surprising, given that the preliminary results with the colored stripe suggested the polarity was stronger on the sides of the arch (higher density regions). In this central region the polarity is *perpendicular* the orientation of the particles ($\arg(f_1) = 0, \arg(f_2) = \frac{\pi}{2}$), thus this effect cannot be put down to the self-propulsion and has to originate from the repulsion! Except for this "anomaly" the polar angle profile is in accordance with the advection of particles: the particles on the side (which corresponds to the begin and the end of the curves) have a small polarity which is parallel to their direction and is oriented toward the left ($\arg(f_1) = \pi, \arg(f_2) = 0$).

One can notice the asymmetry on the polar field profile. This is a small effect caused by the long-time drift of the arch. Indeed, performing averages implicitly assumes that arch doesn't move on timescales of t_{avg}, as this is not the case it creates a slight asymmetry. While the effect is not significant it might it is worth to be acknowledged.

2.6.1.3 Arches width

In [53] it is also stated that the arches they observe have a typical width L which depends of the activity parameter α and scales as $L(\alpha) \propto |\alpha|^{1/2}$ and as such would be the result of a wavelength selection. In our case we report that this kind of observation has never been achieved in the microscopic simulations nor using the hydrodynamics equations and that arches can exhibit arbitrarily sizes (up to $L = 4096$) and thus show *long range order* [16] Even though no evidence of such selection has ever been seen in our simulations, both in the microscopics and the hydrodynamics, we tried to check if such regime could be highlighted in a particular region of the parameters space.

[16] This claim is not to be taken literally as it is of course in contradiction with previous papers and only quasi long-range order should exist on larger scales

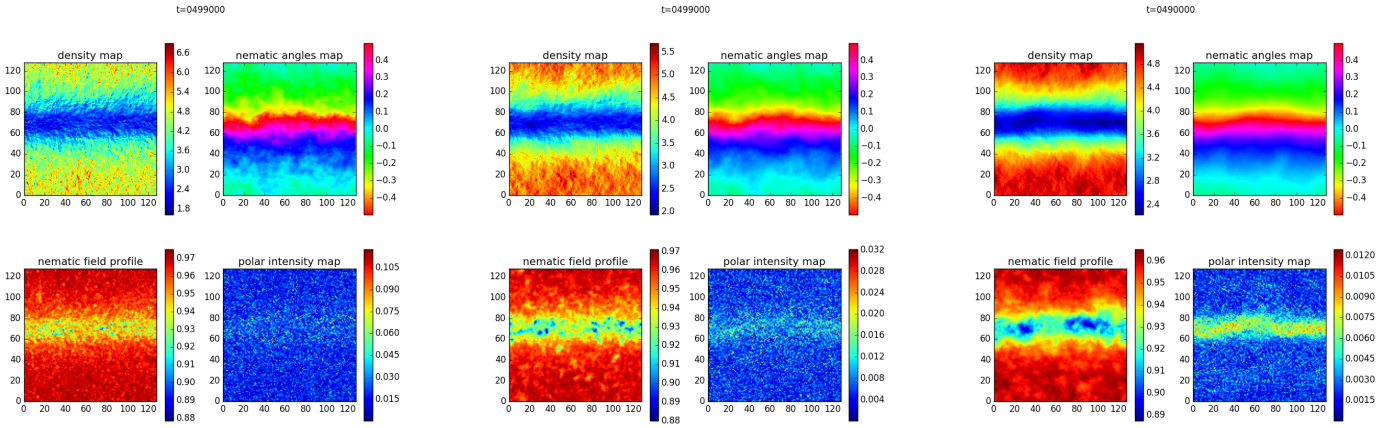

(a) arch fields after 100 timesteps of averaging

(b) arch fields after 1000 timesteps of averaging

(c) arch fields after 10000 timesteps

FIGURE 2.31: Effect of self averaging the fields over time. The density field is on the top left hand corner, the nematic angle on the top right hand one, the nematic order field on the bottom left hand corner and the polar order field is on the bottom right corner.

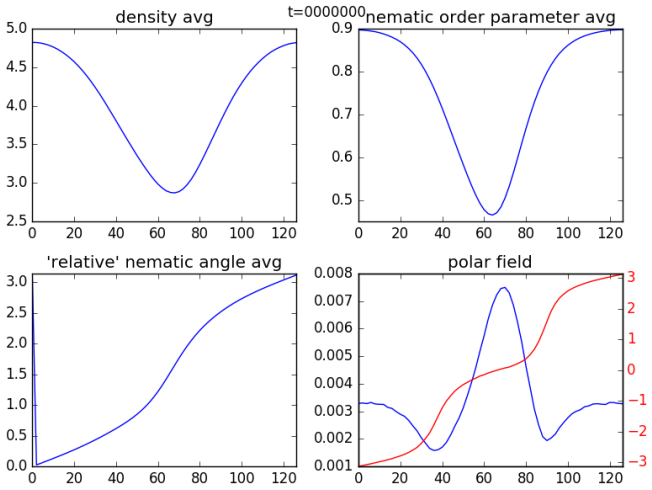

FIGURE 2.32: 10^6 timesteps of averaging is sufficient to observe that indeed, sign of arch polarity are visible on the fields themselves.

Varying v_0 In this first phase we consider the microscopic velocity v_0 as the a candidate quantity to match the activity and check if given an arch which has been generated with some given v_0 initially will split for a different v_0'. That is not the case as figure 2.33 shows, after having relaxed for a sufficient time ($\approx 10^7$ timesteps) we observe steady profiles of arches which differ slightly in their shape, but not fundamentally, none showing a wavelength. Even though the system could be not large enough and the discrepancies could appear for larger system size there's no sign of these finite size effects. For a quick check of this assumption we have checked the autocorrelation function of the nematic field, which definition is (2.25) written

in all generally for a complex field $f(x)$ defined in vectorial space (which is here the 2D euclidean space) and where x corresponds to the position in the coarse grained map. Note that due to the prohibitive computational cost of exploring large square systems we used elongated arches oriented along (Ox) ($L_x = 128 L_y = 1024$). Such choice might seem bad because arches breaking could likely occur along the arch [17] but long simulations on large square systems are not accessible for now.

$$C(x) = \int_{-\infty}^{+\infty} f(x) f(x + x') dx' \tag{2.25}$$

This operation has a big numerical cost as it grows quadratically with the number n_b of coarse graining boxes because we need to compute all $\frac{n_b n_b - 1}{2}$ pairs. The fastest way to circumvent this issue is to go to Fourier space as we show next (2.29) , in that case we can easily compute $C(x)$ as the Fourier backward transform of the products of the functions in Fourier space . This operation not only simplifies writing the correlation functions but allows to lower the cost of its computation.

Demonstration:
Let's define $\tilde{f}$ as the Fourier transform of f, the kth mode of $\tilde{f}$ reads as :

$$\tilde{f}_k = \int_{-\infty}^{+\infty} f(x) e^{-ikx} dx \tag{2.26}$$

we define a quantity $\tilde{U}$ as :

$$\tilde{U}_k = \tilde{f}_k \tilde{f}_k^* \tag{2.27}$$

But as we know the Fourier transform of a product is the convolution product (noted * , don't mix with the superscript notation for the conjugate) of the Fourier transforms, and using (2.27) the Fourier transform of the conjugate $\tilde{f}^*$ is $f^*(-x)$, note that as we work with real valued fields we can drop the $*$ on f that we note for convenience $g(x)$:

$$\int \tilde{f}_k^* e^{+ikx} dk = (\int \tilde{f}_k e^{-ikx} dk)^* = f^*(-x) = f(-x) = g(x) \tag{2.28}$$

$$\begin{aligned} U(x) &= \widetilde{f f^*}(x) \\ &= \int f(x+t) g(-t) dt \\ &= \int f(x+t) f(t) dt \\ &= C(x) \end{aligned} \tag{2.29}$$

We just showed that the Fourier transform of $U\tilde{(k)}$ is $C(x)$

Next in figure 2.34 are the auto-correlation functions for the function $\frac{\vec{v}}{||\vec{v}||}$ and therefore $C(x) = \int \cos(x) \cos(x + t) dt$ for the same arches. As we can

[17] from what we observed on square systems, defects pair will likely nucleate in the center of the arch because of the lower density. This is a similar mechanism happening in 2.6.2

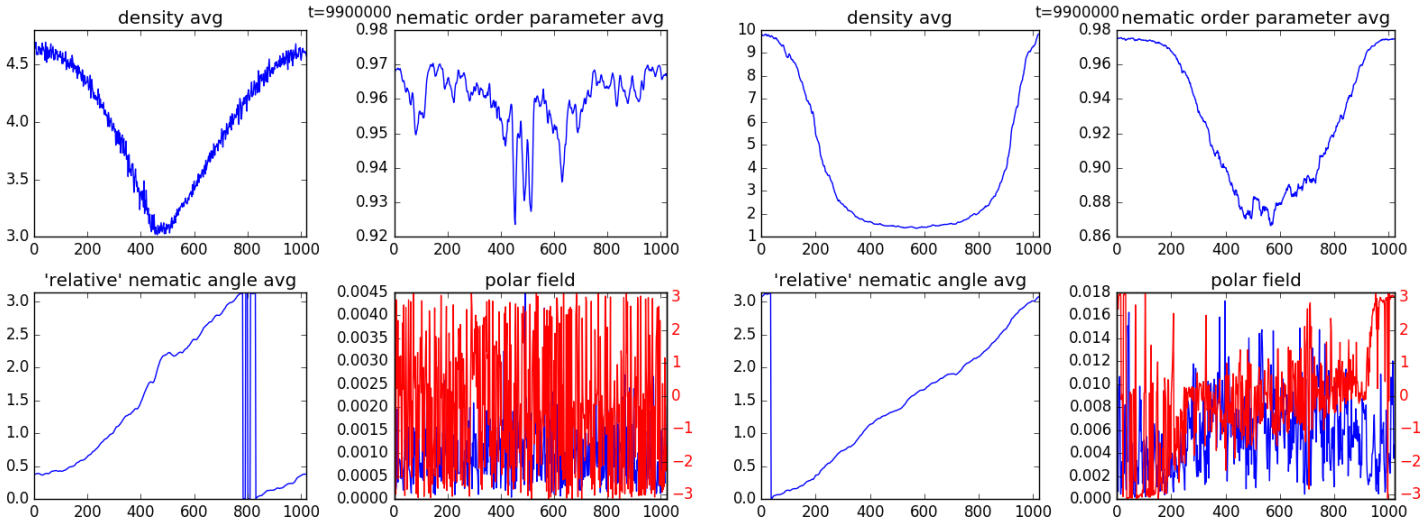

(a) $v_0 = 0.01$

(b) $v_0 = 2.0$

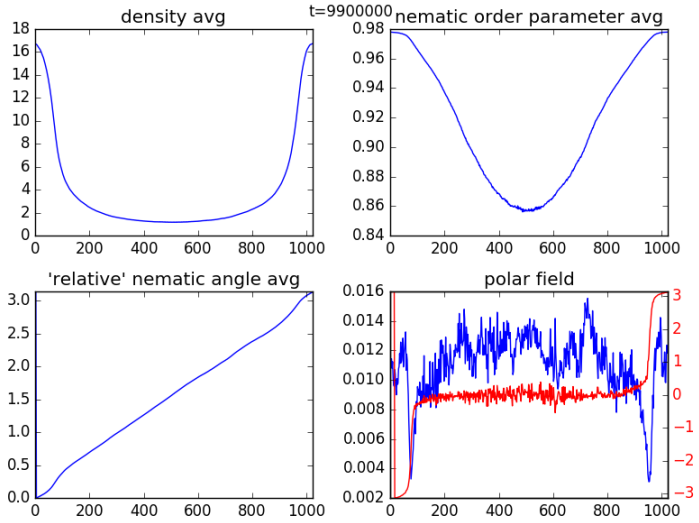

(c) $v_0 = 5.0$

FIGURE 2.33: Different profiles of arches for different v_0 , arches are elongated ($L_x = 128, L_y = 1024$) . The most interesting one is the density profile (top left hand corner) which shows that the density difference between the center and the edges of the arch increases with increasing v_0

see there is a tendency to have a higher decay for correlations when v_0 increases, however these correlations decay, at most, by a factor ≈ 6 in the case $v_0 = 5$. Thus whether the arch have fixed size for ridiculously high v_0 or we conclude that arches in our case have arbitrarily big sizes.

Putting different sizes arches together Another way to prove the absence of any given wavelength selection is to generate configurations of arches of different sizes. Here the system is globally $L_y = 1024$ and we put side by side two arches which sizes are respectively $L_x/4$ and $3L_x/4$. The goal is to see if such configuration of the system is steady or if will decay and lead

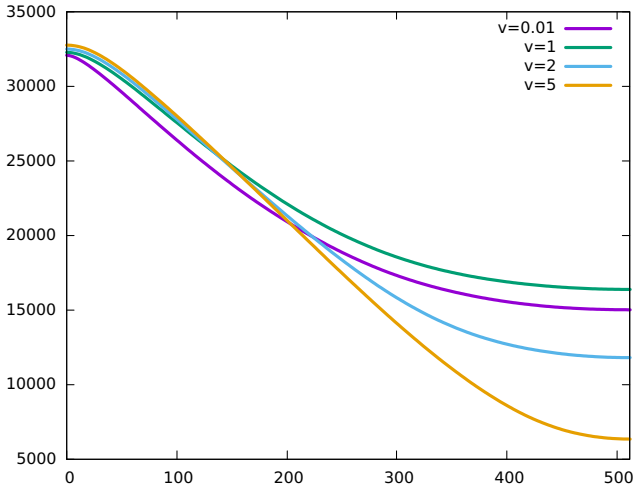

FIGURE 2.34: auto-correlations function of the nematic field for different v_0. The decay is very slow and not significant for the range of v_0 considered.

to another final state. In 2.35 we can see that in a matter of few hundred thousand timesteps, the initial configuration (left-most caption) relaxes to a configuration where the two arches persist but are then equally large.

Modifying β Another possibility is to consider that the repulsion parameter β can have an influence of the width of arches.Indeed we know that for 0 repulsion arches don't exist as these structures have never been reported so far in [38]. Actually we can check that arches break rather quickly when we turn off the repulsion **without creating defects** and "flattens out" to a nematic state, there are no more sign of the arch existence except in the density field because homogenizing density requires particles to diffuse over the whole system and that can take very long times compared to the disappearance of the other fields. Now, these evidence suggest that there is a transition in β parameter space between region where arches are existing and region with an absence of arch (a region which only phase is the homogeneous nematic). A possibility is that near the transition, the arches get fixed width and therefore it is probably a good idea to look at what happens in between to observe the arches in this region.

2.6.1.4 Minimal arch width

We will see in 2.7 that the phase diagram in the (ρ, k_f) plane for this microscopic model differs from the one obtained by simulations of the hydrodynamic theories. Notably the gap between the undulational instability region and the existence region of the arches is several order of magnitudes wide (arches $k_f \geq 0.1$, undulations $k_f \leq 10^{-3}$) in the microscopics whereas it is very small in the hydrodynamics. Even though there is no claim to have a 1:1 correspondence between the microscopics and the hydrodynamics we have a really simple explanation which would make the gap smaller in the limit of infinite system sizes: transitions, here from arch to homogeneous nematic, are known to be characterized by divergence of several

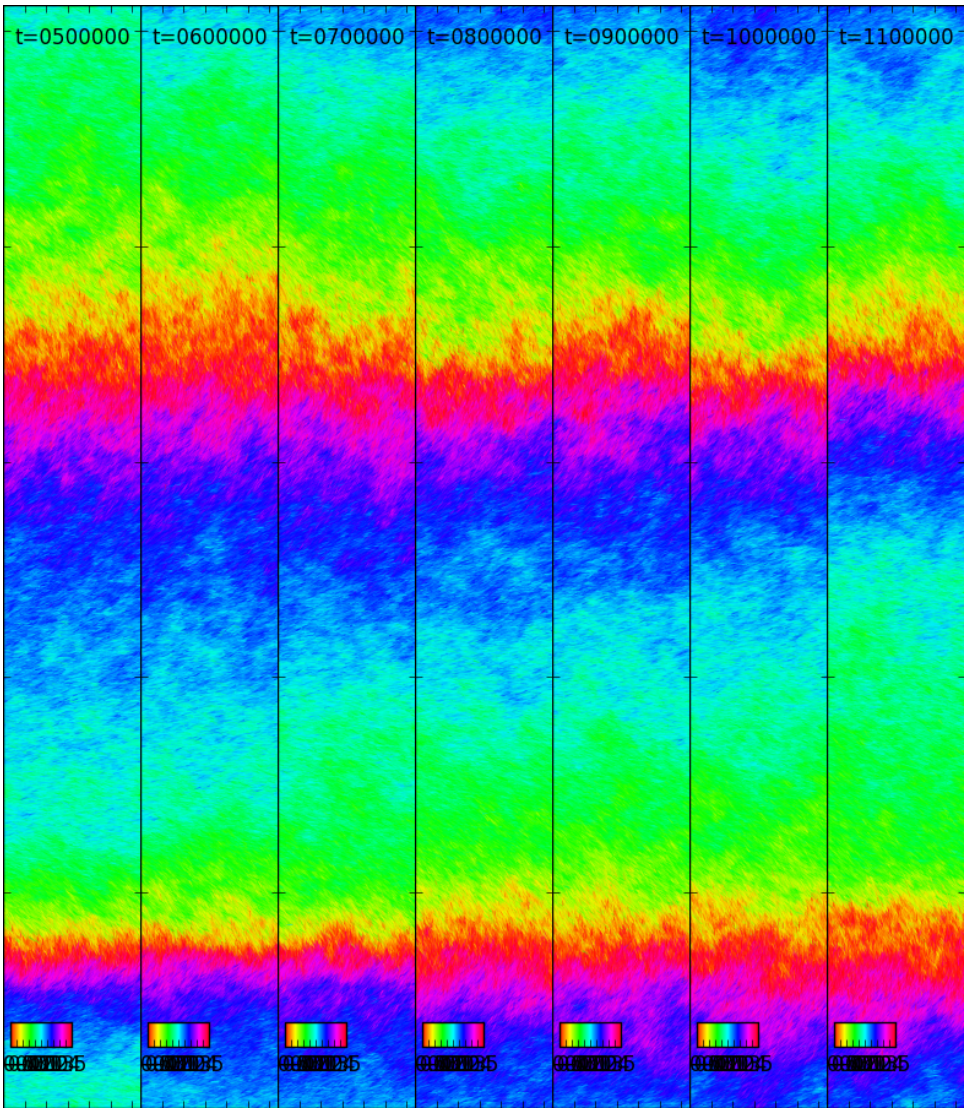

FIGURE 2.35: Two arches of different sizes are put side by side, they relax to two equally sized arches after $\approx$ 600000 timesteps

quantities, there is the possibility that the wavelength λ_a associated to the arch, which is constrained by the boundary conditions not to excess the system size, becomes unstable as we decrease k_f, as we know that the limit of $\lambda \to \infty$ is the nematic it is probably a good guess. So for any system size all $\lambda \leq \lambda_a$ are unstable and the arch should break. And indeed as figure 2.36 shows, the minimal arch width λ_a grows with decreasing k_f which means that in the (ρ, k_f) plane the arch stability line would probably move toward smaller k_f with increasing system size, such exploration for large systems being impossible but this small experiment proves to be useful as a piece of evidence.

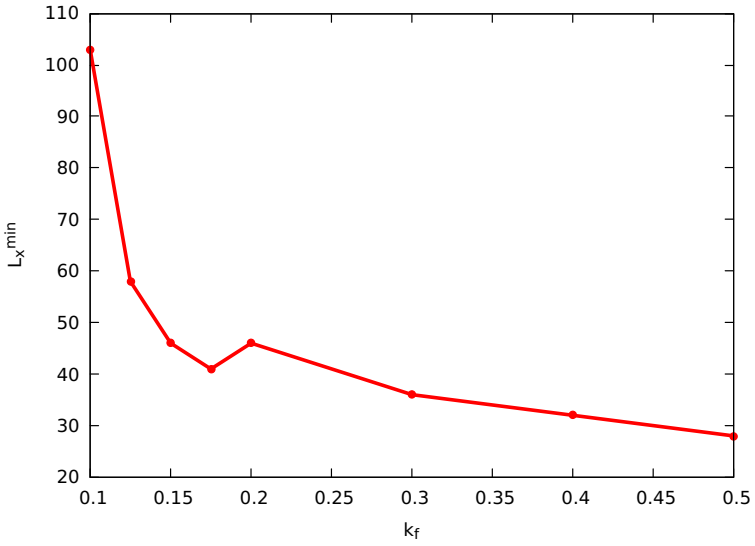

FIGURE 2.36: Minimal arch width as a function of the flipping rate k_f

2.6.2 Polarly ordered defects

Polarly ordered defects refers to a configuration where + defects self-propel in the same direction, constantly nucleated and annihilating at the same rate, being very close they also recombine with each other as we will see in 2.6.2.2.

This regime of polarly ordered defects has been shown in [53]. They consider equations derived from Toner-Tu symmetry principles and at fourth order in derivatives of the nematic order tensor $\mathbf{Q}$ and they describe the fluid flow $\vec{v}$. The equations are driven by a few set of parameters:

- r is a parameter controlling the transition from nematic to isotropic state in the passive case (it intervenes in the Landau-De Gennes free energy functional of a passive nematic). For $r \leq 1$ the stable configuration is isotropic while for $r \geq 1$ it is nematic.
- The introduction of an activity $\tilde{\alpha}$ controls the coupling between the stress exerted by particles and the fluid flow. $\alpha = 1$ corresponds to maximal coupling while $\alpha = 0$ corresponds to no coupling. Microtubule bundles correspond to $\alpha \leq 0$ because they exert "extensile stresses"

In Figure 2.37(a) the phase diagram of this model is shown, as a function of these two parameters. Among other things the lines indicate the transitions obtained from linear stability analysis: the passive isotropic-nematic transition for $r = 1$ is conserved while the activity α introduces for $r \geq 1$ a few other phases separated by blue and green lines: the nematic at lowest activities, the undulating nematic [18] at intermediate activities and the arches at even higher activities. Note that at highest activity (purple line) we reach the chaotic regime as the nematic order unstable.a

The same figure 2.37(a) indicate with points the state of the system during numerical simulations of these equations, which correspond more or less to the phases predicted by the linear stability analysis. Indeed the three previous phases are obtained: at lowest activity α the uniform nematic state is stable (black diamonds), at intermediate activity the is an undulating state is indeed obtained (purple triangles) and the arches are even higher activities (blue disks).

However the numerical simulations of the equations suggest there is a fourth regime between the arches and the undulating nematic, *what we refer as polarly ordered defects*: stable configuration of defects aligned polarly see fig 2.37(b) appearing (filled green stars) in the phase diagram 2.37(a).

It is not clear from our point of view if the configuration they see are steady or not. Limited spatial resolution or system size could lead their hydrodynamics equations to be numerical stabilized in such states. However from what we know about these simulations we can discriminate the isotropic $r \leq 1$ case where the defects configuration seems not to be perfectly static after relaxation with no net movement and the case $r \geq 1$ where these defects seems to be constantly moving, this drift makes the defect self-propel

[18] this undulating nematic basically correspond to the configurations of undulational instability which would face "kinetic arrest"

in the tail to head direction. These moving configurations have also been reported in [42].

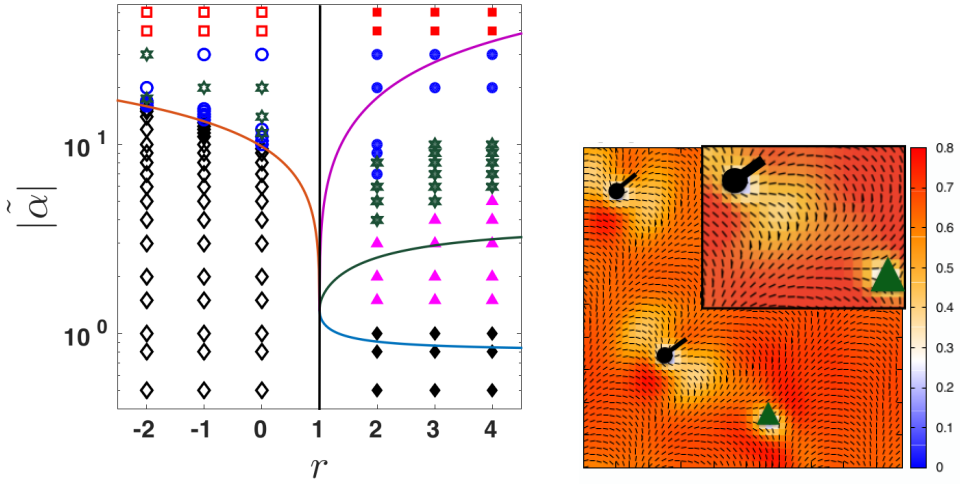

(a) Phase diagram with linear stability analysis lines and symbol for the observed states in numerical simulations. Polarly aligned defects move in the One can see that between to the undulating states and same direction.
the arches there is an additional state: this is the polar
ordered defects regime (filled green stars)

(b) The ordered defects configuration.

2.6.2.1 Arch formation at "low velocity"

We confirm the existence of such organized structures. First at high densities as a transient regime. We recall that in section 2.4 we discovered that the positive defect velocity v_+ was related to the SPP particles speed v_0. And that in the limit of "low velocities" $v_0 \leq 0.09$ we discovered that defects were reversing their direction of motion and moving "upward", toward their head. In that case we only studied the regime of short timescales and long distances between the pair of defects, *i.e* the so called "asymptotic" initial behavior.

What happens on longer timescales is also interesting. Indeed, if we let the defect move upward its dynamics evolves as shown in figure 2.37: the defect is looping around the system boundaries several time and avoids the $-$ defect several times. Two very different phases can be identified: when they are close to one another they move coherently with the impression that the $+$ defect pushes the $-$ one, these are relatively long phases and similar to what happens during an arch formation at high velocity. The new phase is when the $+$ defect is far from its negative counterpart: it freely moves upwards and when it completely looped a new "arch" is created. After a many many loops, annihilation finally occurs and we observe several arches. This process is very different from the "high velocity" regime where the defects indeed loop around the system but the phase where the $+$ defect moves alone is missing.

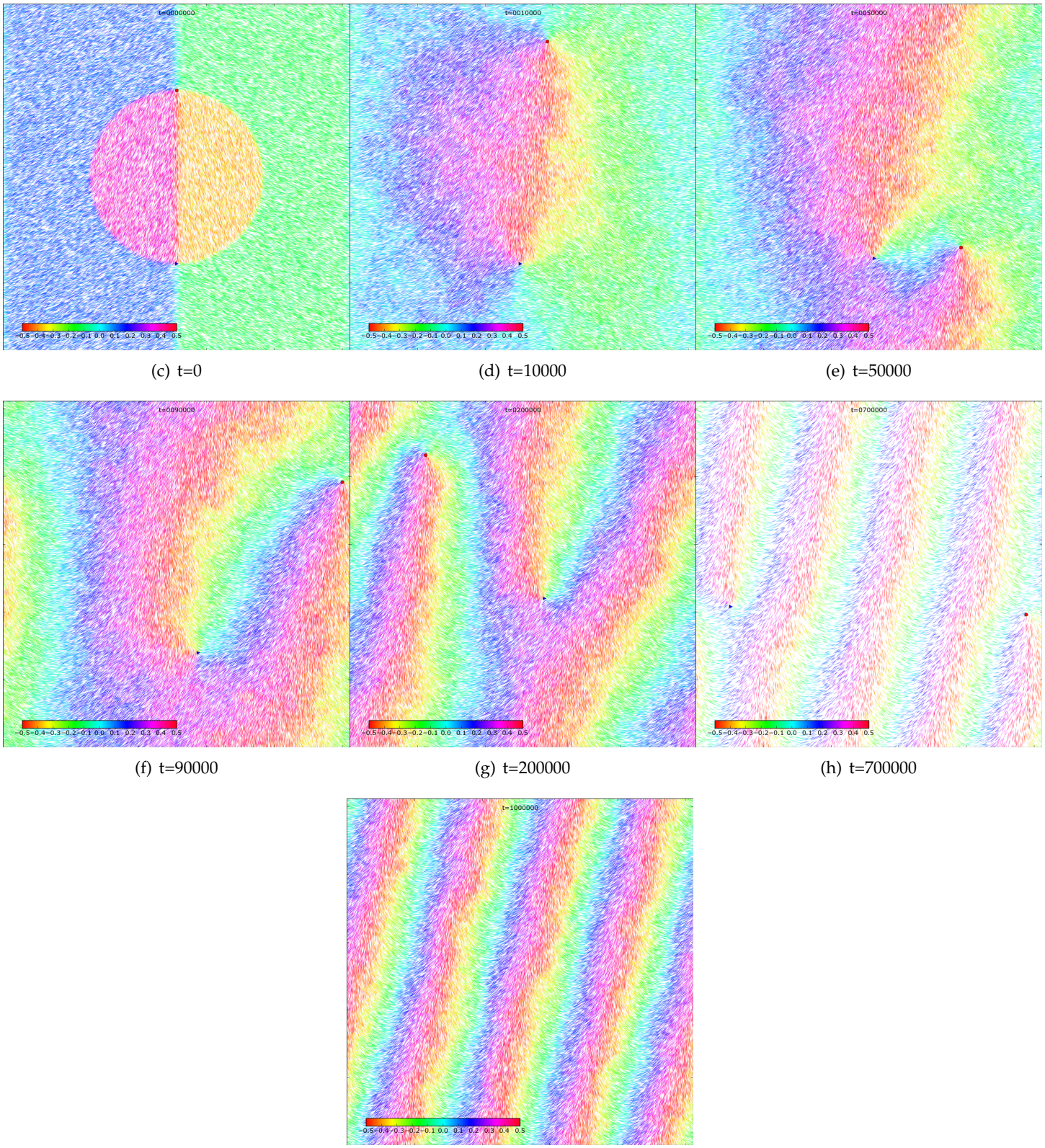

(c) t=0 (d) t=10000 (e) t=50000

(f) t=90000 (g) t=200000 (h) t=700000

(i) t=1000000

FIGURE 2.37: evolution of the pair of defects at low speed and high density $v = 0.05, L = 256, k_f = 0.5$

2.6.2.2 Polarly ordered defects require low density

At lower density ρ, the previous process in which the $+$ defect loops still exist. However in addition density fluctuations are much higher and allows defects nucleation and annihilation, mainly at the "center" of the arch (low density region). This provokes the so called polar ordered defects state, where defects are located in in the arches vicinity and, thus, are *convected* by the neighboring arches, coherently with what we've seen in 2.6.1 where we illustrated a polarity in arches. Actually from what we've seen about the pair of defects dynamics and from the arches shear stress we uncovered in 2.6.1.2 we understand clearly what happens now : defects are very likely to be nucleated at the "center" of arches because the density in this region (and we decreased the global density, thus the density is even lower here), but contrarily to the high v_0 case, pair of defects have a tendency to go apart from each other and therefore are sustained for a long time. These defects going apart from each other leave themselves an arch in the trail, generating polarity and propelling other defects. We now understand this spontaneous polarity of defects self-propulsion as a mechanism which involves a constant feedback between arches creation, defects nucleation and self-propulsion of defects.

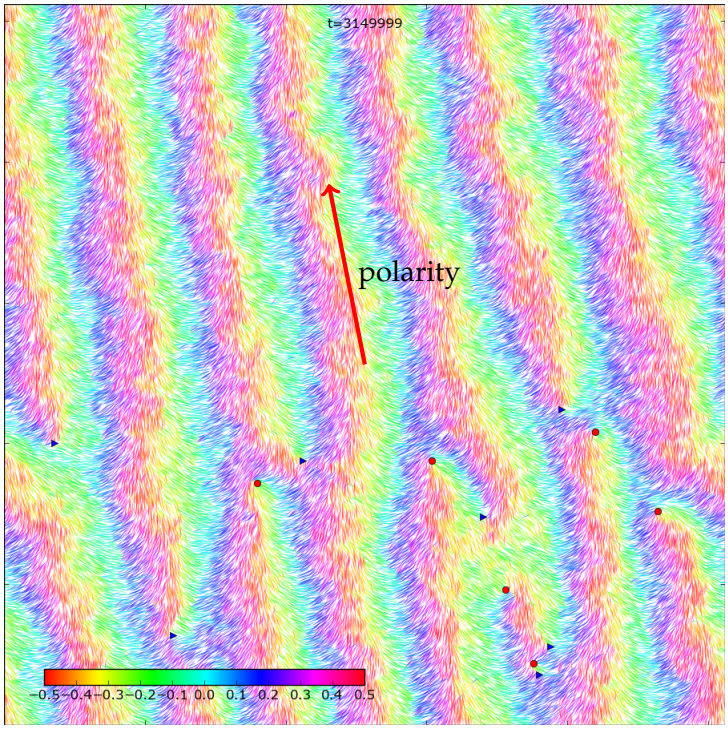

FIGURE 2.38: At lower density, smaller arches and defects density sustained. The arrow indicates the direction of motion of $+$ defects : $L = 256, k_f = 0.5, \eta = 0.1, \rho = 2.0$

2.6.2.3 Phase Diagram for pure active nematics $k_f = 0.5$

Now that we have a clearer vision of all the structures exhibited by our model at maximal flipping rate $k_f = 0.5$, we can now build its phase diagram at high velocity $v_0 = 0.3$ in figure 2.39. We let the low-velocity regime

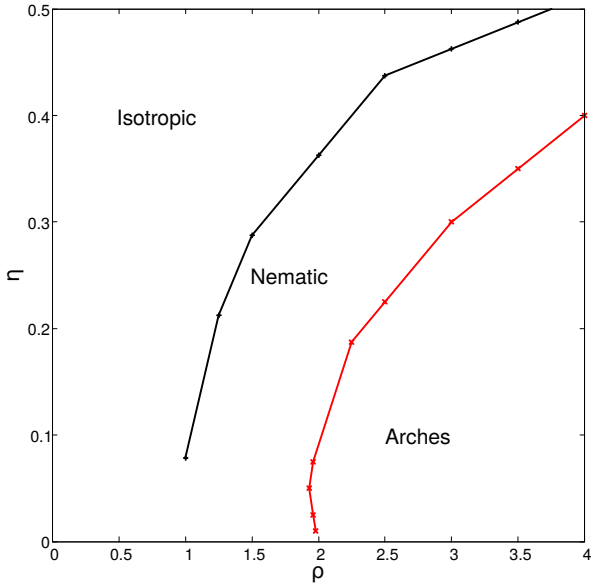

FIGURE 2.39: The phase diagram at maximal flipping rate $k_f = 0.5$ and high velocity $v_0 = 0.3$

and its polar-ordered defect structures for further studies given that the its existence region are hard to probe without proper criterion (these structures requiring a low density the limit between the isotropic state and the polar ordered regime is not clear neither from the order parameters nor from the system structure observation). Simulations were performed on a 128×128 system. Arches where generated at $\rho = 4, \eta = 0.1$ and quasi-statically displaced in parameter space with varying steps, decreasing them more and more as we get closer from the limit of stability. Again the reason is that waiting for defects to spontaneously nucleate in an initial nematic configuration would take gigantic times.

Compared to the rods $k_f = 0$ case:

- There is also a region where only the nematic is stable
- The arches which originate from the introduction of the density, similarly to the undulational instability, don't hold at low densities and require a minimal density $\rho_m \approx 2$ to exist.
- Similarly, the Isotropic-Nematic transition doesn't meet the (0,0) point neither. The isotropic state is thus the the only one persisting under a minimal density ρ_m^i. This "proves" again that at low density the repulsion dominates whether the particles diffuse or self-propel should not make any difference.

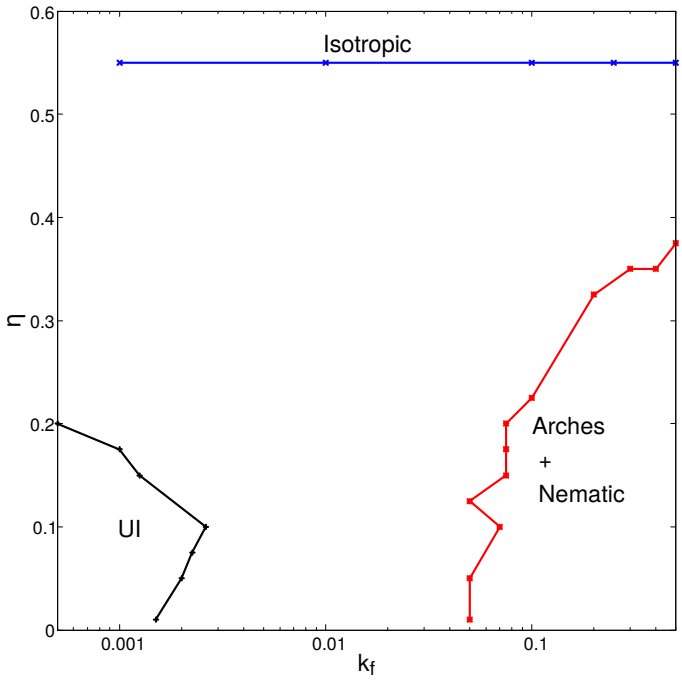

FIGURE 2.40: The phase diagram in the (k_f, η) phase diagram showing most new structures of this model (except the polar ordered defects which appear at low v_0) of this model. On the left hand side UI stands for Undulational Instability.

2.7 Connecting the two cases : varying the flipping rate

Now that we established that the pure active nematics ($k_f = 0.5$) and self-propelled rods $k_f = 0$ regions exhibit very different structures, it seems interesting to vary the only parameter we didn't modified as for now, that is the flipping rate k_f. Thus we will see the phase diagram in the (k_f, η) parameters space. Simulations were performed at size $L_x = L_y = 128$ for the arches system whereas higher system sizes $(256 \times 256, 512 \times 512)$ have been considered for other types of transition.

Looking at figure 2.40 the isotropic-nematic transition appears at a constant noise $\eta_c \approx 0.57$. Below we can see the nematic stable state spans most of the phase diagram, except at low flipping rate where it is unstable because we are in the undulational instability region. At high flipping rate on top of the nematic state we can see arches. Notice the UI region is well separated from the arches one, showing that previously considered limits $k_f = \{0, 0.5\}$ were legitimate and relevant.

2.8 Comparison with the hydrodynamics theory

In order to conclude properly we shall finish with some comparisons with the microscopics which reveal some successes.

2.8.0.1 Some success of the hydrodynamics equations

As we have mentioned the hydrodynamic theory has been fruitful in the previous models [46, 38] and this is still the case. However it is important to note that this is even more surprising that the BGL methods still works because most of the time we are working at high densities, density which plays an important part because of the repulsion we introduced in the model. Indeed the BGL method assume binary collision which should imply a dilute limit, this is not the case but yet these equation works. We thus now briefly address some results of this theory.

Rods For the rods case we recall that in the microscopics simulations we obtained many phases: polar bands, undulational instability and stable nematic. On the hydrodynamics side, the polar bands haven't been observed yet, given that their mechanism of existence is probably the smecticity, which is not taken into account by the BGL method. Otherwise the equations indeed predict the undulational instability 2.41(b) and lead to an almost entirely qualitatively agreeing phase diagram. 2.41(a):

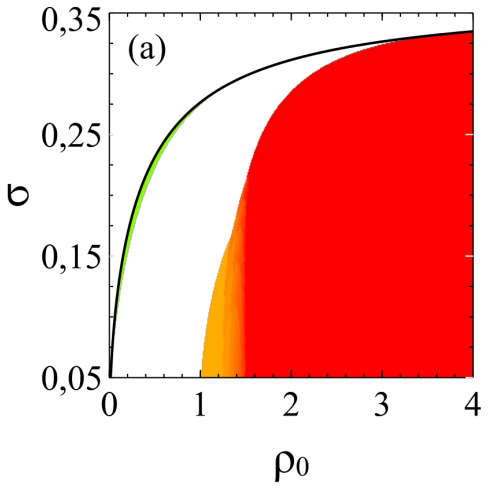

(a) Phase diagram for rods ($a = 0.1$) from the hydrodynamics equations. The color on the UI region indicates the most unstable mode wavelength. A very thin colored region near the transition is visible, indicating the presence of the "transversal" instability not visible in the microscopics simulations.

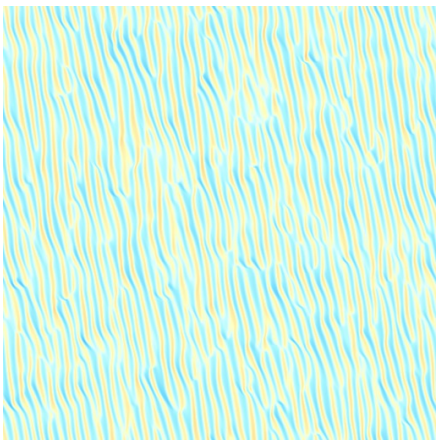

(b) The undulational instability, the color indicates the angle.

FIGURE 2.41: The agreement between the hydrodynamic theory and the microscopics dynamics is quite good

The main discrepancy concerns the isotropic-nematic transition curves which meet the $(0,0)$ point whereas it doesn't in the microscopics case, nonetheless we already explained the probable main reason was an increase of the overall repulsion importance at low densities in section 2.5.5.

Pure active nematics ($k_f = 0.5$) On the opposed side of the spectrum we have the diffusing particles known as active nematics. With the introduction of a repulsive term a new phase known as "arches" appeared and described in 2.6.1. Such structures have been observed in the hydrodynamics simulation as well. Below 2.42 is a comparison of arches profiles from hydrodynamics and "micro" simulations, showing that the overall agreement is good.

The only slight discrepancy concerns the polar angle. In fact in the hydrodynamics case it is slightly varying around π thus an appearing discontinuity. On the contrary in the microscopics, probably for geometrical constraints: the particle have to perform a full 2π rotation as the nematic profile already performed a full π rotation. The nematic angle and its polar counterpart are both defined from the particles orientation and thus coupled, the characteristic full π rotation of the nematic angle of arches *implies* a full 2π rotation on the polar angle. Such coupling is probably not necessary between f_1 and f_2 in the hydrodynamics case because the relation between f_1 and f_2 are only the terms of the BGL equation which conserve symmetries but not necessarily the geometrical meaning of the fields.

2.9 Conclusions and perspectives

In the previous sections we briefly sketched the rich phenomenology a the simple model of "active nematics with velocity reversal and repulsion" exhibit.This model is an extension of the previous models in two ways, first we have introduced a repulsion torque-like term β and we've made the connection between diffusing particles and self-propelling ones by introducing the flipping rate k_f. First to study solely the influence of the flipping rate we considered the two limits already studied without repulsion which are $k_f = 0$ and $k_f = 0.5$ namely pure rods and pure active nematics.For both case, phase diagrams in the (ρ, η) plane were obtained.Both case exhibit similar shapes for the nematic-isotropic transition lines have been exhibited. However new phases appear with the addition of repulsion : for the rods case we highlighted different coexisting phases chaos of self-propelling defects, smectic polar bands and polar lanes. As for the nematic case we focused on the new phase introduced by the repulsion : arches.

For both cases, existence domain of these phases have been produced. The qualitative agreement is very good with the hydrodynamics equations. Comparing with the hydrodynamics equations, domains of existence lead to good qualitative agreement for the arches, chaos and nematic stable phases. Such qualitative match is achieved for profiles shape in the high velocity regime.

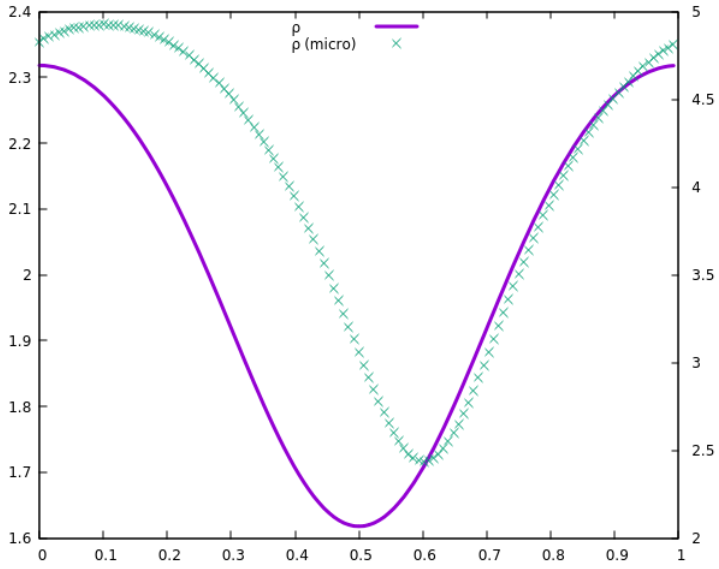

(a) Comparison of the density profile.

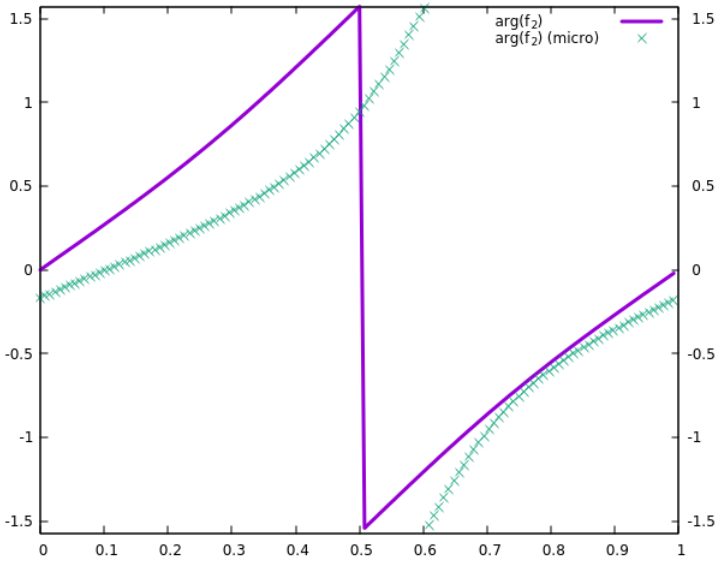

(b) Comparison of the *nematic angle* profile.

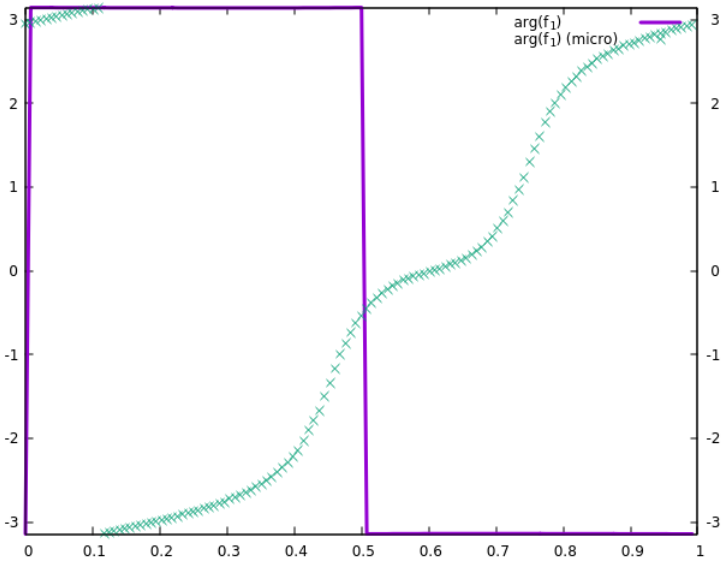

(c) Comparison of the *polar angle* profile.

FIGURE 2.42: Comparison of profiles for arches generated from hydrodynamics simulations and from microscopics simulations. Plain lines are for the hydrodynamics simulations and points for the microscopics ones. The position along the axis is normalized to 1.

We then connected the two cases by modifying continuously the flipping rate k_f and obtained *in the high* ρ limit a view in the (k_f, η) plane where arches and chaos are well separated regions , where lies in between the only surviving phase is homogeneously nematic.

In the chaotic region, guided by the results obtain from the linear stability analysis of the uniform nematic state, we've characterized this regime for which exists only at low noise η. We also highlighted the presence of strong smectic order in this region which is intrinsic to the way we implement the repulsion in our microscopic model. However this smecticity is necessary to obtain well defined growing stripes typical of this regime.

Chapter 3

Neisseria Meningitidis

3.1 Physics generalities

We start this chapter by a general introduction on physics matter in relation to biology. Indeed biological system share features with common physical systems which may or may not already been explained yet. Consequently we will review first of all the aggregative properties of *Neisseria Meningitidis* through the prism of model system such as Diffusion-Limited Aggregation *etc.*. Next we will address the its peculiar motility by considering the Levy walk model. And finally we will see the essential rheology experiments which gave quantitative results to aggregate properties

3.1.1 Liquid, Solid and Gas state of matter

The literature on colloidal suspensions is of particular interest in order to gather notions which will be useful for our study, more detailed reviews can be found in [56] and [22]. The first measurements of colloidal systems of many hard spheres suspended in a liquids were performed by Jean Perrin in order to prove Einstein's theory on Brownian movement. Measuring the displacement of μm sized gum resin particles under the influence of the gravity, the other forces are the viscous drag (Stokes force) the thermal fluctuations and the Archimedes' force he described the steady situation after some relaxation dynamics. This equilibrium which is now known as "sedimentation equilibrium" is as follows: the density of particles is not homogeneous with respect to depth z - confirming Einstein's prediction - and follows an exponential profile along the vertical axis z: $\rho \propto e^{-\alpha z}$. What's more - related to the density profile - the phases are changing with varying depth: one can notice that at the bottom the high density region is closely packed and motionless whereas the low density region at lower depth seems almost freely diffusing. Colloidal systems are thus very likely to form solids at high concentrations or a fluid phase at lower concentrations.

In order to characterize the state of the system the usual parameter is the packing fraction $\phi = \frac{V_{spheres}}{V}$, where $V_{spheres}$ is the volume occupied solely by the colloid and V is the total volume (namely liquid + colloid). For instance in the model of spheres without any interaction the solid phase is characterized by a configuration where arrangement of the colloidal spheres tend to favor maximal compactness. This requirement leads to a positional

order given by a FCC arrangement (Face Centered Cubic) well known in crystallography, with $\phi_{FCC} = \frac{\pi}{3\sqrt{(2)}} \approx 0.74$ the maximal compactness possible for an arrangement of equally sized spheres. In this phase the particles are jammed and their position fluctuates but on average stays static with no rearrangement of pairs whatsoever. On the contrary in the fluid phase, as there is more room the positions are not steady: colloidal particles are diffusing on large timescales but they might collide with each other from time to time leading to a finite mean-free path.

A good summary can be found in figure 3.1, showing which phase(s) are present with varying packing fraction as the control parameter. To go more into details, the solid-fluid transition is of the 1^{st} order kind, as such there exist coexisting regions and hysteresis phenomenons. Increasing the packing fraction ϕ continuously we observe the fluid coexist with some solid clusters. Increasing again ϕ only the crystal phase persists. Another interesting phenomena such as glassy transition occurs when we increase abruptly the packing fraction ϕ and lead to amorphous liquid, however such glassy dynamics is beyond the scope of this thesis.

An important note: from our point of view what's referenced as "liquid" in figure 3.1 should be instead qualified as a fluid, the difference being that the particles in a fluid occupy all space available , contrary to the common meaning of *liquid* which implies a fixed density. Consequently there can't be any liquid in a system of non interactive hard spheres. In a liquid the density is homogeneous (because a liquid is supposed to be almost incompressible), for this to be possible we need an attractive interaction between the colloidal particles or at least a mechanism favoring cohesion. The most widespread model for common liquids consists of pointwise atoms subjected to a Lennard-Jones potential which accounts at the same time for the attractive interactions as well as the repulsive part - the latter gives a spatial extent to atoms/colloidal particles - but other models can be considered. Indeed in the following chapters *the liquid phase is a cohesive (aggregative) phase.* Note also that the supercooled regime refers to the persistence of the liquid phase into the solid one, which is mostly due to the requirement that impurities big enough need to exist (here small liquid droplets) in order to grow because the nucleation of crystal clusters is only possible above a critical size.

3.1.2 Formation of aggregates

Considering we will study aggregates it is worthwhile to consider model systems which show how aggregation manifest itself in nature. Noting that in none of these models any attractive force is at stake and different mechanisms lead to either macroscopic aggregates 3.1.2.2 or phase separation 3.1.2.3. We will finish in 3.1.2.4 by introducing the structure of aggregates shown by *Neisseria Meningitidis*. Aggregation processes have been studied studied for a long time by physicists because these phenomenon occur in many situations: from the most common immiscible liquid-oil mix [] to the more complex but essential phase-separation of p-granules (liquid) inside the cell cytoplasm (liquid also) [23], phase separation is ubiquitous

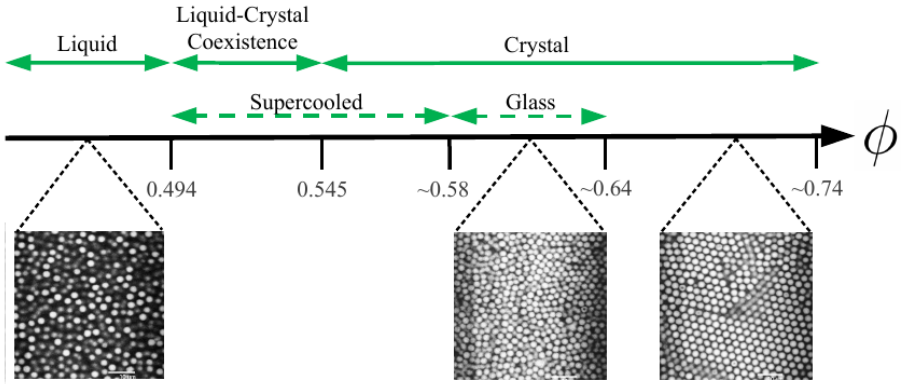

FIGURE 3.1: Experimental phase diagram for non-interacting hard spheres, sourced from [22].

when different components are put into contact. Again we stress the importance of minimal model in the the quest of looking for universal mechanisms which are the elementary parts to understand the more complex mechanisms at stake.

3.1.2.1 "Standard" liquids: attractive forces

It is worthwhile to note that a standard "Lennard-Jones" fluid (in the sense of a similar phase diagram) exist at the colloidal level as long as similar interaction exist between the colloidal particles. These can be electrostatic forces as some colloidal systems are composed of charged particles but there exist also a relevant example in a biological context, attraction-depletion is one of the mechanism leading to such forces: when the distance between colloid is short, macro-molecules can't penetrate the gap in between and create an entropic attractive force (because of the excluded volumes these molecules can't reach). For instance PMMA particles mixed with polystyrene molecules show a similar phase diagram of a standard liquid. This is the mechanism at stake in p-granules formation inside the cell cytoplasm (figure 3.2), these p-granules show all features of standard liquids: they fuse, possess a surface tension etc.

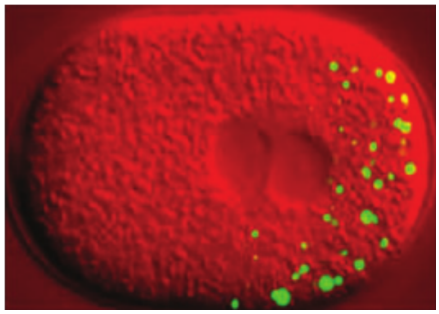

FIGURE 3.2: P-granules (green) inside the cytoplasm of *Caenorhabditis elegans*

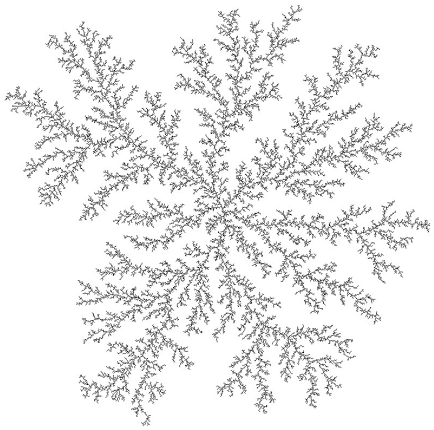

(a) A fractal tree generated by DLA from a point-like initial seed, source http://paulbourke.net/fractals/dla/

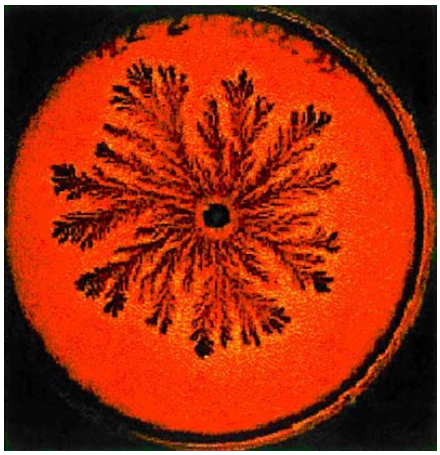

(b) A bacterial colony of *Paenibacillus dendritiform* , from [48]

3.1.2.2 Diffusion Limited Aggregation

An interesting model describing aggregation in a biological context was built by Witten, T.A. and Sander, L. M. in [65]. The model dynamics starts with a seed, which can be a particle or a region of space, then particles are randomly generated at a constant rate and diffuse via thermal motion. The only rule is that when these particle comes to contact with the seed their motion stops and the ensemble seed+particles becomes the new seed. After many steps interesting patterns showing fractal structures are created as can be seen in figure 3.3(a). These fractal pattern are frequently seen in electrodeposition experiments but more interestingly in biological systems such as bacterial colonies of *Paenibacillus dendritiform* 3.3(b). When these bacteria are voluntarily starved they start to describe DLA like patterns while seeking for food. This experiment is not fully understood as many effects can have significance over the experiment: food diffusion, chemotaxis etc.

Despite the algorithmic simplicity of DLA dynamics, it is still resisting to analytical studies and most results are numerical, however it still is an essential minimal model reproducing biological systems properties.

3.1.2.3 Phase separation through activity

It is interesting to note that the previous model was tailored to lead to formation of a macroscopic aggregate, by construction, but there exist mechanisms in nature which can lead to aggregates via phase-separation without explicit constraint. In the introductory chapter we already mentioned the Motility-Induced Phase Separation ([10] see 1.2.2) in another context but there are several other mechanisms (very similar though) leading to phase separation.

In [63] the author show that, for purely Brownian particles, two populations with different effective temperatures will unmix. The "cold" ones forming aggregates as the hot ones tend to produce something akin to "pressure forces" on the aggregate. When the difference of effective temperature is

high the resulting aggregates are showing very high structural order as can be seen in figure 3.3. Another model similar model is considered in [19] for which Brownian particles are mixed with self-propelled ones. The final result being that in such system phase-separation can also occur if the two "effective temperatures" of "hot" (the self-propelled ones) and "cold" (the diffusive ones) particles differ.

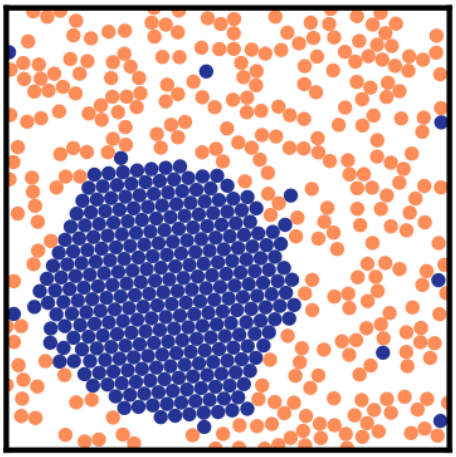

FIGURE 3.3: Phase-separation is the consequence of activity difference between "hot" and "cold" particles. source:[63]

3.1.2.4 Neisseria's aggregates

Now that we have seen different sorts of aggregate it is time to put into perspective the ones formed by *Neisseria Meningitidis*. We already mentioned the aggregate liquid aspect in chapter 1 but it is essential to use a deeper level of detail. As can be seen in figure 3.4, Wild-Type aggregates are showing high roundness, similar to MIPS aggregates, but lack structural order if compared to those of figure 3.3. In fact they are more akin to liquid droplets than to out-of-equilibrium systems. The first clue supporting this claim is the motility: the missing structural order is associated to large displacements (similar to the "fluid" in section 3.1). The second clue is related to the dynamics of coalescence: put side by side, two bacterial aggregates will fuse and leave a bigger round one after a while, with an evolution similar to a liquid droplet as show in figure 3.5. This phenomenon known as coalescence is treated in section 3.1.4.2.

But those aggregates also exhibit properties of out-of-equilibrium systems such as MIPS, indeed the motility of these bacteria originate from the out-of-equilibrium nature of their molecular motors which we were able to detect. Even if this is a hard to detect such thing, we were able to measure a coefficient diffusion higher inside the aggregate than those of free particles (see figure 3.6.1.1 for the numerical part) but also a signature of the ballistic regime, that is when pili pull against each other in section 3.6.2.

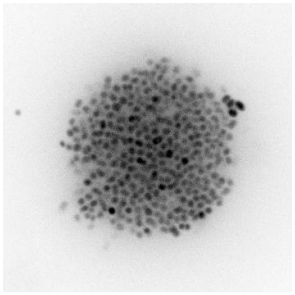

FIGURE 3.4: A Wild-Type aggregate is round but doesn't exhibit strong hexagonal order inside, source:G. Dum'enil's group.

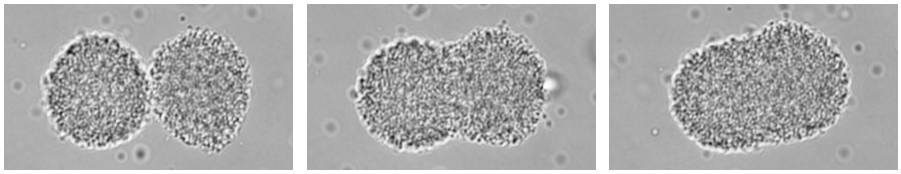

(a) Two aggregates are put in close contact

(b) They fuse, after 50 seconds the contact disk is still visible

(c) After 180 seconds it is not visible anymore and the resulting aggregates starts to round out.

FIGURE 3.5: The coalescence dynamics is similar to those of a standard liquid, source: G. Duménil's group

3.1.3 Bacterial motility

Bacterial propulsion has triggered the interest of physicists in the early 1970s because bacterial exploration also named *bacterial foraging* could be considered as an effectiveness optimization problem and thus is at the edge of both mathematics and physics [67]. We will now see some model systems showing different motility tactics.

3.1.3.1 Levy Walk

The movement of most bacteria is far from random, bacteria such as *Escherichia coli* (more known under its abbreviated name *E. coli*) show ballistic movement over large distances triggered by their flagella. This kind of trajectories recalls the Levy walk named after Paul Lévy who first described them. A levy walk is defined as follows: if we call D the length of a flight, then the "survival" probability of this random variable being more or equal than some given value d can be generically written as:

$$Pr(D > d) = \begin{cases} 1 & \text{if } d < 1 \\ d^{-\alpha}, & \text{if } d > 1 \end{cases}$$

We see that small steps $d \leq 1$ have a 1 probability saying that any jump is at least ≥ 1 whereas long jumps have a distribution decaying with a

power-law. Given this slow decay it implies very large displacements are significant.

In order to make it a continuous time process one needs to introduce a waiting time distribution that is the probability distribution of the time one needs to wait between the next jump.

In Lévy flight the particle hops instantaneously and then waits for a random time until next hop, because of the probability distribution of jumps length which decays slowly the MSD is ill defined for some values of α (as MSD is a second order moment it diverges if $\alpha \leq 2$). On the contrary in Lévy walk particle moves as constant speed and thus the duration of the jump and its length are coupled which allows to define properly the MSD. Additionally one can also introduce waiting time in Lévy walk, depending on the modelization, but that is not necessary.

E. coli motility is known as "run and tumble", exhibiting long ballistic motion (run) separated by phases of rotates where it changes its motion direction (tumble). This can be explained by the two modes of rotation of its flagella which can rotate: clockwise (CW) which corresponds to the tumble phase and counter-clockwise (CCW) which corresponds to the run phase.

In [68], figure 3.6(a) shows the probability distribution for duration each phases. The run phase (CCW mode) is in grey (and in the inset in the top left corner) and the CW mode is in dark. The fit shows that the run phases distribution is compatible with a power-law decaying behavior (linear fit in log-log scale) which is the sign that a Lévy walk is a good model for the run part.

Now considering that the *flight-length is bounded*, these bounded Lévy walks exhibit on one hand slightly ballistic behaviors at short time scales ($MSD \propto t^{\alpha}$, $\alpha > 1$) and on the other end (sub-)diffusive scaling at larger times $alpha \leq 1$, for example data from [50] show clearly a crossover in the case of human walking in various location in figure 3.6(b) though one can notice the behavior is only slightly super-diffusive $1.08 \leq \alpha \leq 1.8$ for short timescales and is sub-diffusive for longer timescales $0.19 \leq \alpha \leq 0.85$ [1].

In the context of optimality it is easy to understand that diffusion is maybe the worst kind of tactic when it comes to space exploration. On the contrary Lévy walk offers better efficiency. Indeed, in order to find food optimally one needs to explore space over large distances, thus requires some directed movement, but also require randomness to scan all available space [59]

It is worthwhile to mention that these Lévy walk are not restricted to bacteria but are rather ubiquitous in the living world: similar behavior are shown in sharks , human hunters are also relevant.

3.1.3.2 Twitching motility

Neisseria - and related bacteria using Type IV Pilus - has a particular way of displacement on substrates , its mode of displacement is referred to as *twitching motility*. The name comes from the fact that if one observes these

[1] Though

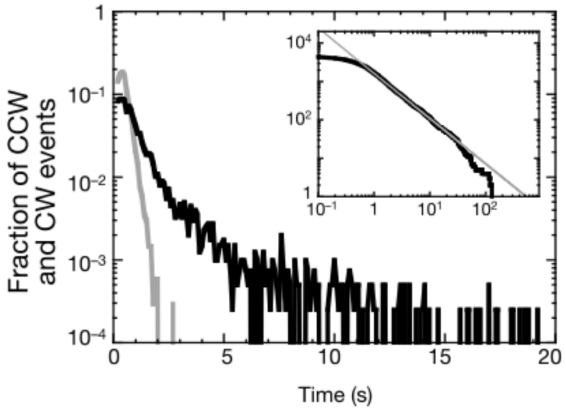

(a) Distribution function for duration time of run (CW) and for tumble phases (CCW), the inset exhibit clear exponential decay. From [68]

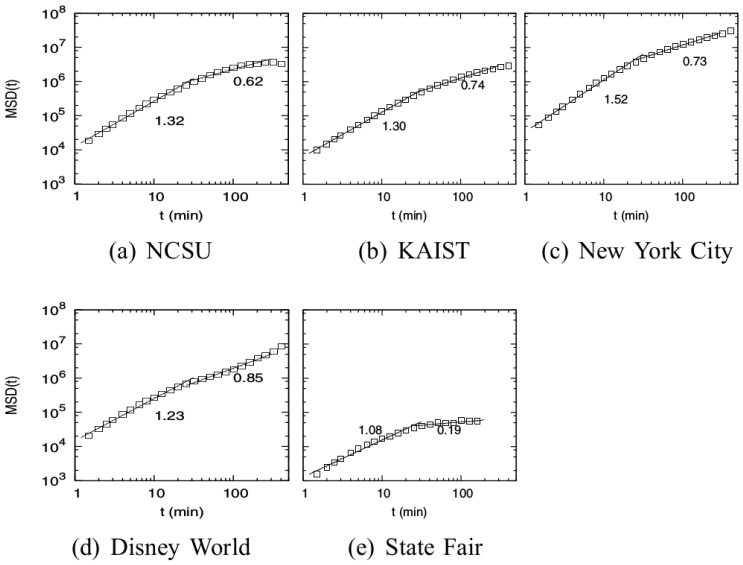

(b) Human trajectories tracked by GPS on various location show features of truncated Lévy walk, from [50]

FIGURE 3.6: Feature of Lévy walks for very different systems

bacteria lying on the substrate [2] we can clearly see bacteria spending most of its time in long stages of "arrested motion" , where in fact the bacteria is in a stalled state caused by the competition between its pili and from time to time one can see brief jumps over large distances. Indeed the bacteria is at the center of a tug-of-war game where pili on each side of the bacteria are pulling against each others in opposite directions. Eventually one side will win and exert more force and enable the bacteria to enter in the short stages of long distance ballistic motion which are simply caused by the retraction of the pili on the side that won to the strength the game. This mechanism has been extensively studied in [69] and with an even more complex modelization in [30]. The essential results are :

- Trapping events are caused by the equalization of the forces between competing pili.
- On the contrary the fast ballistic motion occur when there is an imbalance between pili forces.
- The elongated shape of the bacteria is essential: the movement is essentially perpendicular to the long axis.
- The duration of the ballistic events is increased by the fact that the pili detachment probability is dependent of the force the other pili are exerting onto it.

[2] See http://www.ncbi.nlm.nih.gov/pmc/articles/PMC4190650/bin/mmc2.mp4 for a movie showing a biological assay of twitching motility

However it is not clear from these results if twitching motility is an optimal foraging behavior nor does it explain its interest with respect to other types of motilities.

3.1.4 Rheology of cellular aggregates

The science of probing mechanical properties is Rheology, applications of rheology in a biological context are quite novel. In [20] the author have developed the theoretical analysis of a quite new technique to study multicellular aggregates visco-elastic properties. They extended this technique which was already known in the case of single cells and for low deformation only [40]. They provide the general framework allowing to obtain the elastic modulus E and the viscosity η from simple micropipette measurements. We briefly summarize these results and their derivation here.

3.1.4.1 Modelization of an aspirated droplet

Let's consider a drop aspirated in a pipette as shown in figure 3.7. We neglect all wetting phenomenon which could happen at the interface with the pipette.The shape of aspirated droplet is an hemispherical cap on front and on the back. We can write the energy difference $\mathcal{F}$ between the droplet at rest and under aspiration as follows:

$$\mathcal{F} = (4\pi R^2 + 2\pi R_p L)\gamma - \pi R_p^2 L \Delta P$$

- γ is the liquid/air interface surface tension
- R_p is the radius of micropipette (and thus the radius of the hemispherical tongue in the pipette)
- R is the radius of the aggregate outside the pipette (assumed constant over time if $R_p << R$ which also implies the volume of the spherical cap is kept constant $\approx \frac{4}{3}\pi R^3$)
- $L(t)$ is the length of the pipette tongue inside the pipette
- ΔP is the excess applied pressure (measured with respect to the exterior pressure P_0)

The energy is partitioned between two contributions: the first two γ terms account for surface energy, the last one for the work produced by pressure forces. The last term needs more explanation, we can understand it as the pressure difference times the volume sweeped by the tongue during its progression.

Now we can also write the value of the aspiration force: $f = \pi R_p^2(\Delta P - \Delta P_c)$, where ΔP_c is the minimal pressure difference required to compensate the surface pressure. Indeed it can be shown that under a trigger pressure ΔP_c the steady state of the system will be , as shown in figure 3.7 a non hemispherical cap with a curvature radius r given by the Young-Laplace law: $P = 2\gamma(\frac{1}{r} - \frac{1}{R})$. Thus when r reaches R_p the value of the critical pressure is $\Delta P_c = 2\gamma(\frac{1}{R_p} - \frac{1}{R})$ above which there is no longer a steady state and the resulting state is a constant velocity progression of the tongue.

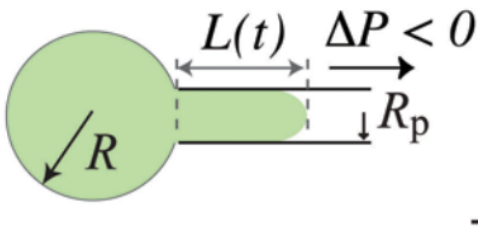

FIGURE 3.7: Schematic of an aspirated droplet during its progression in the micropipette, taken from [20]

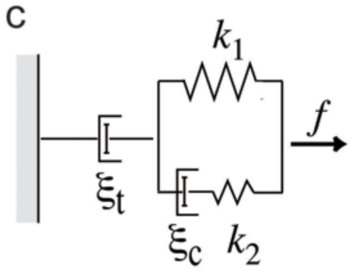

FIGURE 3.8: the Maxwell idealized system, also taken from [20]

Assuming an elastic response in the short time regime we can write $\sigma = \frac{f}{\pi R_p^2} \approx E\frac{\delta}{R_p}$ by definition of the elastic modulus or $f \approx \pi R_p E\delta$ in other words x

On the contrary in the long time regime the force is compensated by the viscous drag $f = 3\pi^2\eta R_p\dot{L} + 2\pi k R_p L\dot{L}$ where the first term accounts for the volume viscous drag whose viscosity is η and the second term k represents the friction with the wall.

These two regimes can be described in a common framework using a modified Maxwell model, that is idealizing the response of the system to a simple spring-dashpot circuit as shown in figure 3.8. This yields the evolution equation of $L(t)$:

$$L(t) = \frac{f}{k_1}(1 - \frac{k_2}{k_1 + k_2}e^{-\frac{t}{\tau_c}}) + \frac{f}{\xi_t}t$$

There are consequently two time regimes. For short times $t << \tau_c$ we can write $L(t) \approx \frac{fk_1}{k_1}(1 - (1 - \frac{t}{\tau_c})\frac{k_2}{k_1+k_2}) + \frac{f}{\xi_t}t$

Finally we can obtain the viscosity η by fitting the curve $1/v(P)$ using formula (3.1):

$$v = \frac{R_p P}{3\pi\eta} \tag{3.1}$$

3.1.4.2 Droplet coalescence

We haven't yet characterized the surface tension of the aggregate. From a purely energetic point of view two droplets of a fluid put in contact will coalesce and form a bigger droplet in order to minimize surface tension energy. Excepted these energy considerations the early dynamic of the contact surface is in itself an interesting subject: it depends on the viscosity η and the surface tension γ. The evolution of the contact disk radius $r(t)$ follows equation (3.3):

$$\frac{\eta \dot{r} r^2}{R_0^2} = W \tag{3.2}$$

$$\tag{3.3}$$

or in the integrated form (3.4):

$$r^3 = \frac{W R_0^2}{\eta} \tag{3.4}$$

Using this relation and the viscosity obtained from the micropipette experiments we can extract the surface tension by means of tracking the contact disk radius $r(t)$.

To summarize, the modelization as a liquid droplet allows us to obtain formulas (3.1) and (3.6) , and to relate the tongue velocity to the viscosity and the surface tension of the whole liquid.

$$v = \frac{R_p P}{3\pi\eta} \tag{3.5}$$

and

$$P = 2\gamma(\frac{1}{R_p} - \frac{1}{R_v}) \tag{3.6}$$

3.2 Neisseria Meningitidis

3.2.1 Neisseria's features

3.2.1.1 The pilus

Pilus are quite common appendices which exist at the surface of many bacteria. They have various functions but we will focus on Type 4 Pili[3] (abbrev: T4P) for which studies are quite novel, at least in the physics field. However there is an extensive biological literature addressing the properties of these molecular structures, which are helical polymer of diameter $6\,\mathrm{nm}$ which base unit is named a "pilin unit" (also named PilE) which weights $\approx 15\,\mathrm{k}$–$20\,\mathrm{k}$ atomic mass , the length of a pili is typically of a few $\mu\mathrm{m}$ [27] but it is highly variable. The essential property of the pili from the mechanical

[3]The singular noun is a pilus

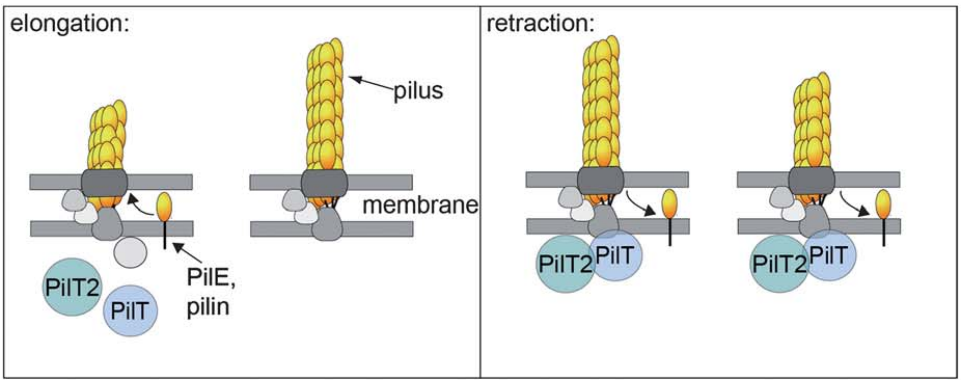

FIGURE 3.9: Rough schematics showing the two working modes of the molecular motor: on the left hand side a sub unit of the pili is added which elongates the pili, whereas it can be destroyed when the pili retracts. Source:[27]

point of view it their ability to exert high forces up to $100\,\mathrm{pN}$ for a single pilus which are enormous given the $\mu\mathrm{m}$ size of bacteria. Even more they can bundle and exert nN forces. In [26] pili have been modelized at the molecular level as an ensemble of small motor moving an helical filaments, they obtain data agreeing with biological data such as the force-velocity relations and parameter dependence for the stall force (maximum force the molecular motor can work, over this value it is blocked)

3.2.1.2 The capsule

The aggregation of *Neisseria gonorrhea* bacteria, which is also presenting T4P has been studied by biophysicists [41] by mean of experimental methods but also by the elaboration of theoretical model, for instance in [54]. However there is an essential difference between these two bacteria, which is that *Neisseria Meningitidis* is composed of a hard capsule. This capsule is an essential difference because for bacteria like *Neisseria Gonorrhea* lacking one, they are very sticky. In other words for *Neisseria Gonorrhea*, at close range the predominant interaction isn't mediated by pili but by these adhesion forces. The evidence are obvious when observing the aggregates, *Gonorrhea* aggregates are not "liquid" but exhibit very dense, static structures. They also show similar properties such as aggregation but the timescales involved differ highly, when for *Meningitidis* the timescales involved are a question of minutes or even seconds, for *Gonorrhea* it is about hours.

3.2.1.3 Aggregation properties: mutants

One of the key that led us to a better understanding of the bacteria was the production of mutants of the original "Wild-Type" bacteria. These mutants are interesting because the level of control reached is important: most of them have only one property that differs from the original bacteria. Nevertheless the aggregative properties are significantly affected for some of these mutants. The fact that we can notice significant change over small

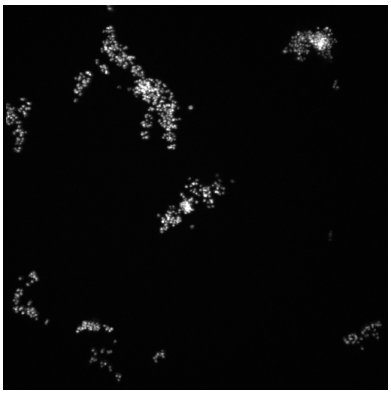

(a) The PilT aggregates lack roundness and show structural disorder

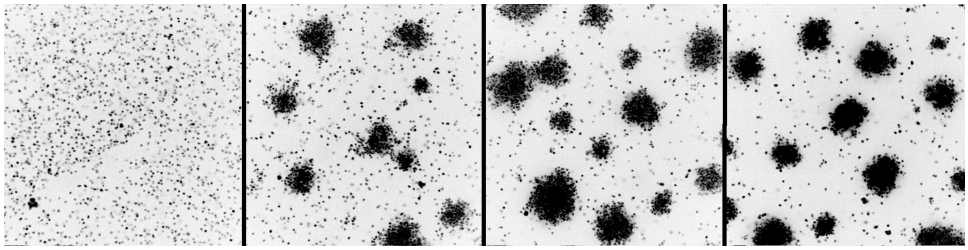

(b) The $PilF_{ind}$ mutant with increasing IPTG from left to right

FIGURE 3.10: Genetically modified mutants alter drastically the aggregates shape and size. Source: G. Duménil's group

changes on the bacteria properties is essential to pinpoint what is the function of each biological "component".

SiaD SiaD is the mutant lacking a capsule. As we can expect aggregates are closer to *Gonorrhea* ones. What appears is that there are still aggregates but they are a lot more "viscous" and more static. The measured viscosity is $\approx \times 6$ higher than the WT one.

PilT The PilT mutant is probably the more intriguing mutant: it lacks the ability to depolymerize the pili and is thus condemned to generate lots and lots of them. It is expected that, lacking retraction, there is no possibility to have liquid aggregates. But it is less expected that from the mechanical point of view it appears that there are still aggregates which are very solid-like, lacking roundness as one could expect from a liquid. What's more their structure is reminiscent of fractal and consequently of the DLA model (section 3.1.2.2).

$PilF_{ind}$ The $PilF_{ind}$ was also very useful to confirm that pili retraction was essential to generate the liquid properties of *Neisseria* aggregates. We can control the pili production capability of this mutant using a molecule named IPTG. Decreasing the concentration of this chemical reactant, the number of pili is decreased. The essential result visible in figure 3.10(b)

being that when the concentration drops below a threshold ($\leq 10\,\mu\text{mol}\,\text{l}^{-1}$, extreme-left panel), meaning that the average number of pili is low, this aggregative capability disappears and on the contrary aggregates are bigger with increasing IPTG concentration.

3.2.2 Mutants cell-sort

In [41], the authors mix engineered strains which are similar to PilF_{ind} with more "strong" ones. We mix these strains, they naturally "cell-sort", meaning in the physicist vocabulary that they phase-separate: cells of the same strain group altogether as can be seen in figure 3.11 where two different strains which are colored differently. The more piliated strain (red) goes in the center while the less piliated one (green) forms the outer shell. The authors propose that the mechanism arising to this cell sorting is a consequence of the tug of war [30] at stake here: given that pili properties differ between the bacteria among the strain possessing the strongest force will win the game more frequently, therefore the weak strain is disadvantaged when mixed with the strong one. This is another proof that the pili mechanical forces generation are a key factor in the aggregates properties.

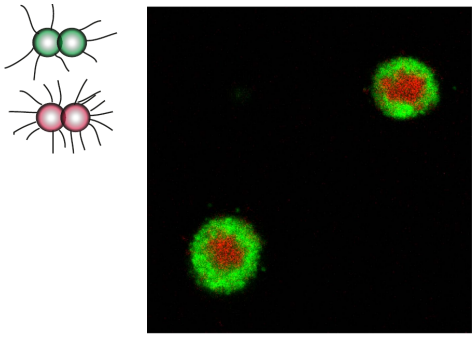

FIGURE 3.11: Two different strains cell sorting, the green colored are less piliated and form the outer shell (from [41])

We report a similar mechanism when mixing strains of WT and PilF_{ind}.

3.3 Goals of this Chapter

The modelization we will discuss in further sections was first and foremost built in order to reproduce the features of the biological system. As such the path we will follow is mostly historical and reflects how the model was improved in order to be more and more accurate.

Chronologically, the starting point of all this model was the aggregation experimentOn which we built a model which would first of all aggregate solely based on a mechanism of intermittent attractive force. Later on we eventually conjectured some features of the model like the unusual (non monotonous) behavior of the aggregation rate in 3.5.6.2 not confirmed yet and the peak of diffusion in 3.6.1.1 which was indeed observed later on. In order to do so we built a minimal model, keeping only essential ingredients, in a similar spirit to 2. Sections 3.4 and 3.5 will address the first

modelization: we will discuss this model which allows to obtain solid, liquid and gas when varying appropriate control parameters related to the pili dynamics and the system "effective" temperature. As a starting point we will study the effect of an intermittent force on the two-particles dynamics in section 3.4.1 which already show how by tuning the attraction time of an intermittent force, particles will more or less separate. In section 3.6 we will see how an essential feature of the system, the force-velocity work-mode of the pili, affects the system dynamics. Finally in the last section 3.7 we will perform comparison with the experimental results of Duménil's team.

3.4 First model(s): particle based interactions

In this first part we address how we were able to modelize *Neisseria meningitidis* pili with the simplest approach possible.

Pili are embedded as an additional *degree of freedom or scalar variable* on the the particle (the bacteria) themselves which evolution is stochastic. This degree of freedom is very simple to understand, a particle has two states, either it will be **ON** or it can be **OFF**. The new variable is acting on the particles dynamics via a pair potential which is not only a function of the respective positions of the particles but also on both of the state this variable.

Most of the time, models targeting the dynamics of the bacterial world get rid of any acceleration term. This overdamped hypothesis is quite common in µm sized systems. Indeed if we consider the mass m and the viscosityη of the surrounding fluid we can define a characteristic timescale T of acceleration $T \approx \sqrt{\frac{m}{\eta}} \approx \sqrt{\frac{\rho r^3}{\eta}} \approx 10^{-7.5}\,\mathrm{s}$, this timescale is way smaller than any observed timescale we are looking to, consequently the acceleration regime is unobservable and all forces are instantaneously balanced.

Another way to see this damping is to look at the Reynolds number $\mathcal{R}$: we humans of length $1\,\mathrm{m}$ move at $\approx 1\,\mathrm{m\,s^{-1}}$ in the air of viscosity $\eta \approx 20\,\mu\mathrm{Pa\,s}$, our Reynolds is thus: $\mathcal{R} \approx 5 \times 10^{+4}$ whereas bacteria are $1\,\mu\mathrm{m}$ long , have speeds $\approx 1\,\mu\mathrm{m\,s^{-1}}$ and are mostly in water which viscosity is $\eta = 1 \times 10^{-3}\,\mathrm{Pa\,s}$ which give $\mathcal{R} \approx 10^{-3}$. That's a huge change and we have to keep that in mind to understand that bacteria don't swim in water as we'd do. Therefore the equation of the dynamics for continuous time is the overdamped Langevin equation we recall here (3.7):

$$\frac{d\vec{r}_i}{dt} = \frac{1}{\gamma}\sum_{j\in\partial i}\vec{F}_{ij} + \sqrt{4D}\vec{\eta} \tag{3.7}$$

where

- "∂i" are the voronoï neighbors of bacteria i
- η is a uncorrelated Gaussian noise with 0 mean and unit variance: $<\eta(t)\eta(t')>=\delta(t-t')$
- D is the diffusion coefficient
- $\vec{F}_{ij}$ is the force between neighbors: it is yet to be determined.
- γ is the friction coefficient of the liquid, in the following we get rid of it from now one by setting it to 1 (via a change of unit).

As we are dealing with stochastic differential equations it is very important take care of how we deal with the stochastic terms such as the noise. Thus for discrete timesteps Δt the equations of the dynamics become (3.8):

$$\vec{r}_i(t+\Delta t) - \vec{r}_i(t) = \sum_{j\in\partial i}\vec{F}_{ij}\Delta t + \sqrt{4D}\vec{\eta}\times\sqrt{\Delta t} \tag{3.8}$$

Indeed we have to make sure the noise scales correctly and thus the $\sqrt{\Delta t}$ term in front of the noise was chosen according to the classical Euler–Maruyama method of integration for stochastic differential equations.

This integration doesn't take into account of the stochastic nature of the force as we will see, but it's not a problem because the timescale over which the randomness of the force arise are by construction larger than Δt Now what makes this model unique is the nature of the force force between particle i and j, this force depends on the internal variable s_i and s_j , for now. . The force is composed of two parts as shown in figure 3.12. We chose a simple form for the force. It is repulsive at short range ($r \leq d_0$) and attractive at longer range ($r \geq d_0$).

$$\vec{F_{ij}}(r) = \alpha \left(e^{-r}\left(1/r + 1/r^2\right) - \beta/r^2\right)\vec{u_r}$$

The only important consideration is to assume the attractive part of the force (for $r \geq d_0$) depends on s_j and s_j and is canceled (set to 0) if $s_i = 0 || s_j = 0$.

We see that we have a permanent short range repulsive component and a longer range attractive part which is only present when the interaction is ON. This definition allows us to avoid discontinuities at d_0 which could lead to numerical instabilities (if we'd define energy there could be a constant energy drift as noted in [4]). This force is "derived" from the potential (not strictly speaking because the force is defined by part) $V(r)$ (see figure 3.13):

$$V(r) = -\alpha\left(\frac{e^{-r}}{r} + \frac{\beta}{r}\right), r \in]0, l_p]$$

Because we wanted to introduce a sharp repulsive potential at short range and an attractive part at longer range (up to l_p).

Where we have defined the following parameterization:

- r is the distance between bacteria's centers.
- $\vec{u_r}$ is the unit vector pointing from particle j towards particle i.
- The characteristic length d_0 corresponds approximately to the value where the repulsive part would cancel if it wasn't defined by part. This is simply the diameter of the cell. More precisely it is the center to center length when particles are closely packed, as bacteria are spherically shaped for now (the repulsive potential is isotropic) this is equivalent.
- l_p correspond to the maximal bacteria to bacteria center distance, therefore it is **twice** the pili length (because pili can eventually catch up at their tip) + the diameter of the cell d_0 (because the distance is defined center to center)
- The intermittent attraction correspond to both particles being **ON** (case $s_i = s_j = 1$)
- α and β are just regulating the potential shape

When the attractive part is turned **ON** we can see that this interaction correspond to a force which stable equilibrium point is located at d_0

It is tempting to condensate the previous formula introducing the product $s_i \cdot s_j$, in the earlier stages of the modelization this was the case, unfortunately it is non-physical: indeed when both parts of the force where present we had the same force, however when only the repulsive part is present (*i.e* one of the particle was **OFF**) we are confronted to a long range repulsive part $\propto e^{-r}/r$) which is an undesired phenomenon and leads to other effects.

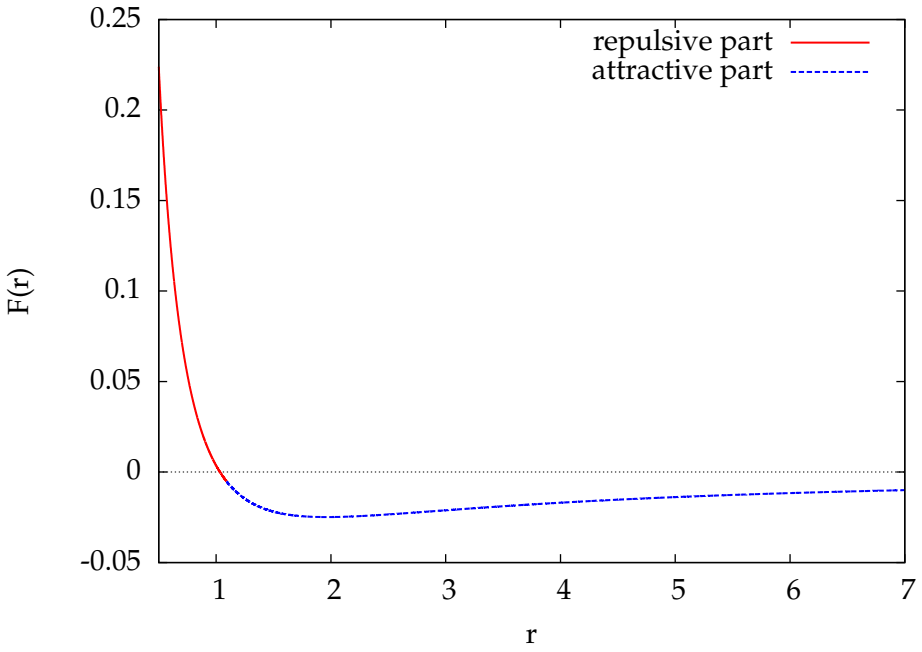

FIGURE 3.12: The force F_{ij}:
the repulsive part (solid line) is permanent while the attractive part (dashed line) is intermittent

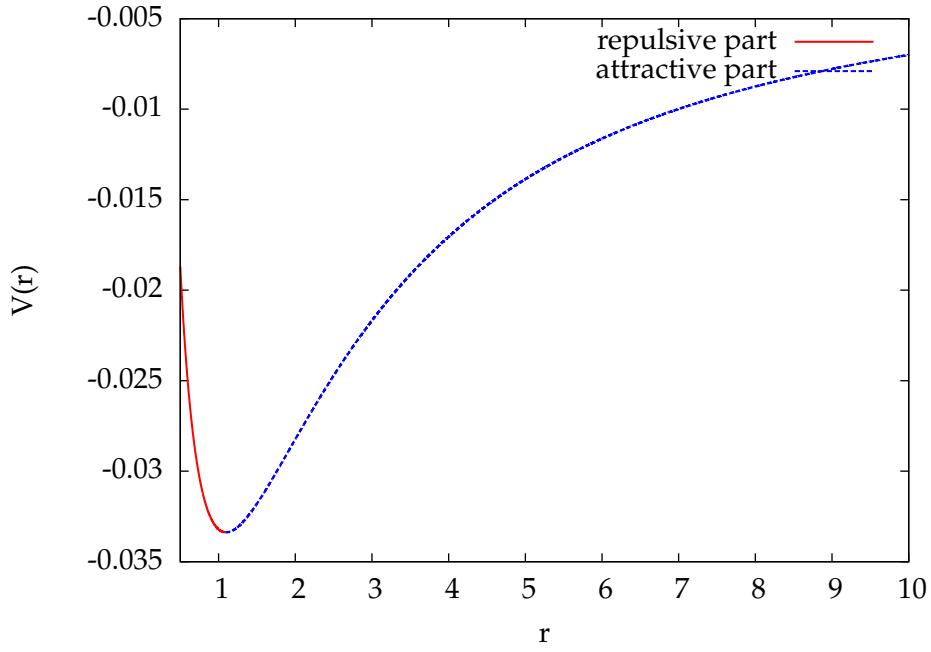

FIGURE 3.13: The corresponding potential

Our model still lacks an ingredient, that is the dynamics of the $s_i(t)$, we are using a stochastic model (3.21) where

$$\begin{aligned} P(s_i = 0 \to s_i = 1) &= dt/\tau_{OFF} \\ P(s_i = 1 \to s_i = 0) &= dt/\tau_{ON} \end{aligned} \tag{3.9}$$

Thus the variable s_i are constantly switching from values 1 to 0 with the transitions probabilities given above. What's more the characteristic time spent in each states are given by τ_{OFF} for the $s_i = 0$ state and τ_{ON} for the state $s_i = 1$.

3.4.1 Stochasticity of the potential and two particles dynamics

Before going to the "collective" level, exploring the consequences of this stochastic process at the particles level could prove interesting to see what happens when we vary the two characteristic timescales τ_{ON} and τ_{OFF}.

We generate a pair of particle whose initial configuration is as follow:

$$\begin{aligned} \vec{r_0}(t = 0) &= (0, 0) \\ \vec{r_1}(t = 0) &= (0, 0.99\, l_p) \end{aligned}$$

This choice of configuration is dictated by the need to allow a little bias in favor of attachment as we want to study the dynamics of attachment, meaning we need the two particles to be interacting with each other even

from the start, thus it requires them to be in the attractive range $r \leq l_p$. In other words if the initial configuration distance is $\geq l_p$ the interaction will be only diffusive until they catch each other, which is very unlikely. With this initial configuration, as they are at the limit of the interacting range, we can guess that the probability that the particles escape the potential is roughly a $\frac{1}{2}$, simply because the diffusion process is symmetric whether they hop to get closer whether they hop to escape from each other.

We then measured their relative distance $||\vec{r_0} - \vec{r_1}||$ over time, averaged over a large number of runs (ranging from 1000 up to 10000). The fact is that the equation of motions are not analytically derivable because of the telegraphic attractive part. We recall that for the real world system we expect the pili to pull so strongly that at some point it's balanced with the friction force (the Stokes force) from the surrounding fluid, i.e:

$$\begin{aligned} & m\frac{\mathrm{d}\vec{v}}{\mathrm{d}t} = \vec{0} \\ \iff & = \vec{F_p} + 6\pi\eta\rho r\vec{v} \\ \implies & ||\vec{F_p}|| = 6\pi\eta\rho r||\vec{v}|| \end{aligned} \tag{3.10}$$

Relation (3.10) can give us a good estimate of the force in our units.

We've played with the noise diffusion coefficient D with permanent attraction as well as the transition times τ_{ON} and τ_{OFF} for a fixed noise. l_p is set to 3 so as the separation distance ($0.99l_p$). What we can essentially keep remind from this experiment is the fact that the ON/OFF dynamics plays a similar role than the noise does at equilibrium: it counteracts on the attraction force but still we reach some equilibrium, or at least a stationary state for small noises and small τ_{OFF}.

On the contrary, we see that imposing high noises or high τ_{OFF} will lead to the particles having the same faith: while for short times the inter-distance decays (no shown: for even higher noise or τ_{OFF} the decay phase is not even visible), ultimately the inter-distance increases and overpass l_p meaning that most replica experiments led to separation of the two particles.

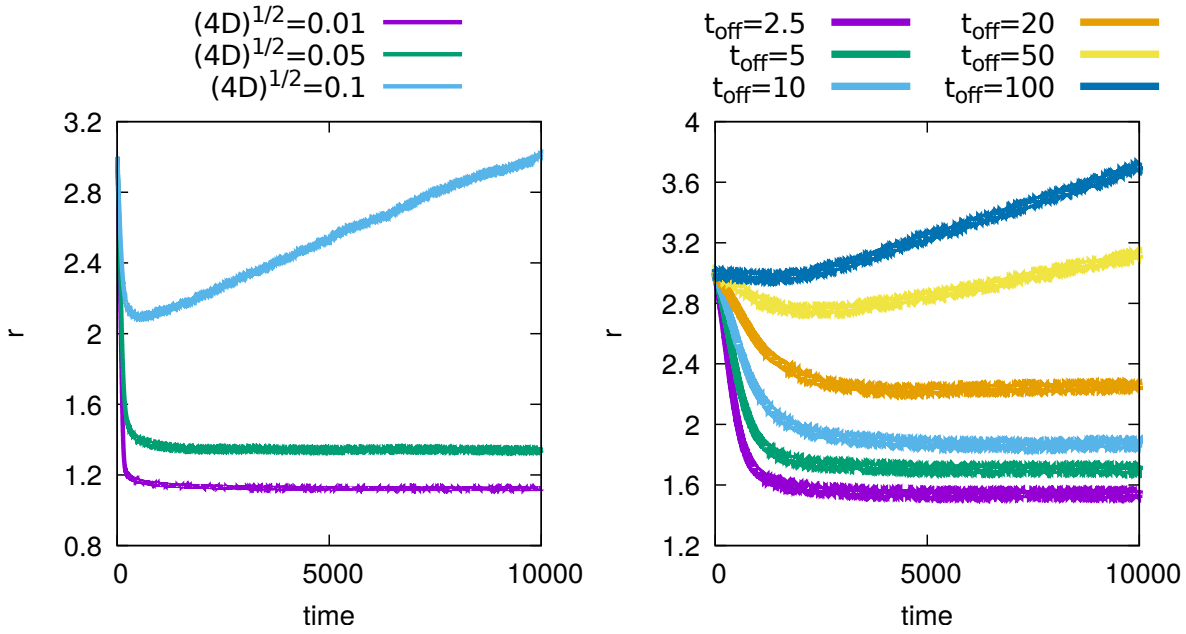

(a) Averaged inter-distance changing the noise diffusion coefficient D *with permanent attraction.*

(b) Averaged inter-distance changing τ_{OFF} ($4D = 0.03$ and $\tau_{OFF} = 5$)

FIGURE 3.14: The noise and the ON/OFF dynamics have similar effects on the ensemble averaged inter-distance

3.4.2 The Voronoi tessellation

How can we define the neighborhood of a point taking into account the fact that particles are very likely to screen what is behind them? The Voronoi tessellation is the neighborhood definition that accounts for this possibility. On the other way it is now common to modelize dense assemblies of cell approximating their area as the Voronoi tessellation of their barycenters (a cell is a point and occupies the space let by the Voronoi tessellation of all its neighbors), as in [7], using such assumption they discover a jamming transition in these dense assemblies of cells.

The Voronoi tessellation of an ensemble of points $1, 2, .., i, ..$ is a paving of space where each pavement $\mathbf{S}_i$ can be associated to a point i and its surface is the ensemble of points which are closest from point i than any other point $j \neq i$. As a consequence the boundary of each pavement are defined by the intersection of all the mediating line between neighbors points. This naturally tends to define the notion of neighborhood: considering a point i all its neighbors points ∂i are sharing a mediating line, or boundary, with it. One can then recursively define level of neighborhood, neighbors of neighbors can be considered as neighbors and so on. However we restrict ourselves to the first definition.

Related to the notion of neighbors, there is another useful mapping: we can draw a graph composed of the ensemble of segment that link each point i to its neighbors ∂i , this graph is called the Delaunay tree. It is actually what we use to represent the pili because we ascertain that pili are very much likely to link neighbors in the Voronoi sense when they are created which means in other word that we assumes that the neighbors are "hiding" what's behind them.

There are other kind of neighborhoods and we can define *metric* ones which are purely based on distance considerations, all particles within range are neighbors, without consideration about hiding what's behind oneself, for theoretical reasons it might be easier to consider such neighborhood. However considering that pili are not "A potential" but physical entities which have to reach their target to be able to pull it seems unreasonable to consider metric neighbors. The Delaunay tessellation provides the most natural way to define which neighbors are available to create pili with the relevant biological property.

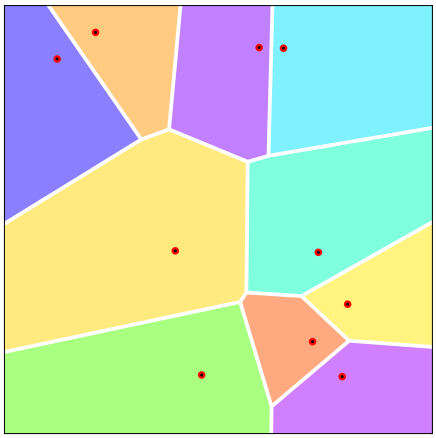

(a) A Voronoi pavement, the points are in red and their respectives cells are colored: this allows to differentiate different adjacent pavement, source wikpedia.org

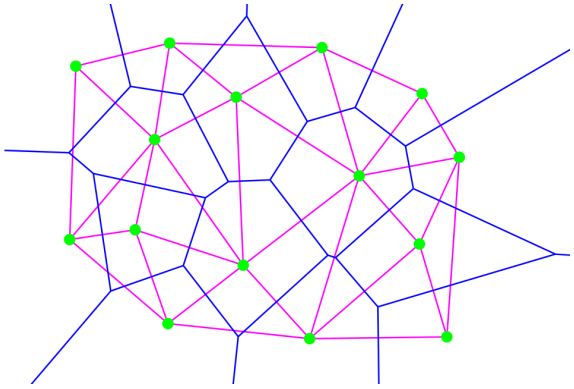

(b) A set of points (green), their Delaunay tessellation (blue) and the Delaunay graph linking neighbors in purple, source http://liris.cnrs.fr/david.coeurjolly

FIGURE 3.15: The Voronoi pavement and the Delaunay tessellation are "dual", they allow interesting modelizations of the notion of neighborhood.

3.4.3 Relevant quantities

3.4.3.1 Diffusion

The erratic movement of pollen particles were first observed by Robert Brown in 1827. Almost a century latter the particles undergoing what is now known as Brownian motion have been described by Albert Einstein in his paper [15]. Thanks to Einstein's work we know that the correct law (3.11) in order to describe the displacement of a series of particle in a fluid describe a linear evolution with time of the variance of the displacements of the particles $< x^2(t) >$ which is linked to their radius r, and the environment which is itself described by the viscosity of the fluid η , the temperature T and the Boltzmann constant k_B :

$$< \Delta x^2(t) >= 2dDt \tag{3.11}$$

where the relation between D and the other parameters of the system is given by the Stokes-Einstein relation (3.12)

$$D = \frac{k_B T}{6\pi\eta r} \tag{3.12}$$

Relation (3.11) imposes to correctly define the variance of the displacement $< \Delta x(t)^2 >$. The usual definition is to choose an ensemble average, thus if the system is composed of n particles, we have

$$< \Delta x(t)^2 >= \frac{1}{n}\sum_{i=1}^{n} x_i(t) - x_i(0) \tag{3.13}$$

For an ensemble of purely diffusing particles this should converge to the diffusive scaling (3.11) for a sufficient number of points n. However in real life our ensemble of particles is not arbitrarily large. We can circumvent this problem by using the sliding average defined as:

$$< \Delta x(t)^2 >= \frac{1}{n}\sum_{i=1}^{n} \frac{1}{N_t}\sum_{t'} x_i(t'+t) - x_i(t') \tag{3.14}$$

Where $N_{\delta t}$ is the number of trajectories of the system where both $x_i(t'+t)$ and $x_i(t)$ are defined [4].

Equation (3.14) is based on the hypothesis that the diffusion process is invariant by translation over time, hence all trajectory starting at time $t' \neq t''$ can be considered independent.

[4] Assuming the sampling duration is $t_{\max}$, we have $N_t = \frac{t_{\max}-t}{dt}$ for discrete time sampling.

3.4.3.2 Effect(s) of noise truncation

The noise term in equation (3.8) can be the source of numerical instabilities, especially when particles are very close to each other, because usually there's no boundary on the values of the displacement step Δx the particles can experience from time to time big jumps essentially given by the tails of the probability density function of the noise. We've had a rather peculiar (in the sense we've never seen this in the context of physics) procedure to remove the possibility to have excessively long jumps exceeding a threshold value $\Delta x \geq \Delta x_{th}$. Numerically we've implemented the noise ξ as an output generated by a Gaussian distribution of variance $2D$: $P(\xi = x) = \exp(\frac{-x^2}{2\sigma^2})$, additionally we're cutting-out values exceeding a threshold value, typically $||\xi|| > 2 \times \sigma$, that means when the random variable exceed this threshold it is ruled-out and redrawn. This allows obtain a distribution without "tails", that is the values we don't want to consider, and without consideration about the kind of distribution. In figure 3.17 are presented the distribution with and without the truncation at 2σ. As we can see, over the range of considered values this procedure is conserving the the shape of the distribution. Aside from the formal definition, globally this modification is barely affecting the diffusive properties, indeed the coefficient D is modified without affecting the diffusive aspect ($< (x(t) - x(0))^2 >$ still scales $\propto t$) as we can see in 3.18 where we show the MSD for a system of independent and freely diffusing points ($N = 10000, \Delta t = 1, 2\sigma = 0.03$).

What's more we've performed measurements of the diffusion coefficient $D(\sigma)$ and obtained the following relation $D(\sigma) \approx 0.77\sigma^2$ as we can see in figure 3.16

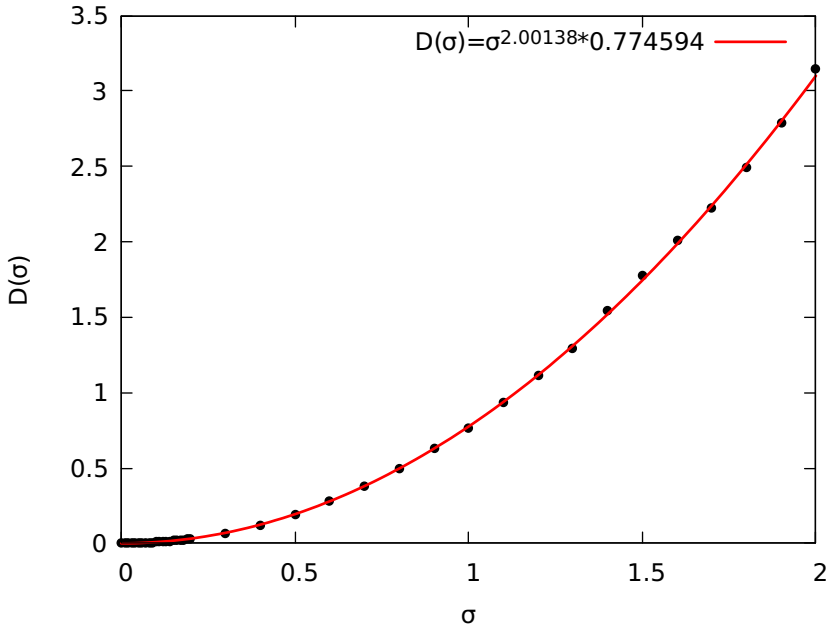

FIGURE 3.16: Data points and fit for the diffusion coefficient as a function of the standard deviation

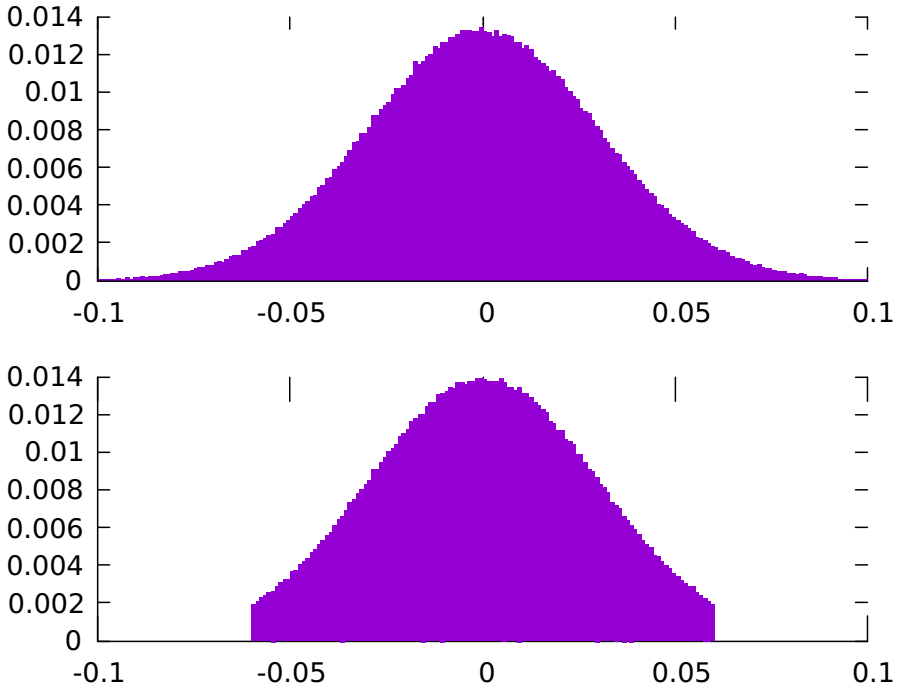

FIGURE 3.17: The distribution function of the noise, on top without truncation, below with the truncation at $2\sigma = 0.06$

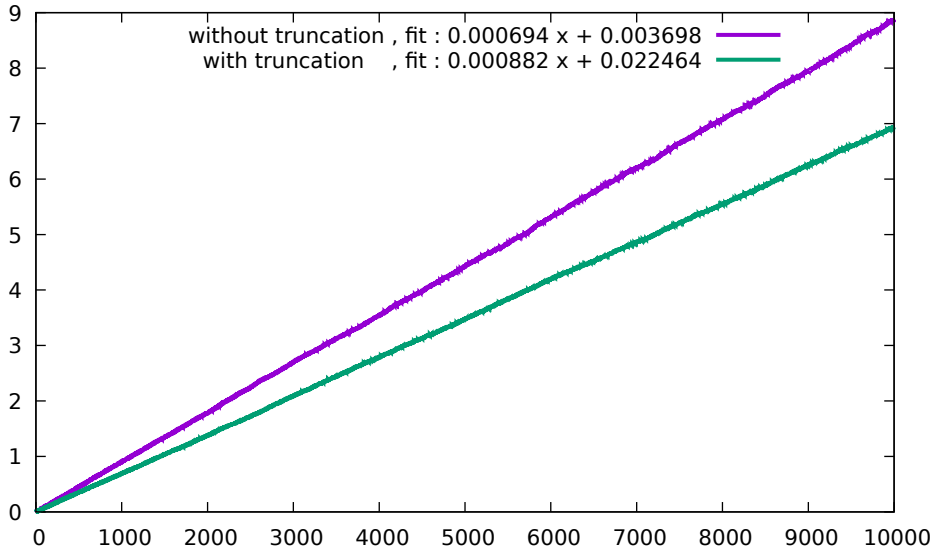

FIGURE 3.18: MSD for free non interaction particles, comparing the effect of the truncation on the diffusive behavior: the effective diffusion coefficient D shifts from 0.00086 to ≈ 0.0007 because of the truncated noise but everything still scales linearly with time

3.4.3.3 Gyration radius

Another relevant quantity to quantify a cohesive aggregate is the radius of gyration. Considering n points particle, it is simply defined as the mean of the squared distance from their barycenter r_c , formally written it reads

(3.16):

$$R_g^2(t) = \frac{1}{n}\sum_{i=1}^{n}(r_i(t) - < r_i(t) >)^2 \tag{3.15}$$

thus we obtain

$$R_g(t) = \sqrt{\frac{1}{n}\sum_{i=1}^{n}(r_i(t) - < r_i(t) >)^2} \tag{3.16}$$

and

$$r_c = \sum_{i=1}^{n} r_i(t)$$

Actually we will see that it is better to consider the squared gyration radius (3.15) because in the gas phase it scales linearly with time similarly to the MSD.

3.5 First measurements

Now that the model is defined we start with some exploration of the features that this model provides. We will see that starting from a solid state at low noise we can tune the parameters to range from solid to gas.

For this part the numerical value were the numerical values were set according to table 3.1:

coefficient	value
α	0.1
β	0.7
d_0	1.09
l_p	7
$4D$	0.03

TABLE 3.1: Values used in section 3.5

Here an afterwards we will start initially most of the time by an initial configuration of N particles on a square box of size of size $L \times L$. Contrarily to the Vicsek model the particles in this model evolve in free space meaning that the initial concentration of particles tends to evolve depending on the cohesive nature of the system:

- If the system is aggregative, in any case the concentration of the aggregates is not fixed by the initial configuration but by the aggregates properties
- If the system is not aggregative it will permanently expand and the speed of expansion is an interesting piece of information which would be limited by finite size effects if we'd work with fixed boundaries

What's more working with free boundary conditions is justified from the computational point of view: the cost to work with periodic Voronoi tessellation is multiplied by 9, which is the number of copies of the system required to have a periodic Delaunay graph. Another possibility that only slightly increase the computational cost is to would be to work with non-periodic but still fixed boundary conditions by imposing a stiff repulsive potentials at the limit of the domain. However this hard core wall would imply finite size effects on the gyration radius which allow us to accurately delimit the liquid-gas transition.

3.5.0.1 Permanent attraction, tuning the noise

The first observations we've proceeded with, which are probably classical results for people familiar with molecular dynamics of fluids but nonetheless essential to understand what is the interplay between noise and attraction. We started by performing a slow heating of the system by gradually increasing the "temperature" of the Brownian particles, that is the variance of the noise σ, keeping the attractive force permanent (corresponding to the parameters $\tau_{ON} \to \infty, \tau_{OFF} = \Delta t$). To try to determine precisely the phases transitions the procedure adopted is to progressively heating the aggregate with a series of "temperatures" $(\sigma_1, \sigma_2, \sigma_3, .., \sigma_i)$ chaining the simulations, that is taking as initial condition for temperature σ_{i+1} the final state of simulation done as σ_i. The simulations have been performed for $t = 10^5$ numerical time with a time-step $\Delta t = 0.1$.

First we will start with purely qualitative observations. For moderate size aggregates ($N = 100$) we can see compact solid aggregates for $\sigma \in [0 : 0.04]$, these aggregates lack a circular shape. For $\sigma \geq 0.05$ we start to see the liquid character of the aggregates. Indeed we can see local rearrangements of particles from time to time, meaning that contrary to the solid where particles positions fluctuates around an average, in the liquid particles are able to hop stochastically on long distances. These aggregates are more round and we notice that the rearrangements are more frequent on the boundaries rather than in the center, for $\sigma \geq 0.17$ the aggregates start to loose their roundness. Finally for $\sigma \geq 0.3$ there's no more cohesive state and we are in the gas phase where particles freely diffuse. This is means that the temperature is high enough to overcome the attractive barrier created by the potential. We've summarized the following in figure 3.19 where we don't show values $\sigma \geq 0.2$ because in the gas phase we barely see the particles.

As a side-note, we can't help but notice that the particles are overlapping, the problem has a physical explanation: given that the potential we use is relatively soft and, if the translational energy contained in the Brownian motion, which is given by the equipartition theorem $\frac{3}{2}k_BT$ overcomes V_0, the width, of the potential then the particle might overcome the repulsive barrier even though it's marginal (meaning that the interpenetration distance of the disks is not that high). This phenomenon is of course increased when the noise increases and is unavoidable, regardless of the algorithm used. We can however in that case define an *effective* radius of the particles r_{eff} given by $V(r_{eff}) = \frac{3}{2}k_BT$

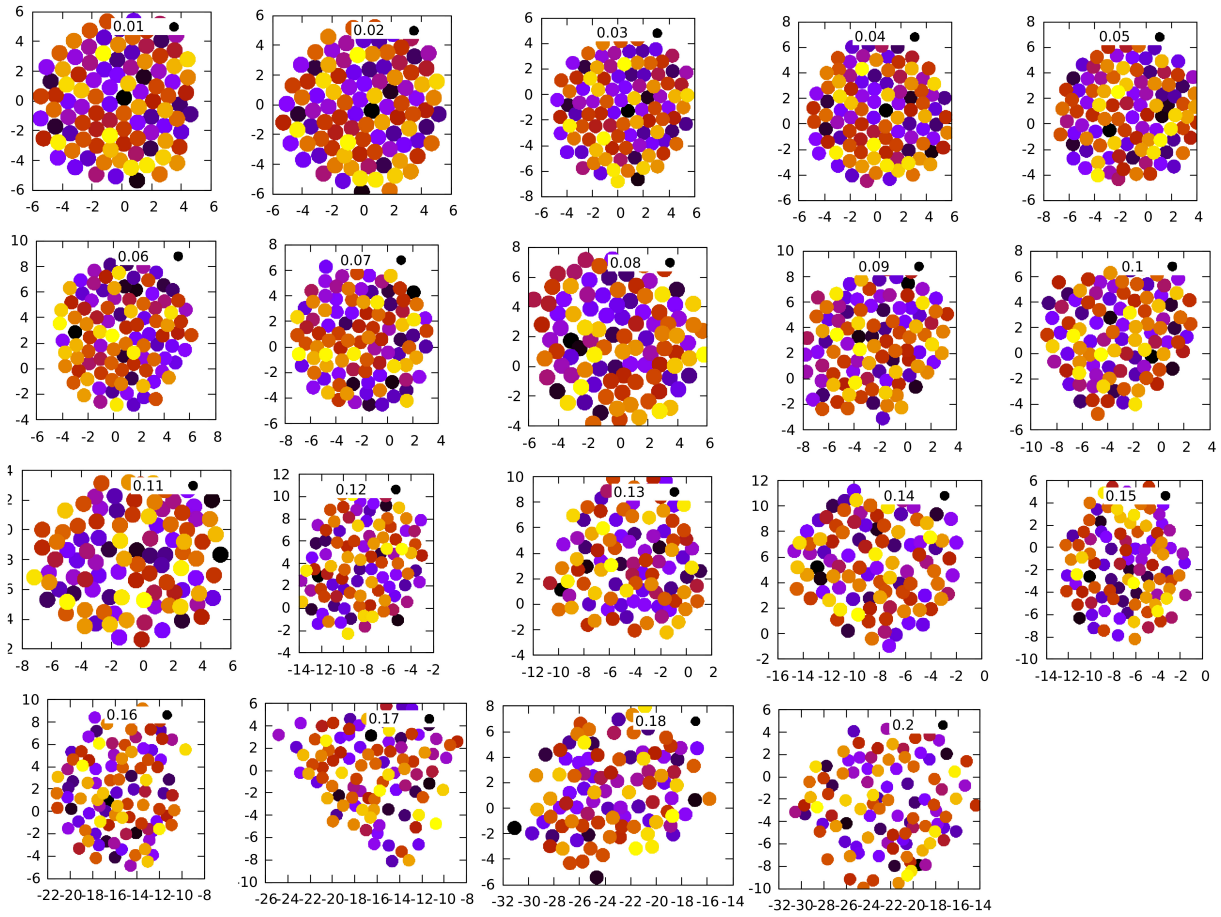

FIGURE 3.19: Snapshots of the aggregate obtained for purely attractive potential with increasing temperature, to be read from left to right and top to bottom (σ is indicated on top of each snapshot)

An obvious solution is to opt for an hard spheres model, meaning that we have an infinite energy barrier $V(r \leq r_0) = \infty$. This can be performed as an exercise, algorithmically this means that there are "specular reflection" of particles and for this we just need a simple collision detection algorithm. However as we're mostly interested in the cohesive phases where collision are likely to occur *very* frequently, making the computational cost prohibitive.

Still being qualitative, we can use the Voronoi tessellation to have an idea of the free space left for particles to move. We can interpret the Voronoi cell as the cage the particle are able to move into. Typically in the solid or glassy phase there is little to no space, hence the impossibility for particles to hop and the fact that just oscillate around their average position, in the liquid phase the space left is sufficient for the hoping to occur. We've plotted such tessellation in 3.20 , obviously in the low noise regime the particles are very constrained whereas in the liquid regime many particles have a very large cage compared to their surface.

It's time to move to more quantitative measurements: we've previously defined in 3.4.3 two quantities in order to characterize the solid-liquid and liquid-gas transition. In 3.21 we see the evolution curve of the gyration

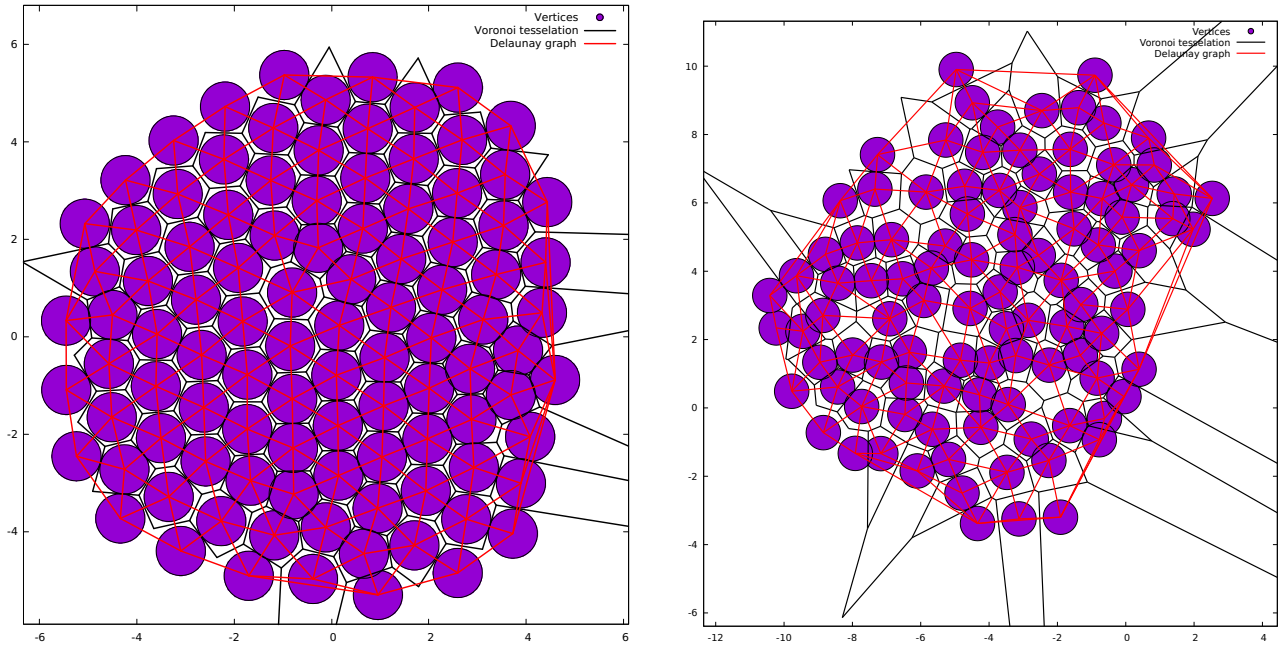

(a) In the solid regime ($\sigma = 0.01$)

(b) In the liquid regime ($\sigma = 0.13$)

FIGURE 3.20: Voronoi tessellation and Delaunay graph of aggregates in the solid and liquid state. The delaunay edges are drawn in red while the voronoi cells boundaries are in black. One can see the disks fills the Delaunay cell surface in the former case while there is empty space in the latter case.

radius for the process of thermalization by increasing σ. This confirms our previous observation, the gyration radius is fluctuating around a mean value for $\sigma \leq 0.2$. For $\sigma \leq 0.13$ the gyration radius is barely affected by the increase of temperature, starting from $\sigma \geq 0.13$ it grows but then at $\sigma = 0.20$ it decreases, this region is quite problematic from this point of view but it is a sign of the liquid behavior , but more importantly for $\sigma \geq 0.2$ we see a change of behavior and an the gyration radius starts to increase linearly with time, sign that this time we are in a non cohesive phase, the liquid-gas transition is therefore located at $\sigma \approx 0.2$.

We can now focus on the MSD to observe the liquid behavior. We've taken the simulation given by the thermalization procedure the previous simulations, and to avoid transient effects of the thermalization we've started to measure the MSD after a relaxation of 100000 units of time. The obtained MSD are gathered in figure 3.22 for small aggregates, however finite size effects (particles can't diffuse over a distance greater than the typical aggregate diameter) are causing measurements rather difficult, rendering the determination of a liquid-solid transition rather harsh. A rather straightforward option to improve the "quality" of the data is to correct the MSD of the effects of center of mass diffusion, observing the aggregates it is obvious that the center of mass $\vec{x}_{cdm} = \frac{1}{n}\sum_{i=1}^{n}\vec{x}_i(t)$ is itself diffusing, this affects the measured diffusion. We can just measure the MSD in this new referential which defines the corrected MSD : $< \Delta x(t)^2 >= \frac{1}{n}\sum_{i=1}^{n}(x_i(t) - x_{cdm}(t)) - (x_i(t=0) - x_{cdm}(0))$ This quantity is however not giving much improvements over our data. However it is still interesting to keep in memory these data because, from a qualitative point of view, real life aggregates behave more than our small aggregates in the regime where the boundaries are "jittery", which is less the case for bigger aggregates.

For bigger aggregates $N = 1000$, the solid-liquid transition is also found for $\sigma \geq 0.2$ but for the more interesting data are found to be concerning the MSD, these data which appear in figure 3.23 show that the diffusion coefficient is clearly jumping for $\sigma \in [0.05, 0.06]$ (in yellow and blue), for $\sigma \leq 0.05$ the particle diffuse on distances $\leq d_0$ while for $\sigma \geq 0.06$ the particles diffuse over much larger distances meaning we moved from a regime of fluctuations of position around an average position to the liquid regime which is characterized by hops enabling particles to diffuse in the whole aggregate.

Finally we summarize these data in figure 3.24 showing how both the diffusion coefficient and the gyration radius slope evolve with σ. The two transitions are characterized by a jump from zero to nonzero values of the slope, both for the MSD as well as the gyration radius. We've also included the MSD for free particle in order make the difference clearer, in aggregates there is an obvious reduction of the diffusion compared to the free case.

Figure 3.25 shows particle tracks for different σ. This qualitative view agrees relatively well with the quantitative data. We can notice that in the solid aggregates, particles near the edges are traveling larger distances because rearrangements are more probable.

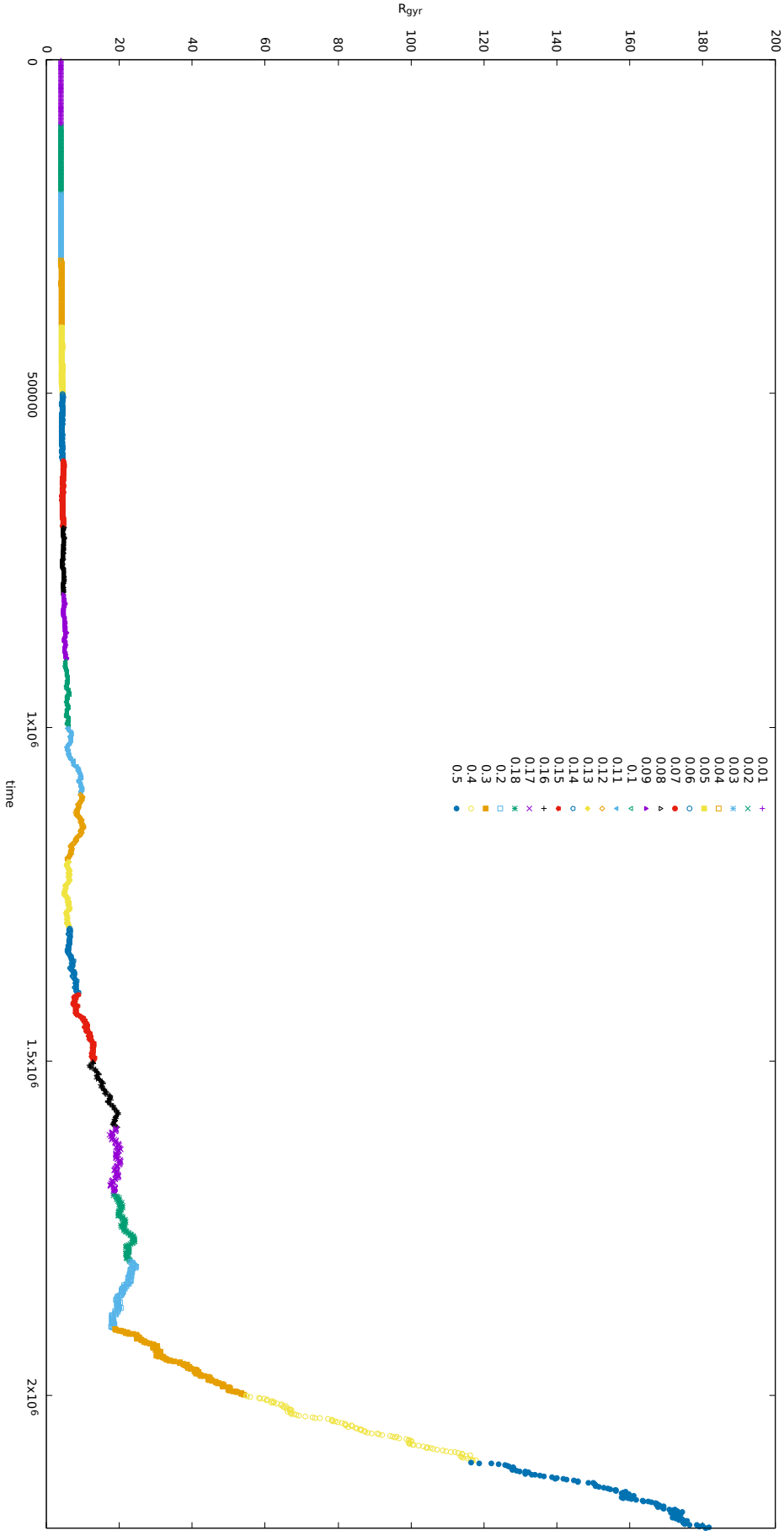

FIGURE 3.21: Evolution of the gyration radius for increasing σ

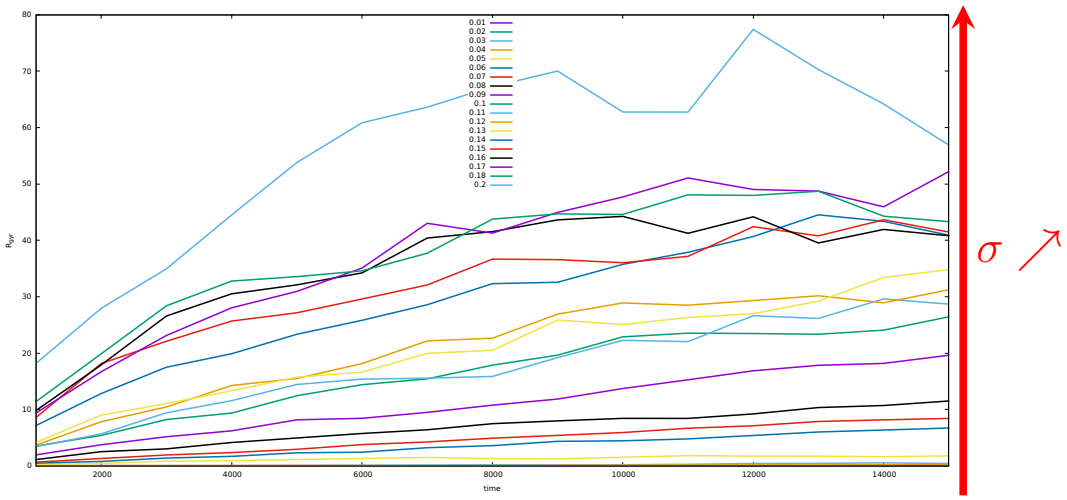

FIGURE 3.22: MSD in the solid an liquid regime for increasing σ, for small aggregates finite size effects are really strong.

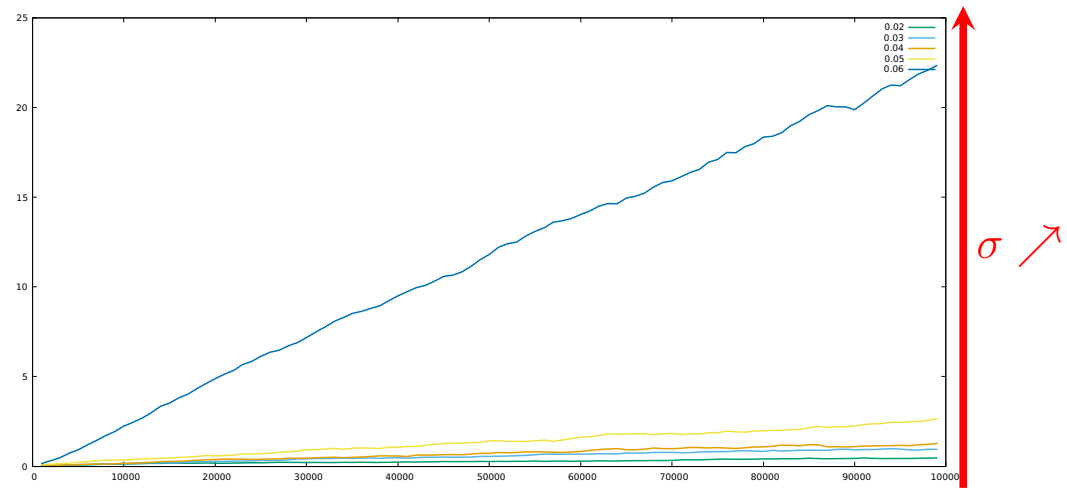

FIGURE 3.23: MSD in bigger aggregates, the finite size effects are gone and a clear jump of diffusivity is seen for $\sigma \in [0.05, 0.06]$

3.5.1 Tuning the transition times

After the previous results one can wonder why going for a stochastic potential when the previous section 3.4 shows that it is possible to obtain a liquid state which is a good candidate to represent *Neisseria Meningitidis* aggregates we were seeking for. However assuming that the dynamics comes solely from the thermal noise is unsatisfactory to some extent.

A first reason is that from the physics point of view it is still interesting to study this model because the ON/OFF switches of the attraction are themselves generating a kind of noise that is different from thermal fluctuations as we will see and we should characterize this.

A second reason is that the regime we observed previously is not *Biologically* relevant. Indeed, as we've already mentioned, the PilT mutant is the one

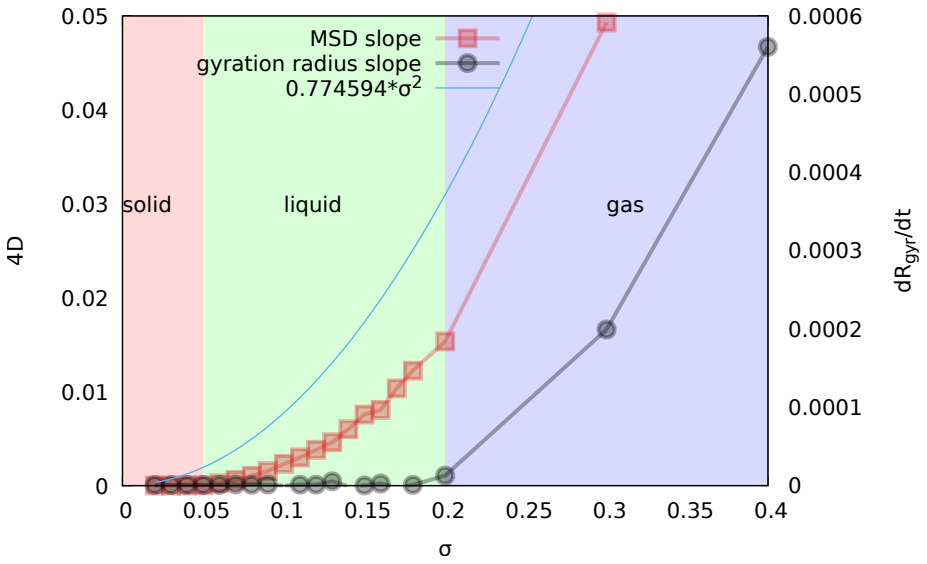

FIGURE 3.24: Summarizing plot showing the transitions

that constantly generate pili, it is therefore probably the one which is the closest approximation to the previous situation with a permanent attractive potential. This mutant is mostly solid (actually it's more like behaving like a gel), whereas non piliated mutant freely diffuses. Consequently if the ON/OFF mechanism is relevant we should be able to move from a solid state to a liquid by its sole presence and then go to a gas state (which is obviously the case when $\tau_{OFF} \to \infty, \tau_{ON} \to 0$).

3.5.1.1 Phase diagram on the (τ_{ON}, τ_{OFF}) space

We now focus on the effects of two transition times τ_{ON} and τ_{OFF} by first observing the resulting aggregates, for fixed noise $\sigma = 0.03$, low enough so that we can obtain a solid phase for $t_{OFF} \to \infty$). $\tau_{ON} = 500$ value is chosen so that *theoretically* it is sufficient for two particles at distance l_p to come close to each other

The snapshots showing the state of the system with increasing τ_{OFF} are gathered in figure 3.27. We can notice that for $\tau_{OFF} \in [1, 250]$ aggregates are very solid and keep memory of the initial generating square box, for $\tau_{OFF} \in [500, 2000]$ we're most likely in the liquid regime with less and hexatic arrangements, signs of "solidity", visible.

What's more we performed MSD and gyration radius slope systematical measurements. With respect to the previous procedure we have to note that the way we prepared the aggregate is different. For all simulations the initial condition is random particles positions in a box of size $L \times L$, relaxed for 10^6 units of time, after which we performed the measurements. These procedures might give different results about the position of the transition if there are hysteresis effects but we weren't preoccupied by this level of subtlety. Essentially the procedure is tailored for a different questioning here: for a given initial condition is the final state an aggregate or not and if so, what are its bulk properties?

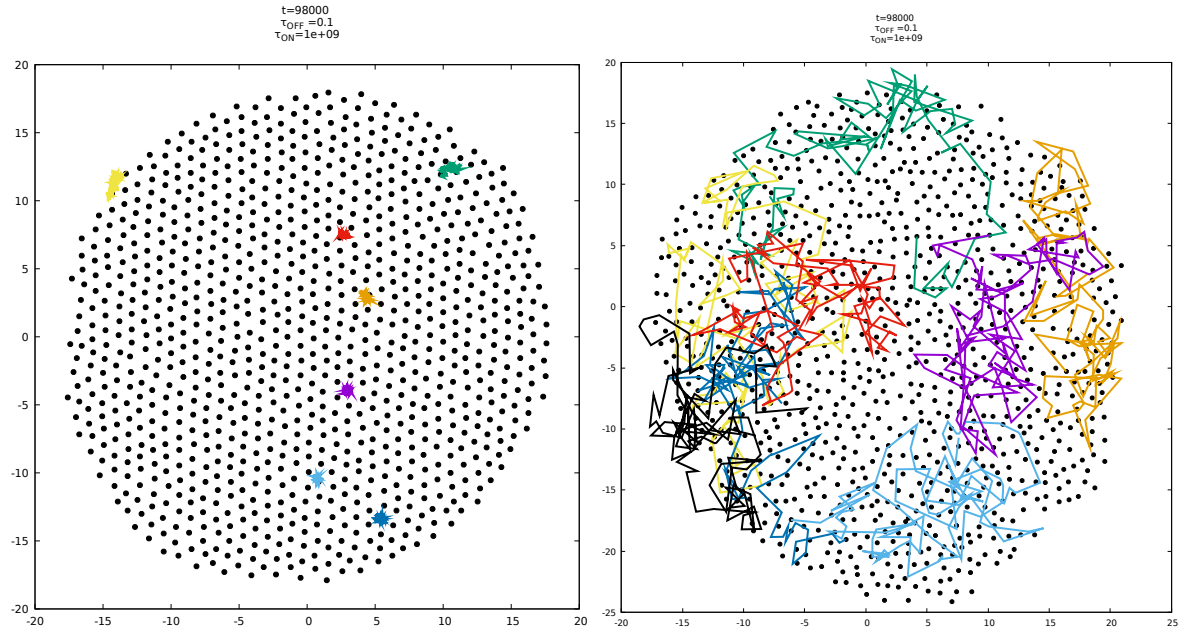

(a) Tracks in the solid regime ($\sigma = 0.04$) , particle oscillate mostly around an average position

(b) In the liquid regime ($\sigma = 0.13$) , diffusive behavior very different tracks most particles are able to explore all the aggregate

FIGURE 3.25: Tracks in the liquid and solid regime for $\approx$ 100000 time-steps

The results are gathered in the two maps 3.26 where we used by convenience the ratio of transition times $\frac{\tau_{OFF}}{\tau_{ON}}$ as a parameter, indeed we can guess that the state of the aggregate is mostly dependent of the average ratio of ON particles over OFF particles which is most likely a function of the ratio of transition times. As we can see this approximation is sufficient to describe the bulk properties of the aggregates and doesn't depend on τ_{ON} for a wide range of τ_{ON}.

Therefore we can restrict the analysis of (see figure 3.28) the MSD and gyration radius for a single $\tau_{OFF} = 500$ value. Compared to figure 3.24, we see that qualitatively the ratio $\frac{\tau_{OFF}}{\tau_{ON}}$ plays a similar role as the noise variance σ^2, with increasing ratio we explore the solid, then liquid, then gas phase. We identify the solid-liquid transition occurs at $\frac{\tau_{OFF}}{\tau_{ON}} \approx 0.2$ whereas the liquid-gas is located around $\frac{\tau_{OFF}}{\tau_{ON}} \approx 2$.

3.5.2 Micropipette experiments

We're now focusing on the modelization of the micropipette aspiration technique we've introduced in 3.1.4. The team of G. Duménil used the same experimental procedure and obtained precise measurements of aspiration velocities of several strains of *Neisseria Meningitidis* aggregates: for the PilT, WT and SiaD aggregates as well as the PilFi for which the concentration of the IPTG chemical reactant controls the number of pili. The validity of the measurements assume a liquid-like behavior, as we can see in 3.29 the

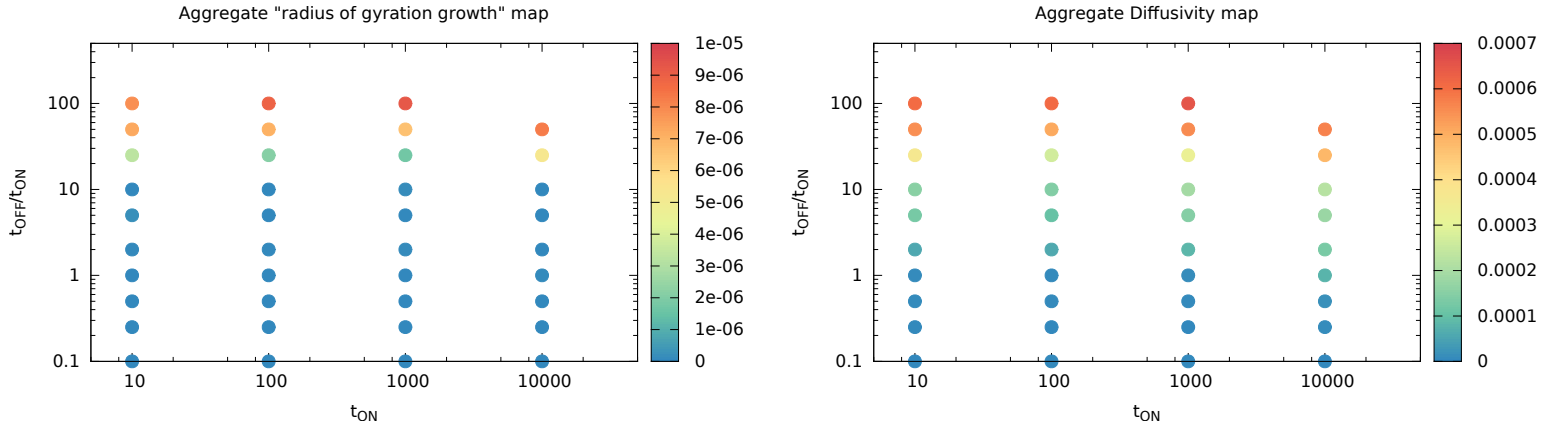

(a) The MSD in the $\tau_{ON}, \frac{\tau_{OFF}}{\tau_{ON}}$ space

(b) The MSD in the $\tau_{ON}, \frac{\tau_{OFF}}{\tau_{ON}}$ space

FIGURE 3.26: The "full" phase space of the potential based model.

tail of the drop stays perfectly spherical whereas the tongue is hemispherical which confirms this assumption (at least one can say that there's high surface tension).

3.5.2.1 Experimental results

In figure 3.30 we show the summarized values obtained via the micropipette experiment and derived with the formula of section 3.1.4. These results suggest that the viscosity is monotonously decreasing with decreasing piliation level (the average number of pili).

Considering that the ratio of transition times $\frac{\tau_{OFF}}{\tau_{ON}}$ is what determines the average number of pili in our model, this gives us a rough idea on how the piliation levels are linked to this ratio. There probably exists a relation such as piliation $= f(\frac{\tau_{ON}}{\tau_{OFF}})$

3.5.2.2 How to define an interface?

Though the qualitative comparison is interesting, more quantitative results would be interesting. We thus address the modelization of such micropipette experiment. However we're missing a detail: we have no notion of interface in the model yet and we need to define such in order to be able to evaluate pressure forces. In other words we need to locate which particles lie at the "edge" of the aggregate. This intuitive notion is not simple to define, the most and more natural definition is the **convex hull**: take a cloud of points and put an elastic around it with the points blocking the retraction of the elastic. The elastic will naturally form an envelope formed of segments which define, inside, a convex ensemble. The ensemble of points contained in this envelope forms the convex hull: S_{conv}. However as we can see on the left-hand side of figure 3.31 depending on the "granularity"

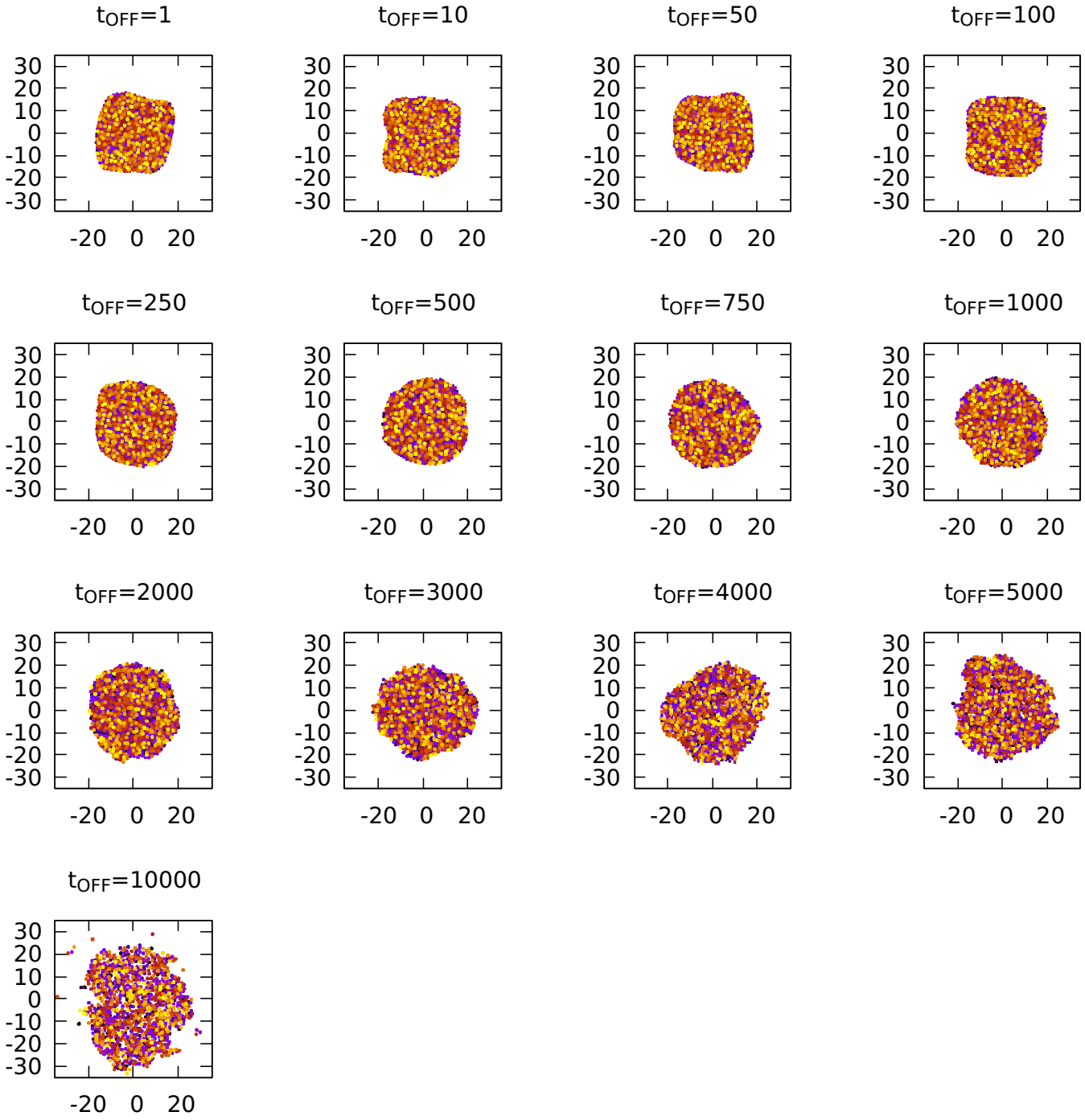

FIGURE 3.27: Snapshots of relaxed aggregates for increasing τ_{OFF} ($\tau_{ON} = 500$)

we want for the interface one could consider that it is not sufficiently rough interface.

Consequently in the following we will consider the **concave hull** or α shape: the α shape can be envisioned as the result of the following game (see fig. 3.31(c)): assume a disk of radius $\sqrt{\alpha}$, coming from ∞ (outside the cloud of points), this disk disk cannot cross points. We see that moving this disk all

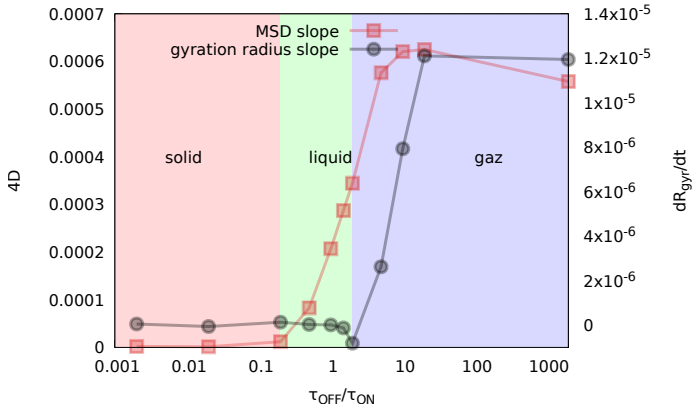

FIGURE 3.28: MSD and gyration radius as a function of $\frac{\tau_{OFF}}{\tau_{ON}}$ ($\tau_{ON} = 500$)

around the cloud it will penetrate more or less deeply in the interior of the cloud, it will be blocked if it encounters a pair of point which distance is smaller than its diameter: when it is the case we draw a segment between the two blocking points. One can proceed to the same game coming from the interior of the cloud of point. Doing this procedure recursively, at the end of the game we obtain a set of connected points which represents the concave hull, eventually it can include single points if the disk is able to rotate around the point (these are not connected by any segment). There are two singular limit to this game: if $\alpha \to \infty$ we recover the convex hull, on the other hand if $\alpha \to \infty$ we have the entire set of points.

Given that we introduced another parameter α, we should take care to set its value reasonably: greater than the typical interdistance in the aggregate but not too large if we want to obtain a smooth interface.

Having an interface is not enough, we need to decide how to orientate the pressure forces. Figure 3.32 illustrates our choice :

- Forces are oriented perpendicularly from the segments of the concave-hull, what's more they are additive that is for particle i' the final force is oriented by $F_{i'i''} + F_{ii'}$.
- The modulus of the force F exerted on each segment is constant $||F_{ii'}|| = ||F_{i'i''}| = F$. These pressure forces have no dependence on interface size and thus on $r_{ii'}$'s. Indeed the real pressure forces are exerted on the particle surface S, thus their value is proportional to the particle exposed surface S, $F \propto S\Delta P$ (which is the half hemisphere $S = \frac{1}{2}2\pi r_0^2$).

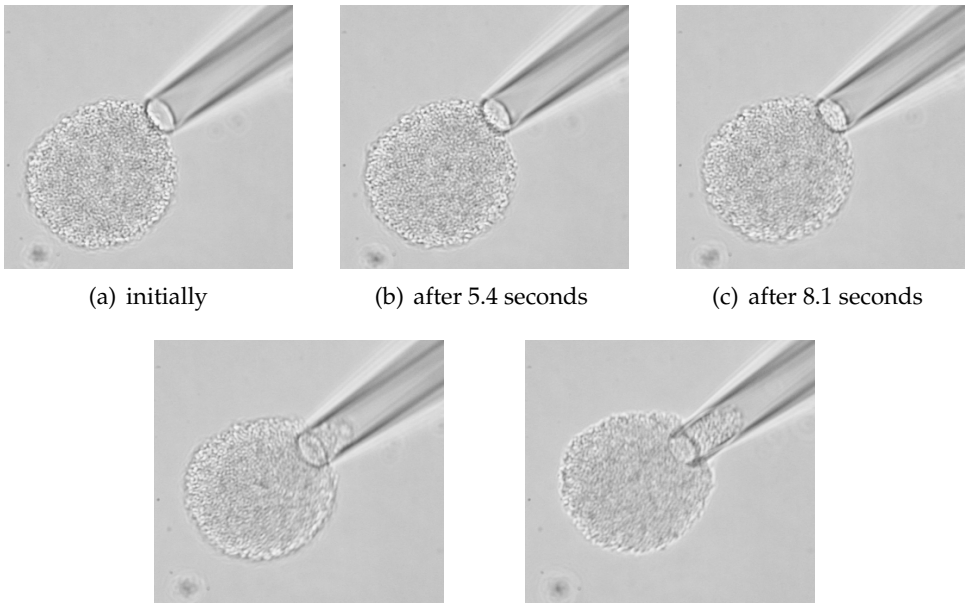

(a) initially (b) after 5.4 seconds (c) after 8.1 seconds

(d) after 10.8 seconds (e) after 13.5 seconds

FIGURE 3.29: liquid-like behavior of the aggregate under aspiration (experiment done by Valentina)

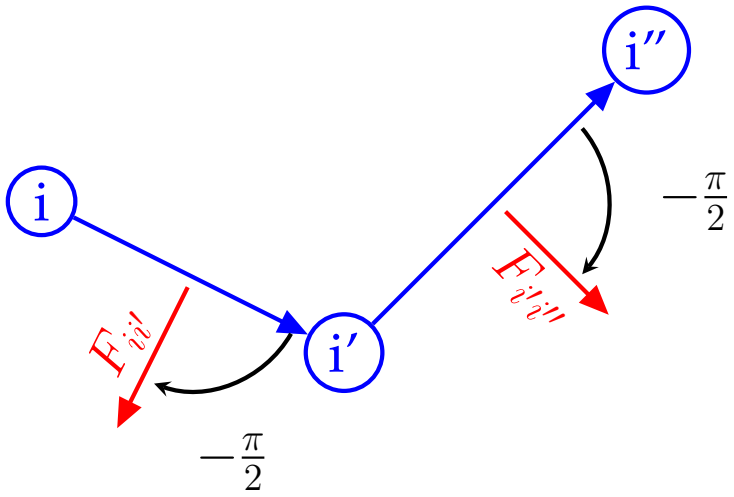

FIGURE 3.32: Computation of pressure forces.

Finally we detail how we modelized a typical pipette rheology experiment which consists of two phases: a first (rather quick) approach phase where we push the aggregate against the edges of the pipette and a second phase where we activate the pressure forces.

3.5.2.3 Measurements

We can now focus on the results obtained from the simulations. First it is important to check if the progression of the tongue scales linearly with time. What's clear from the look at the tongue progression (figure 3.33(a)) is that initially there is rather quick regime where the progression is nonlinear. Two causes can be considered regarding this first stage: it can either be the

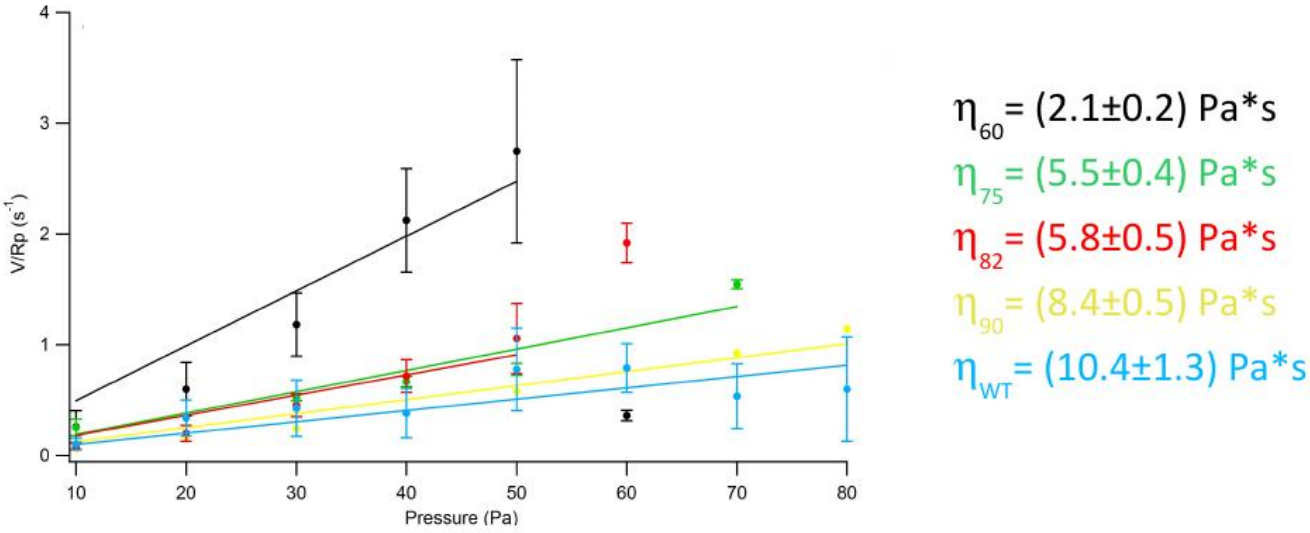

FIGURE 3.30: Tongue progression speed as a function of exerted pressure force in the micropipette experiment for the PilFi mutant with different IPTG concentrations and the WT (the respective "piliation" is indicated with subscripts), the linear fit gives the viscosities indicated in the left-hand side panel

aggregate adapting to the external forcing (the "pressure"), or in light of the description of section 3.1.4 it might come from the visco-elastic nature of the material where two regimes can be seen the first being nonlinear and corresponds to the elastic response, the second is linear and is the viscous response.

In real life experiments it's probably possible that both response exist and can be estimated, but we lack both temporal and spatial accuracy accuracy to be able to measure such short time regime response. However we are mostly interested in an estimation of the viscosity and we indeed see a *more or less linear* progression regime of the tongue shortly after, the fluctuations being probably caused by the discrete nature of the pressure forces. We therefore conducted systematic measurements of the progression velocity as a function of the exerted pressure for three aggregates chosen in the liquid phase with various degrees of solidity: $\tau_{OFF} = (250, 500, 750)$ which respectively correspond to mostly solid, liquid and very liquid conditions from what we've seen in 3.28.

The first data we can extract is the tongue progression speed v as a function of the exerted force, which is summarized in 3.33(b). These data confirm that the ON/OFF mechanism is sufficient to substantially change the aggregate properties: for each sample the speed scales linearly with the exerted pressure. For each sample we can therefore extract an adimensionalized viscosity taking the slope $\eta(\tau_{ON}, \tau_{OFF}) \propto dP/dv$. The results both for experiments and simulations are summarized in figure 3.33: we can see a decrease of η with $\frac{\tau_{OFF}}{\tau_{ON}}$, comparing with the experimental results which suggest a linear scaling with the piliation percentage p it tends to confirm that these two quantities are linked somehow. Keeping in mind that $\frac{\tau_{OFF}}{\tau_{ON}} \in \mathcal{R}+$

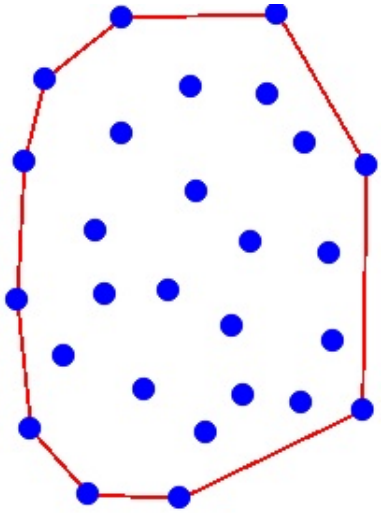

(a) The convex hull is a poor approximation to an interface

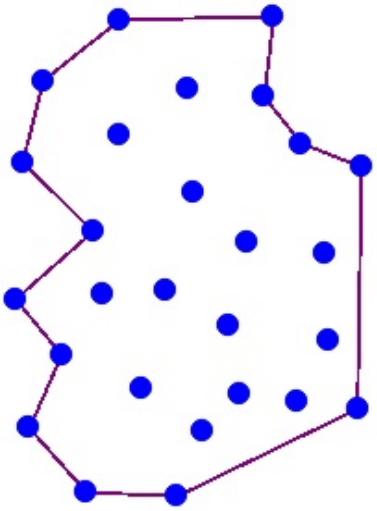

(b) On the other hand the concave hull seems better

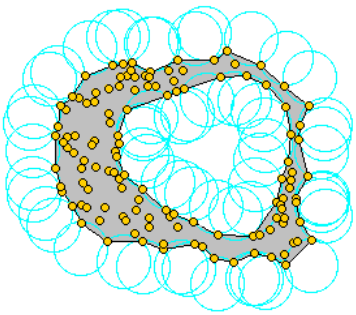

(c) The α shape construction game with a disk, source: http://doc.cgal.org/latest/Alpha_shapes_2/index.html

FIGURE 3.31: Comparison of concave vs convex hull computation. The concave hull is closer to the real interface.

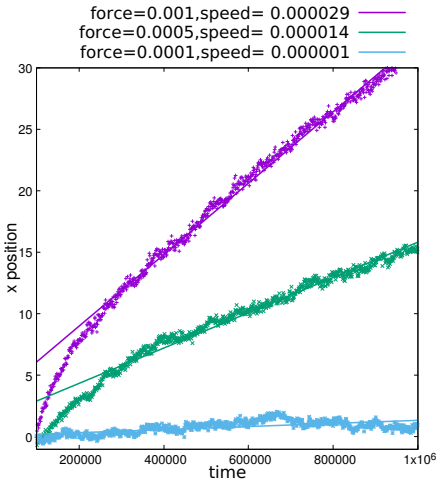

(a) Example of the progression for the position of the tongue for various forces, notice the initial progression ($t \leq 200000$) is faster. Fits are performed on intervals $\in [2e5, 2e6]$

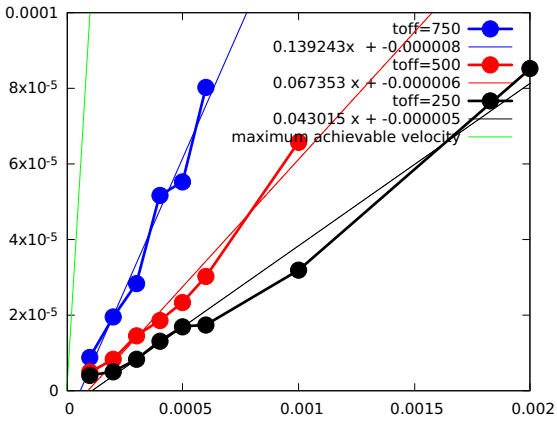

(b) Progression velocity as a function of the exerted pressure

whereas $p \in [0, 1]$, thus the relation might not be as simple as a direct proportionality relation.

3.5.3 Dimensionalize the problem: rescaling the time

This model begun as a proof of concept that stochastic interaction could allow a liquid phase but slowly moved toward something more quantitative. An essential data not yet used in the model is the fact that T4P retraction speed is a well fixed value and has been estimated to $1\,\mu\mathrm{m\,s}^{-1}$ [8]. This velocity parameter doesn't appear at all in our modelization and even after rescaling. However an appropriate choice for instance to rescale the retraction speed of the pili to be the average of the speed given by the attractive part of the potential, looking at the shape of F_{ij} we see that when $2 \leq r \leq l_p$ we have $-0.035 \leq F_{ij}(r) \leq -0.010$, these values are the same order of magnitude and we can assume it is constant and take the average value as the mean speed of retraction $v_0 \approx 2.25 \times 10^{-2}\mu\mathrm{mntu}^{-1}$ where "ntu" stands for "numerical time unit". Keeping in mind we already chose the distance unit by setting the diameter of the particle to 1 which corresponds to $1\mu\mathrm{m}$

The connection is thus straightforward: $2.25 \times 10^{-2}\mu\mathrm{mntu}^{-1} C = 1\,\mu\mathrm{m\,s}^{-1}$ therefore $C = \frac{1}{2.25\times10^{-2}}\mathrm{ntu\,s}^{-1}$ or equivalently $1\mathrm{s} \approx 45\mathrm{ntu}$

Most of the previous data were acquired without rescaling, however we provide in the following table 3.2 which is redundant but the reader can refer to this correspondence between simulated and real units when necessary:

However we have to remember the fact that we already imposed the timescale by setting the diffusion coefficient , indeed we have $D = \frac{<x^2(t)>}{2dt}$ which gives another scaling. We've extracted from the movies the free bacteria diffusion constant $4D \approx 1\mu\mathrm{m}^2\,\mathrm{s}^{-1}$. Numerically we've set the value to

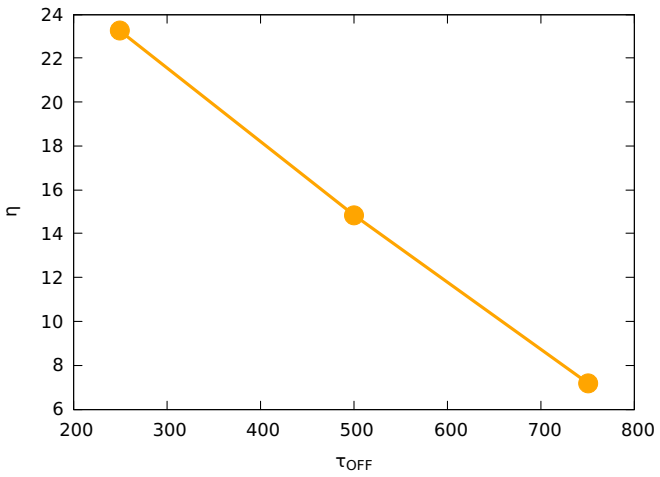

(c) Adimensionalized viscosity decreases with τ_{OFF}

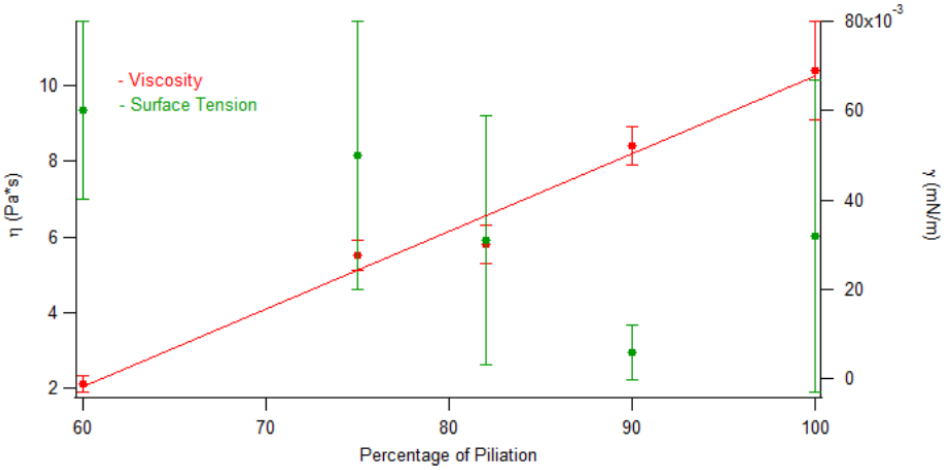

(d) Experimental measurements of the viscosity (red points) for the PilF mutant as a function of piliation level show a linear evolution. The surface tension is also shown by green points.

FIGURE 3.33: Comparison of both simulated and experimental values of the viscosity

$\sigma = 7\mathrm{e}-4$ as we've seen in 3.4.3.2 $4D = (0.03)^2 \mu\mathrm{m ntu}^{-1}$ therefore the conversion leads to $1\mathrm{ntu} \leftrightarrow 7 \times 10^{-4}\,\mathrm{s}$. This scaling gives different result and implies that we have to introduce a second conversion

quantity	numerical value	experimental value	numerics $\rightarrow$ real units
v_0	2.25×10^{-2}	$1\,\mu\mathrm{m\,s}^{-1}$	$1.4 \times 10^{+3}$
d_0	1	$1\,\mu\mathrm{m}$	$\times 1$
time	1	$2.5 \times 10^{-2}\,\mathrm{s}$	$\times \frac{1}{45}$

TABLE 3.2: This table helps to translate numerical units to "real" ones.

3.5.4 First modification of the model: still potential based more quantitative

We highlighted in 3.4 a promising model which already shown that a ON/OFF mechanism was able to generate liquid aggregates. However the model is only quantitative because of the poor choice of potential which has some troubling issue:

- the attractive part is distance-dependent
- not very tunable (the attractive and repulsive part are interdependent.)

In a second time, in order to get more quantitative we opted for changing the shape of the force profile by a tunable piece-wise function $F(r)$ defined by (3.17):

$$\begin{aligned} F(r \leq r_0) &= \alpha \frac{1}{r^2} \vec{u}_r \\ F(r > r_0) &= -v_0 \vec{u}_r \end{aligned} \tag{3.17}$$

Thus, this change allows to solve the previous situation that two incompatible timescales existed if we'd choose diffusion or the force as the leading mechanism, we can see the shape of the force and the associated potential in 3.34.

Also, we've simplified the units translation as shown in tabular 3.3. Consequently no arithmetic is necessary to compare quantities from simulations and experimental ones.

quantity	numerical value	experimental value	numerics → real units
v_0	1	$\approx 1\,\mu\mathrm{m\,s}^{-1}$	$\times 1$
d_0	1	$1\,\mu\mathrm{m}$	$\times 1$
$4D$	1	$\approx 1\,\mu\mathrm{m}^2/\mathrm{s}$	$\times 1$
time	1	$1\,\mathrm{s}$	$\times 1$

TABLE 3.3: The new units avoid to convert numerical to real units

3.5.5 Phase diagram

We report in 3.35 the diagram for $\tau_{ON} = 1$. Compared with the previous situation we are clearly missing a solid phase: even for $\tau_{OFF} \to 0$ the diffusion is non vanishing. The origin of this difference is, as we've seen in previous chapters (3.5.0.1) the permanent attraction state can be liquid. However we will see in the next section 3.5.6 that we can recover a solid state. Except from this discrepancy, the transition liquid-gas transition occur for similar $\frac{\tau_{OFF}}{\tau_{ON}}$ ratio with respect to the previous model. In some sense it confirms our initial guess that the ON/OFF mechanism is a leading mechanism for the system final state of matter.

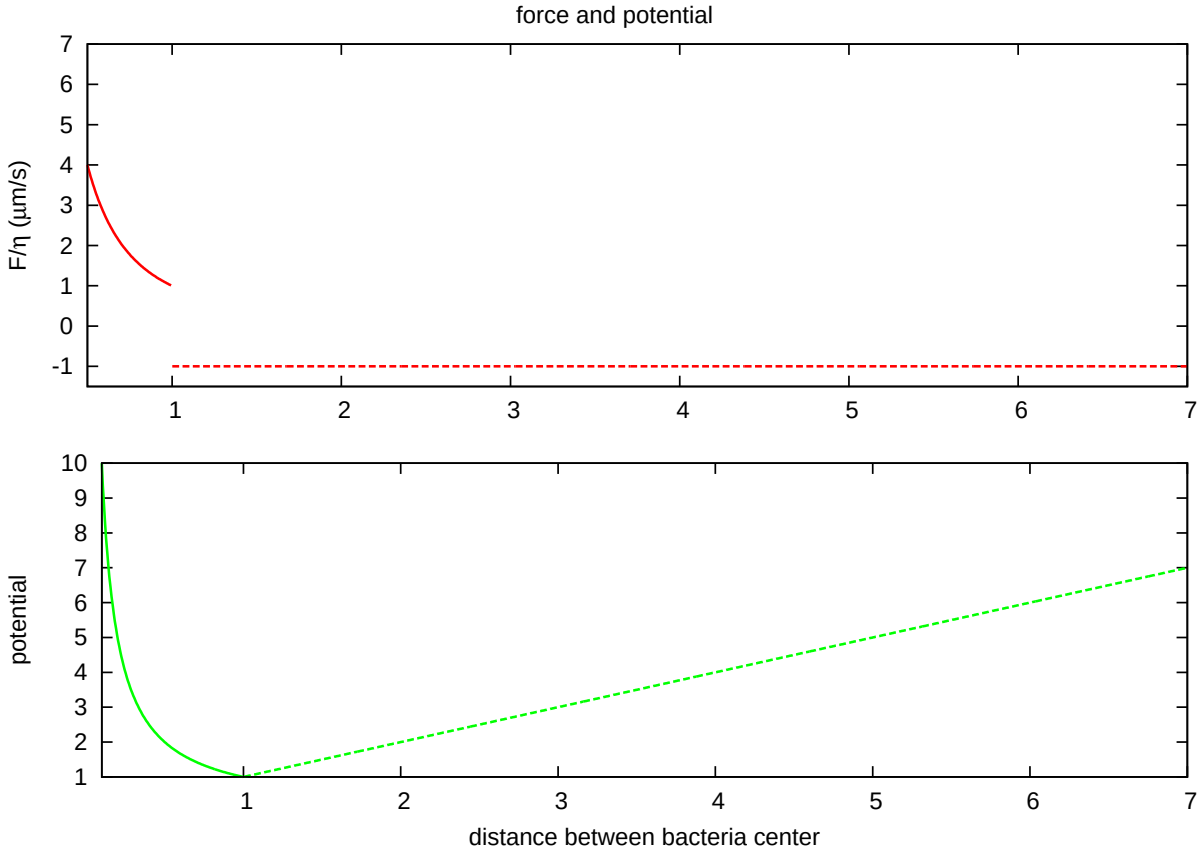

FIGURE 3.34: The shape of the new potential.

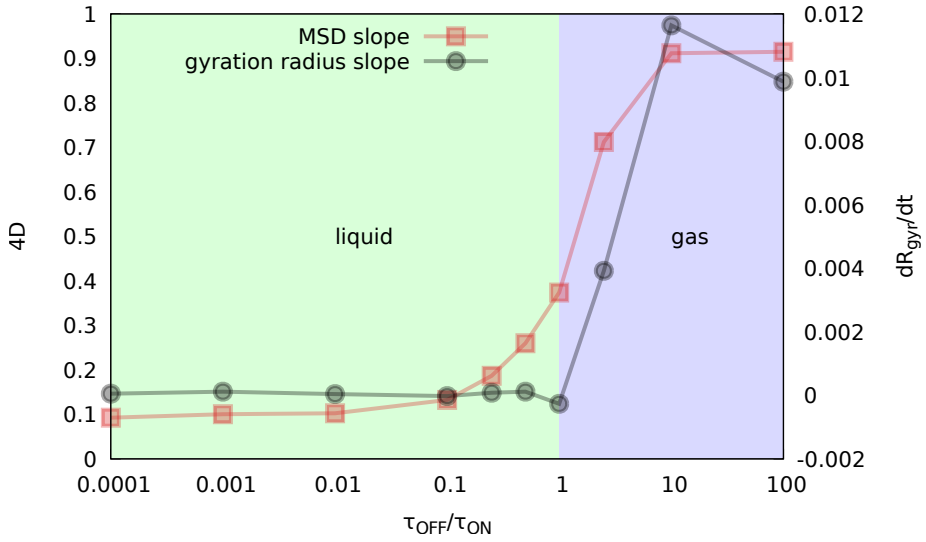

FIGURE 3.35: Phase diagram of the model with tunable force.

3.5.6 Recovering the solid phase

We've just seen that with parameters closer to reality the model is missing a solid phase, therefore this model lack to represent the PilT mutant which displays a characteristic "frozen" structure which should be visible for $\tau_{OFF} \to 0$. However, we can circumvent this issue by using a "trick" which is justified as follows: if we consider a biologically relevant regime, the aggregates are in a situation where the forces in action (pili forces and also pressure forces) have far greater magnitude than Brownian noise. In that sense, it seems fair to neglect the noise term when these forces are present. A formal justification can be the following one , consider the overdamped Langevin equation with a "drag force" exerted by pili, we introduce an effective viscosity term η_{eff} to account for the fact that the molecular motor has a complex mode of operation and is always able to pull at a constant speed :

$$0 = -6\pi r \eta_{\text{eff}} \frac{d\vec{x}}{dt} + \vec{F}_{\text{drag}} + \sqrt{2\eta k_B T}\vec{\xi}$$

This implies that, in order of magnitude:

$$\frac{dx}{dt} = \frac{F_{\text{drag}}}{6\pi\eta_{\text{eff}} r} + \sqrt{\frac{2k_B T}{\eta_{\text{eff}}}}\xi$$

Knowing that we want $\frac{d\vec{x}}{dt} \approx 1\,\mu\text{m}\,\text{s}^{-1}$ and $F \approx 100\,\text{pN} = 10 \times 10^{-10}\,\text{N}$, which translates to $\eta_{\text{eff}} \approx 5 \times 10^3\,\text{Pa}\,\text{s}$. This viscosity is way above the viscosity of water. It means that when the drag force is acting, this is equivalent to change the noise amplitude like $\xi \to \xi \times \frac{\eta}{\eta_{\text{eff}}} \approx 5 \times 10^{-3}$, we remove it in practice.

We thus consider that pili are very hard to stretch which is reasonable and but also hard to to bend which might not be entirely realistic. Of course for "free" (without attached pilus) bacteria, the noise is the only relevant term ruling their dynamics and in that case we cannot neglect it.

Therefore a numerical scheme we considered was to simply suppress the noise for particles in the ON state ($s_i = 0$). This is obviously an oversimplification but it contains the essential idea that the noise has to be highly attenuated when other forces are in action.

Another scheme consists to consider that pili are indeed very strongly pulling but we also have to consider that the constraint is uni-axial and therefore it is only legitimate to suppress the noise *along the pili axis* when such pili pulls. This implies that basically for bacteria at the center of the aggregate the noise would still be totally suppressed, on the contrary at the edges, given that the number of neighbors can be low, the noise strength could still be important.

3.5.6.1 Phase diagram

Again we reproduce the phase diagram for the model with the noise trick in 3.36 all parameters being the same. As we see, we are able to recover the solid phase at low enough τ_{OFF}/τ_{ON}. Except from this important addition, not much is changed.

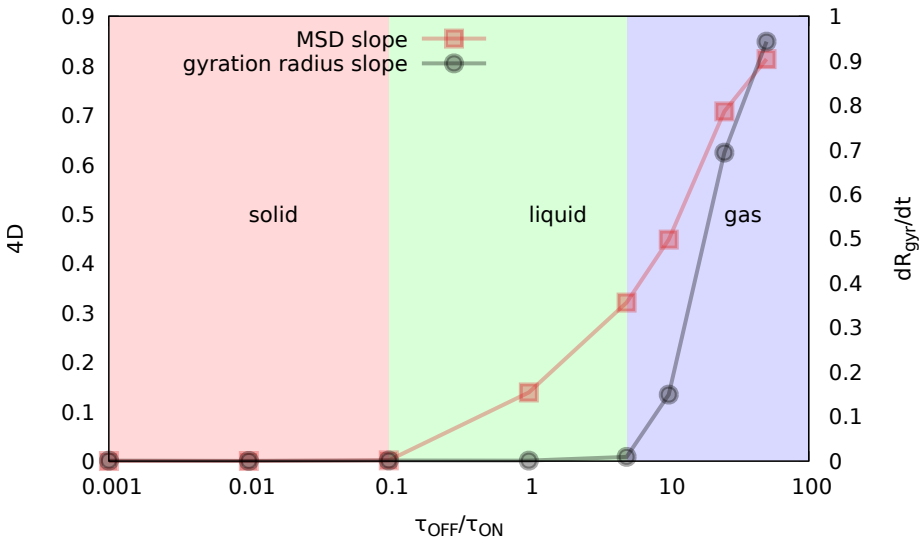

FIGURE 3.36: Phase diagram of the model with tunable force and noise suppression rule.

3.5.6.2 Aggregation dynamics

Now that we have model displaying 3 phases and with correct parameters we can focus our interest in the dynamics of aggregation. Meaning that we're not interested on the properties of one aggregate but instead we're looking for a statistical description of *assemblies* of aggregates. Being limited

by the Voronoi tessellation computational cost (which scales as $N\log(N)$) we studied assemblies of $N = 10^5$ particles. This study is justified from the biological point of view for two reasons:

- Aggregates properties might depend on their size. For instance small aggregates might diffuse more and merge quickly whereas bigger ones will see their positional diffusion vanish. Given that aggregates in the bloodstream have no reason to be single sized this study is relevant.
- From the technical point of view these are relatively easy observations. Most of the necessary experiment already existed in order to compare aggregates from the different mutant strains upon visual inspection. We used the generated movie by post-treatment means in order to obtain comparative data.

3.5.6.3 How to define clusters

For that purpose we need to define two sub-populations: freely diffusing bacteria and aggregating ones, on top of that we need to identify to which aggregate belong each of these bacteria, i.e perform a "clustering" process. In that sense we add to each particle an additional observable: their cluster index c_i for particle i.
This variable takes integer value and its meaning is to index the aggregates, that is particles sharing the same c_i will belong to the same cluster. In other words a cluster K which index is k is defined as:

$$\text{cluster } K \iff \{i, c_i = k\}$$

After the clustering algorithm is performed the rest of the particles (freely diffusing ones) are grouped under the cluster index $\{c_i = 0\}$
The rule used here is a simple proximity criterion: let's assume that two particles are close enough ($r < l_c$), in that case they will belong to the same cluster. As the aggregates both in the solid and liquid phase have high packing fractions we usually choose the distance l_c to be of the order of two diameters d_0. The algorithm sweeps over all pairs of particles, for each pair the 3 different situation we might encounter are sketched in 3.37.

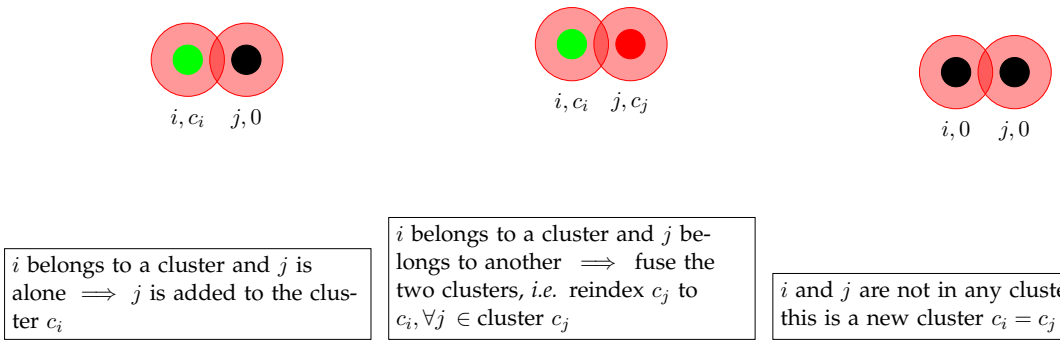

FIGURE 3.37: The clustering algorithm rules description.

This simple set of rules is sufficient to give good result as you can see in figure 3.38

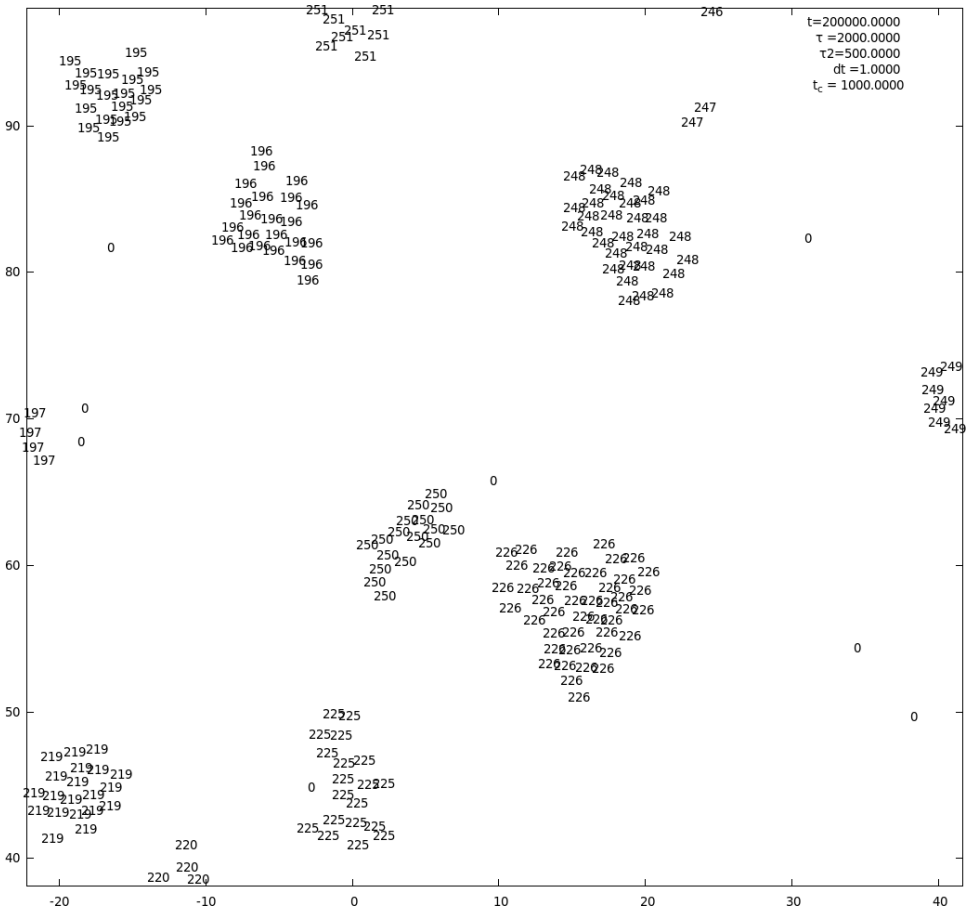

FIGURE 3.38: A sample of space showing the effectiveness of the algorithm, aggregate indexes c_i are shown as we can see different aggregates are well identified as well as free particles ($c_i = 0$).

3.5.6.4 Quantification

To be able to compare some results we still need to define what quantity to track. For an aggregate indexed k ($k \in 1, k_{\max}$) the number of its constituents $n(k)$ is given by: $n(k) = \sum_{i,c_i=k} 1$. Therefore the aggregates size distribution $P(k)$ is given by 3.18, notice that we exclude free bacteria in that case ($k \neq 0$):

$$P(k) = \frac{n(k)}{\sum_{j=1}^{k_{\max}} n(j)} \tag{3.18}$$

An interesting quantity is the aggregation rate, that is the ratio of aggregated particles 3.19:

$$R = \frac{\sum_{j=1}^{k_{\max}} n(j)}{N} = 1 - \frac{n(0)}{N} \tag{3.19}$$

And we define the average aggregate size as (3.20):

$$S = \frac{\sum_{k=1}^{k=k_{\max}} n(k)}{k_{\max}} \tag{3.20}$$

3.5.6.5 Results

First of all we have tracked over time the aggregation ratio R for various system sizes (or concentration) and τ_{OFF} as we can see in 3.39. As we can see we can ascertain that the simulation size are enough given that we reach pretty quickly a (almost) stationary regime given by a plateau in the value of R. However, we notice the aggregates at the limit of the liquid-gas transition, corresponding to $\tau_{OFF} = 2.5$, fail to reach the maximal ratio $R = 1$. This means that there is an "equilibrium" situation where a fraction of particles never aggregate. This can be understood as a balance between particles exiting aggregates and starting to freely diffuse and the opposite situation where these particles free particles start to join aggregates. Of course, this is concentration dependent and we can thing that for infinitely dilute aggregates, particles leaving would never be caught and then ultimately there would be only a gas. However in the same situation the aggregation is only possible for also infinite waiting time. Still, we see that in our case the situation is stationary for reasonable experimental times.

Therefore it is sufficient in order to compare the aggregation in these different situation, taking the final value of the aggregation rate given that the situation is stationary. We've summarized the obtained results as a function of τ_{OFF} and system size in figure 3.40.

The interesting result is the non monotonous behavior. Indeed we expected this function to be monotonously decreasing, because for a permanent attraction, at low τ_{OFF} particles cannot escape aggregates. The problem is that the bigger aggregates become, the lower their diffusion becomes. On the contrary for liquid aggregates the aggregates diffusion is much higher, the aggregates are more deformable and yet there is no flux of exiting particles. This might explain what we see here. Visual inspection seems to confirm these data (see 3.41) for $\tau_{OFF} = 0.1$ deep in the solid phase, aggregates looks smaller than those at larger τ_{OFF}.

We were interested to see if these predictions were obtained in real life experiments. Indeed in the biologist mind, there is some optimality in nature has ways to select optimal parameters: if for some reason the bacteria is advantaged when having bigger aggregates this might explain why it precisely adjusted obtained this liquid aggregative like behavior and not a solid one. However it seems rather complicated to extract proper distributions of size because of some effects:

- As we are working in 2D we have to estimate aggregates radius size from a slice which might be inaccurate.
- Non clustered bacteria and small clusters take a long time to to precipitate and reach the focal plane and thus is a constant flux of incoming particles, which is not the case in our simulations.

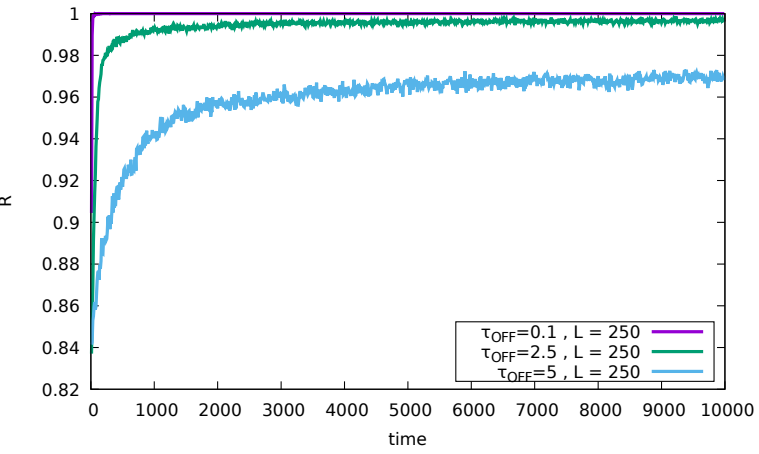

(a) L=250

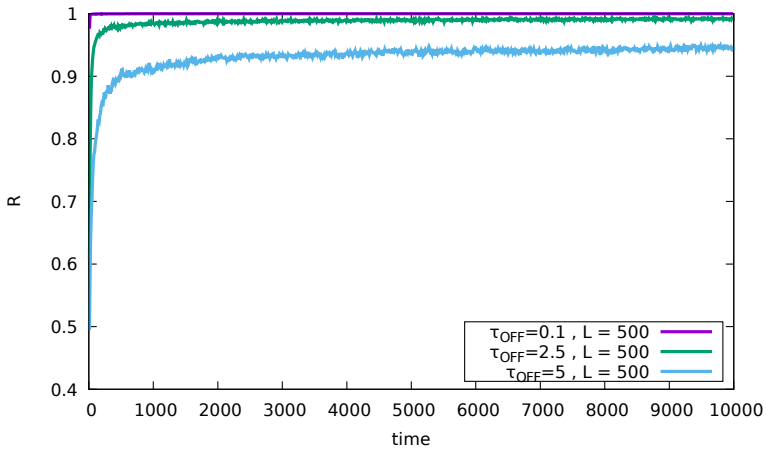

(b) L=500

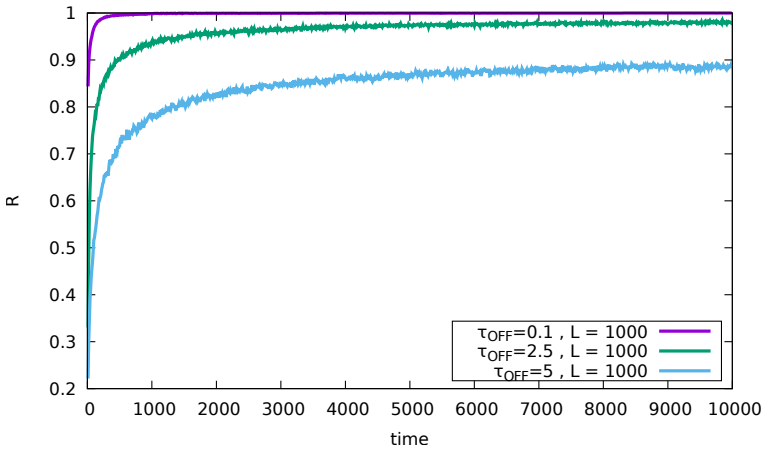

(c) L=1000

FIGURE 3.39: Timeseries of the aggregation rate for various system sizes and τ_{OFF}

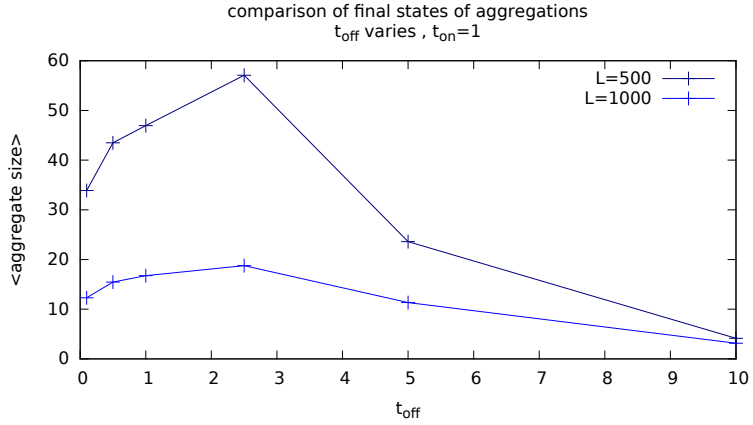

FIGURE 3.40: Final values of aggregation rates for various τ_{OFF} and two systems size $L \in 500, 1000$

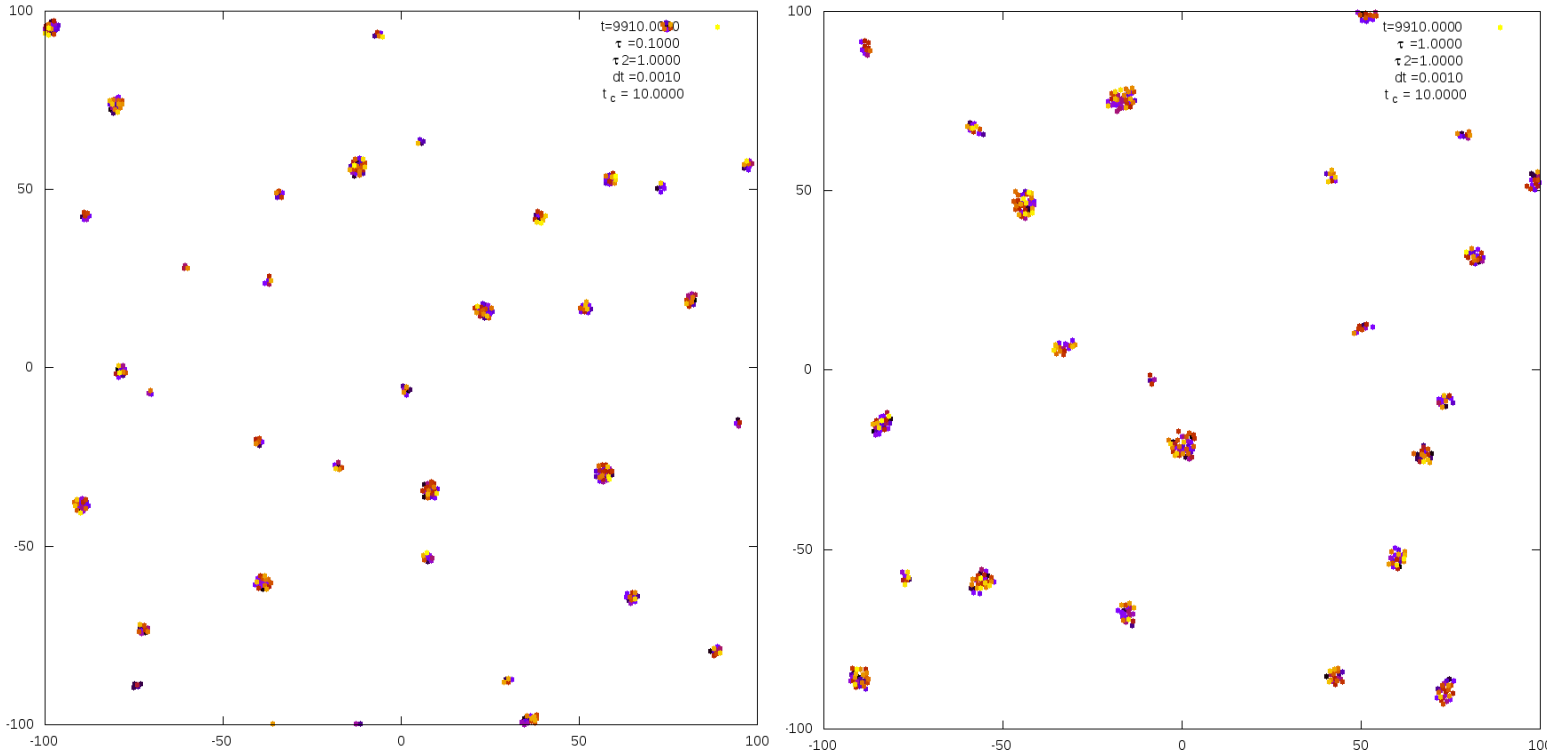

(a) solid phase $\tau_{OFF} = 0.1$ (b) liquid phase $\tau_{OFF} = 1.0$

FIGURE 3.41: Typical aggregates size in the solid and liquid phase

3.6 Link based model

In this section we will see the more evolved model we investigated which consisted in a nutshell to promote the scalar variable s_i to a more complex structure containing additional degrees of freedom. The aim of introducing these additional parameters is aimed at reproducing more closely the dynamics of pili. Indeed the previous modelization was lacking some elements that could be important to render optimally all the aggregates properties, among which:

- In a particle based model a particle going from ON to OFF state will most likely connect to several neighbors immediately after switch, for a range of τ_{ON} values. This model solves this problem, given that creating multiple pili simultaneously has a vanishing probability. In summary we want to have **independent pili**.
- Pili are not constant force molecular motors *per se* but are rather motor working at constant speed . Thus a retraction event can be seen as a process where we need to impose the length of the pili over time and only consequently the force is adjusted to enforce that constraint. Therefore we need a feedback process between the force exerted (at a certain time t) which depends on earlier pili length (at time $t - \Delta t$). This **memory requirement** couldn't be contained in the simple potential we considered in the potential based model.
- The previous point is linked to the issue highlighted in 3.5.4: even if we could dimensionalize the problem we still need a trick (to suppress the noise when the attraction interaction exist) in order to obtain the matching state of matter (liquid) of the aggregate corresponding to these parameters (especially the noise)
- This is essential to obtain such high-forces generation for the micropipette experiment. In that case we need to attain high drag forces (resp high drag velocities) which can only drag the whole aggregate if the forces internal to the aggregate (that is the pili forces) are $\gg$ than these forces

3.6.1 Description of the model

The previous way to create pili was unsatisfactory to some extent, the asymmetry between ON and OFF states was an issue in the sense that the control over the number of neighbors was not possible, nor was the fact that we could simultaneously create multiple links when one particle would switch from OFF to ON. As a consequence the pilus creation and destruction processes are now independent of the particle state but now depend on pairs of bacteria. Therefore a link between particle i and j is called s_{ij} and its evolution is given by the following transition probabilities between time t and time $t + \Delta t$ of equation (3.21):

$$\begin{aligned} P(s_{ij} = 0 \to s_{ij} = 1) &= \Delta t/\tau_{OFF} \\ P(s_{ij} = 1 \to s_{ij} = 0) &= \Delta t/\tau_{ON} \end{aligned} \tag{3.21}$$

This simple rule is not sufficient to describe the generation of pili. With the potential based models, both the creation and destruction were implicitly included in the ON/OFF dynamic of the s_i and we didn't have to worry about which set of particles theses processes apply to. When pili are independent, destruction and creation of pili are distinct processes and don't necessarily apply to the same set of particle pairs, it is thus necessary to append a rule which specifies to which particles these processes apply:

- The creation process applies to bacteria which are Voronoi neighbors at a given time t, "as previously". However we now we keep an history of the pair (i, j) hence the indexing s_{ij} - we call it a link or pili from now on.
- The destruction process applies to these existing pili. This is a different procedure than before where creation and destruction were applying to the same set of particles: Voronoi neighbors (in other words the links were always a subset of the edges of the Voronoi tessellation). Here, on the contrary, it is important to note that these are different that *these links can still persist for particles which are no longer Voronoi neighbors*.

Again if we take the graphic representation of the bacteria + pili system by two disks, one for the attractive range the other for the repulsive region we have for the pili creation and destruction processes: However this actual

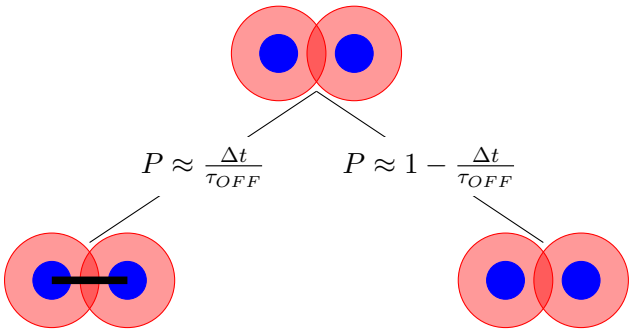

FIGURE 3.42: The neighbours are close enough, there is a probability $\frac{\Delta t}{\tau_{OFF}}$ that they will interact by creating a pili

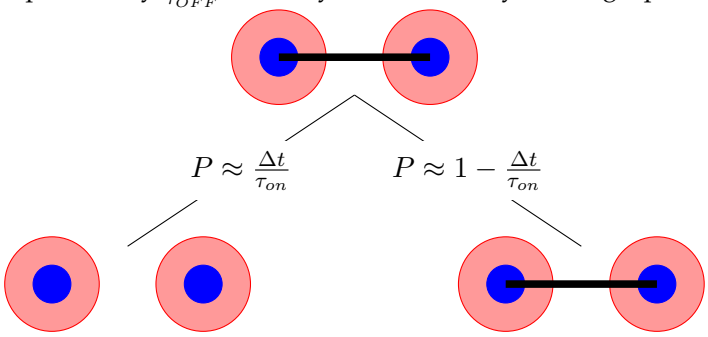

FIGURE 3.43: The reverse process of destruction has a probability $\frac{\Delta t}{\tau_{on}}$

set of rules is not entirely satisfactory as the purpose of such model was given by the fact that we wanted to take on step forward to a more realistic model. The last change was to drop the potential based interactions in favor of a force that takes into account the force-velocity relation shown in [30].

That is we wanted to explicitly enforce constant approach speed v_0 for two attracted particles over time. The algorithm is as follows: The equation for the pili length r_{ij} gives

$$\begin{aligned} \mathrm{d}r_{ij}(t)/\mathrm{d}t = \\ = -v_0 - 1/\mathrm{dt}\ \max((r_{ij} - r_{exp})(t), 0) \end{aligned} \tag{3.22}$$

Where r_{exp} is the expected distance at time t:

$$\begin{aligned} r_{exp}(t) &= \min(r_{exp}(t - \Delta t) - v_0 \Delta t, r_0) \\ &= \min(r_{ij}(t_0) - v_0(t - t_0), r_0) \text{ after "integration" between } t \text{ and } t_0 \end{aligned} \tag{3.23}$$

Globally (3.23) gives the auxiliary variable r_{exp} which is just linearly decreasing with time up to r_0 , meaning pili achieved complete retraction. It's the length the pili should have it there weren't any constraint. This variable enters in (3.22) , where the second term compensates the error in terms of displacement (3.24) at time t (meaning the difference between what the length should be if the pulling was unperturbed vs what it is really) :

$$\max((r_{ij} - r_{exp})(t), 0) \tag{3.24}$$

Giving the additional term. Notice the max() function which indicates this displacement isn't applied if particles went close enough. This equation is note written for each particle but the displacement being symmetric it is straightforward to write the equations for each particle.

In the end this process is equivalent to put a moving potential over time which looks like figure(3.44) A way to see it is to consider that the potential "glides" on the line defined by $y = v_0.x$. From the point of view of a fixed particle at position x we see it will feel higher and higher forces over time.

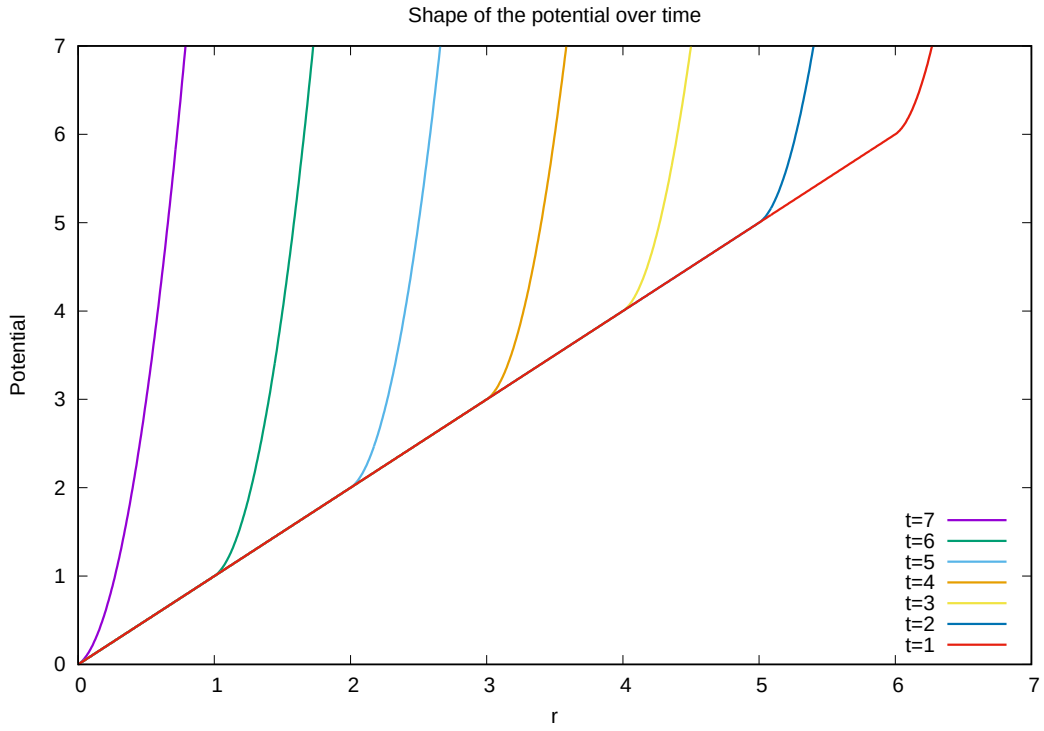

FIGURE 3.44: Pili modelized as a potential which "moves" towards smaller distances over time

Last but not least, this algorithm can lead to indefinitely increasing forces in the solid regime. This is cause of the quenching caused by the competing pili pulling in opposite directions (after all it's what opponents in a tug of war do, they pull more and more strongly until one breaks). Therefore we need to the maximum force to be bounded (3.25):

$$||\mathrm{d}r_{ij}(t)/\mathrm{d}t|| = \min(-v_0 - 1/\mathrm{dt}\ \max((r_{ij} - r_{exp})(t), 0), f_{\max}) \tag{3.25}$$

3.6.1.1 Phase diagram of the new model

This new phase diagram 3.45 is very interesting for several reasons. If the two usual transitions are well identified for $\frac{\tau_{OFF}}{\tau_{ON}} = 0.1$ and 2.5 for the solid-liquid and liquid-gas one respectively, what's more intriguing is the diffusion spike around $\frac{\tau_{OFF}}{\tau_{ON}} = 0.9$, right "in the middle" of the liquid region. The second, and even more intriguing fact is the value of the diffusion coefficient which exceeds those at the beginning of the gaseous phase and even those of freely diffusing particles ($D \approx 1$ when $\frac{\tau_{OFF}}{\tau_{ON}} \to \infty$) . These two points make sense once we take into account what is at stake here: for a dense liquid the only small ballistic displacements are authorized because of the lack of space, leading to small diffusion. On the contrary for a gas mean free path is not bounded by spatial constraints but there's no more

ballistic displacements. Thus when both these properties are present favoring high length ballistic displacements it makes the global diffusion rise significantly. One could then wonder why this intermediate regime was not visible for the previous models: essentially because the ballistic motion were insignificant, at most they were at a speed of $\approx 1\mu m\, s^{-1}$ whereas here they can exceed this value due to the slingshot effect when the tug-of-war breaks. An important point to note that when taking the MSD we've taken the short time MSD when two clear regimes were visible on the timeseries, as shown in section 3.6.2.

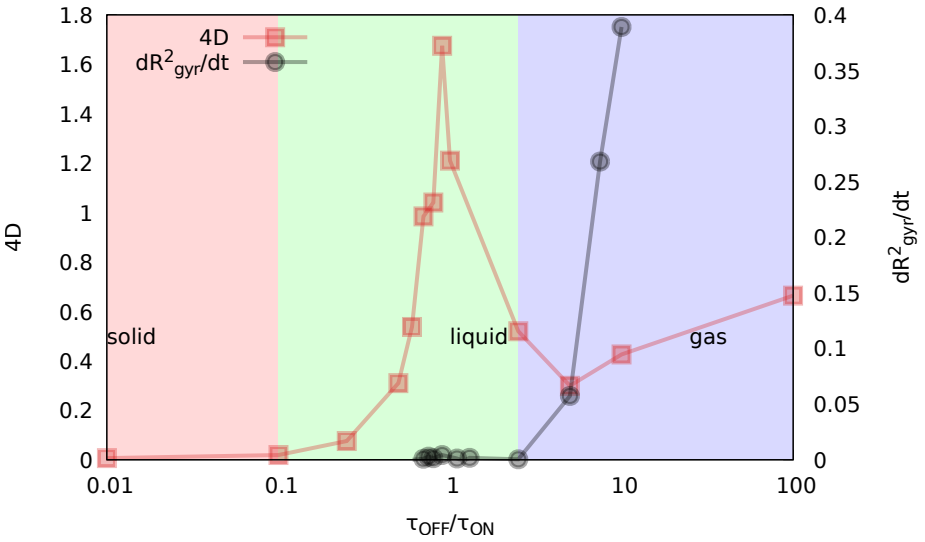

FIGURE 3.45: The phase diagram for the model with independent pili

3.6.2 Ballistic signature

In [30] the authors were also are able to show the signature of the ballistic steps, i.e. the transition from hyper-diffusive MSD $\propto t^2$ at short timescales to diffusive behavior $\propto t$.

Can we identify such transition with our data? The positive answer is not obvious as our system mixes both Brownian and ballistic motility. In order to be able to discriminate between the signatures of these noises requires for instance a timescales separation. Looking at MSD curves for the "best case" $\frac{\tau_{OFF}}{\tau_{ON}} = 0.9$ 3.46 shows two clearly distinct regimes. This is another piece of evidence proving that the pulling events have a significant impact on the diffusive behavior up to some timescale. We can compare with, as an example $\frac{\tau_{OFF}}{\tau_{ON}} = 0.5$ far from the "excessive diffusion" area, and indeed only one diffusive behavior can be seen from the MSD curve. However these data aren't showing signs of hyper-diffusion which is probably hidden by diffusing effects as we've suggested earlier. Our guess is that given that both diffusion and ballistic motion events are acting at the same time this might be ultimately hidden in the diffusion. What's more even though the $\tau_{OFF} = 0.9$ aggregates are sparser than the relative distances stay short,

thus the ballistic events are of short duration making it even harder to find them.

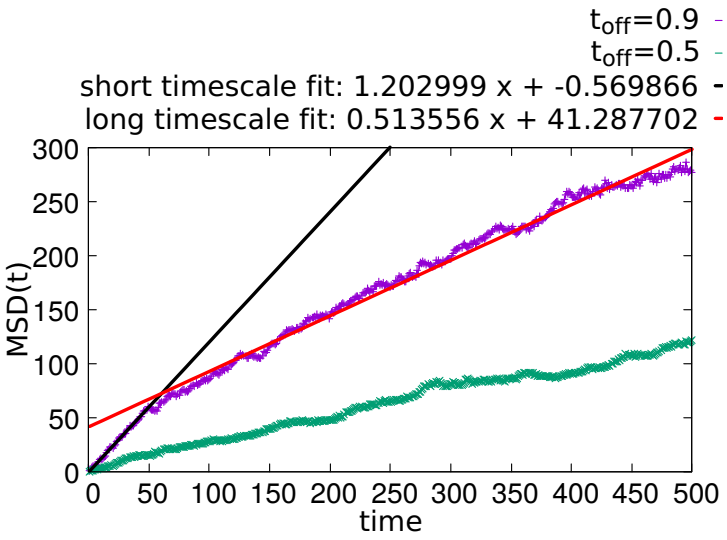

FIGURE 3.46: MSD for $\tau_{OFF} = 0.9$ with fitted diffusion coefficients for short and large times. As a comparison the MSD is also shown for $\tau_{OFF} = 0.5$ is shown, showing only one regime

3.6.2.1 Pipette

One of the main objective of this model was to obtain more realistic pipette progression speed. As previously we've run pipette simulations for various τ_{OFF} in the liquid and estimated the progression speed case by case as can bee seen in figure 3.47. The data are quite noisy, even we can clearly see correct trends, that for instance the speed increases with increasing τ_{OFF} it is quite difficult to beyond the quantitative level and estimate viscosity coefficients for instance. The cause of this noise is again the high forces generated in the aggregate, especially at the borders, where particles are very motile because pili can be established between particles several bacteria-length away from each other. As we are specifically focusing our measures to these particles the results are perturbed by these fast movements of the interface. An improved procedure would comprise averages over several pulling experiments, but it is far to be guaranteed to provide smoothed curves.

3.6.2.2 Reversibility

Something we haven't yet explored yet is the elastic behavior of *Neisseria* aggregates. In the same paper ([20]) , the authors also analyze the aging of cells by noticing that cycles of aspiration-relaxation of the aggregates lead to smaller and smaller deformation cycles, meaning that the biomaterial, when it ages, tends to get more viscous. It is probably similar in Neisseria

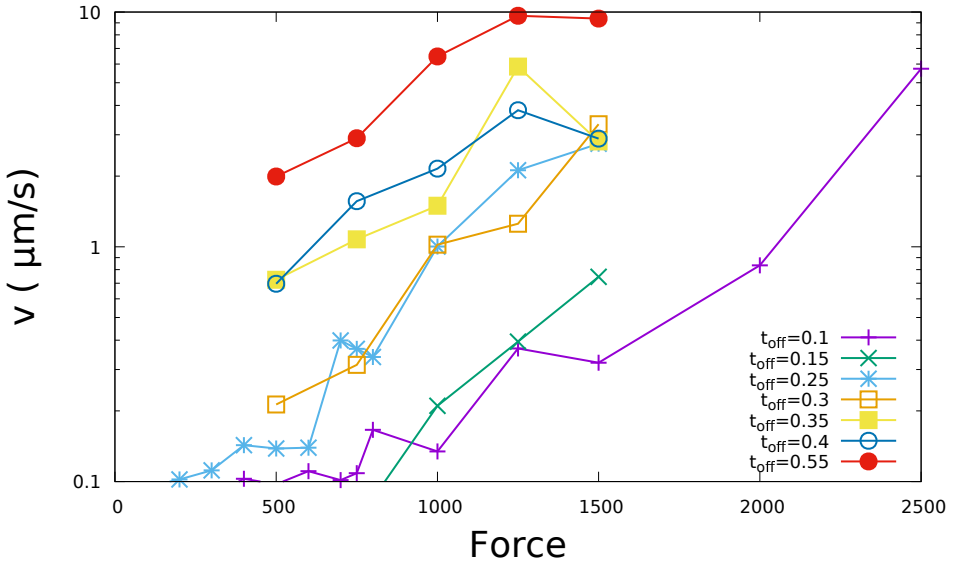

FIGURE 3.47: Tongue velocity obtained for various τ_{OFF} in the pili model

aggregates. Of course in the simulations there is no reason that such phenomenon should occur. However we still can check the *elastic* (reversible) nature of aggregates by looking at their relaxation without force.

3.6.2.3 Pipette in 3D

Facing the poor results of the pipette experiment in the 2D system we've taken a lea of faith and guessed that the difference might originate from the lower dimensionality of the system. Indeed it is not obvious that surfaces tension forces "translate" to line tension forces in a 2D model. Hence we've performed simulations for similarly sized aggregates (radius $\approx 20\mu\text{m}$) but this time in 3D ($N = 10^5$ particles) and estimated the tongue progression speed for various τ_{OFF} in figure 3.48. These results are not to be considered out of their qualitative value. The velocities estimates have been performed very roughly because most liquid aggregates ($\tau \geq 0.25$) didn't resist the force after a few seconds. Indeed if all the previous concepts (α-shape and Voronoi neighbors) are all easily translatable in 3D there is still the question to know how to translate the way we pull on particles in 2D (perpendicularly to the edges). From what we see here, it is not equivalent to pull perpendicularly on a tetrahedron of the surface.

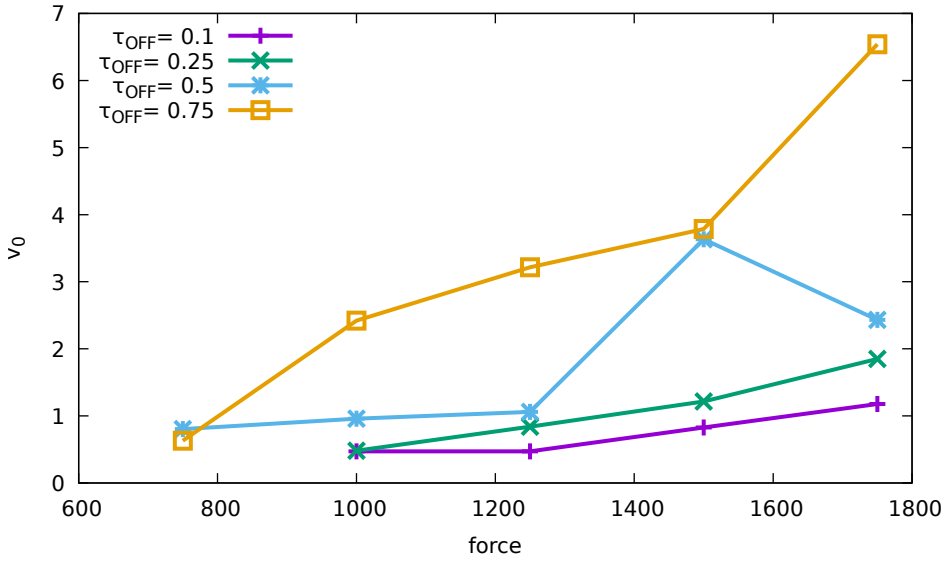

FIGURE 3.48: Pipette progression velocities for the model in 3D. The lines are still in the correct order liquid to solid up-down but the linearity with respect to the force is not visible.

3.6.3 Effects of bacteria anisotropy: diplococci

Bacterial division has been yet neglected. For now our model was limiting to particles which were point-like but with an isotropic repulsive potential strong enough to treat them as disk in the two dimensional case or spheres in 3D. However in real life aggregates a significant fraction of the bacteria doesn't look spherical. *Neisseria meningitidis* belongs to the *diplococcus* group of bacteria, that it is composed of two symmetrical interpenetrating spheres. However as it is undergoing cell division it has to divide in two identical *monococcus* which will then regain their initial *diplococcus* shape 3.49 , this division stage being quick in comparison to the steady stationary phase.

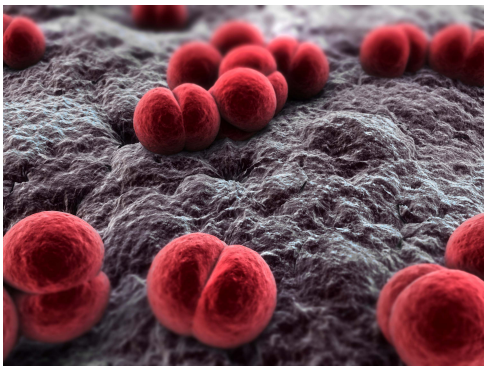

FIGURE 3.49: A 3D representation of a diplococcus of *Neisseria Meningitidis* , source: http://bioquell.asia/technology/microbiology/neisseria-meningitidis

At first, we didn't include such level of detail in the model as we wanted to simply study the aggregation properties of the bacteria. However anisotropy in the bacteria shape has consequences as we have seen at the individual level for the twitching motility in [69, 30] , we recall that their data clearly show that their is a clear preference for the diplococci to self-propel **perpendicularly** to its main axis, they claim that this mechanism caused by the fact that the pili distribution is uniformly flat and thus the larger sides are the more able to cause pili forces imbalance (the stronger side, *ie* the one which has more pili, is able to cause breakage of the weaker side and wins the tug of war.). On the smaller sides there its very unlikely to generate several pili which would lead to this imbalance (there is most likely 1 or 0 pili on these sides, unable to sustain the load caused by the other pili which are most likely located on longer sides)

However these models as well as the experiments as we've already stated are dealing with bacteria on a substrate and thus bacteria are not subject to diffusion. Now that we are dealing with non-spherical objects in addition to positional diffusion we should incorporate rotational diffusion. First derivation of rotational diffusion coefficients was performed by Jean Perrin in [44] for ellipsoids. However as we're not dealing with such shape, even though in first approximation it could be legitimate to approximate diplococcus as ellipses, added to the fact that we're working on 2D geometry and such derivation deals with 3D case we've adopted another scheme. In the

spirit of [12] where authors are dealing with dumbbells diffusion , we've implemented the rotational diffusion as an effective diffusion, indeed we assume that each diplococcus is a doublet of particle $(i, i+1)$. Each particle is subject to the previous set of equations (3.26) plus an additional potential to make the two particles stay close:

$$\begin{cases} \frac{d\vec{r}_i}{dt} = \sum\limits_{j\in\partial i} \vec{F}_{ij} + \sqrt{2D}\vec{\eta}_i + V_i^{i+1} \\ \frac{d\vec{r}_{i+1}}{dt} = \sum\limits_{j\in\partial i+1} \vec{F}_{i+1j} + \sqrt{2D}\vec{\eta}_{i+1} + V_{i+1}^{i} \end{cases} \tag{3.26}$$

Note that in that case i and i+1 are excluded from the Voronoi neighborhood. Rewriting this set of equation with the appropriate variable change $(\vec{r}_i, \vec{r}_{i+1}) \rightarrow (\frac{\vec{r}_i+\vec{r}_{i+1}}{2}, \frac{\vec{r}_i-\vec{r}_{i+1}}{2})$, which are the coordinates of the center of mass and the direction of the main axis of the diplococcus (or the angle θ characterizing its orientation) , we can see that the center of mass as well as θ are themselves diffusing.

We didn't characterize yet the potential V_i^{i+1} , the authors use a sharp elastic potential preventing pair of particles to get away from each other in addition to a Weeks-Chandler-Anderson (best known as WCA) potential providing the repulsive part in order to prevent the two spheres interpenetration.

Our choice is different, we force the two beads interdistance to stay constant. That is *at each timestep* we:

- Compute the bacteria pair center of mass $(\frac{\vec{r}_i+\vec{r}_{i+1}}{2})$
- Keep memory of the orientation of the particle $(\frac{\vec{r}_i-\vec{r}_{i+1}}{2})$
- Reset the distance between the pair of diplococci so that $\vec{r}_{ij}$ is equal to d_0 for all t. Each particle is put at a distance $\frac{d_0}{2}$ symmetrically with respect to the center of mass, oriented along $\pm\frac{\vec{r}_i-\vec{r}_{i+1}}{2}$

This mechanism is naturally providing a source of rotational diffusion caused by the implicit coupling between positional and the rotational diffusion. In order to comfort this assertion we've computed rotational MSD for an ensemble of freely diffusive diplococci. As figure 3.50 shows there is indeed diffusion for durations up to $\approx 50\text{s}$, but then the regime becomes slightly super-diffusive with MSD scaling $\approx\propto t^{1.2}$. Our mechanism is thus indeed a diffusive regime for short timescales but maybe is not best fitted to maintain "normal" diffusion over long timescales.

3.7 Comparison with experimental results

3.7.1 Aggregates properties

3.7.1.1 Variable diffusion

Experimentally, movies of aggregates show visually that the "core" of the aggregate seems to show reduced diffusion compared to the edges. Low

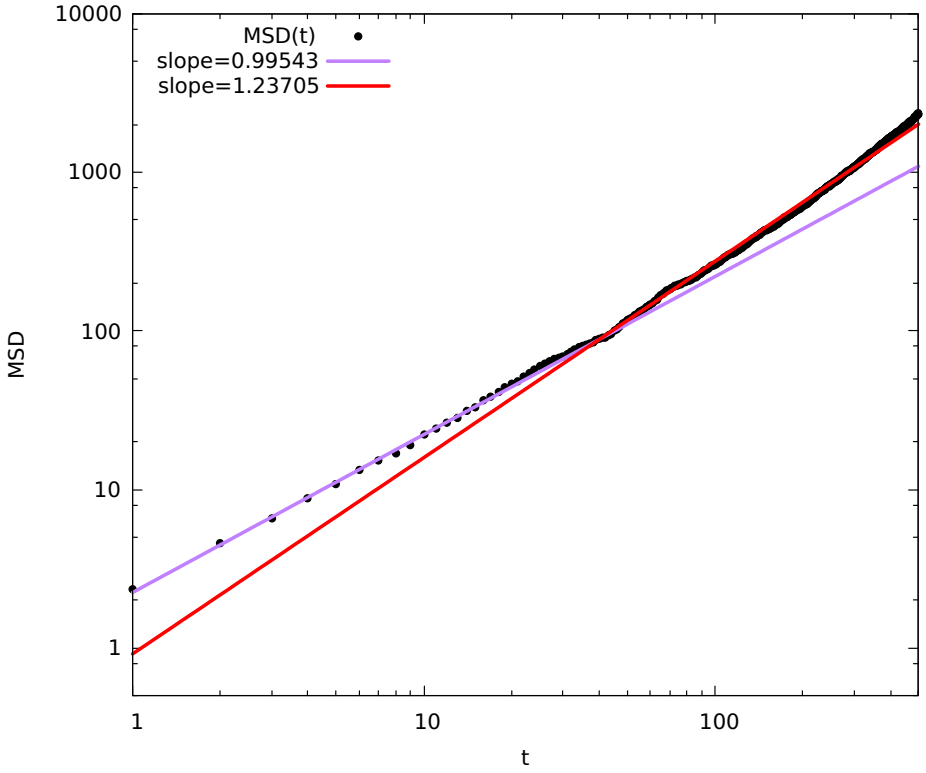

FIGURE 3.50: Rotational MSD as a function of time, in log-log scale, also ploted are the fitted diffusion exponents for short and long timescales

temporal resolutions movies were giving very poor results because we are looking at slices of a 3D aggregate, consequently particles frequently exit the focal plane. In order to gather more data about the biological system we produced movies with high temporal resolution, at a frame rate around $\frac{1}{30}$ s^{-1}, this highly improved the tracking algorithms convergence. The obtained tracks (figure 3.51) are shown with a coloring referring to the average speed during the track. With all the bias that the tracking can produce - particles permutation, wrong estimate of positions... - this still quantitatively shows a clear difference between the center and the edges, we can even see a gradient of diffusion from the center to the outside. As a biological system we cannot exclude that the source of this gradient is a lack of nutrient - simply because the nutrient has difficulties to cross the aggregate "shell" - giving a lowered activity at the center. We can produce tracks as in figure 3.51 , however we are able to provide evidence that this phenomenon can arise as an effect of a "caging" effect which is stronger at the center. Taking simulated aggregates we've measured the MSD for particles within several shells indexed $s_1, s_2, ..., s_n$ (3.27):

$$MSD_i(t) = \frac{1}{\sum_{k \in s_i} 1} \sum_{k \in s_i} (x_k(t) - x_k(0))^2 \tag{3.27}$$

These shells are chosen with an arbitrary criterion: we compute the aggregate radius R , consider n shells and define s_i as the volume $\{\frac{i}{n} \leq r \leq \frac{i}{n+1}\}$. For instance we've considered 3 shells in 3.52 and two aggregates states

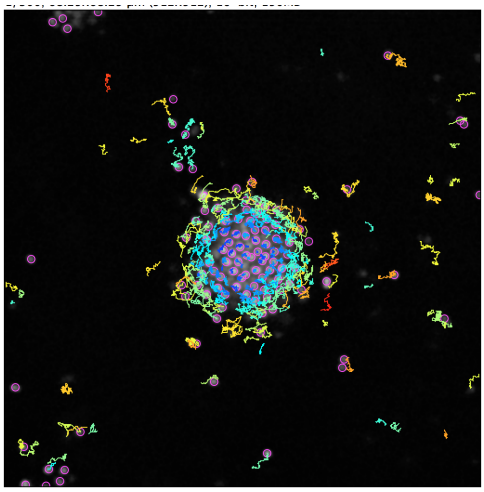

FIGURE 3.51: Tracking obtained for a real aggregate, the center shows lower diffusivity. (Coloring shows averaged velocity during tracking.)

of matter. For $\tau_{OFF} = 0.1$, deep in the solid phase, particles are totally jammed within the first two shells and only the ones are the exterior are diffusing. For $\tau_{OFF} = 0.5$ the aggregate is liquid but still not uniformly, particles at the center are still caged and diffuse less, we also able see the diffusion gradually increasing from the center to the edges. Notice that the MSD curves are jittery, it is essentially caused by the fact that particles are constantly entering and exiting the shells making the factor $\frac{1}{\sum_{k \in s_i} 1}$ fluctuate over time.

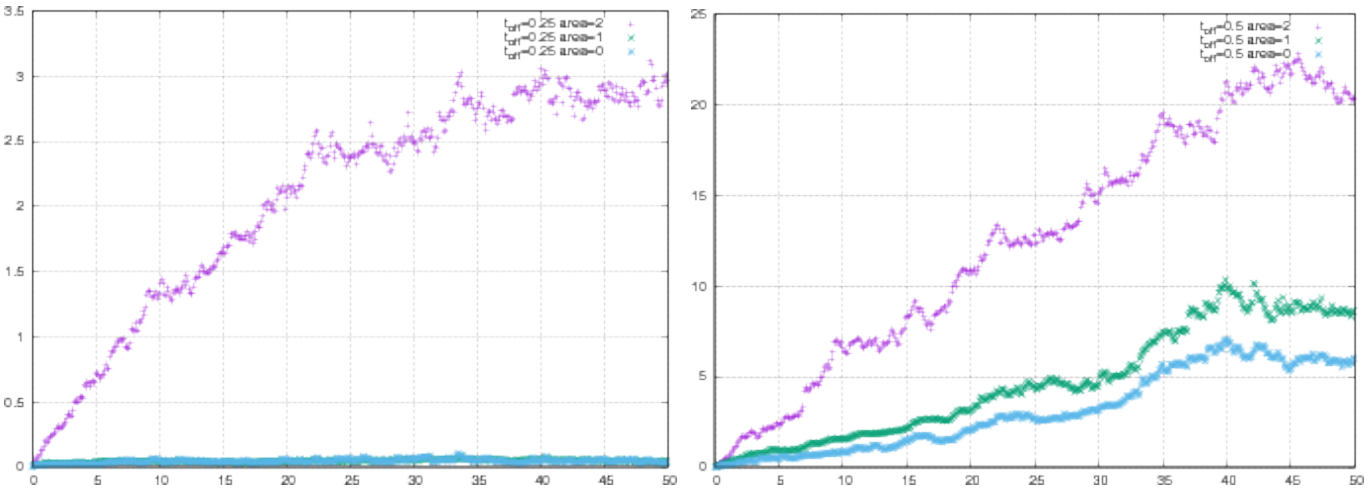

(a) solid aggregate ($\tau_{OFF} = 0.25$): high differences are visible between particles at the center and to the edges

(b) liquid phase ($\tau_{OFF} = 0.5$): the difference is less measurable but still visible

FIGURE 3.52: The MSD as defined in equation (3.27) show high variability of the MSD between the core of the aggregate and its core. Shells from the center to the outter one are respectively blue green and purple.

Finally we can produce some data proving that our model can at least quantitatively fit "internal rheology" of real life aggregates. In figure 3.53 we see

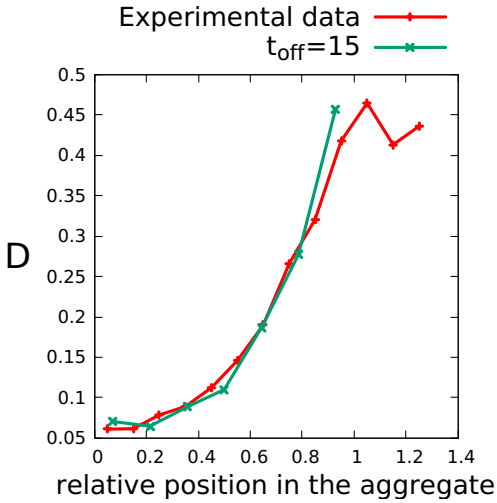

FIGURE 3.53: Comparison of the internal diffusion between experimental data and simulation extracted data

that the diffusion coefficient D inside the aggregate matches the one of experimental data for $\tau_{ON} = \tau_{OFF} = 15$. This value is reasonably good as the experiment shown in 3.7.4 leads to value in that range.

3.7.1.2 Orientational order parameter

So far, we defined two quantities to study the system phase transition, namely the MSD and the gyration radius. If for the former we can extend its scope to a local definition, the gyration radius on the other hand is a global parameter and its definition can't be modified to display inhomogeneities inside the aggregate. Even for the MSD, it is quite hard to define it locally, indeed if one tracks a particle in a defined region, the diffusion will drive it out of the region sooner or later. To circumvent this limitation, one has the possibility to accumulate trajectories which stay in the region and average them. That's a procedure we followed in 3.7.1.1. For the particular case of the liquid/solid transition it is however possible to define a **local** order parameter that allows us to detect homogeneities inside the aggregate. Next follow some definitions and sketches to understand how we can characterize this transition.

Consider the N_i neighbors of particle i, we call this neighborhood ∂_i. Then we can define the hexahedron scalar order parameter ((3.28))

$$s_i = \frac{1}{N_i} \sum_k e^{j6\theta_k} \tag{3.28}$$

To have an idea what it means, imagine that all particles neighboring i are exactly arranged according to an hexahedron. Consequently we can say that $\theta_k = \theta_0 + j\frac{2\pi}{6}$ with θ_0 , say, the angle for the particle which satisfies $2\pi/6 \geq \theta_0 \geq 0$. Therefore the exponential reads $e^{i6(\theta_0 + j\frac{2\pi}{6})} = e^{i6\theta_0}$. Hence the argument $6\theta_0$ characterize the relative tetrahedron orientation and the norm quantifies how close we are to the perfect arrangement (1 for perfect

hexahedron, less for disarranged configurations down to 0 for a random configuration).

3.7.2 Other characterization of the transitions

MSD and gyration radius might not the best suited quantities to seek for the transition. Here we introduce possible alternatives we tested in order to refine our characterization of these transitions.

If we consider particle i which coordinates are x_i. An essential difference between a solid and a liquid is that the neighbors configuration will be steady in the solid phase. That is to say, the quantity at time t the neighbors of particle i ∂_i will not change over time. On the contrary ,for a liquid, particles will frequently change their neighborhood. Thus, quantifying how frequently they keep their neighbors might therefore be a relevant parameter characterizing the liquid to solid transition. In other words, we could define a *persistence time* which characterize how long particles stay neighbors.

3.7.3 Aggregation dynamics

3.7.4 Highlighting the pili to pili interactions

As for now we had to fit the model with bulk properties of the experimental system: viscosity η , surface tension γ , diffusion coefficient D_0 , aggregates size, etc. However in order to make a point about the scientific soundness of the model it is important to measure that,indeed, there are sporadic pili-pili retraction events leading to directed motion. These events are similar to twitching but in addition should drive symmetrically the two particles of the aforementioned pair

Compared to Biais *et al.* experiments it is important to underline the influence of the substrate. The configuration used in their case is such as the non-capsuled *Gonorrhea* is tightly adhering to the substrate, to the extent that they are able to separate nonadhesive bacteria (for some reason) from adhesive ones by simply water washing the petri dish. This also implies that thermal fluctuations are almost completely erased. Last thing is that they focus on single particle events, therefore their is no "spatial constraint" whatsoever: any free bacteria can be tracked and its trajectory post-processed and analyzed. In that sense these experiments are of a lower level in terms of difficulty:

- The capsule prohibits adhesion with the substrate: as the bacteria are not stuck to the surface we still have to deal with thermal fluctuations and the trajectories are therefore not purely Lévy walk like because they always contain Brownian movement even for the shortest times.
- We want to observe ballistic and symmetric pili-pili interactions. Consequently we need to be at high concentrations enough to have close enough pairs, keeping from being too high in order to avoid multiple particles (3 , 4 or more) interactions.

3.7.5 Should τ_{OFF} be distance-dependent?

Experimental data suggest that the duration of interaction is highly dependent on how-close bacteria are. Figure 3.54 shows the frequency of interaction events with respect to the distance of the bacteria pairs *at the beginning of the retraction event*, tracked in the micro-chambers. There are strong indication that retraction events are more likely when bacteria are close.

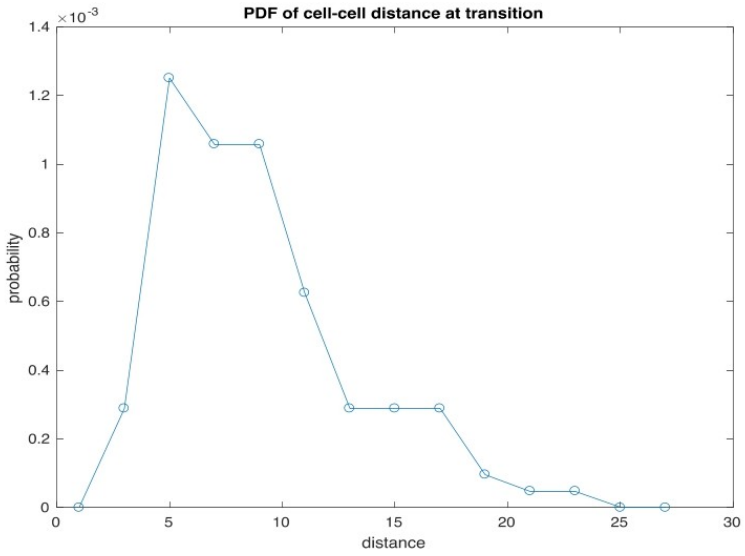

FIGURE 3.54: Probability distribution function of attachment as a function of distance in the chamber experiment. There is a strong decay after $\approx 5\,\mu\mathrm{m}$

Two simple arguments come to mind to back this idea:

- One can understand this as follows: if pili are generated random direction, the probability for one pilus to find a target decreases as the distance between the pili originating point and the target increases. We can for instance imagine that this probability should proportional to the solid angle with which the particle is seen by its neighbors. Therefore the probability P should vary with the distance r and the diameter of the bacteria d proportionally to the solid angle over which is seen the bacteria: $\mathrm{P}(r) \propto 2\pi(1 - \frac{r}{1-\sqrt{r^2+d^2}})$. Then, at long distance $r \gg d$ we thus have $\mathrm{P}(r) \propto 2\pi(\frac{d}{r})^2$
- The second argument is linked to the growth of the pili: we've already shown evidence that pili polymerization (as well as depolymerization) is performed at a constant velocity $v \approx 1\,\mu\mathrm{m\,s}^{-1}$. Therefore the time for a pili to encounter the neighbor particle is at least limited by the time for the pili to elongate, this time for two bacteria separated by a distance d is $\frac{d}{v}$.

How much of each of these process are relevant is not something we can quantify for now due to complex biological modelization. At least these two arguments show that τ_{OFF} should at least be distance dependent. For

that purpose we propose another coefficient β which modifies τ_{OFF} according to the *initial* distance (corresponding to the creation of the link between neighbors) between neighbors r_0 :

$$\tau_{OFF} \rightarrow \tau_{OFF} \times r_0^{\beta} \tag{3.29}$$

The β exponent is a simple scaling law which allows to examine very different behaviors from $\beta = 0$ which goes back to the previous distance independent model, whereas for $\beta = 2$ we are matching the long distance ($r_0 \gg d$) approximation proposed before. Of course other scaling should be considered in light of supplementary biological data, but it's extremely complicated to probe these properties: One would require to have statistically significant assembly of bacteria on 2D substrates, which require a wide view angle, and to be able to detect the interaction events, therefore requiring high temporal and spatial resolution, and hereafter perform *a posteriori* the statistics on these particular retraction events.

As we've said, introducing this parameter is not only a guess but is strongly baked by observations. Indeed, going back to the micro-chambers experiment, we were able to extract some statistically significant data, more or less "by hand" , in order to make a point about what we could clearly observe with the eyes. The data in figure 3.54 clearly show, even with limited precision, that retraction events are more frequent when particles are close ($\leq 10\,\mu\mathrm{m}$).

We should pinpoint the biological evidence showing that there is a strong variability of the capacity among bacteria to produce pili [25]. This includes for instance the retraction ability which might vary from bacteria to bacteria and be the source more or less intense retraction event, or else. Our model lacks such feature but the most important one: average number of pili. Indeed it is accounted "on average" by the stochastic attachment term and we think that it is sufficient to encompass this natural variability.

3.7.5.1 Case $\beta = 2$

We didn't perform extensive studies varying β. This is justified by the fact that based on observations, not much of the aggregation dynamics was qualitatively modified. However to understand more quantitatively what modification such parameter would introduce, we focused on the $\beta = 2$ case to seek any contribution on the behavior in the τ_{OFF} parameter space. As usual the two quantifiers of the model are the MSD and $\frac{dR_{gyr}}{dt}$. What is obvious in figure 3.55 is the peak in the liquid region which drastically diminished, to the point where the diffusion is not anymore higher in the liquid phase than in the gas. We can understand such thing as what gives this region this super-diffusion is mostly particles at the edges of the aggregate which are able to move larger distances. However the effect of the variable τ_{OFF} is to reduce the frequency of these large distance retraction events, thus, damping the "excess" of diffusion in this particular region.

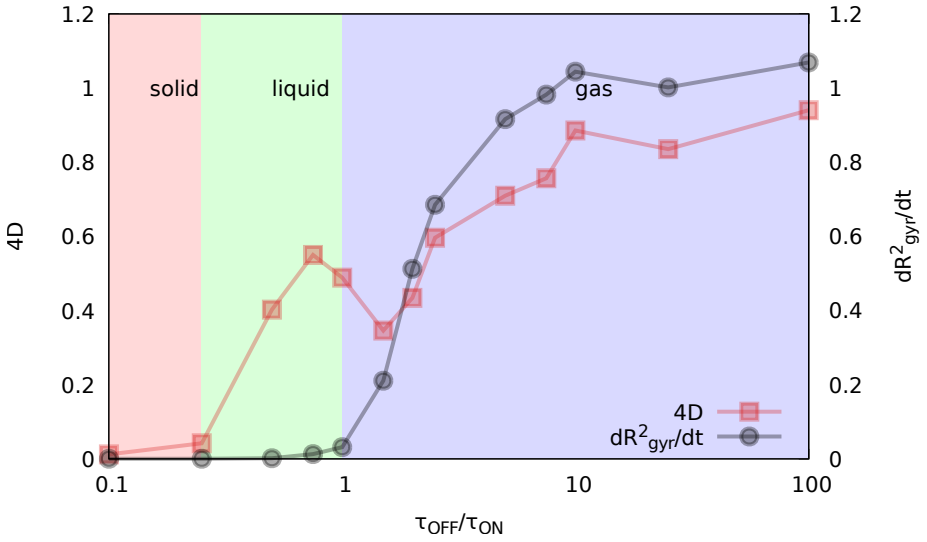

FIGURE 3.55: Diffusion coefficient and squared gyration radius slope for $\beta = 2$

3.7.5.2 Other improvements

Another factor we need to have knowledge about is that about 60 % of the bacteria are not producing any pilus [25]. The origin of such piliation deficiency is still unclear for biologists but we ascertain that our model include this fact in some sense that non-piliated bacteria have little to no influence over the interacting ones. Indeed we've proceeded with simulation where a fraction of the particles were not piliated and observed the resulting phases. While the two population were mixed at the begining we see phase separation of both interacting and noninteracting particles (see fig. 3.56). That means that overall the properties of aggregates will remain unchanged. That also means means that in experimental setup the risk when measuring properties inside an aggregate to have our measurements polluted by noninteracting particles is minimal.

3.8 Highlighting the pili-pili retraction events

Now that we've studied extensively several modelization of *Neisseria* aggregates and compared with bulk rheology measurements as much a possible. The next step was to build an experimental setup allowing highlight the stochastic nature of the pili to pili retraction events. While other experiments already shown and described with much details stochastic retraction events happen in the pili to substrate case with the help of micropilar [8] or a coated beads in a laser trap systems [29] as substrates. Nothing proves that the encounter of two bacteria pili would lead to similar pili behavior. Additionally, we are trying to obtain an idea of both transition time τ_{ON}, τ_{OFF} when other experiments are only able to get what's similar to τ_{ON} , which can be extrapolated from the exponentially decaying distribution of detachment times 3.57 they claim to measure.

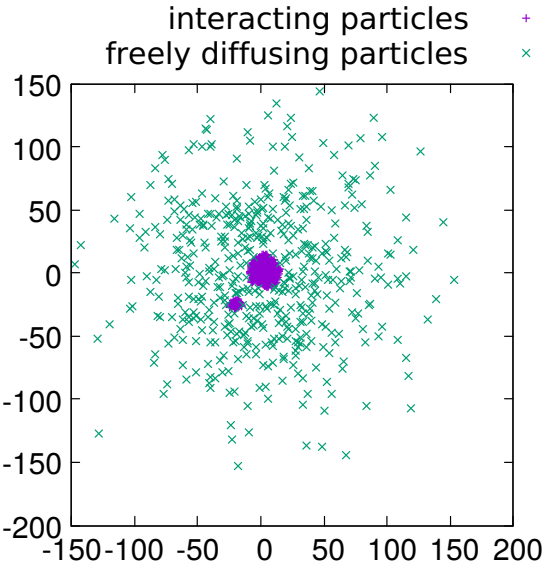

FIGURE 3.56: 50/50 mix of interacting particles (in purple, one can see big aggregate and a smaller one at the center) and non-interacting ones (green, œ) after $\approx$ 4500 sec

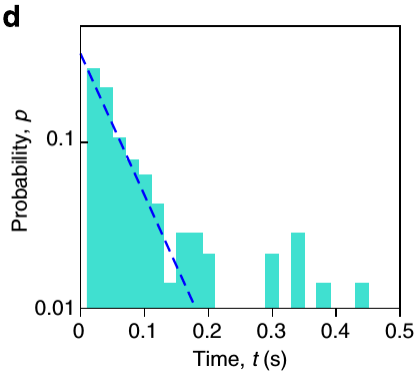

FIGURE 3.57: Exponentially decaying detachment times (note the log-scale on the y-axis) of pilus tethered to a bead trapped by a laser, the laser trap force is 5 pN (from [30])

3.8.1 Setup

The experimental setup Duménil & a.l. realized is composed glass coated substrate on which lies a series of molded capsules made of agar, a jelly and easily sculptable material. They are an ideal environment to specifically probe the bacteria-bacteria interaction because they allow:

- Trapped particles in a defined geometry which permits:
  - Via the cell density: control of the density of bacteria in the cell
  - Quasi-2D setup i.e. we limit the z axis displacement of the particles as a result of the relatively low capsule height.
- The coating is specifically engineered in order to inhibit pili to adhere on it:

- Negligible twitching, when no pulling events particle should freely diffuse.
- Only pili-pili or pili-bacteria interaction will produce ballistic motion.

The next step of the experiment is to post-process the movies ($\approx 100\mu s$ time resolution and diplococcus span several pixels in size) and obtained with a software such as "ImageJ" which provides efficient tracking algorithms. As an example, a typical experiment is shown in 3.58 where we see 10 bacteria tracks of 12 seconds length. On the center we can see a typical pili-pili retraction event, indeed the blue and yellow tracks clearly show both high directional persistence and are symmetrical.

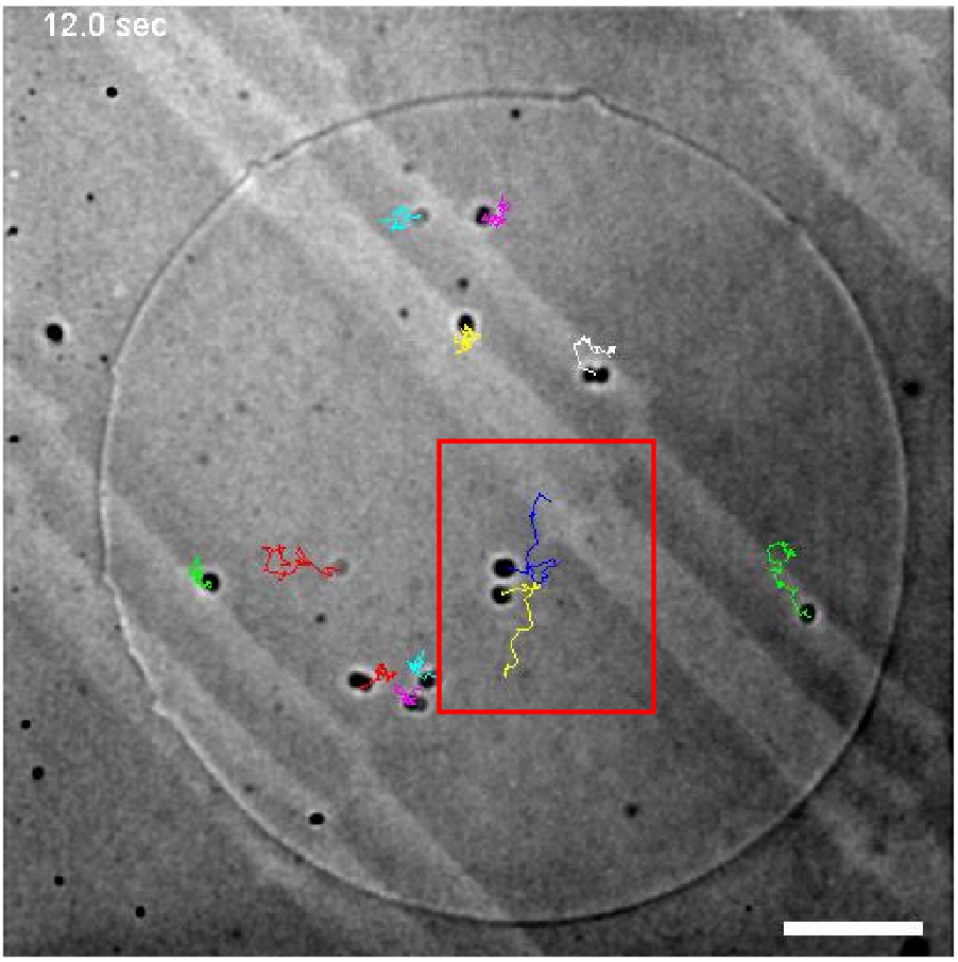

FIGURE 3.58: Tracks over 12 sec in a capsule of $\approx 20\,\mu m$, the rectangular region highlights a typical retraction event.

In an ideal world the experiment would show clear and numerous pulling events but in real life we encountered some problems making the results less convincing:

- Simple confocal microscopy led to very difficult tracking: the optics field of view is so small in the z direction that we were losing track of bacteria which z position were far from the bottom, especially during retraction events.

  - Fluorescent microscopy seems to solve this problem. However we lose track of the cavity contour (because we are looking at bright objects).
    Thus we need to keep track of the contour by taking picture of the cavity in bright light.

- The cavities rooftops were collapsing because the bending rigidity K of the agar is fixed and there's a critical cell size above which this collapsing occurs (because of it's own weight) ,this rigidity might also depend of the cell height.

  - We had to come to a compromise between the cavities size in order to have solid ones and the fact that with this density of bacteria cavities were empty and many contained two or three bacteria at most which forbid good experimental data.

3.8.2 Systematic detection of the retraction events

It is important for us to define a method enabling us to obtain systematic measurements of the particles tracks during retraction events. In order to do so we need to provide a characterization of the particles motion at these specific moments. From a practical point of view we take the set of particles position over time , namely $\{x_i(t)\}$ for track i. At this point the trajectories are too jittery for two reasons: firstly because there is an optical and detection algorithm based uncertainty over particles center of mass position and also because the bacteria are still subject to thermal fluctuations.

We've opted for the simplest method, defining smoothed trajectories which are simply the track containing the averaged position of the particle over its next n timesteps 3.30:

$$x_i^s(t) = \frac{1}{n}\sum_{k=1}^{n} x_i(t + k\Delta t) \tag{3.30}$$

Figure 3.59 show the effect of such smoothing on a typical track. Most of the jitters is removed with $n = 5\Delta t$. With $n = 50\Delta t$ we have a nice looking trajectory but we are far from the initial positions. Depending what we need to obtain we have to make a trade-off between smoothing and positions accuracy.

Lastly as we are interested in pair of particles we will work with the relative particles position $r_{ij} = x_i - x_j$ over which we apply the previous smoothing, defining the smoothed position r^s and speed $v^s = \frac{\mathrm{d}r^s}{\mathrm{d}t}$. We also need to have a criterion to discriminate between real retraction events and fortuitous approach events. We can suppose that if the speed and position vectors are opposed for a sufficiently long time , that is $C_v^r(t) = \frac{v^s . r^s}{||v^s|| ||r^s||} \approx -1$, this correlation is a sign of retraction. Consider figure 3.60 which shows the timeseries of this correlation parameter C_v^r as well as the relative distance $||r_{ij}||$, we see several long duration events of particle pair approach. It is manifested by a drop of relative distance, but also - as expected - to drop of

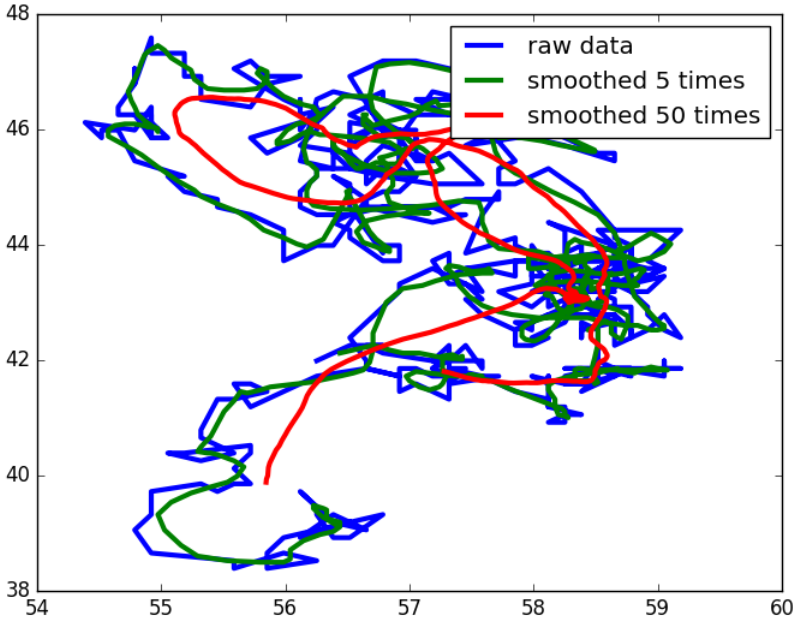

FIGURE 3.59: Effect of trajectory smoothing, raw track and averages 5 (1 sec) and 50 timesteps (5 sec)

C_v^r to the -1 value. With a little faith we can pinpoint retraction events at $t = 5000, 42000, 60000\mu s$

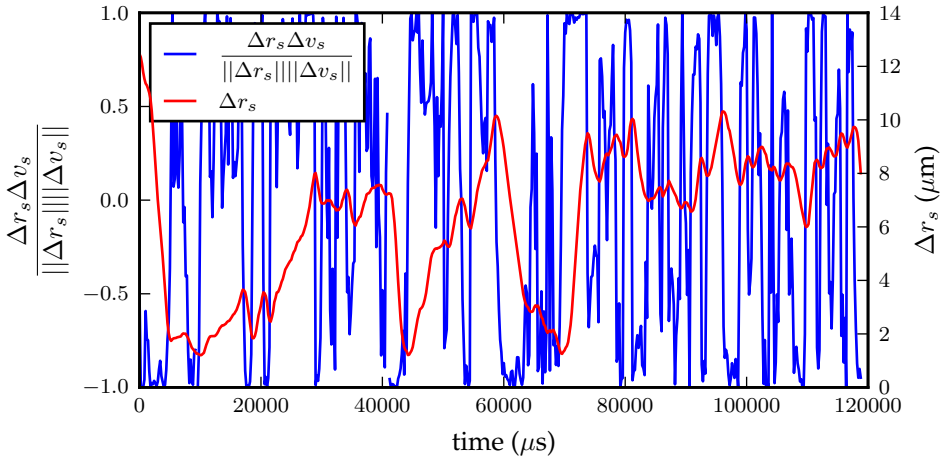

FIGURE 3.60: Effect of trajectory smoothing, raw track and averages 5 (1 sec) and 50 timesteps (5 sec)

Finally a procedure was found in order to semi-automatically detect retraction events and free diffusion ones from these timeseriesand was iterated on hundred of timeseries. It led as to distribution functions of pulling times (fig. 3.61(a)) and diffusion times (3.61(b)). Given the Poisson process we use in the model we'd expect exponentially decaying distribution for both pulling and waiting events, this is hopefully the case. With these data we estimate $\tau_{OFF} = \tau_{ON} \approx 15$.

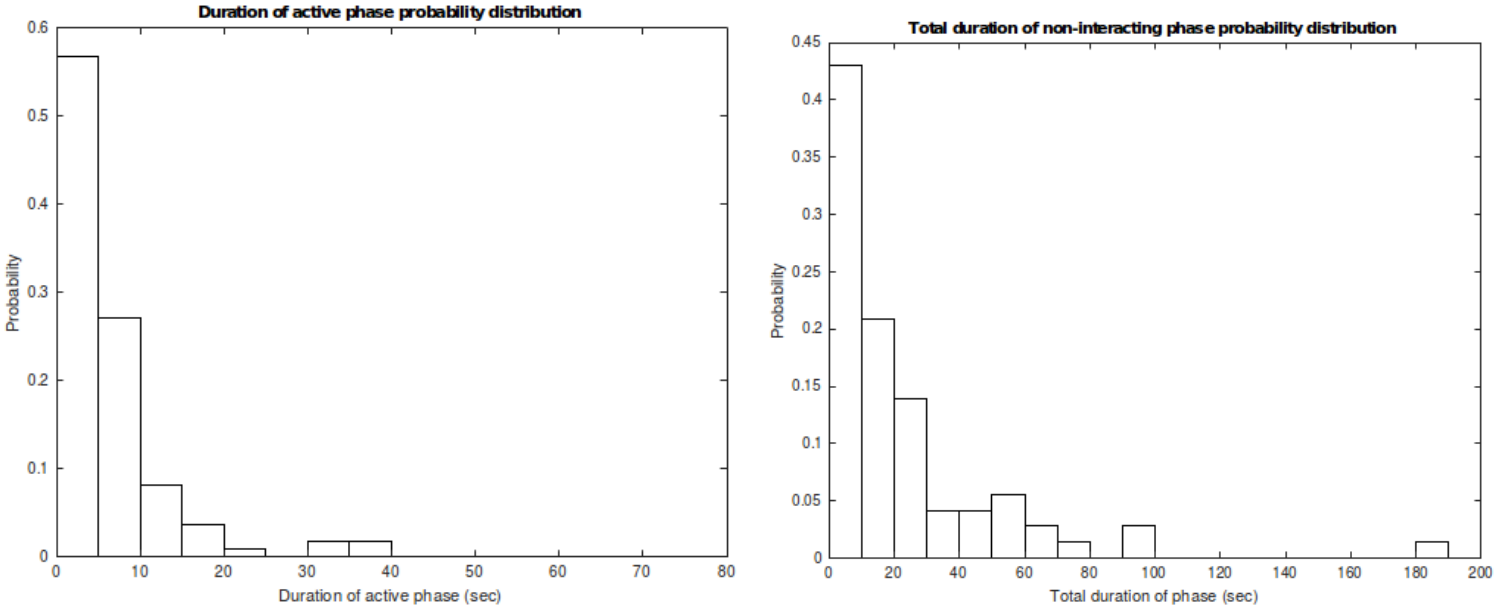

(a) The distribution of pulling times leads to τ_{ON}

(b) The distribution of diffusion times leads to τ_{OFF}

FIGURE 3.61: Experimental data show exponentially decaying distribution for both waiting and pulling times

3.9 Conclusion and further improvements

We started by showing a first model which is more a "proof of concept" that stochastic attraction leads to an athermal type of noise, even though this first model was obviously missing quantitative aspects. Even after adapting the shape of the force potential we were unable to obtain data with good quantitative agreement even though the micropipette experiment seems appealing to the eye.

We then moved to a more evolved modelization, though we failed into obtaining quantitative results for the micropipette experiments, other results are more satisfying such as the of internal diffusion profile inside aggregates. The pursuit of more evolved modelization is probably the best way to obtain more quantitative results. At the expense of increasing number of parameters which might be not well tabulated. However it is useful to mention some possible line of thought for the future.

For instance in a recent study [13] the authors consider a model where pili are modelized as chains of beads, subject to thermal fluctuations and subject to two spring-like potentials: one for the spatial part, modelizing the elongation of the pili, the other part accounting for angular deformations, i.e. the bending of the pili. While we only considered pili existence during the retraction phase in the sense that we don't modelize explicitly the elongation but embedded them in the stochasticity of the attachment, the authors show that the stiffness of their structure might play a role during the elongation phase: for very stiff pili the ability to have high persistence lengths is enhanced meaning it takes shorter time to explore large distances for stiff pili than for flexible ones. In our case the the interaction radius is the only parameter akin to a persistence length: the attachment probability

doesn't depend on the actual length of the pili and this might be problematic. In that sense, it is interesting to introduce a variable attachment probability that depends, at least on the distance between neighbors (for lack of "physical" flexible pili in the model).

We should also note that a study [28] reports that the re-elongation probability might increase with increased exerted force. Therefore we can imagine a feedback mechanism between enhanced pili-pili interactions in aggregates and aggregation itself. This would be interesting in that sense to explore the consequences of such mechanism which might provide a biological justification of aggregation.

The last effects we cannot exclude are the hydrodynamic ones. On closely packed assemblies of particles, hydrodynamic interactions might have a significant role to play. The flow generated by bacteria which are rotating or ballistically propelling in a fluid might affect the motility of neighboring particles and explain some differences between experimental data and numerical ones.

Overall we think that such improvements would have little effects on the properties of the aggregate as a material. Added to the prohibitive cost of such mechanisms - in terms of modelization complexity - we find no additional value for such modification as for now.

Bibliography

[1] Aparna Baskaran and M. Cristina Marchetti. "Nonequilibrium Statistical Mechanics of Self-propelled Hard Rods". In: *Journal of Statistical Mechanics: Theory and Experiment* 2010.04 (Apr. 2010). arXiv: 1002.3831, P04019. ISSN: 1742-5468. DOI: 10.1088/1742-5468/2010/04/P04019. URL: http://arxiv.org/abs/1002.3831.

[2] Aparna Baskaran and M. Cristina Marchetti. "Self-regulation in self-propelled nematic fluids". In: *The European Physical Journal E* 35.9 (2012), pp. 1–8. URL: http://link.springer.com/article/10.1140/epje/i2012-12095-8.

[3] Ch. Becco et al. "Experimental evidences of a structural and dynamical transition in fish school". en. In: *Physica A: Statistical Mechanics and its Applications* 367 (July 2006), pp. 487–493. ISSN: 03784371. DOI: 10.1016/j.physa.2005.11.041. URL: http://linkinghub.elsevier.com/retrieve/pii/S0378437105012689.

[4] Ludovic Berthier and Gilles Tarjus. "The role of attractive forces in viscous liquids". In: *The Journal of Chemical Physics* 134.21 (2011). arXiv: 1103.0432, p. 214503. ISSN: 00219606. DOI: 10.1063/1.3592709. URL: http://arxiv.org/abs/1103.0432.

[5] Eric Bertin, Michel Droz, and Guillaume Gregoire. "Boltzmann and hydrodynamic description for self-propelled particles". In: *Physical Review E* 74.2 (Aug. 2006). arXiv: cond-mat/0601038. ISSN: 1539-3755, 1550-2376. DOI: 10.1103/PhysRevE.74.022101. URL: http://arxiv.org/abs/cond-mat/0601038.

[6] Eric Bertin et al. "Comparison between Smoluchowski and Boltzmann approaches for self-propelled rods". In: *Physical Review E* 92.4 (Oct. 2015). arXiv: 1507.07812. ISSN: 1539-3755, 1550-2376. DOI: 10.1103/PhysRevE.92.042141. URL: http://arxiv.org/abs/1507.07812.

[7] Dapeng Bi et al. "Motility-Driven Glass and Jamming Transitions in Biological Tissues". en. In: *Physical Review X* 6.2 (Apr. 2016). ISSN: 2160-3308. DOI: 10.1103/PhysRevX.6.021011. URL: http://link.aps.org/doi/10.1103/PhysRevX.6.021011.

[8] Nicolas Biais et al. "Cooperative Retraction of Bundled Type IV Pili Enables Nanonewton Force Generation". en. In: *PLoS Biology* 6.4 (2008). Ed. by Manfred Schliwa, e87. ISSN: 1544-9173, 1545-7885. DOI: 10.1371/journal.pbio.0060087. URL: http://dx.plos.org/10.1371/journal.pbio.0060087.

[9] Arianna Bottinelli, David T.J. Sumpter, and Jesse L. Silverberg. "Emergent Structural Mechanisms for High-Density Collective Motion Inspired by Human Crowds". en. In: *Physical Review Letters* 117.22 (Nov. 2016). ISSN: 0031-9007, 1079-7114. DOI: 10.1103/PhysRevLett.117.228301. URL: http://link.aps.org/doi/10.1103/PhysRevLett.117.228301.

[10] Michael E. Cates and Julien Tailleur. "Motility-Induced Phase Separation". en. In: *Annual Review of Condensed Matter Physics* 6.1 (Mar. 2015), pp. 219–244. ISSN: 1947-5454, 1947-5462. DOI: 10.1146/annurev-conmatphys-031214-014710. URL: http://www.annualreviews.org/doi/10.1146/annurev-conmatphys-031214-014710.

[11] Hugues Chaté et al. "Collective motion of self-propelled particles interacting without cohesion". In: *Physical Review E* 77.4 (Apr. 2008), p. 046113. DOI: 10.1103/PhysRevE.77.046113. URL: http://link.aps.org/doi/10.1103/PhysRevE.77.046113.

[12] Leticia F. Cugliandolo, Giuseppe Gonnella, and Antonio Suma. "Rotational and translational diffusion in an interacting active dumbbell system". In: *Physical Review E* 91.6 (2015), p. 062124. URL: http://journals.aps.org/pre/abstract/10.1103/PhysRevE.91.062124.

[13] Hendrick W. de Haan. "Modeling and Simulating the Dynamics of Type IV Pili Extension of Pseudomonas aeruginosa". en. In: *Biophysical Journal* 111.10 (Nov. 2016), pp. 2263–2273. ISSN: 00063495. DOI: 10.1016/j.bpj.2016.09.050. URL: http://linkinghub.elsevier.com/retrieve/pii/S0006349516308840.

[14] Amin Doostmohammadi et al. "Stabilization of active matter by flow-vortex lattices and defect ordering". In: *Nature communications* 7 (2016). URL: http://www.nature.com/ncomms/2016/160203/ncomms10557/full/ncomms10557.html.

[15] Albert Einstein. *Investigations on the Theory of the Brownian Movement*. Courier Corporation, 1956.

[16] Pierre-Gilles de Gennes, Françoise Brochard-Wyart, and David Quéré. *Gouttes, bulles, perles et ondes*. Belin Paris, 2002.

[17] Luca Giomi et al. "Defect annihilation and proliferation in active nematics". In: *Physical review letters* 110.22 (2013), p. 228101. URL: http://journals.aps.org/prl/abstract/10.1103/PhysRevLett.110.228101.

[18] Luca Giomi et al. "Defect dynamics in active nematics". In: *Philosophical Transactions of the Royal Society A: Mathematical, Physical and Engineering Sciences* 372.2029 (Oct. 2014). arXiv: 1403.5254, pp. 20130365–20130365. ISSN: 1364-503X, 1471-2962. DOI: 10.1098/rsta.2013.0365. URL: http://arxiv.org/abs/1403.5254.

[19] Alexander Y. Grosberg and Jean-François Joanny. "Activity induced phase separation". In: *arXiv:1502.08034 [cond-mat]* (Feb. 2015). arXiv: 1502.08034. URL: http://arxiv.org/abs/1502.08034.

[20] Karine Guevorkian et al. "Aspiration of Biological Viscoelastic Drops". In: *Physical Review Letters* 104.21 (May 2010), p. 218101. DOI: 10.1103/PhysRevLett.104.218101. URL: http://link.aps.org/doi/10.1103/PhysRevLett.104.218101.

[21] Dirk Helbing et al. "Simulation of pedestrian crowds in normal and evacuation situations". In: *Pedestrian and evacuation dynamics* 21 (2002), pp. 21–58.

[22] Gary L. Hunter and Eric R. Weeks. "The physics of the colloidal glass transition". In: *Reports on progress in physics* 75.6 (2012), p. 066501. URL: http://iopscience.iop.org/article/10.1088/0034-4885/75/6/066501/meta.

[23] Anthony A. Hyman, Christoph A. Weber, and Frank Jülicher. "Liquid-Liquid Phase Separation in Biology". In: *Annual Review of Cell and Developmental Biology* 30.1 (2014), pp. 39–58. DOI: 10.1146/annurev-cellbio-100913-013325. URL: http://dx.doi.org/10.1146/annurev-cellbio-100913-013325.

[24] Atsushi Ikeda, Ludovic Berthier, and Giulio Biroli. "Dynamic criticality at the jamming transition". In: *The Journal of chemical physics* 138.12 (2013), 12A507. URL: http://scitation.aip.org/content/aip/journal/jcp/138/12/10.1063/1.4769251.

[25] Dumenil G Imhaus AF. "The number of Neisseria meningitidis type IV pili determines host cell interaction." In: *EMBO J 33: 1767-1783* (2014).

[26] Martin Lindén et al. "Force generation in small ensembles of Brownian motors". In: *Physical Review E* 74.2 (Aug. 2006), p. 021908. DOI: 10.1103/PhysRevE.74.021908. URL: http://link.aps.org/doi/10.1103/PhysRevE.74.021908.

[27] Berenike Maier. "The bacterial type IV pilus system – a tunable molecular motor". en. In: *Soft Matter* 9.24 (May 2013), pp. 5667–5671. ISSN: 1744-6848. DOI: 10.1039/C3SM50546D. URL: http://pubs.rsc.org/en/content/articlelanding/2013/sm/c3sm50546d.

[28] Berenike Maier, Michael Koomey, and Michael P. Sheetz. "A force-dependent switch reverses type IV pilus retraction". en. In: *Proceedings of the National Academy of Sciences of the United States of America* 101.30 (July 2004), pp. 10961–10966. ISSN: 0027-8424, 1091-6490. DOI: 10.1073/pnas.0402305101. URL: http://www.pnas.org/content/101/30/10961.

[29] Berenike Maier and Gerard C. L. Wong. "How Bacteria Use Type IV Pili Machinery on Surfaces". English. In: *Trends in Microbiology* 23.12 (Dec. 2015), pp. 775–788. ISSN: 0966-842X, 1878-4380. DOI: 10.1016/j.tim.2015.09.002. URL: /trends/microbiology/abstract/S0966-842X(15)00204-8.

[30] Rahul Marathe et al. "Bacterial twitching motility is coordinated by a two-dimensional tug-of-war with directional memory". In: *Nature Communications* 5 (May 2014). ISSN: 2041-1723. DOI: 10.1038/ncomms4759. URL: http://www.nature.com/doifinder/10.1038/ncomms4759.

[31] M. C. Marchetti et al. "Soft Active Matter". In: *arXiv:1207.2929 [cond-mat, q-bio]* (July 2012). arXiv: 1207.2929. URL: http://arxiv.org/abs/1207.2929.

[32] Samuel R. McCandlish, Aparna Baskaran, and Michael F. Hagan. "Spontaneous segregation of self-propelled particles with different motilities". In: *Soft Matter* 8.8 (2012), pp. 2527–2534. URL: http://pubs.rsc.org/en/content/articlehtml/2012/sm/c2sm06960a.

[33] Nagy Máté et al. "Hierarchical group dynamics in pigeon flocks." In: *Nature, 464(7290) :890893* (2010).

[34] Ken H. Nagai et al. "Collective Motion of Self-Propelled Particles with Memory". In: *Phys. Rev. Lett.* 114 (16 2015), p. 168001. DOI: 10.1103/PhysRevLett.114.168001. URL: http://link.aps.org/doi/10.1103/PhysRevLett.114.168001.

[35] Máté Nagy, István Daruka, and Tamás Vicsek. "New aspects of the continuous phase transition in the scalar noise model (SNM) of collective motion". In: *Physica A: Statistical Mechanics and its Applications*

373 (2007), pp. 445–454. URL: http://www.sciencedirect.com/science/article/pii/S0378437106006510.

[36] Vijay Narayan, Sriram Ramaswamy, and Narayanan Menon. "Long-Lived Giant Number Fluctuations in a Swarming Granular Nematic". en. In: *Science* 317.5834 (July 2007), pp. 105–108. ISSN: 0036-8075, 1095-9203. DOI: 10.1126/science.1140414. URL: http://science.sciencemag.org/content/317/5834/105.

[37] Sandrine Ngo. "Thèse Sandrine". PhD thesis.

[38] Sandrine Ngo et al. "Large-Scale Chaos and Fluctuations in Active Nematics". In: *Physical Review Letters* 113.3 (July 2014), p. 038302. DOI: 10.1103/PhysRevLett.113.038302. URL: http://link.aps.org/doi/10.1103/PhysRevLett.113.038302.

[39] Biais Nicolas et al. "Cooperative Retraction of Bundled Type IV Pili Enables Nanonewton Force Generation". In: *PLoS Biol 6(4): e87.* (2008).

[40] N Ohshima and RM Nerem. "Application of the micropipette technique to the measurement of cultured porcine aortic endothelial cell viscoelastic properties". In: *Journal of biomechanical engineering* 112 (1990), p. 263.

[41] Enno R. Oldewurtel et al. "Differential interaction forces govern bacterial sorting in early biofilms". en. In: *eLife* 4 (Sept. 2015), e10811. ISSN: 2050-084X. DOI: 10.7554/eLife.10811. URL: https://elifesciences.org/content/4/e10811v2.

[42] Anand U. Oza and Jörn Dunkel. "Antipolar ordering of topological charges and universality in active liquid crystals". In: *arXiv:1507.01055 [cond-mat, physics:physics]* (July 2015). arXiv: 1507.01055. URL: http://arxiv.org/abs/1507.01055.

[43] Anand U. Oza and Jörn Dunkel. "Nematic ordering of topological defects in active liquid crystals". In: *arXiv preprint arXiv:1507.01055* (2015). URL: http://arxiv.org/abs/1507.01055.

[44] Francis Perrin. "Étude mathématique du mouvement brownien de rotation". In: *Annales scientifiques de l'École Normale Supérieure*. Vol. 45. 1928, pp. 1–51.

[45] Fernando Peruani, Andreas Deutsch, and Markus Baer. "Nonequilibrium clustering of self-propelled rods". In: *Physical Review E : Statistical, Nonlinear, and Soft Matter Physics* 74.3 (Sept. 2006), 030904(R). DOI: 10.1103/PhysRevE.74.030904. URL: https://hal.archives-ouvertes.fr/hal-00905230.

[46] Anton Peshkov et al. "Nonlinear Field Equations for Aligning Self-Propelled Rods". en. In: *Physical Review Letters* 109.26 (Dec. 2012). ISSN: 0031-9007, 1079-7114. DOI: 10.1103/PhysRevLett.109.268701. URL: http://link.aps.org/doi/10.1103/PhysRevLett.109.268701.

[47] Tim Sanchez et al. "Spontaneous motion in hierarchically assembled active matter". In: *Nature* 491.7424 (Nov. 2012), pp. 431–434. ISSN: 0028-0836, 1476-4687. DOI: 10.1038/nature11591. URL: http://www.nature.com/doifinder/10.1038/nature11591.

[48] Leonard M. Sander. "Diffusion-limited aggregation: A kinetic critical phenomenon?" en. In: *Contemporary Physics* 41.4 (July 2000), pp. 203–218. ISSN: 0010-7514, 1366-5812. DOI: 10.1080/001075100409698. URL: http://www.tandfonline.com/doi/abs/10.1080/001075100409698.

[49] Xia-qing Shi and Yu-qiang Ma. "Topological structure dynamics revealing collective evolution in active nematics". In: *Nature Communications* 4 (Dec. 2013). ISSN: 2041-1723. DOI: 10.1038/ncomms4013. URL: http://www.nature.com/doifinder/10.1038/ncomms4013.

[50] Injong Rhee NCSU Minsu Shin, Seongik Hong NCSU Kyunghan Lee, and Song Chong. "Human mobility patterns and their impact on routing in human-driven mobile networks". In: *HotNets-VI*. 2007. URL: http://conferences.sigcomm.org/hotnets/2007/papers/hotnets6-final108.pdf.

[51] A. P. Solon and J. Tailleur. "Flocking with discrete symmetry: the 2d Active Ising Model". In: *Physical Review E* 92.4 (Oct. 2015). arXiv: 1506.05749. ISSN: 1539-3755, 1550-2376. DOI: 10.1103/PhysRevE.92.042119. URL: http://arxiv.org/abs/1506.05749.

[52] Alexandre P. Solon, Hugues Chaté, and Julien Tailleur. "From phase to microphase separation in flocking models: The essential role of nonequilibrium fluctuations". In: *Physical review letters* 114.6 (2015), p. 068101. URL: http://journals.aps.org/prl/abstract/10.1103/PhysRevLett.114.068101.

[53] Pragya Srivastava, Prashant Mishra, and M. Cristina Marchetti. "Negative stiffness and modulated states in compressible active nematics". In: *arXiv:1606.08786 [cond-mat]* (June 2016). arXiv: 1606.08786. URL: http://arxiv.org/abs/1606.08786.

[54] Johannes Taktikos et al. "Pili-Induced Clustering of N. gonorrhoeae Bacteria". In: *PLOS ONE* 10.9 (Sept. 2015), e0137661. ISSN: 1932-6203. DOI: 10.1371/journal.pone.0137661. URL: http://journals.plos.org/plosone/article?id=10.1371/journal.pone.0137661.

[55] Michael Tennenbaum et al. "Mechanics of fire ant aggregations". In: *Nature Materials* 15.1 (Oct. 2015), pp. 54–59. ISSN: 1476-1122, 1476-4660. DOI: 10.1038/nmat4450. URL: http://www.nature.com/doifinder/10.1038/nmat4450.

[56] Eugene Michael Terentjev and David A. Weitz. *The Oxford Handbook of Soft Condensed Matter*. Oxford University Press, USA, 2015. URL: http://books.google.com/books?hl=en&lr=&id=d726BwAAQBAJ&oi=fnd&pg=PP1&dq=%22in+a+liquid+that,+despite+the+density+di%EF%AC%80erence+between+the%22+%22the+work+of+Einstein+and+Perrin+laid+the+foundations+of%22+%22colloids+are+model+systems,+especially+when+experiments%22+&ots=SgHpAZNVsC&sig=2rEHu-6abCNH5oZLL0oFap-pK_U.

[57] John Toner and Yuhai Tu. "Long-range order in a two-dimensional dynamical XY model: how birds fly together". In: *Physical Review Letters* 75.23 (1995), p. 4326. URL: http://journals.aps.org/prl/abstract/10.1103/PhysRevLett.75.4326.

[58] Tamás Vicsek et al. "Novel Type of Phase Transition in a System of Self-Driven Particles". In: *Phys. Rev. Lett.* 75 (6 1995), pp. 1226–1229. DOI: 10.1103/PhysRevLett.75.1226. URL: http://link.aps.org/doi/10.1103/PhysRevLett.75.1226.

[59] Gandimohan M Viswanathan et al. "Optimizing the success of random searches". In: *Nature* 401.6756 (1999), pp. 911–914.

[60] Arthur J. Vromans and Luca Giomi. "Orientational properties of nematic disclinations". In: *arXiv preprint arXiv:1507.05588* (2015). URL: http://arxiv.org/abs/1507.05588.

[61] Axel Walther Andreas; Müller. "Janus Particles: Synthesis, Self-Assembly, Physical Properties, and Applications". In: *Chemical Reviews. 113 (7)* (2013).

[62] Christoph A. Weber et al. "Formation and dissolution of bacterial colonies". en. In: *Physical Review E* 92.3 (Sept. 2015). ISSN: 1539-3755, 1550-2376. DOI: 10.1103/PhysRevE.92.032704. URL: http://link.aps.org/doi/10.1103/PhysRevE.92.032704.

[63] Simon N. Weber, Christoph A. Weber, and Erwin Frey. "Binary Mixtures of Particles with Different Diffusivities Demix". In: *Physical Review Letters* 116.5 (Feb. 2016). arXiv: 1505.00525. ISSN: 0031-9007, 1079-7114. DOI: 10.1103/PhysRevLett.116.058301. URL: http://arxiv.org/abs/1505.00525.

[64] Hugo Wioland et al. "Confinement Stabilizes a Bacterial Suspension into a Spiral Vortex". en. In: *Physical Review Letters* 110.26 (June 2013). ISSN: 0031-9007, 1079-7114. DOI: 10.1103/PhysRevLett.110.268102. URL: http://link.aps.org/doi/10.1103/PhysRevLett.110.268102.

[65] T. A. Witten Jr. and L. M. Sander. "Diffusion-limited aggregation, a kinetic critical phenomenon". In: *Physical Review Letters* 47 (Nov. 1981), pp. 1400–1403. DOI: 10.1103/PhysRevLett.47.1400.

[66] Yilin Wu et al. "Periodic reversal of direction allows Myxobacteria to swarm". en. In: *Proceedings of the National Academy of Sciences* 106.4 (Jan. 2009), pp. 1222–1227. ISSN: 0027-8424, 1091-6490. DOI: 10.1073/pnas.0811662106. URL: http://www.pnas.org/content/106/4/1222.

[67] Bo Xing and Wen-Jing Gao. *Innovative computational intelligence: a rough guide to 134 clever algorithms*. Vol. 62. Springer, 2014.

[68] V. Zaburdaev, S. Denisov, and J. Klafter. "Levy walks". In: *Reviews of Modern Physics* 87.2 (June 2015). arXiv: 1410.5100, pp. 483–530. ISSN: 0034-6861, 1539-0756. DOI: 10.1103/RevModPhys.87.483. URL: http://arxiv.org/abs/1410.5100.

[69] Vasily Zaburdaev et al. "Uncovering the Mechanism of Trapping and Cell Orientation during Neisseria gonorrhoeae Twitching Motility". en. In: *Biophysical Journal* 107.7 (Oct. 2014), pp. 1523–1531. ISSN: 00063495. DOI: 10.1016/j.bpj.2014.07.061. URL: http://linkinghub.elsevier.com/retrieve/pii/S0006349514008091.

[70] Johan Zakrisson et al. "Rigid multibody simulation of a helix-like structure: the dynamics of bacterial adhesion pili". In: *European Biophysics Journal* 44.5 (2015), pp. 291–300. ISSN: 1432-1017. DOI: 10.1007/s00249-015-1021-1. URL: http://dx.doi.org/10.1007/s00249-015-1021-1.

[71] H. P. Zhang et al. "Collective motion and density fluctuations in bacterial colonies". en. In: *Proceedings of the National Academy of Sciences* 107.31 (Aug. 2010), pp. 13626–13630. ISSN: 0027-8424, 1091-6490. DOI: 10.1073/pnas.1001651107. URL: http://www.pnas.org/content/107/31/13626.

université PARIS-SACLAY
ÉCOLE DOCTORALE
Physique en île-de-France (EDPIF)

Titre : Descriptions continues et stochastiques de la matière active

Mots clefs : Matière active, Modélisation, Biologie

Résumé : Le but de cette thèse est d'étudier des modèles simples d'agents "auto-propulsés": capables de générer du mouvement en consommant de l'énergie provenant de leur environnement, sans forçage externe. Deux modèles de ce type ont été étudiés lors de cette thèse:
-Dans un premier temps un modèle de type "Vicsek" a été étudié, c'est à dire que les particules représentées par un couple (position,vitesse) ont une évolution régie par des règles simples d'alignement et d'auto-propulsion à vitesse constante. Ici, l'alignement est nématique: les particlules s'alignent selon leur grand axe, au contraire d'un alignement polaire il se fait indifféremment tête à queue ou tête à tête. Par rapport aux précédents modèles de ce type la première nouveauté est l'introduction d'une pseudo répulsion (dans l'esprit Vicsek, modélisée par un terme de type couple) donnant une extension spatiale à ces particules. La seconde nouveauté est la présence d'un "taux de retournement" qui rend compte du temps de persistence de la direction de l'auto-propulsion. Dans cette partie nous décrivons divers diagrammes de phases de ce nouveau modèle qui montrent de nouvelles phases non répertoriées précédemment: les arches mais aussi des bandes "smectiques", quelques propriétés de ces structures ont été mesurées. Des équations hydrodynamiques obtenues via la méthode "Boltzmann-Ginzburg-Landau" ayant par ailleurs été dérivées nous effectuons une comparaison: la plupart des phases ainsi que certaines de leurs propriétés sont retrouvés dans le modèle hydrodynamique.
-Dans un second temps, nous étudions la bactérie Neisseria Meningitidis qui présente la particularité de générer des "pili", filaments de plusieurs micromètres de long. En dépolymérisant ces structures, à vitesse constantes ($\approx$1 μm/s), elle est capable de en générer des forces gigantesques pour le vivant ($\approx$100 pN). Cette bactérie a tendance à former des agrégats sphériques, présentant toutes les propriétés d'un liquide, pour coloniser l'organisme de l'hôte. Des mesures de viscosité et de tension de surface de ces agrégats ont montré le rôle crucial du nombre de pili. Fort de ces constats nous avons bati un modèle microscopique dont la particularité est l'introduction de potentiels stochastiquement attractifs, c'est à dire que les particles transitent entre un état attractif et un état diffusif. Cette partie retranscrit l'évolution du modèle au cours du temps. Nous avons pu reproduire certaines propriétés des agrégats, nous avons notamment mis en évidence une variation de la diffusion entre le centre et le bord des agrégats qui recoupe les données expérimentales.

Title : Stochastic and continuous descriptions of active matter

Keywords : Active matter, Modelization, Biology

Abstract : This thesis purpose is to study simple "self-propelled" agents models: they are able to generate motion by consumming energy comming from their environment, without external forcing. Two models of that kind have been studied:
-In the first part a Vicsek-style model has been studied, that is particles are modeled by a couple (position,velocity) which evolution is dictated by simple rules of alignment and self-propulsion at constant speed. Here the alignment is nematic particles align along their long axis and alignment is not polar, contrarily to a polar alignment particles don't discriminate between head and tail . Compared to previous models of this type, the first novelty is the introduction of a pseudo-repulsion (in the Vicsek-spirit, modelized by a torque-like term) providing spatial extension to these particles. The second addition is a flipping rate which renders the persistence time of the direction of self-propulsion. In this part we describe several phase diagrams of this new model which show new phases not previously classified: arches but also "smectic" bands, some propreties of these structures have been measured. Hydrodynamic equations from the "Boltzmann-Ginzburg-Landau" method have been also developped, comparisons are performed: the hydrodynamic model recovers most phases and some of their propreties.
-In the second part we study Neisseria Meningitidis, a bacteria which particularity is to generate pili: filamentous structures several micrometers long. By depolymerizing these structures at constant speed ($\approx$1μm/s), it is able to generate gigantic forces for the living word ($\approx$ 100pN). This bacteria has a tendancy to form spherical aggregates, showing all propreties of a liquid, in order to colonize the host organism. Viscosity and surface tension measure of these aggregates have shown the crucial role of the pili number. Using these data we've built a microscopic model which particularity is the presence of a stochastically attractive potential, that is to say that particles are transiting between an attractive state and a diffusive one. This part relates the model evolution in time. We've ben able to reproduce some aggregate propreties, in particular we've highlighted a variation of the diffusion between aggregate center and edges which fits experimental data.

Université Paris-Saclay
Espace Technologique / Immeuble Discovery
Route de l'Orme aux Merisiers RD 128 / 91190 Saint-Aubin, France